



Exploration of the peptidergic modulation of pain

Etienne Clauss-Creusot

► To cite this version:

Etienne Clauss-Creusot. Exploration of the peptidergic modulation of pain. Neuroscience. Université de Strasbourg, 2023. English. NNT : 2023STRAJ080 . tel-04412707

HAL Id: tel-04412707

<https://theses.hal.science/tel-04412707>

Submitted on 23 Jan 2024

HAL is a multi-disciplinary open access archive for the deposit and dissemination of scientific research documents, whether they are published or not. The documents may come from teaching and research institutions in France or abroad, or from public or private research centers.

L'archive ouverte pluridisciplinaire **HAL**, est destinée au dépôt et à la diffusion de documents scientifiques de niveau recherche, publiés ou non, émanant des établissements d'enseignement et de recherche français ou étrangers, des laboratoires publics ou privés.

ÉCOLE DOCTORALE DES SCIENCES DE LA VIE ET DE LA SANTÉ
UPR 3212 - Institut des Neurosciences Cellulaires et Intégratives

THÈSE

Présentée par :

Etienne Clauss--Creusot

Soutenue le : 31 Octobre 2023

Pour obtenir le grade de : **Docteur.e de l'Université de Strasbourg**
Discipline / Spécialité : **Neurosciences**

Exploration of peptidergic modulation of pain

Exploration de la modulation peptidergique de la douleur

Thèse dirigée par :

Mr. Alexandre Charlet

DR, Université de Strasbourg, France.

Co-dirigée par :

Mr. Pascal Darbon

MCU, Université de Strasbourg, France.

Rapportrices :

Mme. Julie Le Merrer

DR, Inserm U1253, iBrain, Tours, France.

Mme. Françoise Muscatelli

DR, Parc scientifique de Luminy, Marseille, France.

Examinateur interne :

Mr. Didier Desaintjan

CR, Université de Strasbourg, France.

Examinateur externe :

Mr. Marc Landry

Pr, Université de Bordeaux, France.

Remerciements

Tout d'abord, je tiens à remercier les membres de mon jury de thèse d'avoir accepté d'évaluer mon travail. Une pensée toute particulière pour Didier qui faisait déjà partie de mon comité de suivi de thèse, et dont les conseils scientifiques m'ont été d'une grande aide.

Alex, merci de m'avoir accueilli dans l'équipe et fais confiance. Ta bonne humeur constante et ton optimisme ont rendu la vie au labo très appréciable. Enfin, j'ai particulièrement apprécié que tu me considères comme un collègue, prêt à changer complètement d'avis et de façon de faire tant que la justification tenait la route. Et merci pour les relectures de ma thèse, c'était presque dur de suivre un tel rythme. Merci à Pascal également, tu as su trouver du temps pour t'impliquer, réfléchir et discuter de l'avancement de mes projets malgré les innombrables autres responsabilités que tu portes. Si j'ai fait cette thèse dans ce domaine, c'est en partie grâce à Angel qui, tout comme pour la grimpe, a su me donner le goût de l'électrophysiologie. Ton soutien a été (surtout à certains moments) très important. Merci, ce fut un plaisir de travailler avec toi très cher Guy.

Je souhaite tout particulièrement remercier Sophie et Dom, vous faites un travail monstrueux (que ce soit en quantité ou en qualité). Malgré votre rôle pas facile vous restez d'une gentillesse et d'une humanité remarquable. Votre aide a été très précieuse tant sur l'aspect pratique des chirurgies que sur la manipulation des animaux (et des rats en particulier, sans vous, je n'aurai probablement pas réussi à m'y familiariser). Merci beaucoup.

Merci à Philippe pour ton expertise sur l'électrophysiologie, mais également pour ton soutien quand c'était nécessaire.

En vrac (parce que c'est mieux qu'en sachet), merci aux copaines de promos/du labo : Valod, Jarion, Toto, Baptiste, Colette, Robin, Cacamille, Tatinoz, Karim, Fred, Luigi, Quentin, Flo², Zélia, Louise et forcément toutes les autres que j'oublie, mais je sais que vous vous reconnaîtrez ! Mention spéciale pour Sarah, tu sais que je vais pas faire de long texte donc merci pour ta présence au quotidien et toutes les autres choses que nous partageons.

Merci aux copaines d'avant le master : Mélo, Maïka, Léo, DumDum, Ozan, Ludo, Arnaud et les autres.

Merci à ma famille pour le soutien en toutes circonstances.

Enfin, iels seraient trop nombreu.ses à citer alors un énorme non-remerciement aux personne qui détruisent la planète ainsi qu'à celles qui m'ont motivé à ouvrir le pôle BEE.

Table of content

1	Résumé en français	10
2	Introduction	14
2.1	Pain	14
2.1.1	Definition	14
2.1.2	Physiology of pain	14
2.1.2.1	The nociceptors	14
2.1.2.2	Spinal cord integration	15
2.1.2.3	Projection to the supraspinal centers	16
2.1.2.4	Descending control of pain	18
2.1.2.5	The amygdala in pain	18
2.1.2.6	The periaqueductal gray in pain	19
2.1.3	Pain study in rodents	21
2.1.3.1	Mechanical tests	23
2.1.3.2	Thermal tests	23
2.1.3.3	Chemical tests	24
2.1.3.4	Animal models of pain	24
2.2	The relaxin-3 system	26
2.2.1	The relaxin family	26
2.2.2	The relaxin receptors	28
2.2.3	RXFP3	29
2.2.3.1	Intracellular signaling	30
2.2.3.2	Relaxin-3/RXFP3 interaction's specificity	31
2.2.3.3	RXFP3 (ant)agonist development	31
2.2.3.4	RXFP3 activation and neuronal electric activity	33
2.2.3.5	Distribution	33
2.2.4	Relaxin-3: synthesis, distribution and function	34

2.2.4.1	Nucleus incertus, relaxin-3 and stress.....	35
2.2.4.2	Relaxin-3 and pain	35
2.2.5	Relaxin-3 and the amygdala	37
2.2.5.1	The basal amygdala	37
2.3	The oxytocin system.....	40
2.3.1	The oxytocin.....	40
2.3.1.1	Synthesis.....	40
2.3.1.2	Distribution and release.....	41
2.3.1.3	Oxytocin Receptor.....	43
2.3.1.4	GrabOT a tuned OTR.....	44
2.3.2	Oxytocin and pain	45
2.3.2.1	Periphery effect.....	45
2.3.2.2	Spinal effect.....	46
2.3.2.3	Supraspinal effect.....	47
2.4	Ph.D objectives.....	48
3	Relaxin-3	50
3.1	Material & Method	50
3.1.1.1	Animals.....	50
3.1.1	Stereotaxic injection.....	50
3.1.2	Electrophysiological recordings.....	51
3.1.2.1	Slice preparation	51
3.1.2.2	Approaching the cell.....	52
3.1.2.3	Cell-attached configuration.....	52
3.1.2.4	Whole-cell configuration	53
3.1.3	Immunohistochemistry	54
3.1.4	Data analysis	54
3.1.5	Statistical analysis.....	55

3.2	Results	56
3.2.1	SOM interneurons of the basal amygdala	56
3.2.1.1	Chapter 1: the Gad65 mice	56
3.2.1.2	Chapter 2: the somatostatin-Cre mice	58
3.2.2	Projection neurons of the basal amygdala	59
3.2.3	SOM interneurons of the CeL	61
3.2.4	Neurons of the CeM.....	62
3.2.5	Conclusion	64
4	GrabOT.....	66
4.1	Material & Method	66
4.1.1	Animals	66
4.1.2	Stereotaxic injection.....	66
4.1.3	Slice preparation	67
4.1.4	OT1.0-sensor imaging	67
4.1.5	Analysis.....	68
4.1.6	Statistical analysis.....	69
4.2	Pharmacological characterization - Results.....	70
4.2.1	Oxytocin	70
4.2.2	Vasopressin	70
4.2.3	TGOT	71
4.2.4	Conclusion	71
4.3	Article: An analgesic pathway from parvocellular oxytocin neurons to the periaqueductal gray in rats	74
4.3.1	Introduction	74
4.3.2	Results	74
4.3.3	Personal contribution	75
5	Discussion.....	116

5.1	Relaxin-3 discussion.....	116
5.1.1	Mice models.....	116
5.1.1.1	Gad65.....	116
5.1.1.2	Male vs female	117
5.1.1.3	Naïve vs painful mice	117
5.1.2	Technical considerations	118
5.1.2.1	Electrophysiology as the only method	118
5.1.2.2	Protocol and analysis	119
5.1.2.3	Recordings of BA projection neurons	120
5.1.3	Conclusion & perspective	121
5.2	Oxytocin discussion.....	122
5.2.1	Technical considerations on the Grabot	122
5.2.1.1	Oxytocin and Vasopressin.....	122
5.2.1.2	Ex vivo vs culture EC ₅₀	122
5.2.1.3	OT1.0, OT3.0 or OT42.0?	123
5.2.2	Scientific considerations on the vIPAG article	123
5.2.2.1	What circuit for the OT-dependent antinociception?.....	123
5.2.2.2	Sexual dimorphism in the vIPAG	126
5.2.1	Conclusion	127
6	Appendix	128
6.1	Statistic table	128
6.2	List of publications.....	130
6.3	List of communications	131
6.4	Emerging role of astrocytes in oxytocin-mediated control of neural circuits and brain functions	132
6.1	Rôle émergent des astrocytes dans le contrôle des circuits neuronaux et des fonctions cérébrales modulées par l'ocytocine.....	144

6.2 Star protocol: Calcium imaging and BAPTA loading of amygdala astrocytes in mouse brain slices.....	156
6.3 Publication: CaMK1D signalling in AgRP neurons promotes ghrelin-mediated food intake.....	182
6.4 La grande traversée de l'ocytocine dans le système nerveux pour calmer les douleurs	206
7 References.....	210

Abbreviations

aCSF: artificial cerebro-spinal fluid	INSL-3/4/5/6:
AN: accessory nuclei	LA: lateral amygdala
AUC: area under the curve	LDCV: large dense-cored vesicles
AVP: vasopressin	magnOT: magnocellular OTergic neurons
BA: basal amygdala	OT: oxytocin
CCK: cholecystokinin	OTR: OT receptor
CeA: central amygdala	PAG: periaqueductal gray
CeL: lateral part of the CeA	parvOT: parvocellular OTergic neurons
CeM: medial part of the CeA	PN: projection neurons
CFA: complete Freund's adjuvant	PV: parvalbumin
CRF: corticotrophin releasing factor	PVN: paraventricular nucleus of the hypothalamus
CRF ₁ : CRF receptor	RVM: rostral ventromedial medulla
DIO: double-floxed inverted open reading frame	RXFP1/2/3/4: relaxin/insulin-like family peptide receptors type 1/2/3/4
DREADD: designer receptors exclusively activated by designer drugs	s.c.: subcutaneous
EPSC: excitatory post synaptic currents	SOM: somatostatin
ERE: estrogen regulatory element	SON: supraoptic nucleus of the hypothalamus
GPCR: G protein-coupled receptor	TGOT: [Thr ⁴ , Gly ⁷]OT
Grab _{OT} : GPCR activation-based sensor specific for OT	V1a: AVP receptor
ICM: intercalated cell mass	VIP: vasointestinal peptide
i.c.v.: intracerebroventricular	vIPAG: ventrolateral PAG
i.p.: intraperitoneal	WDR: wide dynamic range
IPSC: inhibitory post synaptic currents	

1 Résumé en français

La douleur est une expérience multi-dimensionnelle comprenant une composante sensorielle et émotionnelle. Elle sert de signal d'alerte pour protéger l'organisme d'une menace potentielle ou réelle. Cependant, elle peut devenir pathologique, et lorsqu'elle dure plus de 3 mois, on parle de douleur chronique. Ces douleurs chroniques peuvent affecter jusqu'à 30% de la population mondiale et s'accompagner de comorbidités telles que l'anxiété ou la dépression. Ces différents facteurs font des douleurs chroniques un enjeu socio-économique majeur.

En condition physiologique, les stimulations nociceptives, potentiellement dommageables à l'organisme, sont détectées par le système nerveux périphérique. Ces informations nociceptives vont être intégrées une première fois dans la moelle épinière, puis remontées jusque dans les structures supra-spinales où elles seront intégrées et seront potentiellement traduites en une expérience douloureuse. Parmi ces structures, on peut retrouver la substance grise péréiaqueducale ventrolatérale (vIPAG), le thalamus, différents cortex, l'amygdale, etc. La douleur peut être modulée par de nombreux facteurs, et parmi eux, les neuropeptides jouent un rôle important. Par exemple, l'ocytocine peut diminuer la sensation douloureuse en agissant sur les nocicepteurs de la peau ou des ganglions rachidiens, ou encore en inhibant les neurones de la moelle épinière. Il existe également des neuropeptides moins célèbres, comme la relaxine-3, qui font l'objet d'études préliminaires suggérant un rôle antinociceptif.

Je me suis donc intéressé au cours de ma thèse à l'effet de ces peptides dans le contrôle de la douleur. Mon projet principal était l'étude de l'effet de la relaxine-3 dans l'amygdale. Ce dernier ne s'étant pas révélé concluant, je me suis redirigé sur l'étude de l'effet neuromodulateur de l'ocytocine, notamment au sein de la vIPAG, et de son impact sur la douleur. Afin de faciliter la lecture, j'ai donc divisé l'écriture de ma thèse en deux parties principales, traitant chacune des deux projets sur lesquels j'ai pu travailler.

La relaxine-3 est un peptide découvert au début des années 2000 faisant partie de la famille des relaxines. Celles-ci sont composées de 51 acides aminé, possèdent 2 chaînes (A et B), et une séquence caractéristique 'RXXXRXX(I/V)' essentielle pour la

liaison à leurs récepteurs. La relaxine-3 est majoritairement synthétisée dans le système nerveux central, et plus particulièrement dans le *Nucleus Incertus*, une structure du tronc cérébral située juste sous le 4^{ème} ventricule. Ce peptide agit principalement au travers d'un récepteur : le récepteur de la famille des relaxines de type 3 (RXFP3). Ce récepteur possède 7 domaines transmembranaires et est couplé à une protéine G_i. Comme tous les récepteurs couplés à une protéine G, l'activation de RXFP3 va agir sur de nombreuses cascades intracellulaires, dont l'inhibition de l'adénylate cyclase, l'augmentation de ERK1/2 phosphorylés ou encore l'hyperpolarisation de la membrane plasmique et donc l'inhibition de l'activité électrique des neurones. RXFP3 est exprimé dans de nombreuses structures cérébrales, dont l'amygdale, où des fibres relaxinergiques ont également été mises en évidence.

L'amygdale est une structure connue pour donner une valence émotionnelle à un événement. Elle est composée de plusieurs noyaux et ceux étant principalement impliqués dans le contrôle des émotions sont l'amygdale basolatérale (BLA) et centrale (CeA). Les informations sensorielles en provenance des cortex ou du thalamus sont envoyés à la BLA qui les traitera et les redirigera vers la CeA qui les enverra vers certaines structures du tronc cérébral par exemple pour produire une réponse comportementale adaptée. Bien que la BLA et la CeA possèdent une cytoarchitecture différente, on retrouve dans ces deux structures des fibres relaxinergiques ainsi que le récepteur RXFP3, majoritairement présent sur les interneurones exprimant la somatostatine (SOM). Ainsi, l'équipe de Marc Landry à Bordeaux s'est intéressé à l'effet de l'injection d'un agoniste de RXFP3 dans la BLA de rongeurs. Ces rongeurs ont au préalable reçu une injection d'un adjuvant complet de Freund dans l'une des pattes postérieures afin de déclencher une douleur inflammatoire. L'injection de l'agoniste est ensuite réalisée juste avant de faire des tests nociceptifs aux rongeurs. L'équipe a ainsi pu observer que l'injection de l'agoniste entraîne une ré-augmentation transitoire du seuil nociceptif, qui est bloquée par l'injection simultanée d'un antagoniste à RXPF3. Il semblerait donc que l'activation de RXPF3 au sein de la BLA induise un effet anti-nociceptif.

Ainsi, l'objectif de ma thèse était de caractériser l'effet de l'activation de RXFP3 au sein de la BLA. Je me suis intéressé à l'effet sur l'activité électrique du réseau de l'amygdale et ai donc effectué des enregistrements électrophysiologiques d'interneurones et de neurones de projection identifiés au préalable. Pour cela, j'ai utilisé une lignée de souris transgénique où j'ai pu faire exprimer la GFP dans les neurones SOM de la BLA ou de la CeA afin de les identifier. La CeA étant la sortie principale de l'amygdale, j'ai également identifié les neurones de la BLA projetant sur la CeA par un traçage rétrograde. J'ai ainsi pu enregistrer électrophysiologiquement l'évolution de l'activité électrique de ces neurones en réponses à l'application des agonistes de RXFP3. Je n'ai jamais pu observer de variation d'activité des neurones de la BLA ou de la CeA après applications de ces agonistes. L'ensemble des approches et des protocoles utilisés n'ont pas permis de mettre en évidence un effet significatif de la relaxine-3 sur le fonctionnement du réseau neuronal amygdalien. Nous avons décidé, après 2 années sur ce projet, de tester un autre neuropeptide, dont les effets sur la perception douloureuse sont avérés.

Pour cela, j'ai participé à un projet étudiant l'effet de l'ocytocine sur la douleur. L'ocytocine (OT) est un nonapeptide hypothalamique, agissant sur un récepteur couplé à des protéines G (OTR), principalement décrit dans le système nerveux central pour être couplé à une protéine G_q et induire une augmentation de l'activité électrique des neurones. L'OT est impliquée dans de nombreuses fonctions, allant de l'accouchement au comportement maternel, et l'une de ses fonctions est la modulation de la douleur. De précédentes études ont montré que l'OT peut, suite à sa libération dans le sang, agir sur les nocicepteurs dans les ganglions rachidiens ou la peau. Elle peut également être libérée dans la moelle épinière pour inhiber les neurones sensoriels de cette dernière. Des OTRs ont également été retrouvés dans l'une des structures principales des contrôles descendants de la douleur : la vIPAG. Nous nous sommes donc demandé si l'ocytocine pouvait également moduler la douleur indirectement en agissant sur des structures des contrôles descendants.

Tout d'abord, en collaboration avec l'équipe de Valery Grinevich à Mannheim, nous avons développé une lignée de rats exprimant la Cre recombinase sous le contrôle du promoteur de l'OTR. Cet outil nous a permis de faire exprimer la GFP par les cellules exprimant les OTR afin de les identifier et d'enregistrer leur activité

électrophysiologique. Ainsi, nous avons pu montrer que ces neurones de la vIPAG réagissent à l'application d'agoniste de l'OTR. Ensuite, nous avons réalisé des expériences de traçages et avons observé la présence de fibres ocytocinergiques en provenance de l'hypothalamus à proximité des neurones de la vIPAG exprimant l'OTR. Grâce à l'utilisation d'un OTR modifié permettant de détecter l'OT, nous avons montré que la stimulation optogénétique de ces fibres permettait la libération d'OT dans la vIPAG. De plus, nous avons montré en électrophysiologie *in vivo* que cette stimulation augmentait l'activité d'un quart des neurones de la vIPAG et diminuait l'activité des neurones de la moelle épinière. Enfin, à l'aide de tests nociceptifs chez les rats, nous avons montré que la stimulation des fibres ocytocinergiques dans la vIPAG entraîne un effet anti-nociceptif réversible chez des animaux femelles et mâles souffrant de douleur inflammatoire. Ma contribution s'est principalement faite sur l'utilisation du senseur d'OT. En parallèle, j'ai également réalisé la caractérisation pharmacologique *ex vivo* de ce récepteur en testant plusieurs doses de l'agoniste de l'OTR, ainsi que de la spécificité de réponse de ce récepteur.

Cette étude a ainsi permis de mettre en évidence une nouvelle population de neurones ocytocinergiques hypothalamiques qui, par l'intermédiaire de la vIPAG, peuvent moduler les seuils nociceptifs chez le rongeur.

Mes travaux de thèse ont ainsi permis dans un premier temps de montrer que l'application d'agonistes à RXFP3 ne permet pas de modifier l'activité électrique des réseaux neuronaux de l'amygdale basolatérale et centrale chez des souris naïves. Dans un deuxième temps, ces travaux ont mis en lumière une nouvelle voie anatomique où des neurones ocytocinergiques hypothalamiques activent des neurones de la vIPAG, eux-mêmes inhibant des neurones de la moelle épinière afin de moduler les seuils nociceptifs chez les rats femelles et mâles. De plus, la mise en place et la caractérisation du senseur à l'OT permettra pour des études en cours et futures d'évaluer avec plus de précision la libération d'ocytocine lors de comportements ou après stimulation des fibres hypothalamiques.

2 Introduction

2.1 Pain

2.1.1 Definition

The International Association for the Study of Pain (IASP) defines pain as “An unpleasant sensory and emotional experience associated with, or resembling that associated with, actual or potential tissue damage” (“Terminology | International Association for the Study of Pain,” n.d.). It results from the conscious interpretation of the nociceptive information that comes from the detection of stimuli potentially noxious for the organism’s integrity. Pain can be characterized by two major dimensions (Talbot et al., 2019):

- the ‘sensory’ dimension, which refers to the spatio-temporal characteristics of the pain,
- the ‘affective’ dimension, which refers to the motivation to take protective action.

Pain’s classification can also depends on its duration. While acute pain is physiological and acts as a warning system for the body, chronic pain persists beyond normal tissue healing time (in humans, the pain has to last more than 3 months) and is a condition in itself despite often taking place because of an injury or a disease (Mills et al., 2019; Orr et al., 2017). In the world, an estimated 20% of the population suffers from chronic pain (Treede et al., 2015), and this number goes up to 30% in France (Chenaf et al., 2018). This results in an enormous economic cost reaching dozens of billions of euros every year for many European countries (Breivik et al., 2013).

2.1.2 Physiology of pain

2.1.2.1 *The nociceptors*

Pain arises from the conscious interpretation of nociception, which is defined by the IASP as ‘the neural process of encoding noxious stimuli’ (“Terminology | International Association for the Study of Pain,” n.d.). It refers to the detection of noxious stimuli by pseudo-unipolar neurons specialized for carrying nociceptive information, more commonly called ‘nociceptors’. Their cell bodies are located either in trigeminal ganglia for the nociceptors of the face, or in the dorsal root ganglia for the nociceptors innervating the rest of the body (**Figure 1**).

Their axons extend into the peripheral nervous system and terminate by forming the receptive fields (**Figure 1**). Some are external (skin, corneas, or mucosa), while the others are internal (muscles, joints, bladder, visceral organs, or intestinal tract). These nociceptors are classified depending on the nociceptive modality they detect: thermal, mechanical, chemical and polymodal (Raja et al., 1988; Robinson and Gebhart, 2008).

Once detected, the information then travels through two types of fibers: the A δ and C fibers. The former are myelinated axons that carry action potentials at a speed of about 20 meters/second, whereas the latter are lightly- or non-myelinated axons and thus conduct action potentials much slower at a speed of about 2 meters/second (**Figure 1**). Because of these properties, pain comes in two phases. The first one is mediated by the fast A δ fibers and is associated with an initial extremely sharp pain. The second comes with the C fibers (often polymodal) and is more prolonged, but less intense than the first phase (*Principles Of Neural Science, Fifth KANDEL*, n.d.).

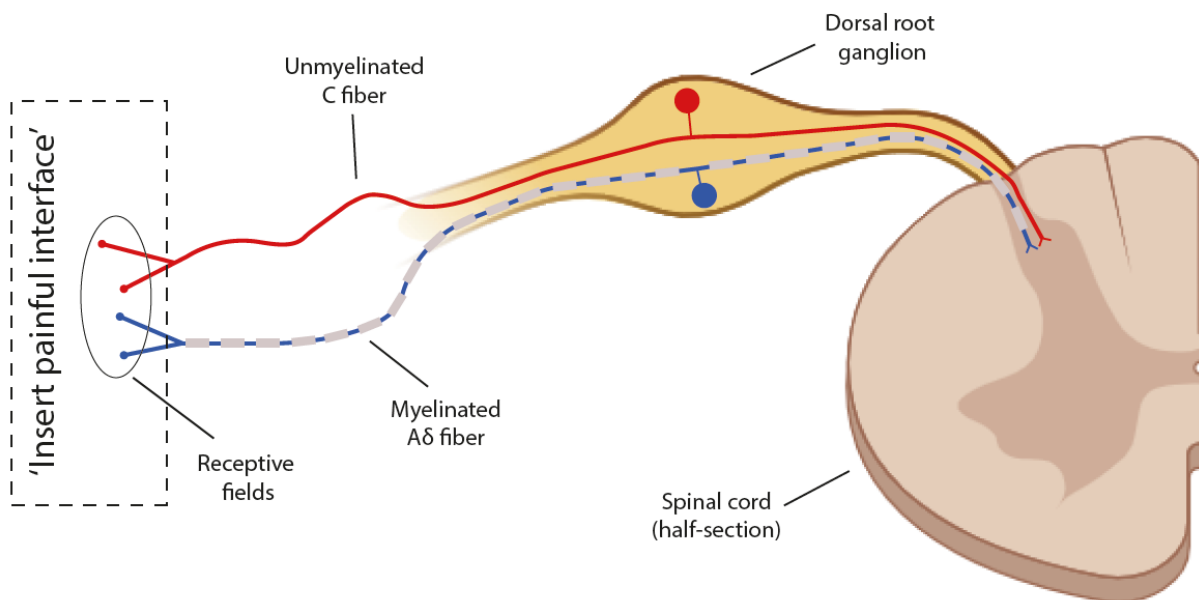


Figure 1 Schematic representation of the two main nociceptors for the detection of pain and their fibers for the transmission of the information from where the noxious stimulus arose to the dorsal horn of the spinal cord.

2.1.2.2 Spinal cord integration

These primary afferent fibers project in the spinal cord, which is the first integration center of the nociceptive information. More specifically, they mainly contact the neurons of the superficial layers of the dorsal horn (**Figure 1**). There, they make synapses with the second order neurons. These synapses are systematically

glutamatergic, making them excitatory, and the C fibers release neuropeptides as co-transmitters, including substance P, calcitonin gene-related peptide, somatostatin and galanin (*Principles Of Neural Science, Fifth KANDEL*, n.d.). The second order neurons can be interneurons (either excitatory or inhibitory), or projection neurons (Bell, 2018). Some of those second order neurons have a specificity: if there is a massive or continuous input to the C fibers, a phenomenon called ‘wind-up’ can occur, which is associated with an increased sensitivity to pain. This phenomenon can be measured in specific neurons of the spinal cord: the wide dynamic range (WDR) neurons. Compared to other neurons conducting the nociceptive information, WDR neurons’ response intensity is proportional to the stimulus intensity. This phenomenon has positive aspects since it allows synapses plasticity, but it also has a dark side. Indeed, if this over-excitation becomes pathological, it can then result in chronic pain (West et al., 2015).

2.1.2.3 *Projection to the supraspinal centers*

After the integration of the nociceptive message in the spinal cord, projection neurons send their axon to supraspinal structures *via* five major ascending pathways: the spinothalamic, the spinoreticular, the spinomesencephalic, the cervicothalamic and the spinohypothalamic tracts (**Figure 2**) (Millan, 1999).

- The spinothalamic tract is a direct pathway toward the thalamus, which then redirects the information to the somatosensory primary cortex, but also toward other structures such as the periaqueductal gray (PAG). This tract is essential for the sensory component of pain (*i.e.* the localization and evaluation of the stimulus intensity) (**Figure 2A**).
- The spinoreticular tract projects to the thalamus by making a relay in the reticular formation. Once in the thalamus, the information is redirected similarly as in the spinothalamic tract (**Figure 2B**).
- The spinomesencephalic (or spinoparabrachial) tract projects to the reticular formation and the PAG but also to the parabrachial nucleus. Since the latter then projects to the amygdala, this tract is therefore thought to contribute to the affective component of pain (**Figure 2C**).
- The cervicothalamic tract’s main feature is that it runs in the upper two cervical segments and project mainly to the thalamus or in the medulla.

- The spinohypothalamic tract projects to the hypothalamic nuclei to control the autonomic responses that accompany the pain such as neuroendocrine and cardiovascular responses.

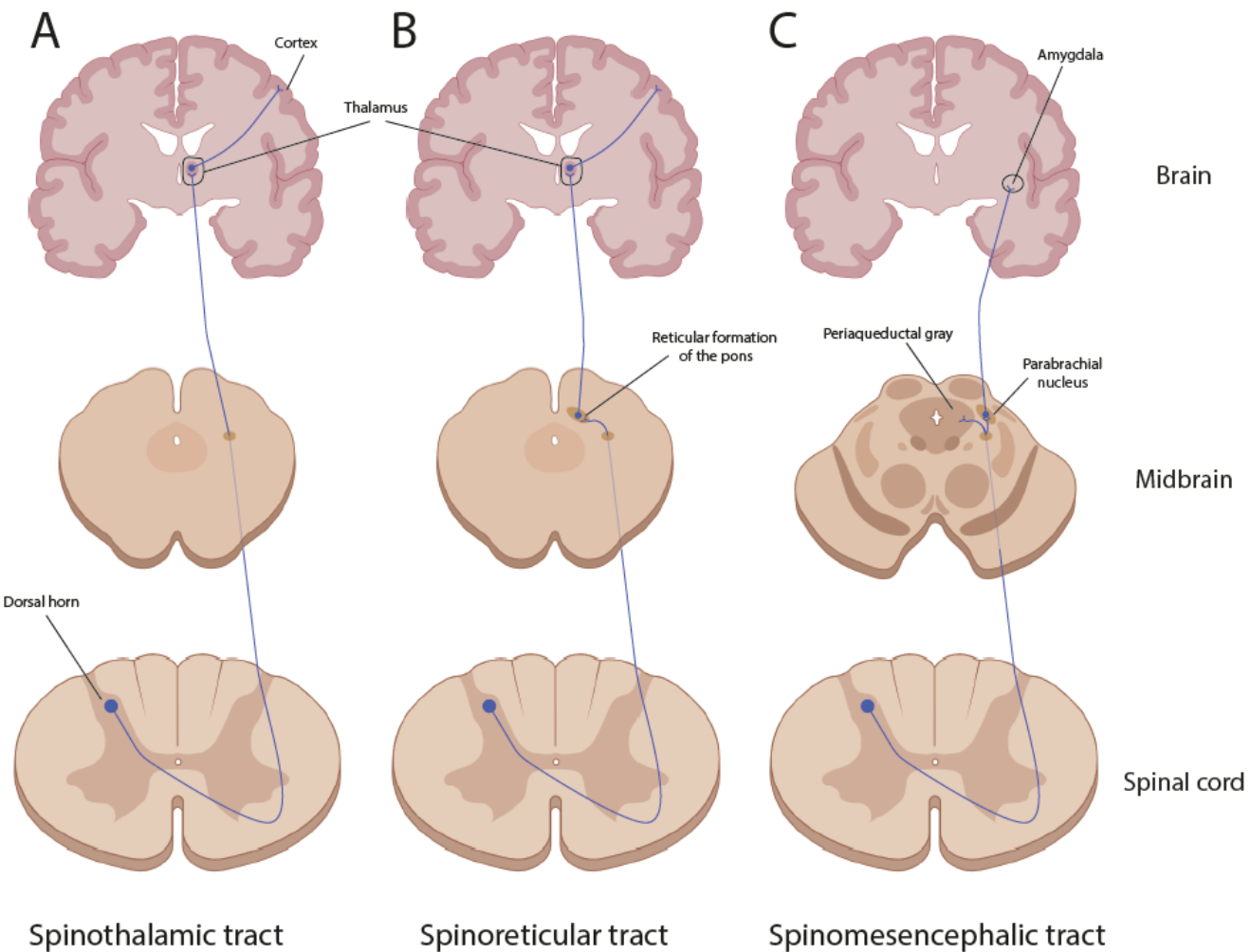


Figure 2 Representation of three out of the five main ascending pathways carrying the nociceptive information from the spinal cord to the supraspinal center. **A.** The spinothalamic tract. **B.** The spinoreticular tract. **C.** The spinomesencephalic tract.

2.1.2.4 Descending control of pain

Once integrated in the different supra-spinal structures, the pain sensation is there. But in some situations, for the sake of survival, the organism will either facilitate or inhibit the pain sensation. This is called the descending controls of pain, and, as one might have guessed, it can be either facilitatory or inhibitory. These pathways are initiated in a multitude of supraspinal structures such as the cortex, the amygdala, the hippocampus, the hypothalamus, the parabrachial nucleus, the nucleus of the solitary tract, the rostro-ventromedial medulla, the locus coeruleus or the PAG (**Figure 3**). The descending controls are very diverse so I will only detail the pathways implicating the amygdala and/or the PAG; but see (Millan, 2002) for a more complete review.

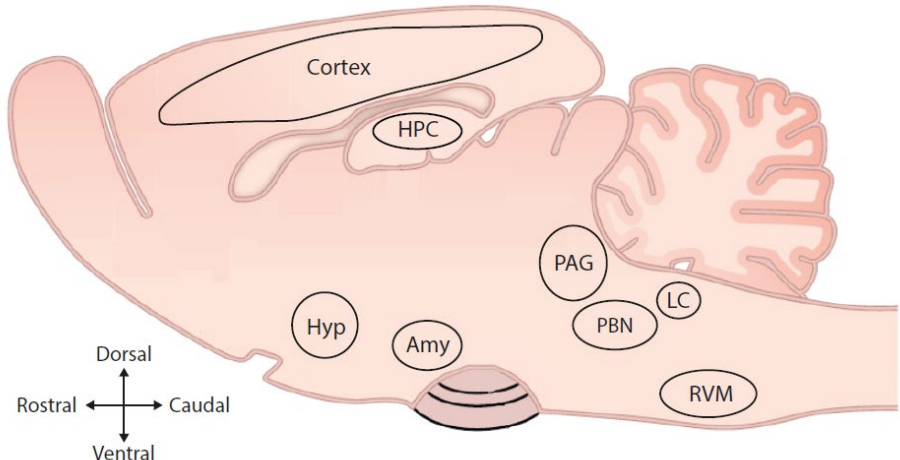


Figure 3 Brain map of the main supraspinal structures involved in the descending control of pain. Amy: amygdala; HPC: hippocampus; Hyp: hypothalamus; LC: locus coeruleus; PAG: periaqueductal gray; PBN: parabrachial nucleus; RVM: rostral ventromedial medulla.

The amygdala is a complex of nuclei that lies in the intern part of the temporal lobe of the brain (**Figure 4**). This structure is mainly known for being the emotions headquarter. More specifically, it gives an emotional valence to an event (Veinante et al., 2013). Amongst amygdala circuits, the champion for emotional processing is the basal-to-central amygdala pathway. In a simplistic view, the basal amygdala (BA) receives the sensory information already pre-processed by the cortex, the

2.1.2.5 The amygdala in pain

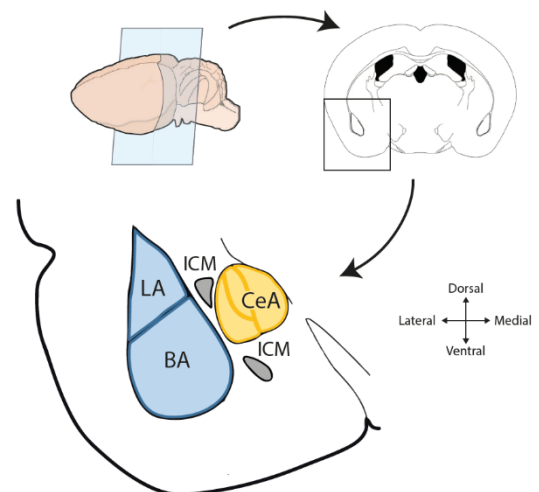


Figure 4 Organisation of the amygdala. Upper panel: coronal slice of the amygdala. Lower panel: position of the intercalated cell mass (ICM), lateral (LA), basal (BA) and central amygdala (CeA).

thalamus, the lateral amygdala etc. These information are then conveyed either directly to the central amygdala (CeA), or indirectly through the intercalated cell-mass (they are cells between the BA and CeA on which the BA can project to exert a feedforward inhibition on the CeA neurons). The CeA will then contact subcortical structures to produce an adapted behavior (**Figure 5**) (Janak and Tye, 2015; Veinante et al., 2013).

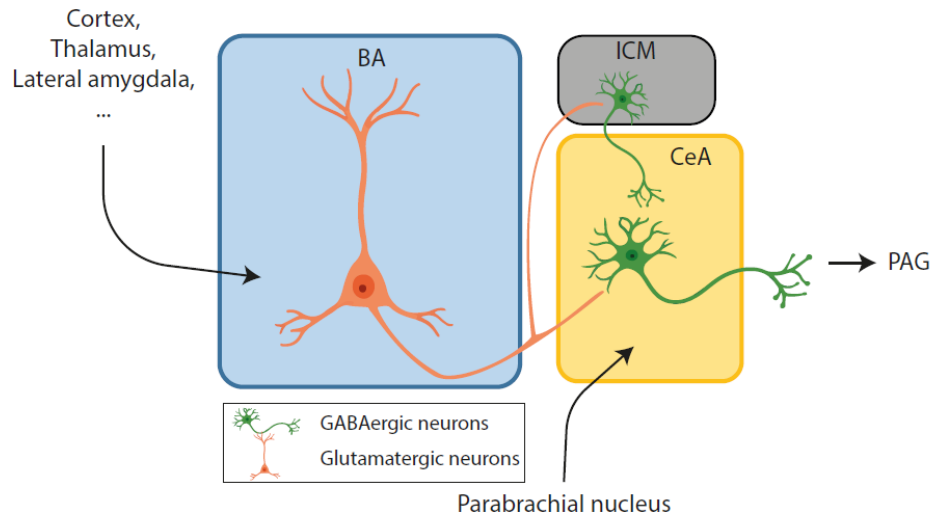


Figure 5 Schematic representation of the amygdala circuit involved in pain processing. BA: basal amygdala; CeA: central amygdala; ICM: intercalated cell-mass; PAG: periaqueductal gray.

Regarding pain processing, the CeA receives nociceptive information directly from the spinomesencephalic tract (through the parabrachial nucleus) and indirectly from thalamic and cortical areas through the BA. The BA is in charge of associating an emotional value to the sensory inputs and transmit it to the CeA (Thompson and Neugebauer, 2017). On the other hand, the lateral part of the CeA (CeL) responds exclusively to noxious stimuli, earning the name of ‘nociceptive amygdala’. Overall, under pain situations, there is a hyperexcitability in the amygdala. Behaviorally, increasing the amygdala outputs elicits pain behaviors, whereas decreasing them inhibits them (Neugebauer et al., 2020; Thompson and Neugebauer, 2017).

One of the structures on which the amygdala project to control the pain-related behaviors is the PAG, one of the pillars of the descending control of pain.

2.1.2.6 The periaqueductal gray in pain

The periaqueductal gray is the gray matter surrounding the aqueduct of Sylvius, which extends rostro-caudally from the level of the posterior commissure all the way to the locus coeruleus (**Figure 6**). The PAG is the climax of neuroscientific cooperation. Not only did they name it for what it literally is, but they also subdivided the structure

depending on the organization of the cell types consistently between the different species! However, even the best fairy tales have their flaws: subdivisions on the dorsoventral axis has not always been clearly described and consistent between species. Therefore, I will only describe it in rats, which is the model we used.

The PAG is divided in three main subdivisions: the medial PAG containing small and elongated cell

bodies, the dorsal PAG with medium and spherical cell bodies, and the lateral PAG composed by large and spherical cell bodies. The latter has been further divided into the dorsolateral PAG and the ventrolateral PAG (vIPAG) using the density and orientation of the cell bodies (Beitz, 1985; Menant et al., 2016). The PAG is involved in different physiological processes such as stress, cardiovascular control, lactation, feeding and pain (Bagley and Ingram, 2020).

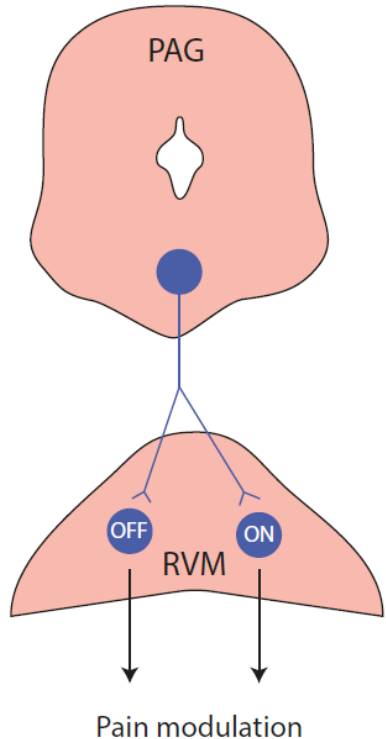
The first report of pain modulation by the PAG goes back to 1969 in a study where the electrical stimulation of the PAG produced a profound antinociception (*i.e.* a decrease in nociceptive-like behaviors) in male rats (Reynolds, 1969). The PAG, and more specifically the vIPAG, is also the most effective site in the midbrain for opiate microinjection- and stimulation-produced antinociception (Fields and Basbaum, 1978). This antinociception is naloxone-sensitive, indicating that this effect is mediated by endogenous opioid release (Bagley and Ingram, 2020). However, retrograde tracing from the spinal cord shows massive projecting neurons throughout the brainstem but not in the PAG (Fields and Basbaum, 1978). This is because the antinociception triggered by PAG stimulation is mediated by neurons projecting to the rostral ventromedial medulla (RVM), the predominant output of the descending control of pain



Figure 6 Organisation of the periaqueductal gray (PAG). Upper panel: coronal slice of the PAG. Lower panel: subdivisions of the PAG. dPAG: dorsal PAG; dlPAG: dorsolateral PAG; mPAG: medial PAG; vIPAG: ventrolateral PAG.

to the spinal cord. In the RVM, there are OFF- and ON-neurons (**Figure 7**). Their names come from their electrophysiological activity during a nociceptive behavior, as OFF-neurons have a reduced activity, while the ON have an increased activity in response to a noxious input (Martins and Tavares, 2017). RVM GABAergic neurons then project onto interneurons of the spinal cord, thus inhibiting them on normal conditions, giving free space for the fibers to transmit the nociceptive information.

Figure 7 Schematic representation of the PAG neurons projecting to the ON- and OFF-neurons of the RVM. PAG: Periaqueductal gray; RVM: Rostral ventromedial medulla.



2.1.3 Pain study in rodents

Most (if not all) of those studies on pain use animals as a model to study pain. More specifically, rodents are the most common animals used in laboratories (Council of the European Union). One could legitimately ask if studying pain in rodents is not somehow suspicious, as asking a mouse or a rat to rate the pain it feels is not an easy task. However, the inability to express about the pain in human language does not mean it is nonexistent. As a result, I will for now on talk of antinociception, which is the decrease of a pain-like behavior in rodents. One way to overcome this lack of understanding between humans and rodents is the use of stimulus-dependent nociceptive tests. Although only indicating about nociception, these tests can assess different modalities of pain: mechanical, thermal and chemical.

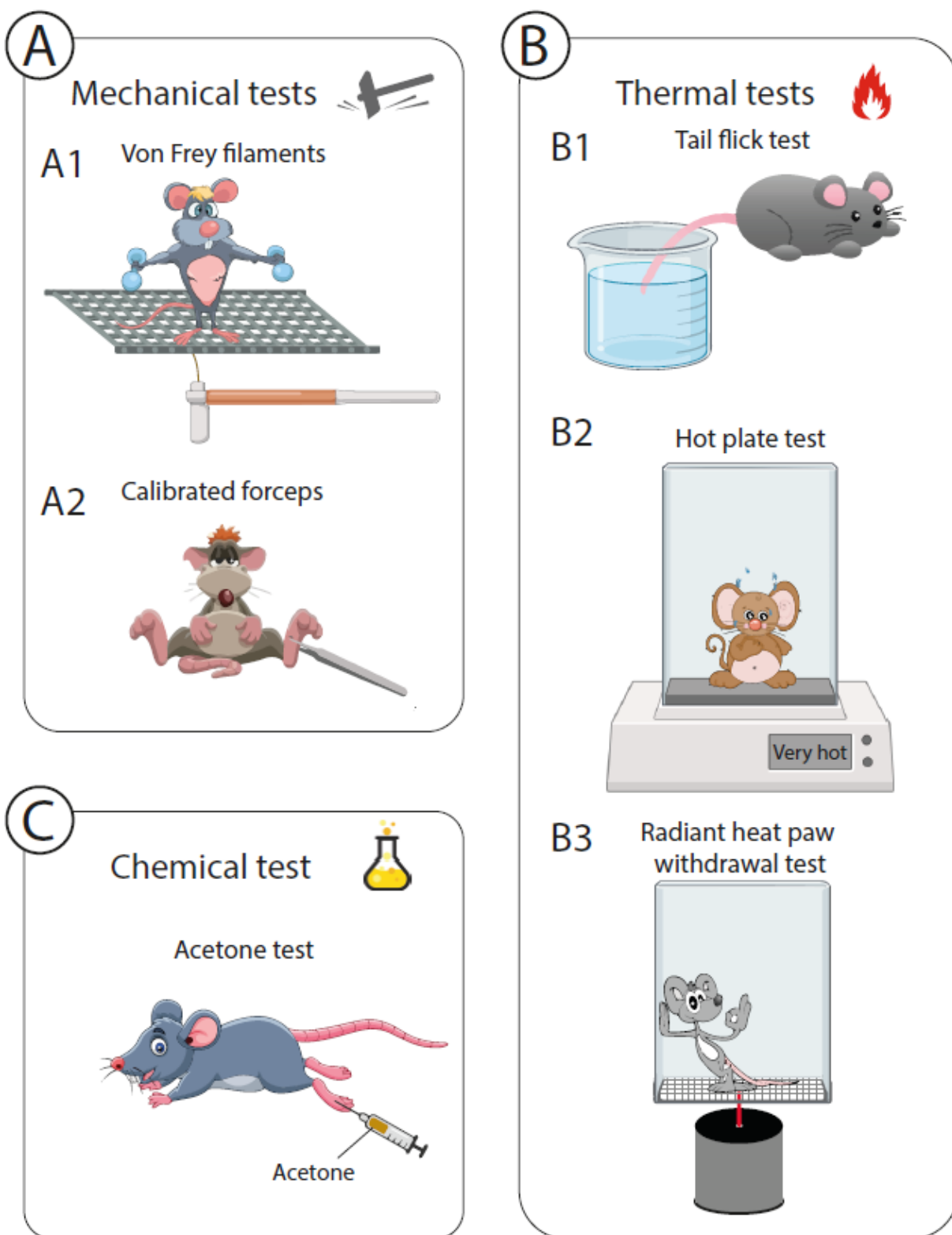


Figure 8 Schematic representation of tests used for the evaluation of the nociceptive behaviours for the three modalities. **A.** Mechanical tests: A1. Von Frey filaments; A2. Calibrated forceps. **B.** Thermal tests: B1. Tail-flick test; B2. Hot-plate test; B3. Radiant heat paw-withdrawal test. **C.** Chemical test: acetone test.

2.1.3.1 Mechanical tests

Mechanical nociceptive tests rely on a mechanical threshold necessary to elicit an avoidance behavior. The most famous one is the Von Frey filaments test, as it is the only one that can be used in both rats and mice, and it is derived from a clinical procedure. The concept is simple, plastic filaments of various diameter are applied on the plantar surface of the paw (usually) to exert a calibrated pressure (**Figure 8A1**). The animal response is usually the paw withdrawal, and the filament used to elicit it gives the value of the mechanical sensitivity threshold in grams. The main drawback of this test is that the results largely depend on the user (Barrot, 2012; Kremer et al., 2021). In addition, even if it is technically usable on rats, this test is almost only used for mice. Indeed, the other two alternatives cannot be used for mice and are preferably used in rats because their drawback are not as unsettling. First, in the Randall-Selitto, the hind paw of the rat is placed between a fixed and a mobile element to exert a controlled pressure until the appearance of a given behavior (paw withdrawal, struggling or a vocalization). In this test, the rat is restrained in a non-natural position to maintain the paw on the apparatus, and thus requires a strong behavioral expertise (Barrot, 2012). Another test, which is easier to use, is the calibrated forceps. The concept is the same but here the rat is loosely restrained on a bench while the mechanical nociceptive threshold is evaluated by applying an increasing pressure on its paw using forceps (**Figure 8A2**). Compared to the Randall-Selitto test, this one is much less stressful, but is more user-dependent as the pressure increment is not automated (Barrot, 2012; Luis-Delgado et al., 2006).

2.1.3.2 Thermal tests

There are two types of thermal nociceptive tests. First, the ones that are based on a fixed stimulus to measure the latency for an avoidance behavior. Here, we find the tail flick test, the hot- or cold-plate tests, and the radiant heat paw-withdrawal test (also called the Hargreaves test) (**Figure 8B**) (Barrot, 2012; Kremer et al., 2021). For all these tests, either the tail or the paws are in contact of warm or cold temperatures until the wanted behavior is observed (i.e. tail flick reflex, licking of the paw, etc.). Another set of tests are based on the measurements of a threshold. For that, dynamic hot- or cold-plates, or the acetone test are used. The formers work with a ramp of temperature, whereas the acetone test works by applying a drop of acetone, which, upon evaporation, produces a cold stimulus usually not detected by naïve animals. These

ramps allow for the detection of the stimulus going from ‘non-nociceptive’ to ‘nociceptive’, thus indicative of a hypersensitivity (Barrot, 2012; Kremer et al., 2021).

2.1.3.3 Chemical tests

Despite multiple irritating chemical agents usable as nociceptive stimuli, the formalin test is by far the most used procedure. The idea here is to inject intradermally a formalin solution to induce a transient inflammation of the tissue, which results in quantifiable behavioral responses such as withdrawal, licking, biting or shaking of the paw (**Figure 8C**). These reactions can then be scored to estimate the intensity of pain (Barrot, 2012).

2.1.3.4 Animal models of pain

The common lines used in rodent studies do not develop spontaneous pain. As a result, it was important to develop models to mimic pain found in humans. For example, after tissue damage implicating the immune system, this system releases inflammatory mediators that activate and sensitize the nociceptive system. This so-called “inflammatory pain” can be induced by injecting the complete Freund’s adjuvant (CFA) where one wants to develop a local inflammatory pain. The CFA is a suspension of inactive *Mycobacterium tuberculosis*. Similar to pacifist protestors that will trigger the police’s violence, those bacteria will activate the immune system. The resulting inflammation will induce a hypersensitivity, decreasing the mechanical and thermal nociceptive thresholds that will last for several weeks (Noh et al., 2021).

Another type of pain results from a lesion or a disease affecting the somatosensory system, which triggers a pain named neuropathic pain. This time, the models are usually traumatic and based on the lesion or constriction of the sciatic nerve. The most used ones are the chronic constriction injury (CCI) and the spared nerve injury (SNI). The CCI consists of three or four ligatures around the main branch of the sciatic nerve (Bennett and Xie, 1988). The SNI is less delicate as it consists of sectioning two of the three branches of the sciatic nerve (Decosterd and Woolf, 2000). Again, this results in a decrease in mechanical and thermal thresholds on the paw of the constricted or injured sciatic nerve.

2.2 The relaxin-3 system

Pain is modulated at every step of its processing by a large range of neurochemicals, including neuropeptides. One of the neuropeptides of interest in the study of pain is the relaxin-3.

2.2.1 The relaxin family

Relaxin-3 is a member of a peptide superfamily, which also includes relaxin-1 and -2 and insulin-like peptide (INSL) -3, -4, -5, -6. These peptides are about 5 kDa and consist of two chains, A and B, with three disulfide bonds (**Figure 9**) (Ma et al., 2017). For the sake of simplicity, I will not describe the INSL peptides in this manuscript, and I will focus on the relaxin, and more importantly on the relaxin-3 peptide.

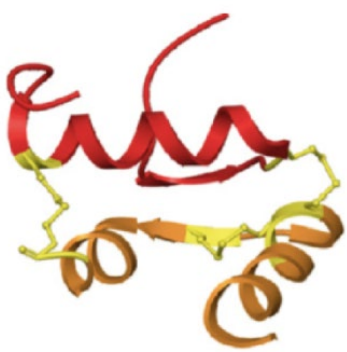


Figure 9 3D representation of the relaxin peptide. In red: the B chain. In yellow/orange: the A chain.

The relaxin peptides characterization is messy; I will try to give a proper explanation. In 1926, Dr. Frederick Hisaw discovered a peptide that he will later call relaxin in 1930 (Fevold et al., 1930; Hisaw, 1926). Much later, in 1983 and 1984, two genes were identified in humans: the *RLN1* and *RLN2* gene, which respectively encode the relaxin-1 and relaxin-2 (Hudson et al., 1984, 1983).

But, which of the two is the one described by Dr. Hisaw you may ask? It is the relaxin-2, and it is largely found in the animal kingdom. The *RLN1* and *RLN2* gene are only found in primates, whereas in other mammals, only the relaxin-2 is present (and is called relaxin) and its encoding gene has cleverly been called *RLN1* (which is different from the *RLN1* gene in primates). Luckily for us, it is much easier for the relaxin-3. Its encoding gene (called *RLN3*) has been sequenced in 2002 in humans and in mice (Bathgate et al., 2002). It is, for now, the last described member of the family.

The relaxin family genes have a similar structure with two exons separated by one intron. Based on the sequences found in the human, mouse or rat databases, it has been supposed that the gene would code for a pre-pro-peptide composed of a signal peptide, a B-chain, a C-chain and an A-chain (Bathgate et al., 2002; Burazin et al., 2002). They also hypothesized the cleavage sites of the signal peptide and the C-chain to give the mature relaxin composed of the two chains A and B. Within the B-chain, all

the relaxin contain a characteristic sequence ‘RXXXRXX(I/V)’ essential for binding their cognate receptors (with, R = Arginine, X = variable amino acid, I = Isoleucine, and V = valine)(Büllesbach and Schwabe, 2000). The A-chain sequence of the relaxin is more heterogeneous: besides the cysteine residues, only one amino acid is highly conserved (Büllesbach and Schwabe, 1994). However, the A-chain is also important in the peptide binding. Indeed, its truncation in the human relaxin-2 leads to a loss of ability for the peptide to bind to and activate its receptors (Hossain et al., 2008).

After almost one page talking about these relaxin peptides, you may wonder: how does this relaxin relax? And as a proper scientific student, I will answer: it depends. In fact, it mainly depends on which relaxin we are talking about. Indeed, Dr. F. Hisaw named it that way because he discovered it while studying the reproductive endocrinology of rodents. More precisely, he injected the serum of pregnant guinea pigs or rabbit in virgin females and observed the relaxation of their pubic ligaments (Hisaw, 1926). And this is how the relaxing story ends already. If we go back to our different relaxin, in human, no relaxin-1 peptide has been isolated yet, despite the *RLN1* gene being the first human relaxin gene to be cloned (Hudson et al., 1983). As a result, its physiological function has yet to be discovered. On the other hand, the relaxin-2 is produced in the corpus luteum of the ovary and circulate in the blood during pregnancy, while in male it is produced by the prostate. The *RLN2* mRNA is also found in other places such as the endometrium, decidua, placenta and the mammary glands. Overall, the relaxin-2 plays a role mainly in the reproductive physiology of both males and females (Bathgate et al., 2013). For the relaxin-3, its only link with any kind of physical relaxation is by resembling relaxin-2. Indeed, this peptide is predominantly found in the brain and is not involved in reproduction (see [Relaxin-3: synthesis, distribution and function](#) for more details on the relaxin-3 known functions). To exert their effects, the relaxin peptides act through different receptors.

2.2.2 The relaxin receptors

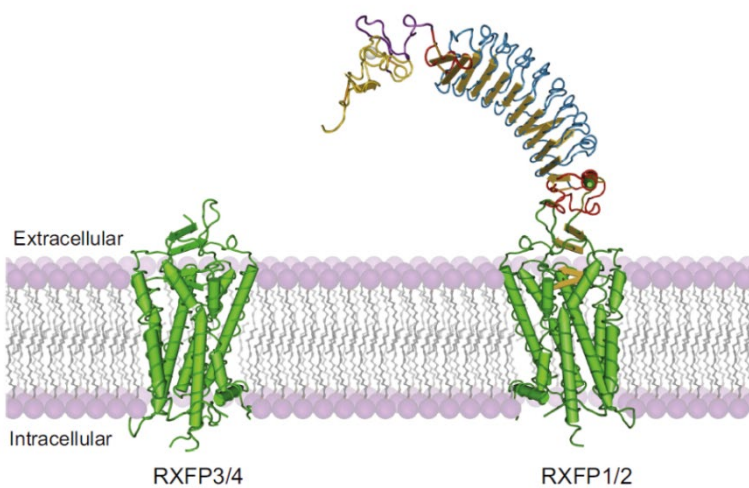


Figure 10 3D representation of the relaxin receptors, with the atypical large extracellular domain of RXFP1/2.

There are four different relaxin/insulin-like family peptide receptors (RXFP): RXFP1, RXFP2, RXFP3 and RXFP4. They are all G protein-coupled receptor, which main characteristics are their seven transmembrane domains. We can distinguish RXFP1/2 from RXFP3/4 based on their structure: while the latter

have a typical G protein-coupled receptor (GPCR) kind of structure, the former have a unique structure among them. Indeed, RXFP1 and RXFP2 have a large extracellular domain containing a ten leucine-rich repeats and a unique N-terminal module (**Figure 10**) (Hsu et al., 2002). Both of them are G_s-coupled receptors (Bathgate et al., 2013). RXFP1 is the cognate receptor for the relaxin-2. In accordance with its peptide functions, RXFP1 is expressed in the reproductive tissues, but also in a variety of peripheral organs. It can also be found in many brain structures, such as the olfactory bulbs, the cortex, the thalamus, the hypothalamus or the amygdala (Ma et al., 2006). On the other hand, RXFP2 is the cognate receptor for INSL-3 and is expressed in some peripheral organs, but not in the brain.

RXFP3 and RXFP4 do not have any structural specificities (**Figure 10**), although they belong to a subgroup of family A GPCR (Hsu et al., 2005). Originally, it was thought that both receptors were the cognate receptors for relaxin-3 as it was the only tested peptide that could bind to them (Liu et al., 2003b, 2003a). However, the expression pattern matched only between relaxin-3 and RXFP3. Indeed, while RXFP3 is predominantly expressed in the brain (Liu et al., 2003b), RXFP4 is mainly found in the gut and other peripheral organs (Liu et al., 2003a), and some expression can be found in the ventromedial hypothalamus and the vagal nerve (Hechter et al., 2022; Lewis et al., 2022). Indeed, Liu and colleagues showed in 2005 that the actual cognate ligand to RXFP4 is INSL-5 as it has the same affinity than relaxin-3 with an expression pattern

that matches RXFP4's (Liu et al., 2005b; Liu and Lovenberg, 2008). Interestingly, INSL-5 can also bind RXFP3 with a largely higher affinity, but it cannot activate it (Liu et al., 2005b).

It is worthy to note that relaxin-3 can also bind to RXFP1 with a lower affinity than relaxin-2 (Liu et al., 2005b), to the rat RXFP2 (Scott et al., 2005) but not the human RXFP2 (Sudo et al., 2003), or to RXFP4 (Liu et al., 2005b). However, only the relaxin-3 has been demonstrated to activate RXFP3 (Bathgate et al., 2013) (**Table 1**).

	RXFP1	RXFP2	RXFP3	RXFP4	References
Relaxin-3	2 nM	Inactive	0.4 nM ; 16.5 nM	1 nM	Liu et al., 2005b; Shabanpoor et al., 2012
Relaxin-2	0.2 nM	1.5 nM	Inactive	Inactive	Liu et al., 2005b
R3/I5	412 nM	Inactive	0.45 nM	0.91 nM	Liu et al., 2005a
Agoniste A2	>10,000 nM	n.d	13.5 nM	79.4 nM	Shabanpoor et al., 2012
R3(BΔ23-27)R/I5	Inactive	n.d	0.67 nM	2.29 nM	Kuei et al., 2007
R3 B1-22R	Inactive	n.d	36.3 nM	Inactive	Haugaard-Kedström et al., 2011

Table 1 Affinity of the different agonists and antagonists for the relaxin receptors.

2.2.3 RXFP3

The discovery of RXFP3 dates back to the first year of this century (2000 for anyone reading this after the year 2100). It was first named somatostatin- and angiotensin-like peptide receptor, due to, as you might have guessed, its high amino acid similarity to somatostatin and angiotensin receptors (not all scientists are creative when it comes to naming things) (Matsumoto et al., 2000). Because it was an orphan GPCR, it was then renamed in GPCR135 (yup, still lacking some personality) (Liu et al., 2003b). At this time all the relaxin receptors were named differently: LGR7, LGR8, GPCR135 and GPCR142 (1,2,3 and 4 respectively). In 2006, Bathgate and colleagues proposed a nomenclature to unite all the receptors of the relaxin family under the same name: RXFP (Bathgate et al., 2006a).

As previously said, relaxin-3 can bind to most of the RXFPs (if not all depending on the species). Although, RXFP3 is considered the native receptor, first because only relaxin-3 can bind and activate it with a high affinity (Bathgate et al., 2006b) (**Table 1**), then because the genes for the peptide and the receptors are conserved

phylogenetically (Hsu et al., 2005; Wilkinson et al., 2005). In addition, relaxin-3 and RXFP3 are found in the same regions in the brain (Bathgate et al., 2013).

RXFP3 is activated by relaxin-3 at nanomolar concentrations. The B-chain, but not the A-chain, of the peptide can also bind to and activate RXFP3 with a lower affinity than the full peptide (Liu et al., 2003b). This suggests that the relaxin-3's B-chain is essential for the peptide binding and the receptor activation, while the A-chain increases the affinity of the ligand-receptor interaction.

2.2.3.1 *Intracellular signaling*

Being $G_{\alpha i/o}$ -coupled, the activation of the receptor triggers multiple intracellular pathways, but I will only detail a few of them here (**Figure 11**); see (Bathgate et al., 2013; Kocan et al., 2014) for more details.

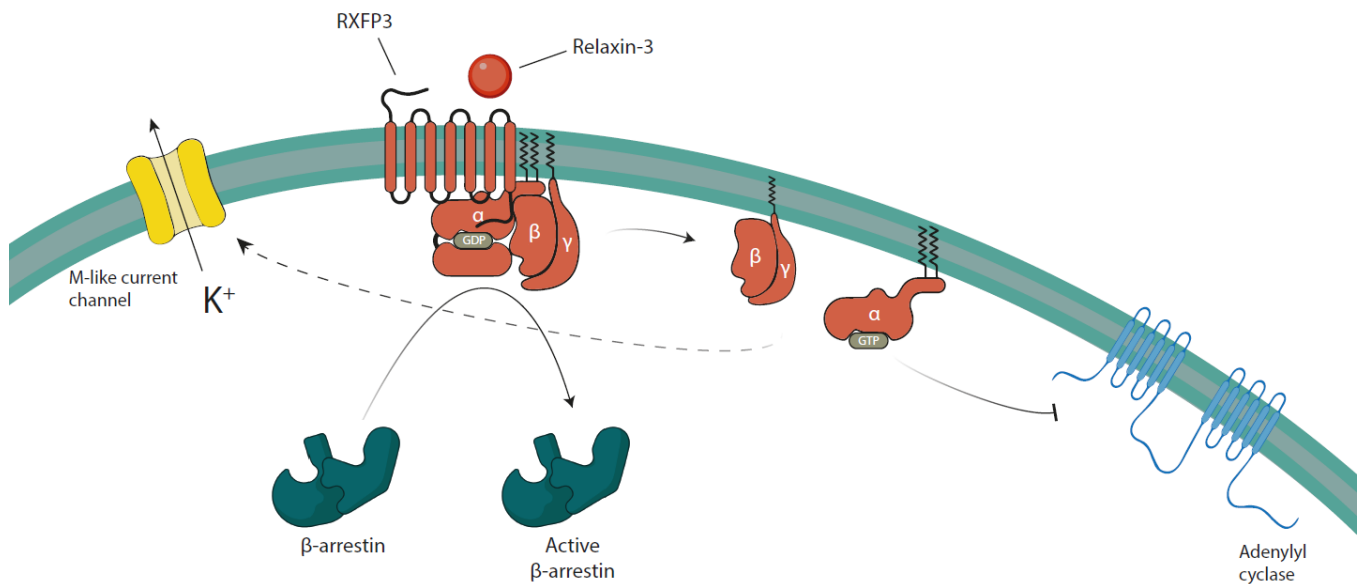


Figure 11 Some intracellular pathways triggered by the activation of RXFP3. The dashed line represent a effect for which we do not know which subunit of the G protein is involved in. → represent an activation and ← represent an inhibition.

The most classical and known one is the inhibition of the adenylyl cyclase by the α -subunit of the G protein. This subsequently blocks cAMP accumulation in the cell (**Figure 11**) (Liu et al., 2003b).

RXFP3 also activates AP-1-linked reporter genes, but this time, the pathway implicated is not as clear. Indeed, depending on the cell line used, the MAPK signaling pathways stimulating this activation are not the same (Van Der Westhuizen et al., 2010).

More recently, a study showed that RXFP3 activation on magnocellular secretory cells of the hypothalamus induces inhibition of their electrical activity mediated by activation of M-like current, which is a K^+ current involved in the regulation of membrane excitability (**Figure 11**) (Kania et al., 2020). However, this effect has not been tested when pre-treated with pertussis toxin, thus we cannot conclude whether this effect happens downstream of $G_{\alpha i/o}$ activation.

Finally, radioligand internalization assays showed that RXFP3 is internalized 10 minutes after being stimulated with human relaxin-3 (Van Der Westhuizen et al., 2010). In addition, Kocan and colleagues showed using BRET studies that this internalization occurs via an interaction with β -arrestin. When pre-treated with pertussis toxin, only about 50% of these interactions are prevented, suggesting that it is not only mediated by $G_{i/o}$ signaling (Kocan et al., 2014).

2.2.3.2 Relaxin-3/RXFP3 interaction's specificity

I previously said that only relaxin-3 can activate and bind to RXFP3 with a high affinity, but it is not entirely true. There is a concept called ligand-directed signaling bias that describes the fact that some ligands binding results in selective activation of downstream signal transduction pathways (Bathgate et al., 2013). This means that one ligand triggers a specific signaling pathway over another. This is what happened for RXFP3 when the first study established the idea that only relaxin-3 could interact with RXFP3. Indeed, they 'only' studied the different peptides selectivity in binding and adenylyl cyclase assays, but they have not explored the potential cross-reactivity with other relaxin peptides over other signal transduction pathways (Liu et al., 2003b). In the studies of Van der Westhuizen and colleagues, they showed that the human relaxin-2 can activate RXFP3 and trigger small changes in the extracellular acidification rate (Van Der Westhuizen et al., 2005). They also showed that it can have stronger effects on RXFP3 than relaxin-3 itself, as shown by the increased activation of AP-1-linked reporter gene (Van Der Westhuizen et al., 2010).

2.2.3.3 RXFP3 (ant)agonist development

As previously said, relaxin-3 is not as faithful to RXFP3 as it pretends to. Indeed, relaxin-3 can bind to RXFP1 (Bathgate et al., 2002), to the rat RXFP2 (Scott et al., 2005), and to RXFP4 (Liu et al., 2005b). This complicates the study of the effect of RXFP3 activation, as using the human relaxin-3 for example will not allow the distinction between the receptors. Selective agonists and antagonists have thus been

developed. First is the agonist R3/I5, a combination of the human relaxin-3 B-chain with the human INSL-5 A-chain. This agonist has a similar affinity for and activates RXFP3 the same way the human relaxin-3 does (**Table 1**). This agonist also has the same properties for RXFP4 but not for RXFP1, for which it has a low affinity (**Table 1**). This is an important point for the study of relaxin-3 in the brain since RXFP4 is not present in the brain, but RXFP1 massively is (Liu et al., 2005a). However, this agonist does not have a complete selectivity for RXFP3 over RXFP1. This is why Shabanpoor and colleagues developed a new agonist by removing the intra-A-chain disulphide bond and deleting 10 residues from the A-chain. This agonist called A2 binds to and activates RXFP3 the same way relaxin-3 and R3/I5 do but does not bind to RXFP1 (Shabanpoor et al., 2012) (**Table 1**).

As we can never test if a molecule is specific to one receptor over all the other existing receptors, specific antagonists also need to be developed. That is how the antagonist R3(BΔ23-27)R/I5, consisting of the INSL-5 A-chain and a modified relaxin-3 B-chain with a replacement of a glycine to an arginine and a truncation at the C-terminus came to existence. This antagonist has a high affinity binding for RXFP3, similar to relaxin-3 but does not bind to RXFP1 (**Table 1**). In addition, it antagonizes relaxin-3 effect on RXFP3 but not RXFP1 in a dose-dependent manner (Kuei et al., 2007). Later, another antagonist has been synthesized and named R3 B1-22R because it uses the truncated chain of the previous antagonist, with a replacement of the native cysteine by a serine. This antagonist has the same properties but, by being a single-chain 44 residues smaller, is more convenient to produce (Haugaard-Kedström et al., 2011) (**Table 1**).

2.2.3.4 RXFP3 activation and neuronal electric activity

Despite dreaming of fame and money, the relaxin-3 peptide is not as notorious as its expectations. As a result, only a unique team of brave scientists adventured themselves in studying the electrophysiological effect of RFP3 activation. They started off by showing that thalamic neurons expressing neuropeptide Y respond to the agonist

R3/I5 by a hyperpolarization and a decrease in action potential firing (**Figure 12**), whereas the neuropeptide Y-negative neurons respond either by a hyperpolarization or a depolarization (Blasiak et al., 2013). Later, using this time the A2 agonist, they showed in the paraventricular nucleus of the hypothalamus (PVN) that neurons are inhibited following RXFP3 activation (**Figure 12**). This inhibition is blocked by the application of the antagonist R3 B1-22R, confirming the involvement of RXFP3 (Kania et al., 2017).

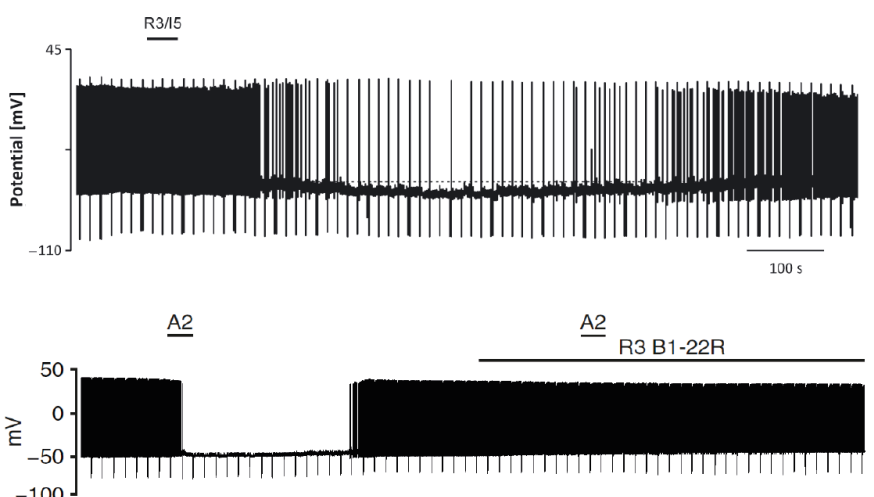


Figure 12 Representative electrophysiological recordings of neuronal activity following the application of RXFP3 agonists (R3/I5 and A2) and in presence of the antagonist R3 B1-22R. Top traces comes from (Blasiak et al., 2013) and bottom one comes from (Kania et al., 2017)

2.2.3.5 Distribution

Expression of RXFP3 is predominant in the central nervous system. Some expression of mRNA can be found in peripheral human tissues such as the adrenal gland, testis, salivary gland and pancreas (Liu et al., 2003b; Matsumoto et al., 2000). In the human brain, RXFP3 mRNA is found in the amygdala, the caudate nucleus, the hippocampus, the *corpus callosum*, the *substantia nigra*, the spinal cord and the pituitary gland. In the rodent, RXFP3 mRNA and binding sites are found in an extensive number of structures including the amygdala, hypothalamus, septum, hippocampus etc. (**Figure 13**) (for the detailed table in mice, see (Sutton et al., 2004); for the rats, see (Smith et al., 2010)).

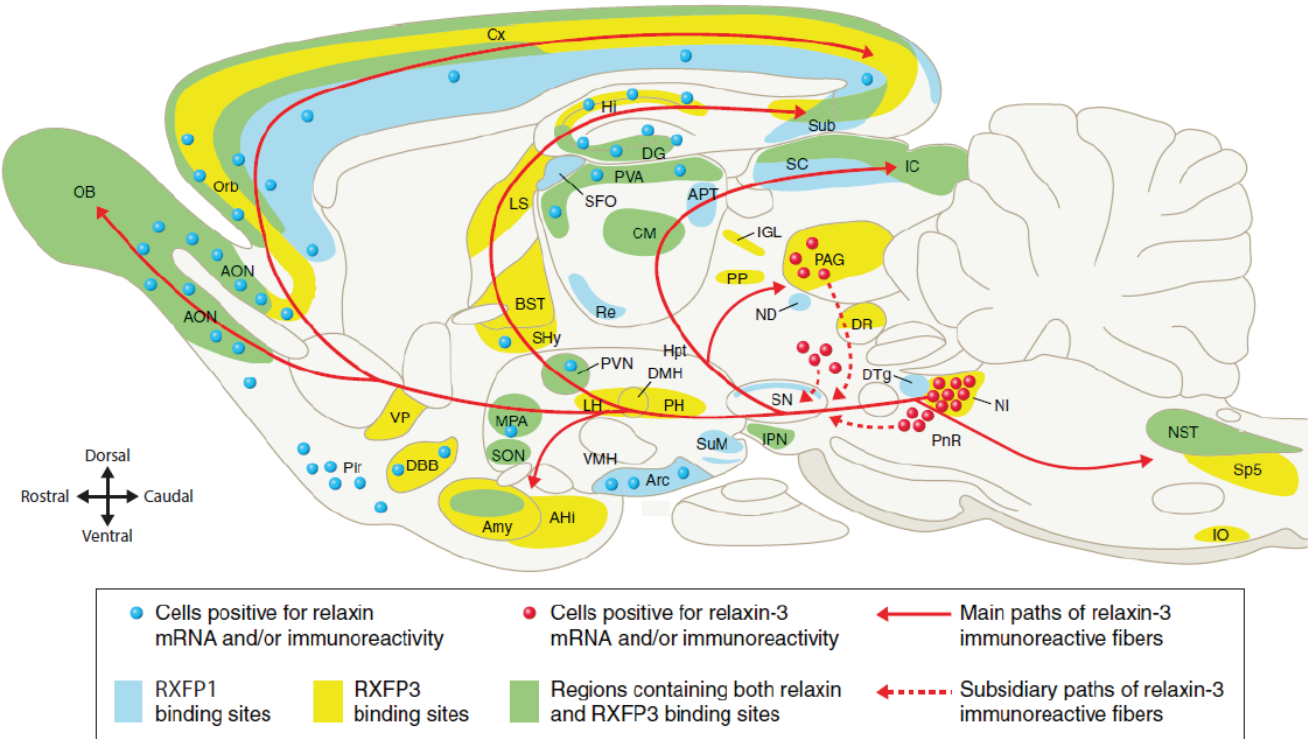


Figure 13 Distribution map of relaxin/RXFP1 and relaxin-3/RXFP3 sites in the rat brain. AHi: amygdalohippocampal area; Amy: amygdala; AON: anterior olfactory nucleus; APT: anterior pretectal nucleus; Arc: arcuate nucleus; BST: bed nucleus of stria terminalis; CM: central medial thalamus nucleus; Cx: cerebral cortex; DBB: diagonal band of Broca; DG: dentate gyrus; DMH: dorsomedial nucleus of hypothalamus; DR: dorsal raphe nucleus; DTg: dorsal tegmental nucleus; Hi: hippocampus; Hpt: hypothalamus; IC: inferior colliculus; IGL: intergeniculate leaflet of the thalamus; IO: inferior olive; IPN: interpeduncular nucleus; LH: lateral hypothalamus; LS: lateral septum; MPA: medial preoptic area; ND: nucleus of Darkschewitsch; NI: nucleus incertus; NST: nucleus of solitary tract; OB: olfactory bulb; Orb: orbital cortex; PAG: periaqueductal gray; PH: posterior hypothalamus; Pir: piriform cortex; PnR: pontine raphe; PP: peripeduncular nucleus; PVA: paraventricular thalamic area; PVN: paraventricular nucleus of hypothalamus; Re: reuniens thalamic nucleus; SC: super colliculus; SFO: subfornical organ; SHy: septohypothalamic nucleus; SN: substantia nigra; SON: supraoptic nucleus of hypothalamus; Sp5: spinal trigeminal tract; Sub: subiculum; SuM: supramammillary nucleus; VMH: ventromedial nucleus of hypothalamus; VP: ventral pallidum. Adapted from (Bathgate et al., 2013).

2.2.4 Relaxin-3: synthesis, distribution and function

In periphery of the nervous system, the relaxin-3 has been observed in the human serum (Erden et al., 2022; Hanafy et al., 2018), in the human breath & plasma, (Moraes-Ferreira et al., 2022) and in the granulosa cells of the chicken (Ghanem and Johnson, 2021). However, it is in the central nervous system that relaxin-3 is mainly expressed. It can be found in the pontine raphe nucleus, medial and ventral periaqueductal grey, and in an area dorsal to the *substantia nigra*. Although, relaxin-3 main expression is in the brainstem with ~2000 neurons grouped together in the *pars compacta* of the *nucleus incertus* in rats (**Figure 13**). These neurons express GABA

as their main neurotransmitter, and the relaxin-3 is stored in large dense-cored vesicles (LDCV) that are transported to nerve endings near the synaptic terminals (Tanaka et al., 2005). This suggests that relaxin-3 is released at the level of the synapse. The *nucleus incertus* sends relaxin-3 positive projections in many different brain structures (**Figure 13**) (Smith et al., 2010). It is worthy to note that the fibers distribution is similar in rat, mouse and macaque (Ma et al., 2009), and that this distribution overall matches that of the RXFP3 mRNA and binding sites (Ma et al., 2007; Smith et al., 2010; Sutton et al., 2004). This variety of projection suggests that relaxin-3 affects a broad-spectrum of functions, and, indeed, relaxin-3 has been reported to be implicated in the regulation of feeding, circadian rhythms, arousal, learning and memory, and in emotional and anxiety-like behaviors. In this manuscript, I will only focus on the latter.

2.2.4.1 *Nucleus incertus, relaxin-3 and stress*

Nucleus incertus neurons abundantly express the corticotrophin-releasing factor receptor 1 (CRF₁), which induces increased levels of relaxin-3 RNA and mRNA (Banerjee et al., 2010). In addition, intracerebroventricular (i.c.v.) infusion of CRF leads to an increased firing frequency of relaxin-3 neurons in the *nucleus incertus*, whereas a decrease in the electrical activity was observed in the relaxin-3 negative neurons (Ma et al., 2013). This suggests that the relaxin-3 neurons from the *nucleus incertus* respond robustly to the stress hormone. Interestingly, i.c.v. infusion of relaxin-3 increases c-Fos and CRF mRNA expression in CRF neurons in the PVN in the rat (Watanabe et al., 2011). This infusion also elevates plasma adrenocorticotropic and corticosterone hormone levels, while intra-PVN infusion of relaxin-3 once again increases the plasma levels of the two previously mentioned hormones, but also the prolactin hormone levels. This suggests a reciprocal interaction between relaxin-3 and CRF system, although further studies are needed as those are not enough to determine if the relaxin-3 effect is direct or indirect.

2.2.4.2 *Relaxin-3 and pain*

To date, no studies have been published regarding the effect of relaxin-3 on pain. However, there is a reason why I dedicated a whole section and part of my Ph.D to it. Marc Landry's lab was interested in a potential effect of relaxin-3 on pain, and thus, injected the A2 agonist i.c.v. during mechanical and thermal nociceptive tests in both mice and rats. These rodents were previously injected with the CFA in order to create an inflammatory pain. As expected, the animals injected with the CFA developed an

allodynia, and they found out that the injection of A2 agonist triggers an increase of the nociceptive threshold, meaning an anti-allodynia. To further clarify this effect, they injected the A2 in specific structures known for their implication in pain processing and management such as the amygdala. Again, they found that the A2 injection in the basolateral amygdala triggers a temporary mechanical and thermal anti-allodynia that last for about 1 hour, and that this effect is completely blocked by the co-injection of an RXFP3 antagonist (*Data from Marc Landry's lab, Figure 14*). These results strongly suggest that relaxin-3 can influence the nociceptive threshold when activating RXFP3 in the amygdala.

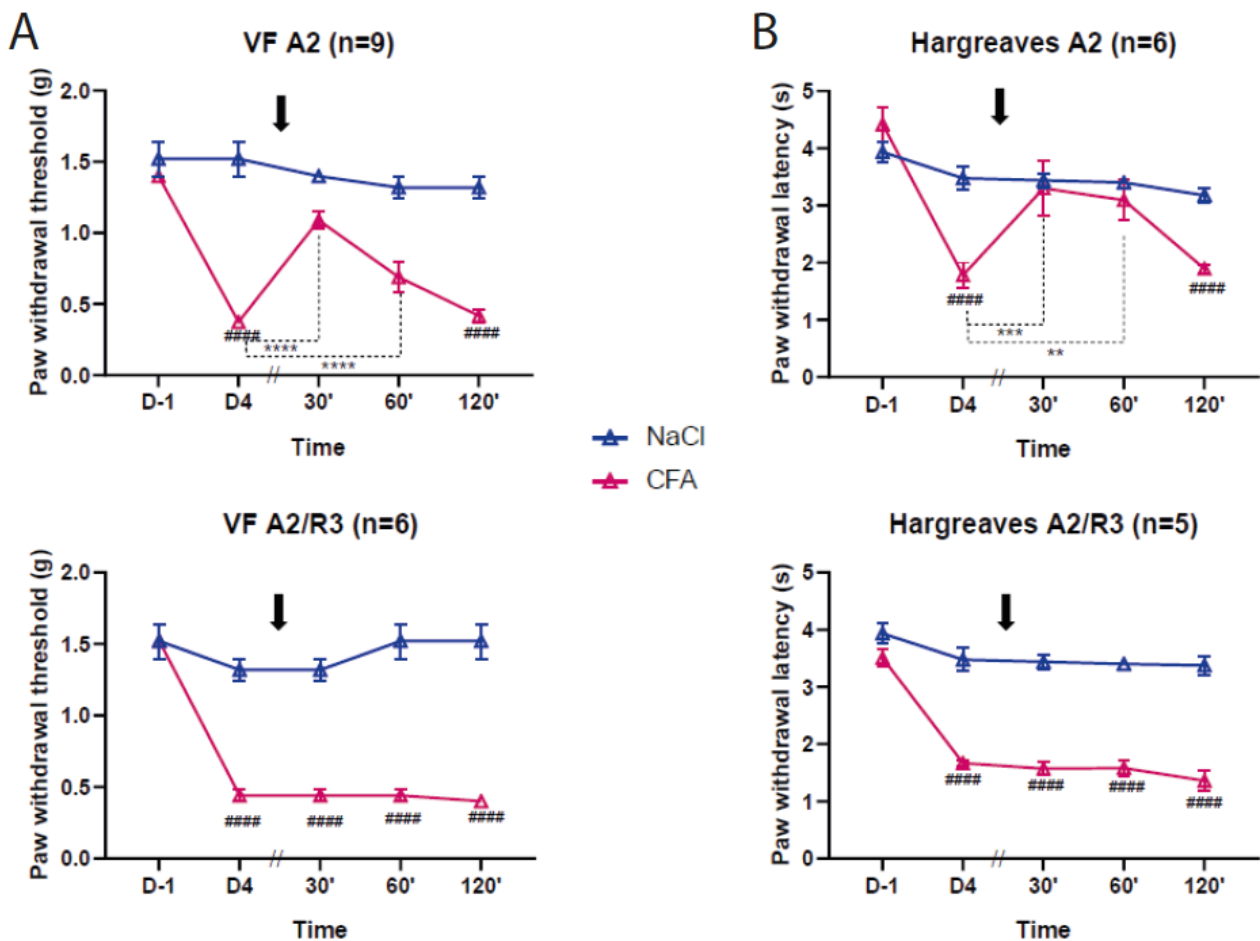


Figure 14 A2 agonist injection in the amygdala triggers a transitory anti-nociception both mechanical (A) and thermal (B) (top graphs). This effect is in both cases blocked by the co-injection of a RXFP3 antagonist (bottom graphs).

2.2.5 Relaxin-3 and the amygdala

As previously described (see [The amygdala in pain](#)), the amygdala, and more specifically the BA-to-CeA circuit, is an essential structure for the emotional aspect of pain.

2.2.5.1 *The basal amygdala*

The basal amygdala is a cortical-like structure containing both the lateral amygdala (LA) and the basal amygdala (BA). They contain glutamatergic pyramidal projection neurons (PN) and GABAergic interneurons (**Figure 15**) (Veinante et al., 2013). Similarly to the cortex' histoarchitecture, the PN are not so diverse compared to the interneurons (Kim et al., 2017). Indeed, based on transcriptional markers, they can be divided into two major populations: the calbindin and calretinin. Then, they can be further subdivided, with the calretinin interneurons co-expressing the vasointestinal peptide (VIP) and the cholecystokinin (CCK) while the calbindin ones express the CCK (without VIP), the somatostatin (SOM) and the parvalbumin (PV) (Mascagni and McDonald, 2003). Another way of discriminating them is to use their electrophysiological profiles (i.e. their action potential responses to an injection of a depolarizing current), although it is quite incomplete and some profiles are not unique to a specific type (**Figure 16**) (Spampanato et al., 2011). Finally, their innervation will be different depending on their transcriptional markers. For example, the VIP interneurons only contact other interneurons, mainly the PV and SOM. These two contact the VIP interneurons back, but they also inhibit each other. In addition, they both contact the PN, with the SOM contacting the distal dendrites, and the PV contacting the proximal dendrites, soma and axon hillock (Guadagno et al., 2021; Wolff et al., 2014). They consequently have a differential role for the inhibition of the PN. Some preliminary studies done by Marc Landry's team suggested that RXFP3 is

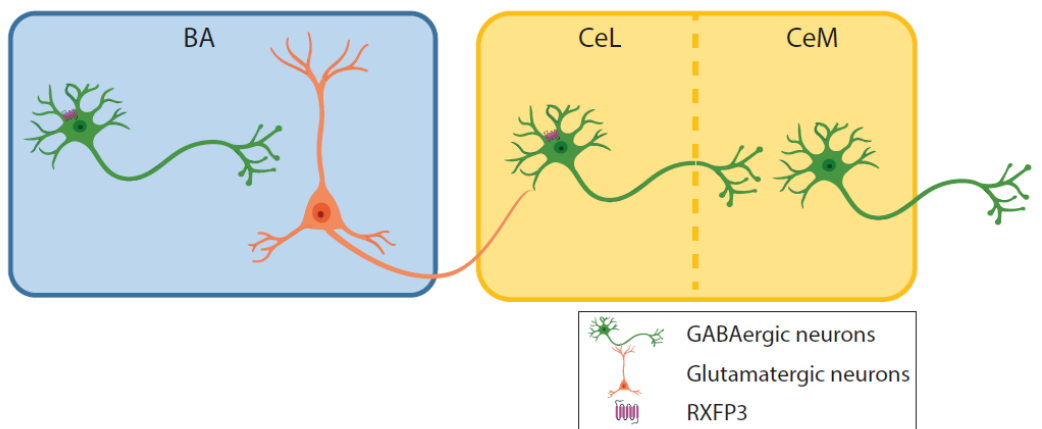


Figure 15 Schematic representation of the basal-to-central amygdala circuit and their cytoarchitecture.

electrophysiological profiles (i.e. their action potential responses to an injection of a depolarizing current), although it is quite incomplete and some profiles are not unique to a specific type (**Figure 16**) (Spampanato et al., 2011). Finally, their innervation will be different depending on their transcriptional markers. For example, the VIP interneurons only contact other interneurons, mainly the PV and SOM. These two contact the VIP interneurons back, but they also inhibit each other. In addition, they both contact the PN, with the SOM contacting the distal dendrites, and the PV contacting the proximal dendrites, soma and axon hillock (Guadagno et al., 2021; Wolff et al., 2014). They consequently have a differential role for the inhibition of the PN. Some preliminary studies done by Marc Landry's team suggested that RXFP3 is

expressed by SOM interneurons, which represent 20% of the total interneurons. Interestingly enough, it seems that neurons expressing RXFP3 in the CeA are also the SOM interneurons, located in the lateral part of the CeA (CeL), which then project mainly on the neurons of the medial part of the CeA (CeM) (**Figure 15**).

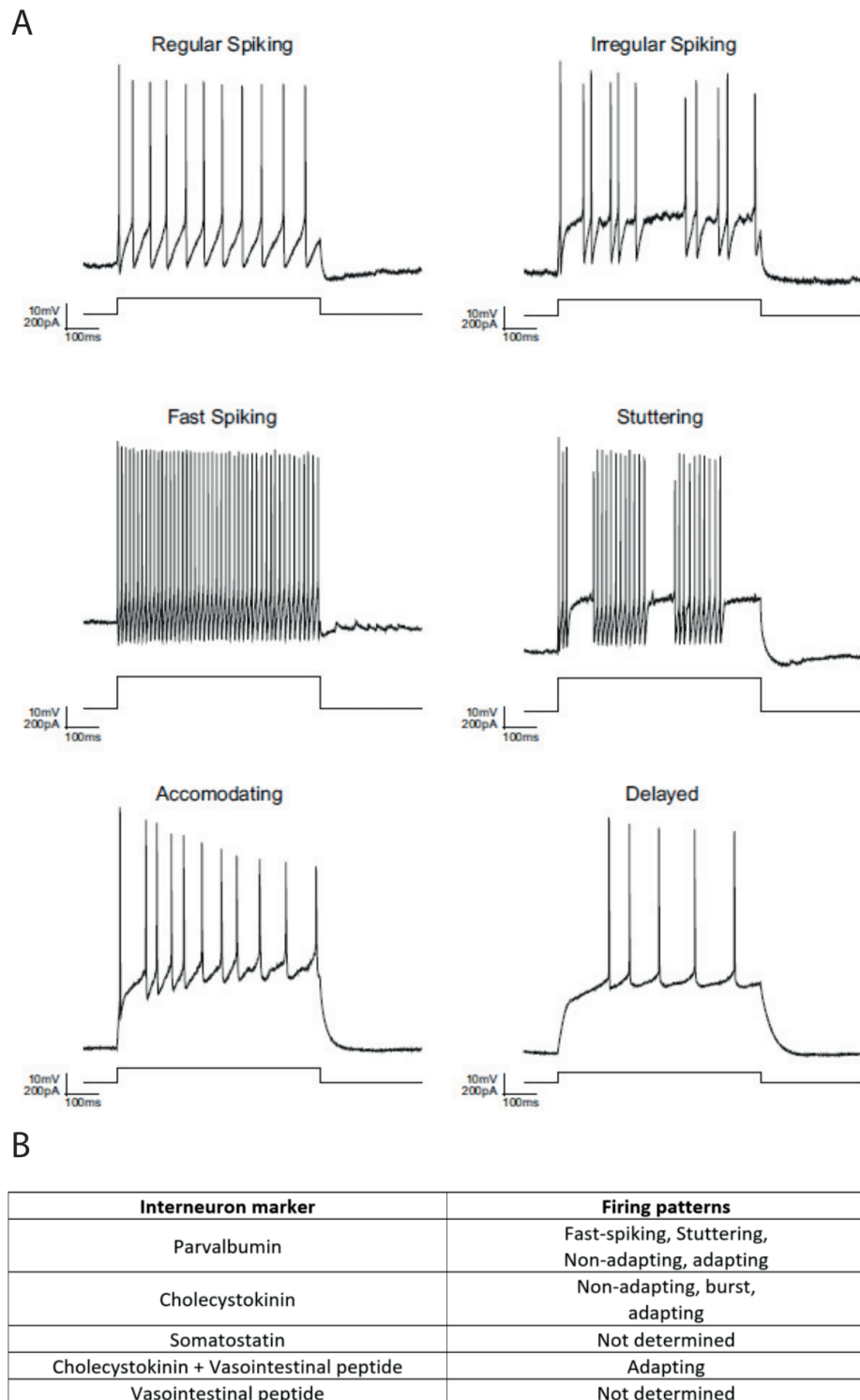


Figure 16 A. Different firing patterns found in the interneurons of the basal amygdala. **B.** Table showing the firing patterns associated to a transcriptional marker. Figure adapted from (Spampinato et al., 2011).

2.3 The oxytocin system

2.3.1 The oxytocin

Compared to relaxin-3, oxytocin (OT) can be seen as a lone wolf as it does not belong to any family. Although, this lone wolf may be one of the most famous peptide hormones, known as the ‘love hormone’. This designation comes from its role in reproduction and social bonding. In addition, OT is more generally implicated in promoting well-being by reducing anxiety or promoting social interactions (Jurek and Neumann, 2018). To exert these effects, this nonapeptide can act either as a hormone, or as a neuropeptide since it can either be released by the posterior pituitary in the blood flow, or by oxytocinergic neurons in the brain.

2.3.1.1 Synthesis

OT is synthetized from a gene named *Oxt* containing three exons. The first exon gives rise to OT and a signal peptide while the other two encode a peptide named Neurophysin 1 (**Figure 17**) (Gimpl and Fahrenholz, 2001). This gene’s transcription can be regulated by multiple regulatory sequences, with one of them being the Estrogen Regulatory Element (ERE), which favors the transcription of *Oxt* in the presence of estradiol (the most active form of estrogen) (Lee et al., 2009). As many neuropeptides, OT mRNA is translated into a prepropeptide called preprotoxyphsin. It is then cleaved to give rise to OT peptide and the Neurophysin 1 protein (**Figure 17**) (Jurek and Neumann, 2018).

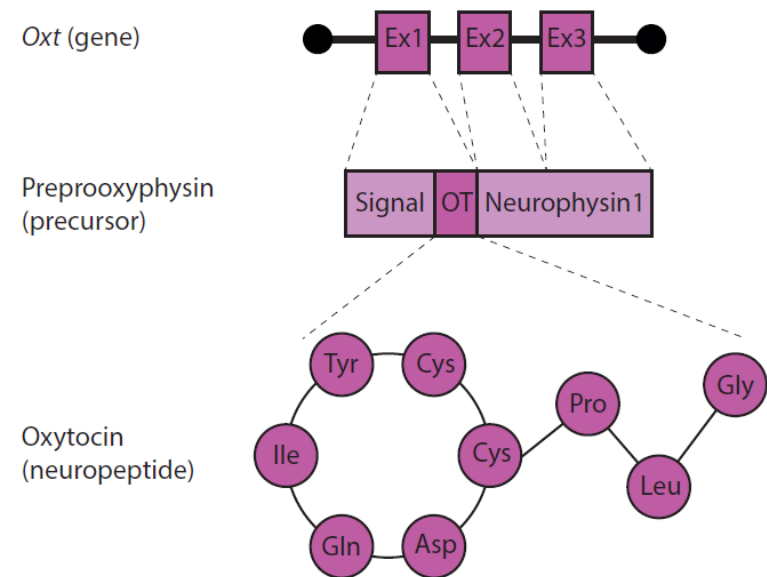


Figure 17 Oxytocin’s gene (top panel) gives rise to the precursor preprotoxyphsin (middle panel) containing the signal sequence and the coding sequences for OT and Neurophysin 1. After maturation, the final OT peptide has nine amino acids and a disulfide bond between the two cysteines. Asp: asparagine; Cys: cysteine; Gln: glutamine; Gly: glycine; Ile: isoleucine; Leu: leucine; Pro: proline; Tyr: tyrosine

OT can be synthetized in many regions of the body, be it inside or outside the brain (uterus, testis and the heart). In the former, it takes place in three nuclei of the hypothalamus, namely the paraventricular nucleus (PVN), the supraoptic nucleus (SON) and the accessory nuclei (AN) (**Figure 18A**), but also in the medial preoptic area of the hypothalamus, the lateral amygdala and the bed nucleus of the stria terminalis (Lee et al., 2009; Otero-García et al., 2016; Young and Gainer, 2003).

2.3.1.2 *Distribution and release*

In the hypothalamus, OT is synthetized from two types of neurons: the big magnocellular neurons (20-35 μm soma diameter) (magnOT), and the small parvocellular neurons (12-15 μm soma diameter) (parvOT). Despite their obvious size differences, there is also a discrepancy in their home structure, their projections and their release sites. Indeed, the magnOT resides in the PVN, SON and AN, whereas the parvOT are found only in the PVN. Furthermore, the magnOT will target the forebrain regions, including the piriform and auditory cortices, the amygdala and the striatum (**Figure 18B**) (Zhang et al., 2021). They also project to the neurohypophysis to release OT in the blood flow, which will then act as a hormone (Jurek and Neumann, 2018). Contrarily, parvOT neurons project to midbrain structures, the brainstem and the spinal cord (**Figure 18B**) (Eliava et al., 2016; Iwasaki et al., 2023; Knobloch et al., 2012; Zhang et al., 2021). As most of the neuropeptides, OT is stored in LDCV that are found in the soma, dendrites, axonal varicosities and synaptic buttons of OT neurons (Leng and Ludwig, 2008). Compared to the vesicles containing the neurotransmitters, LDCV are further away from the membrane, requiring bigger Ca^{2+} entrance in the neurons to provoke exocytosis. It is then necessary to have more action potentials to trigger the release of OT compared to neurotransmitters (Del-Bel and De-Miguel, 2018).

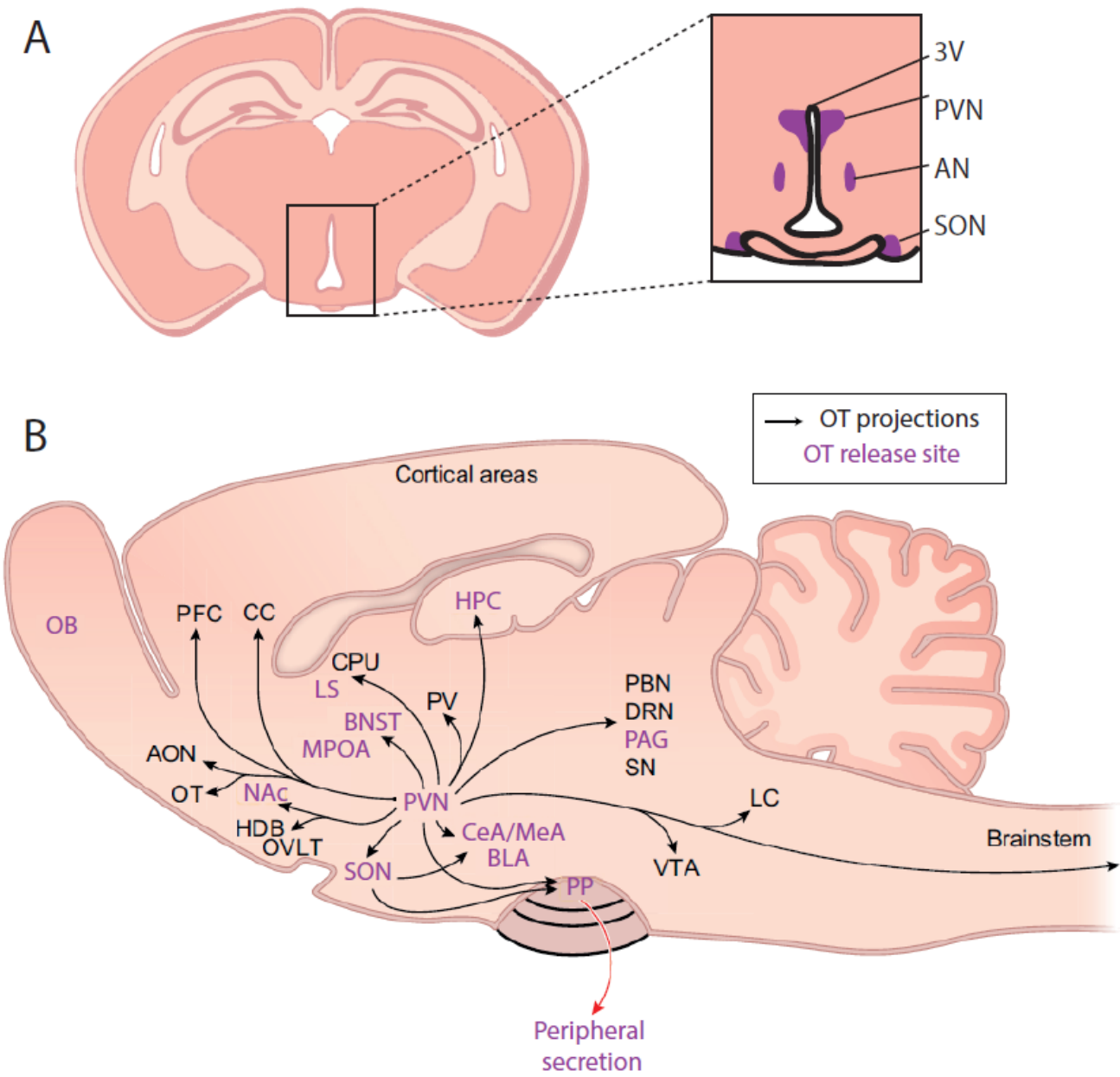


Figure 18 A. Coronal slice of a rodent brain illustrating the three main OT-synthesizing nuclei: the accessory nuclei (AN), the supraoptic nucleus (SON) and the paraventricular nucleus of the hypothalamus (PVN). **B.** Sagittal view of a rodent brain illustrating the OT projections from the PVN and SON and the structures where evidences support its release. Adapted from (Jurek and Neumann, 2018). AON: anterior olfactory nucleus; BLA: basolateral amygdala; BNST: bed nucleus of the stria terminalis; CC: cingulate cortex; CeA: central amygdala; CPU: caudate putamen; DRN: dorsal raphe nucleus; HDB: nucleus of the horizontal limb of the diagonal band; HPC: hippocampus; LC: locus coeruleus; LS: lateral septum; MeA: medial amygdala; MPOA: medial preoptic area; NAc: nucleus accumbens; OB: olfactory bulb; OT: olfactory tubercle; OVLT: organum vasculosum laminae terminalis; PAG: periaqueductal gray; PBN: parabrachial nucleus; PFC: prefrontal cortex; PP: posterior pituitary; PV: paraventricular nucleus of the thalamus; PVN: paraventricular nucleus of the hypothalamus; SON: supraoptic nucleus; VTA: ventral tegmental area.

2.3.1.3 Oxytocin Receptor

Once released and before being degraded, OT is on a ticking clock with only a few minutes to navigate and find the Promised Land: the oxytocin receptor (OTR). This receptor is a seven transmembrane domain receptor G protein-coupled receptor encoded by a single gene *Oxtr*, with, again, an ERE element in its promoter, indicating a control by estrogens. This receptor has the unusual ability to couple both G_q and G_i proteins, although we do not yet have a clear idea of this feature's usefulness. Electrophysiologically speaking, OTR activation leads to an increased neuronal firing, as it has been shown in the amygdala (Knobloch et al., 2012; Wahis et al., 2021), the hippocampus (Bazaz et al., 2022; Tirko et al., 2018), the parabrachial nucleus (Ryan et al., 2017), the ventral tegmental area (Tang et al., 2014), the striatum (Xiao et al., 2017), and the supraoptic nucleus (Wang and Hatton, 2006). Although, it was also shown that OTR activation activates a potassium ion channel, which leads to the hyperpolarization of the neurons in the dorsal root ganglion (DRG) (Gong et al., 2015).

OT binds the OTR with high affinity, but it can also activate the Vasopressin (AVP) receptor (V1a) and, in return, AVP can also bind to the OTR (Manning et al., 2012) (**Table 2**). Because OT can also bind V1a, a selective agonist called [Thr⁴, Gly⁷]OT (TGOT) is often used, this agonist has a similar affinity for OTR than OT, but cannot bind the V1a (**Table 2**).

	OTR	V1a	References
Oxytocin	1 nM	71 nM	Manning et al., 2012
Vasopressin	1.7 nM	2.6 nM	Manning et al., 2012
TGOT	0.8 nM	>10,000 nM	Manning et al., 2012
Atosiban	215 nM	1059 nM	Manning et al., 2012

Table 2 Binding affinities for the OT, AVP, TGOT and Atosiban to the OTR and V1a.

2.3.1.4 *Grab_{OT}* a tuned OTR

In order to detect the presence of OT in the extracellular space, Qian and colleagues recently developed a modified version of the OTR called OT1.0 sensor or the more aesthetically pleasing name *Grab_{OT}* (for GPCR activation-based sensor specific for OT). This *Grab_{OT}* is a modified OTR in which a circularly permuted GFP was inserted in the third intracellular loop of the GFP (**Figure 19A**). This results in a fluorescent receptor that, upon changing its conformation after binding with OT, will shine even stronger (**Figure 19B**). This increase in fluorescence is completely blocked by the co-application of atosiban that acts here as an antagonist (Qian et al., 2023). However, we want to monitor OT release for a certain amount of time, and the OTR is known to be desensitized relatively quickly as it occurs within a few minutes (Busnelli and Chini, 2018). For this reason, they measured the β -arrestin coupling, and observed that this receptor was not capable of coupling to it, suggesting the absence of a β -arrestin-dependent mechanism of internalization. In addition, after incubating the *Grab_{OT}* in OT for 2 hours long, the fluorescence present at the membrane of the cells did not change, suggesting no or negligible desensitization (Qian et al., 2023). Finally, to use this sensor, we need to express it in cells of the structure of interest. This results in an increase number of OTR, which, when we want to study the OT system, might not be the wiser since it might overstimulate the OTergic system. One important feature of this receptor is thus to not trigger intracellular pathways. To verify this point, they performed calcium imaging in cells expressing the *Grab_{OT}* and observed no calcium fluctuations following

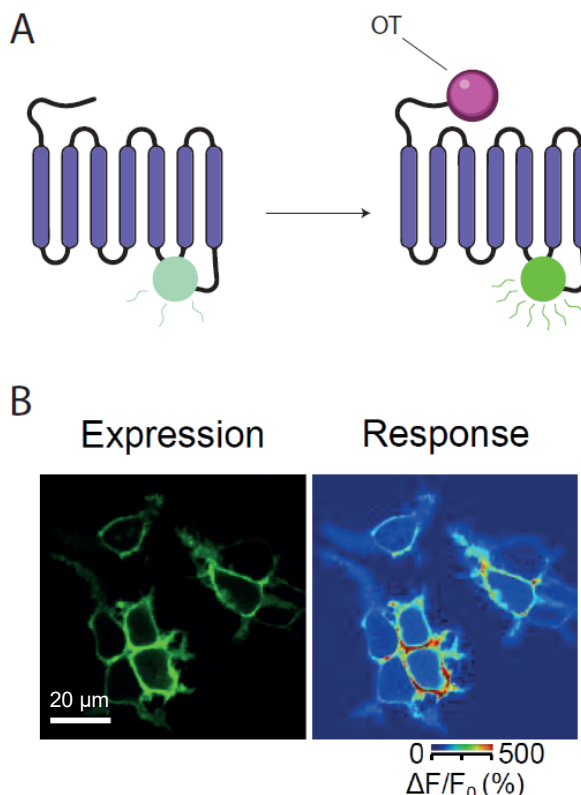


Figure 19 A. *Grab_{OT}* is a modified OTR linked with a circularly permuted GFP (left panel). When an OT molecule binds to it, the GFP's fluorescence increases (right panel). **B.** Example from (Qian et al., 2023) of cells expressing the *Grab_{OT}* with a basal fluorescence (left panel), and the relative increase of fluorescence after the application of 100 nM OT.

the application of OT, strongly suggesting that this modified receptor does not trigger intracellular pathways (Qian et al., 2023).

2.3.2 Oxytocin and pain

The first evidence of OT antinociceptive effects comes from the 80s. In 1984, Hordower and Bodnar showed that intracerebroventricular injections of OT increased the tail-flick latency in rats (Kordower and Bodnar, 1984). In 1987, Madrazo and colleagues injected intracerebroventricularly OT in a terminally ill cancer patient suffering from thoracic pain and observed a strong analgesia for two hours (Madrazo et al., 1987). From there, many studies showed an antinociceptive effect of OT in healthy animals (Agren et al., 1995; Arletti et al., 1993; Lundeberg et al., 1994; Petersson et al., 1996), in rodent models of inflammatory (Petersson et al., 2001; Yu et al., 2003) and neuropathic pain (Condés-Lara et al., 2005; Miranda-Cardenas et al., 2006). In addition, PVN stimulation was shown to increase OT concentration in the plasma, the spinal cord and the cerebrospinal fluid. This stimulation also triggers a mechanical and thermal antinociception (Martínez-Lorenzana et al., 2008). This study strongly suggests that OT acts in the periphery of the central nervous system, in the spinal cord and/or on supraspinal structures to mediate its antinociceptive effect.

2.3.2.1 *Periphery effect.*

Very few studies were interested in the potential effect of OT on peripheral OTR. It is first important to note that OT was shown to not cross the blood brain barrier (Ermisch et al., 1985), suggesting that effects induced by peripheral injection of OT should result from a peripheral effect. Although, none of these studies peremptorily showed that this effect was mediated by peripheral OTR. In addition, OT effect is unclear as some studies showed that intranasal administration of OT in patients with chronic idiopathic constipation reduced abdominal pain (Ohlsson et al., 2005), while others showed that continuous intravenous administration of OT increased visceral pain perception threshold in patients with irritable bowel syndrome (Louvel et al., 1996). De Araujo and colleagues showed that, in mice with chronic visceral hypersensitivity, OT decreased the activity of cultured colonic nociceptors, reducing nociceptive signaling and suggesting an antinociceptive effect of OT on the nociceptors of the DRG (de Araujo et al., 2014). Although, this study lacks *in vivo* effect of OT on behavior. In 2017, the effect of subcutaneous OT has been investigated in chemical nociception using the formalin test, and the activity of the different sensory fibers was recorded. Firstly, the

authors saw that the OTR was expressed in the sciatic nerve and that its expression was not changed by formalin application. Furthermore, they observed that subcutaneous injection of OT in the paw decreased the neuronal activity of the A δ and C fibers in response to the stimulation of the receptive field. This decrease lasted for 100 minutes and was blocked by the co-application of an OTR antagonist. Regarding the behavior, OT injection blocked the nociceptive effect of the formalin application. Using immunofluorescence, they also showed that OTR are present in the skin (González-Hernández et al., 2017). This study suggests that OT can act directly on OTR of the skin to alter the transmission of the nociceptive information through the A δ and C fibers. However, OT effects can also be explained by an action in the central nervous system.

2.3.2.2 *Spinal effect*

OT neurons also project directly in the spinal cord (Eliava et al., 2016), and release OT mainly in the lumbar sections (Juif et al., 2013). In addition, OTR are found in the superficial layers of the spinal cord (Moreno-López et al., 2013). In this structure, it was shown that intrathecal injections of OT induces a decrease in the nociceptive thresholds in both thermal and mechanical tests of an inflammatory pain model (Yu et al., 2003) and a neuropathic pain one (Sun et al., 2018). In addition, the intrathecal injection of OT completely abolishes A δ - and C fibers-evoked responses for almost an hour when injected during the protocol. If OT is injected prior to the protocol, it blocks the increase in the fibers activity (DeLaTorre et al., 2009). This suggests that OT blocks the transmission of the information coming from the A δ and C fibers. In addition, this effect is reproduced when stimulating the PVN just before starting a wind-up protocol (*i.e.* electrical stimulation of the sciatic nerve or the paw) (DeLaTorre et al., 2009) or during the protocol (Eliava et al., 2016). In rats with hypersensitivity due to the stimulation of the sciatic nerve, either this injection of OT or the PVN stimulation reverses the hypersensitivity, bringing the mechanical threshold back to basal conditions. These effects are blocked by the intrathecal injection of an OT antagonist (DeLaTorre et al., 2009). In an inflammatory model of pain, there is an increased OT concentration in the spinal cord, and a tonic inhibition of the C fibers action potentials discharge as shown by increase of action potentials following the local application of the OTR antagonist dOVT (Juif et al., 2013). All these studies suggest that, in the spinal

cord, OT is released mainly in the lumbar section to decrease the activity of the C fibers (and the A δ) to block the nociceptive information and thus produce an antinociception.

2.3.2.3 *Supraspinal effect*

When injected i.c.v. in rodents, OT also induces an antinociception that lasts for about 40 min (Yang et al., 2007). More precisely, OT have been injected in many specific structures to see whether an antinociception could be seen. OT injections resulted in an antinociception when injected in the raphe magnus (Wang et al., 2003), the central amygdala (Han and Yu, 2009), the nucleus accumbens (Gu and Yu, 2007; Li et al., 2010), the ventrolateral orbital cortex (Taati and Tamaddonfard, 2018), the primary sensory cortex (Esmaeilou et al., 2022), the anterior cingulate cortex (Esmaeilou et al., 2022; Li et al., 2021) and the PAG (Ge et al., 2002).

2.4 Ph.D objectives

At its beginning, a long time ago when we were still wearing masks to go out and when the bars were closed, my Ph.D was entitled “Modulation of the basal amygdala by the relaxin-3/RXFP3 system”. At this time, based on preliminary data suggesting an antinociceptive effect of the relaxin-3 in the BA, the objective of my thesis was to describe the circuit in the amygdala modulated by the relaxin-3 leading to this antinociception. To do this characterization, I used *ex vivo* electrophysiology techniques combined with the application of RXFP3’ agonists to assess their potential effect on the electrical activity of the BA neurons of naïve mice.

Because of the results of this first project (I will not spoil, you can make a guess now on whether or not it was conclusive), I moved on to another project. When I got involved into this project, the article was under the second revision. It was the story of an oxytocinergic pathway that activates vIPAG neurons to induce antinociception. One of the demands from the reviewers was to prove that the *in vivo* evoked release of OT in the vIPAG was responsible of the observed antinoception. At this moment, I was starting to characterize the Grab_{OT} *ex vivo* to implement it in the lab, so it was the perfect opportunity to use this new tool, which was my contribution in terms of experiment to this paper. In addition, the only existing characterization was performed *in vitro*, I thus also did the pharmacological characterization *ex vivo* of this Grab_{OT}.

To simplify the comprehension of this manuscript, I will divide the following sections in two: the relaxin-3 and the Grab_{OT} sections. The structure of the relaxin-3 section will resemble that of a paper with a material and method and a result part, while the Grab_{OT} will contain first the material and method and results part concerning the unpublished data of the pharmacological characterization of the Grab_{OT} and then the paper in which I used this tool.

3 Relaxin-3

The relaxin-3 is a peptide synthetized in the *nucleus incertus* that acts through a receptor named RXFP3, which activation decreases the electrical activity of the neurons expressing it (Blasiak et al., 2013; Kania et al., 2017). Both relaxinergic fibers and RXFP3 are found in the BA and the CeL (Smith et al., 2010), and more precisely, RXFP3 mRNA is found predominantly in SOM expressing interneurons of the BA and CeA according to preliminary results. Unpublished experiments showed that RXFP3 agonist injection *in vivo* in the BA increases the mechanical and thermal nociceptive threshold in both rats and mice (Figure 14). In this study, we aimed at characterizing the circuit in the amygdala that induces antinociception after the activation of RXFP3.

3.1 Material & Method

3.1.1.1 Animals

I used males and females C57BL6/J mice (wild-type and Gad65 transgenic mouse line (Lopez-Bendito, 2004)) and C57BL6/N (SOM-Cre transgenic mouse line (Taniguchi et al., 2011)) produced by the Chronobiotron. For the patch clamp experiments, the animals were used between 3 and 8 weeks, and for the stereotaxic injections, they were used at 6 weeks. Animals were housed by sex, in groups of 2 to 5 under standard conditions (room temperature, 22 °C, 45% humidity; 12/12 h light/dark cycle) with *ad libitum* access to food, water and behavioral enrichment. All experiments were conducted in accordance with European law, under French Ministry license APAFIS#23419-2019121210423483.

3.1.1 Stereotaxic injection

Anesthesia was induced with 4% isoflurane, and then mice were maintained with 2.5%. From this point forward, the body temperature was monitored using an anal probe and adjusted if necessary with a heating mat to keep them at 37-37.5°C. The mice head was then trimmed to remove all hairs and Ocrygel was applied on both eyes to avoid dessication. They then received Bupivacaine (sub cutaneous (s.c.), 2 mg/kg) and Lidocaine (s.c., 2 mg/kg) locally at the incision site, and Metacam (s.c., 2 mg/kg). Five minutes after injecting the analgesics, an incision was performed to reveal the skull. The Lambda and Bregma were then aligned to place the skull in ‘flat’ position. Using the coordinates from the Paxinos mice brain atlas (Paxinos and Franklin, 2013) (BA: ML: +/-3.25 mm; AP: -1.3 mm; DV: -5.3 mm; CeA: ML: +/-3.1 mm;

AP: -1.25 mm; DV: -5 mm), holes were drilled in the skull. A virus containing double-floxed inverted open reading frame (DIO)-GFP (pEf1a-DIO-GFP) was injected either in the BA or the CeA of SOM-Cre mice to identify SOM-expressing interneurons. In wild-type mice, retrograde red beads were injected in the CeA to label CeA-projecting neurons from the BA. Each site was injected with 100 nL of either the viral solution or the beads using a Hamilton pipette. The pipette was left in place for 5 minutes before removing it slowly (0.6 mm/min) to avoid an aspiration, which would result in the virus moving back up with the pipette. Finally, a NaCl solution was injected in the flank of the animal (s.c., 100 µL) to help them get rehydrated, and 3-4 stitches were performed at the incision site before placing the rats in a cage warmed by a red light. For viral injections, the animals were then monitored for 3 days to follow their weight and used 2 weeks after the injections. For beads injection however, as they were injected to identify neurons of the BA projecting in the CeA, which is right next to the BA, animals were used 24h after the injection.

3.1.2 Electrophysiological recordings

All recordings were obtained with the software pClamp10 (Molecular Devices, CA, USA) and an amplifier Axon MultiClamp 700B coupled to an analogue/digital interface Digidata 1332A (Molecular Devices, CA, USA). Cells were recorded at a sampling frequency of 20 kHz. All recordings were performed at room temperature.

3.1.2.1 *Slice preparation*

Mice were anesthetized by intraperitoneal (i.p.) administration of ketamine (Imalgene 400 mg/kg) and paxman (Rompun, 80 mg/kg). The paw reflexes were tested, and when the animal was in deep anesthesia, a laparotomy followed by a thoracotomy were performed to get access to the heart. Transcardial perfusion was then performed using an ice-cold, NMDG-based solution (**Table 3**). To do so, a needle was inserted in the left ventricle and the right atrium was opened using scissors. 25 mL were injected to replace the blood by the NMDG-based solution. Mice were then decapitated, an incision was made to have access to the skull, which was removed. The brain was collected and the cerebellum cut out. The brain was glued against an agarose block on the sample holder and 350 µm thick coronal slices containing the BA were obtained. For the CeA, the brain was cut in two and the cortex was cut to flatten the dorsal part of the brain. Both hemispheres were then reassembled and fixed on the sample holder on its dorsal part and 350 µm thick horizontal slices containing the CeA were obtained. In any case, a Leica VT1000s vibratome was used for slicing. Slices were transferred

in a warm (37°C) NMDG-based solution for 10 minutes before being placed in a holding chamber filled with artificial cerebro-spinal fluid (aCSF) (**Table 3**) at room temperature for at least 1 h. Finally, slices were transferred from the holding chamber to an immersion-recording chamber and superfused with aCSF at a rate of 2 ml/min.

Solution	Composition (in mM)
NDMG-based solution	NMDG (93), KCl (2.5), NaH ₂ PO ₄ (1.25), NaHCO ₃ (30), MgSO ₄ (10), CaCl ₂ (0.5), HEPES (20), D-Glucose (25), L-ascorbic acid (5), Thiourea (2), Sodium pyruvate (3), N-acetyl-L-cysteine (10) and Kynurenic acid (2.5)
Artificial cerebro-spinal fluid (aCSF)	NaCl (124), KCl (2.5), NaH ₂ PO ₄ (1.25), NaHCO ₃ (26), MgSO ₄ (2), CaCl ₂ (2), D-Glucose (15)
Intrapipette solution 'K-gluconate'	KMeSO ₄ (125), CaCl ₂ (2), HEPES (10), Na ₂ ATP (2), NaGTP (0,3)
Intrapipette solution 'KCl'	KCl (150), HEPES (10), MgCl ₂ (4), CaCl ₂ (0,1), BAPTA (0,1), Na ₂ ATP (2), NaGTP (0,3)

Table 3 Compositions of the solutions. The pH of all solutions were adjusted using either bases (NaOH for the aCSFs; KOH for the intrapipette solutions) or acid (HCl) after bubbling them with a gas comprised of 95% O₂ and 5% CO₂. In addition, the osmolality of all solutions was controlled to be between 290-310 mOsm.

3.1.2.2 Approaching the cell

The slice was placed in the recording chamber with a harp on it to avoid any movement during the recording. Using a x4 objective, the structure of interest was identified. Cells were then visualized under a x40 objective using an infrared light (590 nm). For each recording, borosilicate pipettes (Ø inside 0.86 mm; Ø outside 1.5 mm) were heat-pulled to get a resistance between 3 and 8 MΩ (Ø at the tip is about 2 µm).

3.1.2.3 Cell-attached configuration

In the cell-attached configuration, the solution was filled with aCSF because we did not open the cell membrane. This configuration was used to record the action potential without altering the intracellular medium. The pipette was brought on top of the wanted cell until a deflection was seen on the membrane. Then, the pressure was removed from the pipette to get the membrane to enter it until a resistance of 30-100 MΩ was reached. If not even one action potential was observed throughout the recording, the

cell was discarded. For the puff application, a second pipette was brought near the cell at ~100 μ m. The recordings lasted for 10 minutes and the molecule of interest was applied by puff application at 2 minutes during 1 minute. The pressure was applied using a syringe.

3.1.2.4 Whole-cell configuration

In the whole-cell configuration, the pipette was either filled with a K-gluconate or a KCl intrapipette solution (**Table 3**). The former was used to mimic the intracellular ion concentrations in order to disturb as little as possible the cell physiology. Using this solution, if we recorded the cell at a physiological membrane potential (*i.e.* ~-60/-70 mV) we would record excitatory post synaptic currents (EPSC). However, because of the chlorine equilibrium potential being at around -65 mV we could not see the inhibitory post-synaptic currents (IPSC) under these conditions. This is why we used the other intrapipette solution KCl, which had a high concentration of chlorine ions, thus inverting the gradient of this ion and amplifying it. As a result, the currents that were supposed to be outward becomes inward with an amplified amplitude.

To reach the whole-cell configuration, the pipette was brought on top of the wanted cell until a deflection was seen on the membrane. Then, the pressure was removed from the pipette to get the membrane to enter it until the giga-seal was achieved, that is a resistance of more than 1 G Ω . At this point, we compensated the fast and slow components of the pipette capacitance, and we then gave a tender kiss to the pipette to create a depression in the pipette that would open the membrane. Then, we compensated the series resistance to avoid any alteration of the recorded signal if we wanted to record in voltage-clamp, or neutralized the pipette capacitance if we wanted to record in current-clamp mode. Once all of this was done, the recording could begin. The recordings lasted for 20 minutes with the molecule of interest being applied at 5 minutes through the perfusion system. In this configuration, the cell recorded was not supposed to express the receptor; hence, the molecule of interest was applied in the bath during either 40 s for the gad65 neurons or 3 min otherwise.

In addition, a current step was performed at the beginning of each recording, first to verify that the cell can fire action potential, but also to have the firing pattern of the recorded cell. To do that, the cell was recorded in current clamp and 500 ms currents ranging from -80 pA to +200 pA were injected with a 20 pA increment.

3.1.3 Immunohistochemistry

When using the Gad65 mice, I added 1 µM of biocytin to the K-gluconate intracellular medium. I did it in order to fill neurons with biocytin during the recording so that I could label them to find them back. At the end of a slice's recording, the slice was put in paraformaldehyde 4 % during 24 hours to fix it. After that, slices were washed 4 times 15 minutes in PBS 1x and incubated 45 minutes in PBS 1x + 0.5 % triton. This step was done to permeabilise the cell membranes. Slices were washed again 3 times 10 minutes in PBS 1x and then incubated in the primary antibodies (**Table 4**) overnight on a stirrer at room temperature. The next day, slices were washed 3 times 15 minutes in PBS 1x and then incubated in the secondary antibodies (**Table 4**) overnight on a stirrer at 4°C. The slices were then imaged using a confocal microscope.

Primary antibodies (or equivalent)	Secondary antibodies (or equivalent)
Rabbit anti-somatostatin (1/500 ^e)	Donkey anti-rabbit Cyanine3 (1/800 ^e)
Mouse anti-parvalbumin (1/2000 ^e)	Donkey anti-mouse AlexaFluor647 (1/2000 ^e)
Streptavidin MarinaBlue (1/100 ^e)	///

Table 4 Antibodies used for the immunohistochemistry.

3.1.4 Data analysis

All this data analysis section was performed using custom-written Python-based scripts available here for spike detection: <https://github.com/Etienneclcr/Spike-detection.git>, and here for current analysis: <https://github.com/Etienneclcr/current-analysis.git>. The action potential and currents were detected using the `find_peaks` function from the `scipy` library. When I recorded in cell attached (10 minutes recording) and applied the agonist using puff application, I used the three following windows:

- Baseline from 1 to 2 minutes,
- Drug application from 2 to 3 minutes,
- Washout from 6 to 7 minutes.

When I recorded in whole-cell (and made a 20 minutes recording) and applied the agonist by bath application, I used the three following windows:

- Baseline from 2 to 5 minutes,
- Drug application from 6 minutes 40 seconds to 9 minutes 40 seconds,
- Washout from 15 to 18 minutes.

3.1.5 Statistical analysis

The normality was tested using the Shapiro-Wilk test. If the distribution was normal, a repeated-measure one-way ANOVA was performed. Because the measures were repeated and not matched, the sphericity was not assumed. If there was a significant difference, the ANOVA was followed by a Dunnett's multiple comparison. If the condition was not normal, a non-parametric equivalent to the ANOVA was used, here a Friedman test. If there was a significant difference, a Dunn's multiple comparisons was used to compare all the different conditions to the aCSF condition. The difference was considered statistically significant for a p-value < 0.05. The results are expressed as mean \pm SEM.

3.2 Results

To decipher how the activation of RXFP3 can induce antinociception, our goal was to characterize the effect of RXFP3 activation on the electrical activity of the neuronal circuit of the amygdala. To do so, we identified the different neuronal types in the amygdala and performed *ex vivo* electrophysiology.

3.2.1 SOM interneurons of the basal amygdala

In the BLA, the RXFP3-expressing neurons are, according to the preliminary data, SOM-expressing interneurons. At this time, we did not have any mice line that allowed us to label specifically these interneurons. However, it is known that SOM-expressing neurons are, in the amygdala, inhibitory neurons expressing GABA thus expressing the GABA-synthesizing hormone Gad65 ([Ueno et al., 2000](#)). In the laboratory, a mice line of Gad65-GFP was available, although it does not allow to differentiate between the other interneuron types. However, we knew that BA interneurons are interconnected (see ‘The basal amygdala’ section), meaning that an effect in SOM neurons might reverberate in other interneurons. To gain information on the recorded cell type, we added biocytin in the intracellular recording medium and performed immunohistochemistry to label both SOM and PV expressing interneurons. We stained those interneuron populations since the former is supposed to express RXFP3, and the latter represent about 50% of BA interneurons ([McDonald and Mascagni, 2002](#)).

3.2.1.1 *Chapter 1: the Gad65 mice*

Taking advantage this Gad65-GFP mouse line, we identified inhibitory interneurons based on their GFP expression ([Lopez-Bendito et al., 2004](#)).

Because RXFP3 activation is supposed to decrease action potential firing, we recorded GFP-positive neurons (**Figure 20A**) in patch-clamp whole-cell configuration. We clamped the current, ideally at 0 pA, or by injecting a current to adjust the membrane potential around -60 mV. A current step was performed at the beginning of each recording to determine whether the cell response to RXFP3 activation could vary depending on its firing pattern. The recording lasted 20 minutes with a bath application of A2 agonist at 500 nM at 5 minutes for 40 seconds. No effect could be seen of the A2 application on the action potential frequency of GFP-positive neurons (baseline 1.97 ± 0.47 Hz; A2 1.71 ± 0.53 Hz; Washout 1.5 ± 0.56 Hz, $n_{\text{mice}} = 6$; $n_{\text{cell}} = 16$, $p = 0.2050$, **Figure 20E**), indicating that the A2 application does not change the electrical activity of the overall population of interneurons in the BA. However, when I

set up the immunohistochemistry protocol, I realized that none of the recorded cells were neither SOM nor PV expressing cells (**Figure 25**). Moreover, none of the SOM or PV cells co-localized with the GFP (**Figure 25**). This indicates that the Gad65-GFP would not label all the GABAergic cells but only a specific population of interneurons. The results obtained in electrophysiology can now be re-interpreted as follows: the A2 application does not change the activity of a population of interneurons that does not express the SOM or PV markers. To overcome this issue, we decided to use a more adapted mice line.

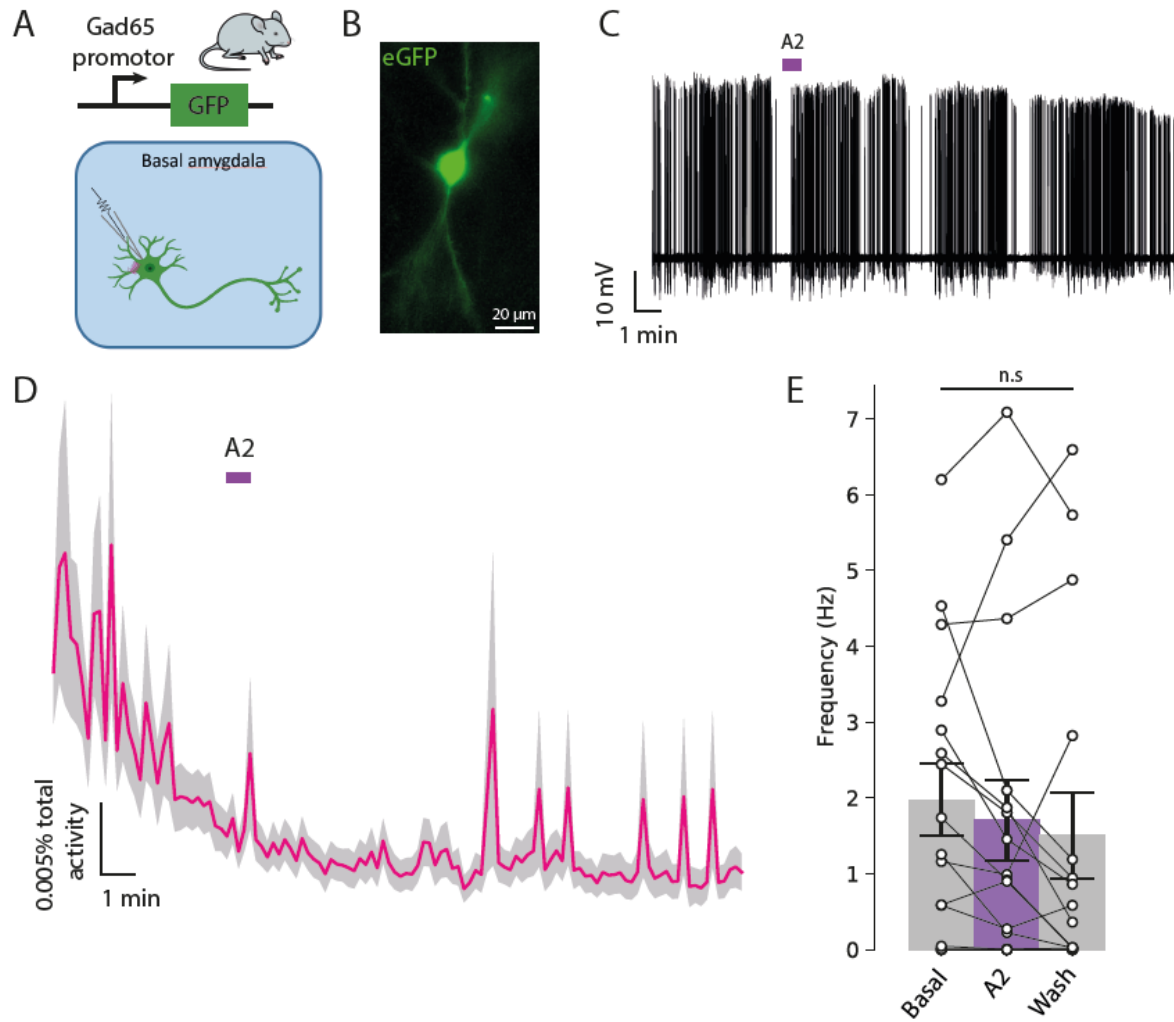


Figure 20 **A.** Neurons from the BA of Gad65-GFP mice were recorded in whole-cell current clamp. **B.** Example picture of a GFP-expressing neuron of the BA. **C.** Example recording of a GFP-expressing neuron. **D.** Time course representing the frequency of action potentials as a percentage of the total activity of the recording in function of time. The pink trace represents the mean of all the recordings and the grey area around is the SEM. **E.** Quantification of the frequency of action potentials before, during and after the application of the A2 agonist expressed as mean \pm SEM. Friedman test ($F = 3.170$, $p = 0.2050$, $n = 16$).

3.2.1.2 Chapter 2: the somatostatin-Cre mice

Since we were only interested in SOM interneurons, we used a SOM-Cre mice line (Taniguchi et al., 2011) combined with the injection of a virus containing a pEf1a-DIO-GFP sequence (Figure 21A). Using this construct, the GFP will be expressed only in Cre-expressing neurons, hence the SOM interneurons. Because we were recording potential RXFP3-expressing neurons and did not need to fill the neurons with biocytin, we were this time in loose cell-attached configuration to avoid the dialysis of the intracellular medium, which could account for the absence of responses seen in the previous experiments. Moreover, for the same reasons, the agonist was applied by puff application, allowing for a better control of the timing and location of A2 application. The recording lasted 10 minutes and the A2 was applied at 2 minutes during 1 minute.

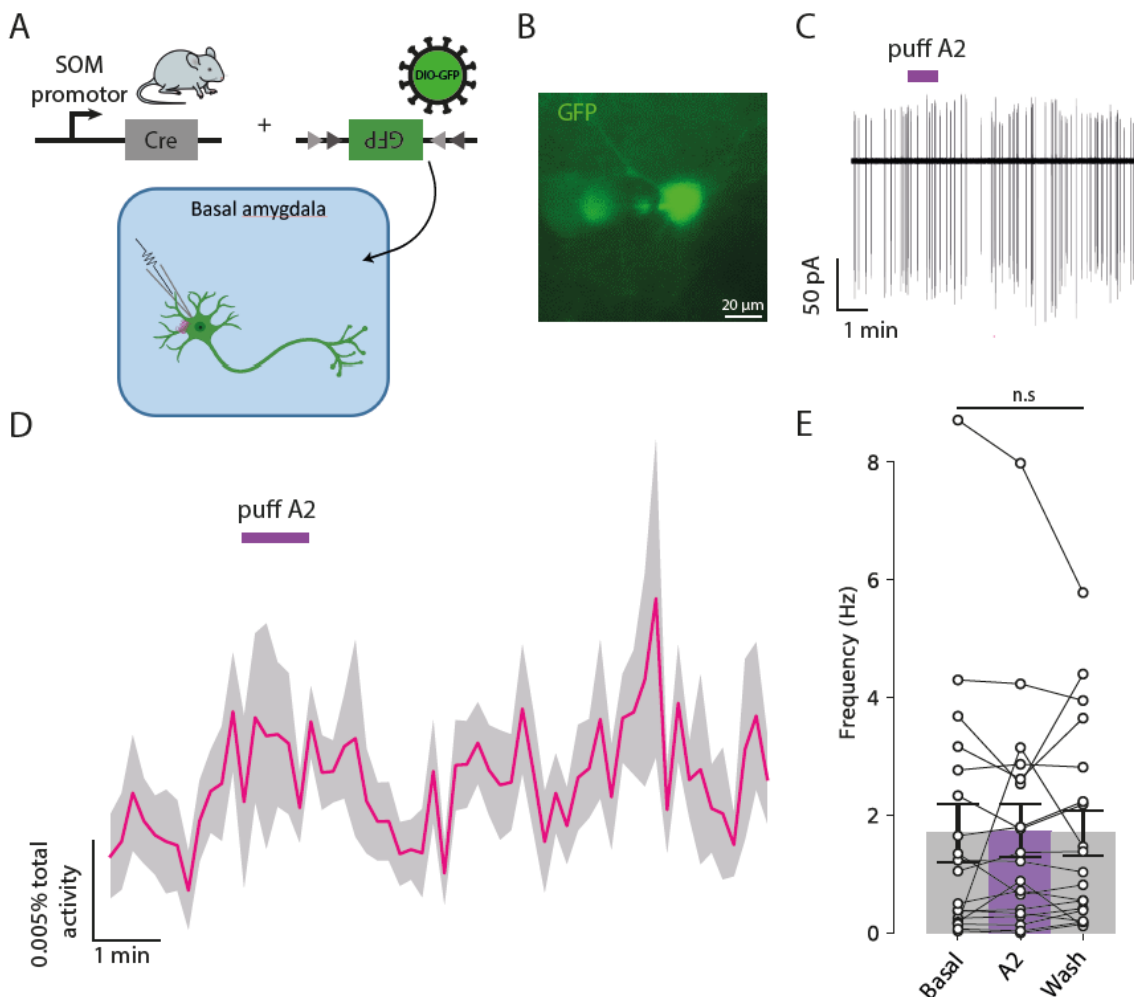


Figure 21 A. Neurons from the BA of SOM-Cre mice previously injected with a DIO-GFP virus were recorded in loose cell-attached. **B.** Example picture of a GFP-expressing neuron of the BA. **C.** Example recording of a GFP-expressing neuron. **D.** Time course representing the frequency of action potentials as a percentage of the total activity of the recording in function of time. The pink trace represents the mean of all the recordings and the grey area around is the SEM. **E.** Quantification of the frequency of action potentials before, during and after the application of the A2 agonist expressed as mean \pm SEM. Friedman test ($F = 1.368$, $p = 0.5045$, $n = 19$).

We observed no significant difference in the action potential frequency of BA SOM interneurons (baseline 1.703 ± 0.49 Hz; A2 1.73 ± 0.44 Hz; Washout 1.7 ± 0.39 Hz, $n_{\text{mice}} = 5$; $n_{\text{cell}} = 19$, $p = 0.5045$, **Figure 21E**). This result shows that the application of A2 on BA SOM neurons does not change their electrical activity. We hypothesized that RXFP3 is expressed on the synaptic terminals, thus the effect of RXFP3 activation might not be visible in the soma of neurons expressing the receptor. We decided to record BA neurons projecting to the main output of the amygdala: the central amygdala.

3.2.2 Projection neurons of the basal amygdala

We injected in the CeA fluorescent red retrobeads (Katz et al., 1984; Katz and Iarovici, 1990), which are retrograde tracer, to identify the projection neurons from the BA to the CeA (**Figure 22A**). These projections neurons are supposed to be contacted by the RXFP3-expressing interneurons. Therefore, we did not risk influencing RXFP3 activity by the dialysis of the intracellular medium. In addition, we wanted to measure whether there was a change in the information received by the projecting neuron and thus recorded the cells in whole-cell mode and clamped the membrane voltage at -60 mV. This mode of recording can be a bit confusing on what it actually measures and how it is displayed. First of all, what was recorded here were the movement of ions through the membrane of the cell (these movements are called currents). These movements account for the neuronal activity of the neurons contacting our recorded neuron. In addition, in this mode, the excitatory currents are going down (compared to the action potential commonly represented going up) and the inhibitory currents are going up. Because the recorded neurons are not supposed to express RXFP3, A2 was applied in the bath during 3 min after 5 minutes of baseline.

Both EPSC frequency and amplitude were quantified. Regarding the frequency, A2 application did not change it significantly (baseline 1.28 ± 0.3 Hz; A2 1.12 ± 0.21 Hz; Washout 0.96 ± 0.18 Hz, $n_{\text{mice}} = 3$; $n_{\text{cell}} = 8$, $p = 0.1813$, **Figure 22E**). Similarly, A2 application did not change the amplitude of EPSC (baseline 10.87 ± 2.11 pA; A2 7.64 ± 0.55 pA; Washout 7.65 ± 0.66 pA, $n_{\text{mice}} = 3$; $n_{\text{cell}} = 8$, $p = 0.1235$, **Figure 22F**). These results confirm that RXFP3 activation in the BA does not modulate the electrical activity of the neurons.

Overall, A2 application in the BA does not have a visible effect neither on interneurons firing frequency nor on the EPSC frequency and amplitude of the neurons projecting

to the CeA. In the CeA, RXFP3 is also expressed mainly by the SOM interneurons. Knowing that the CeA is known as the ‘nociceptive amygdala’, and regarding its proximity with the BA, we hypothesized that the antinociceptive effect induced by the agonist injection in the BA might be due to a spillover reaching the CeA. We thus wanted to test whether A2 application could modulate the electrical activity of CeA

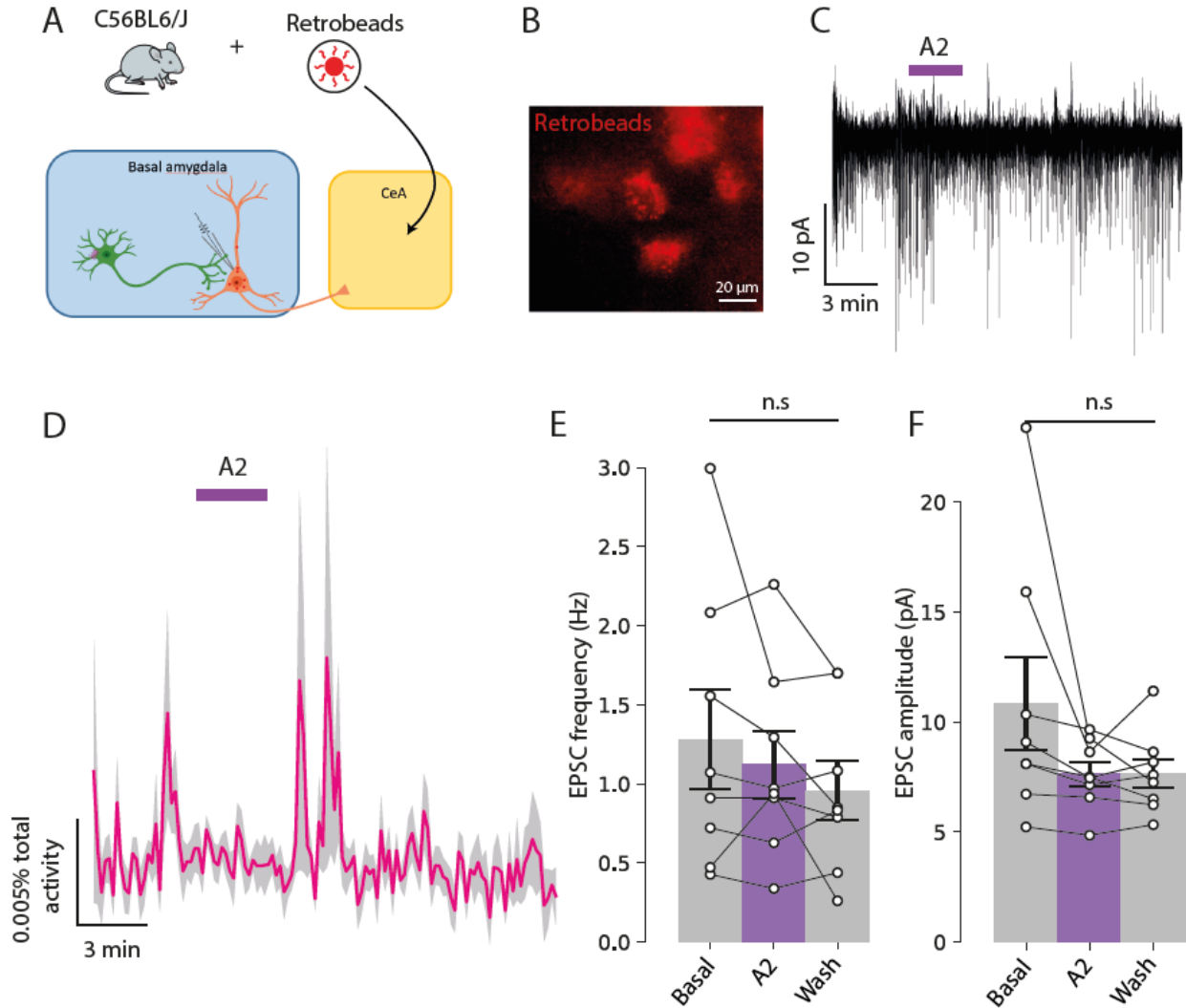


Figure 22 A. Neurons from the BA projecting to the CeA were recorded in whole-cell patch clamp voltage-clamp. **B.** Example picture neuron projecting to the CeA containing red retrobeads. **C.** Example recording of a neuron projecting to the CeA. **D.** Time course representing the EPSC frequency at a given time as a percentage of the total activity of the recording in function of time. The pink trace represents the mean of all the recordings and the grey area around is the SEM. **E.** Quantification of the frequency of action potentials before, during and after the application of the A2 agonist expressed as mean \pm SEM. RM one-way ANOVA ($F = 2.009$, $p = 0.1813$, $n = 8$). **F.** Quantification of the frequency of action potentials before, during and after the application of the A2 agonist expressed as mean \pm SEM. RM one-way ANOVA ($F = 2.960$, $p = 0.1235$, $n = 8$).

neurons.

3.2.3 SOM interneurons of the CeL

The CeA is divided into the CeL and CeM, and as the neurons putatively expressing RXFP3 are mainly the SOM interneurons of the CeL, we first focused on these. To identify and record them, we used the same protocol used for the SOM interneurons of the BA (**Figure 23A**). We injected a DIO-GFP virus in the CeA of SOM-Cre mice. After identifying SOM neurons based on their GFP expression, we recorded their action potential frequency in loose cell-attached configuration, and the A2 agonist was

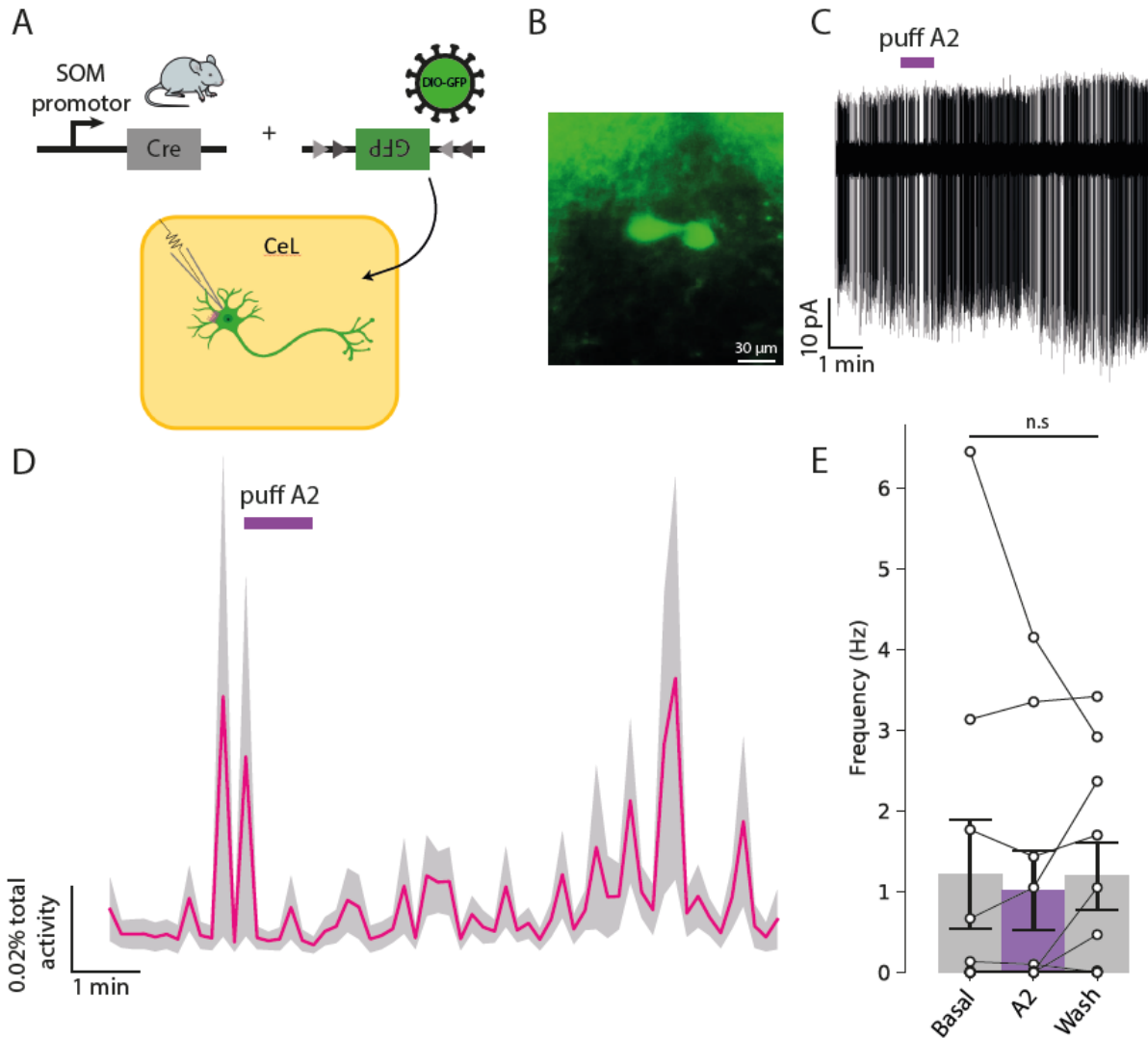


Figure 23 A. Neurons from the CeL of SOM-Cre mice previously injected with a DIO-GFP virus were recorded in loose cell-attached. **B.** Example picture of a GFP-expressing neuron of the CeL. **C.** Example recording of a GFP-expressing neuron. **D.** Time course representing the frequency of action potentials at a given time as a percentage of the total activity of the recording in function of time. The pink trace represents the mean of all the recordings and the grey area around is the SEM. **E.** Quantification of the frequency of action potentials before, during and after the application of the A2 agonist expressed as mean \pm SEM. Friedman test ($F = 1.867$, $p = 0.4320$, $n = 10$).

applied using puff application during 1 minute after 2 minutes of baseline. Again, we did not observe any change of the action potential frequency after applying the A2 agonist (baseline 1.22 ± 0.67 Hz; A2 1.01 ± 0.49 Hz; Washout 1.19 ± 0.42 Hz, $n_{\text{mice}} = 4$; $n_{\text{cell}} = 10$, $p = 0.4320$, **Figure 23E**).

3.2.4 Neurons of the CeM

The CeM is the part of the amygdala considered as its main output. Indeed, many neurons of the BA project to the CeM, or to the CeL, which then project mainly to the CeM. The CeM is thus the place where most of the information coming from the amygdala converge (Duvarci and Pare, 2014). We thought that if some circuit modulation would occur somewhere in the BA or the CeL, it must be visible in the CeM. We thus tried applying on the slice not only the A2 agonist, but also the human relaxin-3 peptide during 3 minutes after 5 minutes of baseline (**Figure 24A**). Because the circuitry in the CeA is only GABAergic, we recorded the CeM neurons in whole-cell configuration, voltage clamp mode with the KCl intracellular medium in order to make visible and amplify the IPSC (see ‘Whole-cell configuration’ section for more details). Again, we quantified both the IPSC frequency and amplitude. But once more, no effect was observed in any of the different conditions (see **Table 5** and **Figure 24**). ^{\$}Note that the Friedman test for the A2 IPSC amplitude is significant, but not the multiple comparisons (baseline vs A2 $p > 0.9999$; baseline vs washout $p = 0.0569$).

Molecule	Parameter	Baseline	Drug	Washout	n and p-value	Figure
A2	IPSC frequency	1.33 ± 0.19 Hz	1.11 ± 0.17 Hz	1.24 ± 0.21 Hz	$n_{\text{mice}} = 4$; $n_{\text{cell}} = 15$, $p = 0.4739$	Figure 23C
A2	IPSC amplitude	19.10 ± 2.98 pA	19.04 ± 3.14 pA	24.01 ± 3.66 pA	$n_{\text{mice}} = 4$; $n_{\text{cell}} = 15$, $p = 0.0408^{\$}$	Figure 23D
Relaxin-3	IPSC frequency	1.41 ± 0.35 Hz	1.42 ± 0.36 Hz	1.33 ± 0.38 Hz	$n_{\text{mice}} = 4$; $n_{\text{cell}} = 6$, $p = 0.6942$	Figure 23G
Relaxin-3	IPSC amplitude	12.83 ± 2.96 pA	12.27 ± 2.25 pA	14.99 ± 4.11 pA	$n_{\text{mice}} = 4$; $n_{\text{cell}} = 10$, $p = 0.7402$	Figure 23H

Table 5 Effect of the application of A2 or relaxin-3 on the IPSC frequency and amplitude of CeM neurons.

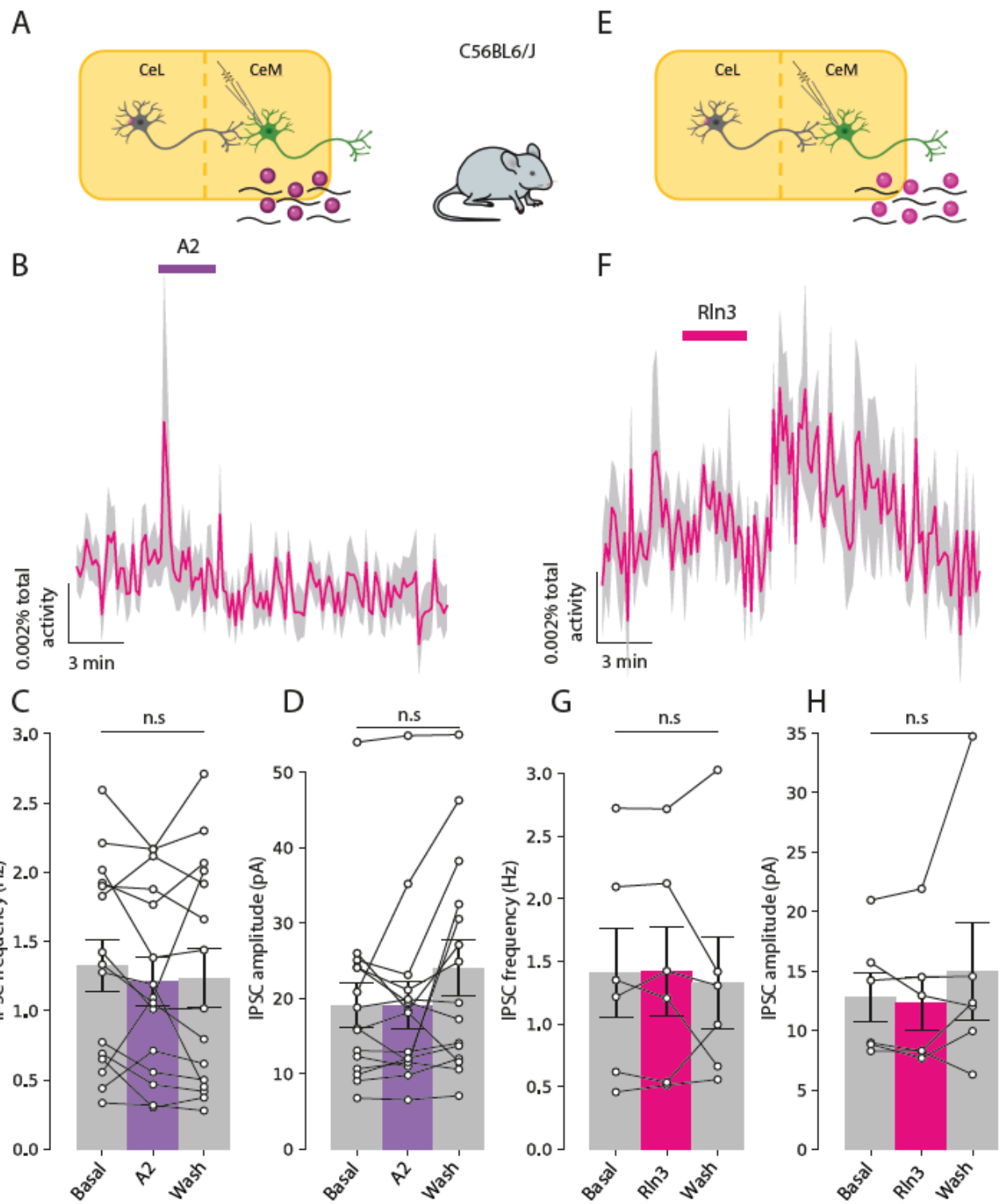


Figure 24 A & E. Neurons from the CeM were recorded in whole-cell patch clamp and the A2 agonist (**A**) or relaxin-3 (**E**) was bath applied. **B & F.** Time course representing the frequency of IPSC at a given time as a percentage of the total activity of the recording in function of time when A2 (**B**) or relaxin-3 (**F**) was applied. The pink traces represent the mean of all the recordings and the grey area around is the SEM. **C & G.** Quantification of the IPSC frequency before, during and after the application **C.** of the A2 agonist; RM one-way ANOVA ($F = 0.6537$, $p = 0.4739$, $n = 15$) or **G.** the relaxin-3; RM one-way ANOVA ($F = 0.2002$, $p = 0.6942$, $n = 6$). **D & H.** Quantification of the IPSC amplitude before, during and after the application **D.** of the A2 agonist; Friedman test ($F = 6.400$, $p = 0.0408$, $n = 15$) followed by a Dunn's multiple comparison: Basal vs A2: $p > 0.9999$; Basal vs Wash: $p = 0.0569$, or **H.** the relaxin-3; Friedman test ($F = 1.000$, $p = 0.7402$, $n = 6$).

These results show that even in the CeA, which is the main amygdala output, and which also contains putative RFPX3-expressing neurons, the application of RXFP3 agonists does not change the electrical activity of neurons.

3.2.5 Conclusion

The application of RXFP3 agonists on amygdala slices does not change the electrical activity of BA interneurons and of neurons projecting to the CeA. In addition, this application does not modulate the activity of neither the CeL neurons expressing SOM, nor the neurons of the CeM. However, unpublished data tend to show that RXFP3 agonists' infusion in the amygdala seems to induce antinociception. Thus, relaxin-3 may modulate another mechanism than the electrical activity of the neurons, or other cell types in the amygdala.

4 Grab_{OT}

OT is one of the most famous peptides in the brain and is widely studied. Recently, a tool called Grab_{OT} that can detect the presence of OT in the extracellular space was developed. This Grab_{OT} is a modified OTR linked with a GFP which fluorescence increase when the OT binds it. However, the only characterization was done in culture, so the aim of this part was to characterize *ex vivo* this receptor in response to the application of OT, AVP and TGOT.

4.1 Material & Method

4.1.1 Animals

Adult female Wistar (>8 weeks old; 250–350 g; Charles River, France) were used for this study. Animals were housed by sex, in groups of three under standard conditions (room temperature, 22 °C, 45% humidity; 12/12 h light/dark cycle) with *ad libitum* access to food, water and enrichment. All experiments were conducted in accordance with European law, under French Ministry license 3668-2016011815445431.

4.1.2 Stereotaxic injection

Anesthesia was induced with 4% isoflurane, and then rats were maintained with 3%. From this point forward, the body temperature was monitored using an anal probe and adjusted if necessary with a heating mat to 37-37.5°C. The rats' head was then trimmed to remove all hairs and vitamin A was applied on both eyes to avoid desiccation. They then received Bupivacaine (s.c., 2 mg/kg) and Lidocaine (s.c., 2 mg/kg) locally at the incision site, and Metacam (s.c., 2 mg/kg). Five minutes after injecting the analgesics, an incision was performed to reveal the skull. The skull was washed using NaCl until the bleeding stops. The Lambda and Bregma were then aligned to place the skull in 'flat' position. Using the coordinates from the Paxinos rat brain atlas (Paxinos and Watson, 2013) (vIPAG: ML: +/−1.01 mm; AP: −7.1 mm; DV: −5.88 mm; with a 10° on the DV-axis and a 45° on the AP-axis; PVN: ML: +/−1.8 mm; AP: −1.8 mm; DV: −8 mm; with a 10° on the ML-axis), holes were drilled in the skull. A rAAV2/9-hSyn-OT1.0-sensor virus was injected into the vIPAG and a rAAV1/2-OTP-C1V1-mCherry virus was injected into the PVN. Each site was injected with 300 nL of viral solution via a Hamilton pipette. The pipette was left in place for 5 minutes to let the virus diffuse before removing it slowly (0.6 mm/min) to avoid an aspiration, which would result in the virus moving back up with the pipette. Finally, a NaCl solution was

injected in the flank of the animal (s.c., 1 mL) to help them get rehydrated, and 3-4 stitches were performed at the incision site before placing the rats in a cage warmed by a red light. They were then observed for 3 days to follow their weight and used 2 weeks after the injections.

4.1.3 Slice preparation

Rats were anesthetized by administering i.p. ketamine (Imalgene 300 mg/kg) and paxman (Rompun, 60 mg/kg). The paw reflexes were tested, and when the animal was in deep anesthesia, an administration of Lidocaïne (Eurocaïne; s.c. 2 mg/kg) was done at four different locations, to have an analgesic covering all along the incision site. A laparotomy followed by a thoracotomy were then performed to get access to the heart. Transcardial perfusion was then performed using an ice-cold, NMDG-based solution (**Table 1**). To do so, a needle was inserted in the left ventricle and the right atrium was opened using scissors. 25 mL of NMDG-based solution were used to replace the blood. Rats were then decapitated, an incision was made to have access to the skull, which was removed. The brain was then collected, the cerebellum cut out, and the meninges carefully removed. A third of the rostral part of the brain was cut to have a flat part where the brain could be fixed. The brain was then glued on its rostral part against an agarose block on the sample support. 350 µm thick coronal slices containing the vIPAG were obtained using a Leica VT1000s vibratome. Slices were placed in a holding chamber filled with normal aCSF at room temperature for at least 1 h (**Table 1**). Finally, slices were transferred from the holding chamber to an immersion-recording chamber and superfused with aCSF at a rate of 2 ml/min.

4.1.4 OT1.0-sensor imaging

The slice was placed in a recording chamber with a stainless steel harp on it to avoid any movement during the recording. The vIPAG was identified using a x4 objective. The spinning disk microscope used to perform OT1.0-sensor imaging is composed of a Zeiss Axio examiner microscope with a x40 water immersion objective (numerical aperture of 1.0), mounted with a X-Light Confocal Unit–CRESTOPT spinning disk. Images were acquired at 2 Hz with an optiMOS sCMOS camera (Qimaging). The fluorescent focal planes were illuminated for 30 ms (at 475 nm) in bright-field mode using a Spectra 7 LUMENCOR. The different hardware elements were synchronized through the MetaFluor 7.8.8.0 software (Molecular Devices). The recording lasted 20 minutes, and the molecules were applied at 3 minutes and 20 seconds in the bath to

arrive in the recording chamber at 5 minutes. Once acquired, the brightness and contrast parameters of images were automatically adjusted using the Fiji software. Given the ubiquitous expression of the Grab sensor and its location at the plasma membrane, no cell could be clearly identified. Thus, the variations of fluorescence were measured on the whole plane recorded. When using atosiban as an antagonist to block the Grab_{OT}, slices were incubated for at least 1 h in 1 μM before being recorded. All recordings were performed at room temperature (25 °C).

4.1.5 Analysis

All this data analysis section was performed using a custom-written Python-based script available here: <https://github.com/Etienneclcr/Grab-pharmaco.git>. The Grab_{OT} response was measured as a change in the fluorescence's Area Under the Curve (AUC) after the light stimulation. It was quantified from the moment the molecule arrived in the recording chamber until the end of the recording. Given the exponential decay of the fluorescence due to the photobleaching, I tried to fit an exponential function to estimate the baseline fluorescence. However, the photobleaching at the beginning was always too strong, which prevents the correct fit of the exponential function. The first thing was thus to remove the first minute of recording. Then, I used a function that fit the first 4 minutes and the last 3 minutes (we will call it 'fit 1'). To choose the parameters of the function, I tried many different ones and chose the one that visually fitted best all the recordings (**Figure 25**). However, the fluorescence increase produced by the application of high concentration of agonist (500 and 1000 nM) were so big that the fluorescence stayed high even during the wash out. This resulted in a bad estimation of the baseline as you can see on the **Figure 25C**. To overcome this bias, I used another fit (yes, this one will be 'fit 2') calculated on the first 4 minutes and then extrapolated until the end of the recording (**Figure 25**). Now, you may be getting tensed wondering "why would he not use this fit 2 for all recordings?". This fit 2 decreases the bias observed with the first fit, however, it does not fit accurately the curves obtained with recordings done with a small or no response (**Figure 25A-B**). I thus defined the Fit 1 as a "default mode" fit and tested, for each recording, if it correctly fit the data. To do so, I subtracted Fit 1 to the data (before being corrected) before the application of the drug, and then computed the absolute mean of the subtraction to estimate the accuracy of the fit. If this was superior to 0.3 a.u., I considered the Fit 1 as inaccurate and used the Fit 2.

To summarize this long section of explanations, I used fit 1 unless the absolute mean of the subtraction between Fit 1 and the data during the baseline exceeded 0.3 a.u., in which case I used fit 2. After this, I measured the Area Under the Curve (AUC) of the whole recording after 4 minutes (which corresponds to the moment the drug is supposed to arrive in the chamber as the first minute is removed during the analysis)

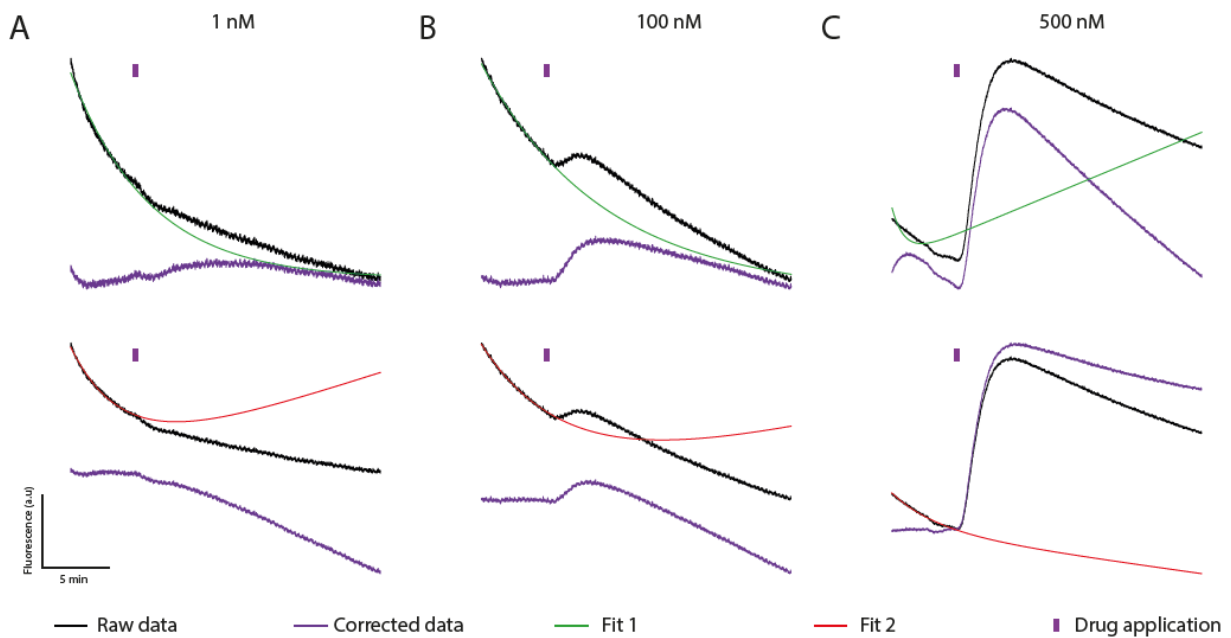


Figure 25. Is the fit fitting? Representation of the two fits used on recordings when applying 1 (A), 100 (B) or 500 nM (C) of TGOT. The black traces represent the raw data. Fit 1 is represented in green on the top traces, whereas fit 2 is represented in red on the bottom traces. The purple traces is corrected data obtained after subtracting the raw data with the fit 1 or 2.

(Figure 25). I then used the evolution of the fluorescence over time to plot heatmaps for all conditions. The AUC was used to obtain the dose-response curves and to compare the response of the Grabot in the different conditions.

4.1.6 Statistical analysis

Data normality was tested using the Shapiro-Wilk test. As one condition in each group did not follow a normality test, a Kruskal-Wallis test was used as a non-parametric equivalent to the one-way ANOVA. If there was a significant difference, a Dunn's multiple comparisons was used to compare all the different conditions to the aCSF condition. The difference was considered statistically significant for a p-value < 0.05.

The results are expressed as mean ± SEM

4.2 Pharmacological characterization - Results

To first test if the OT biosensor named Grab_{OT} was working, I injected the virus (rAAV_{2/9}-hSyn-OT1.0-sensor) bilaterally in the vIPAG (**Figure 26A-B**), and after 2 weeks of expression, I sliced the vIPAG to apply exogenous TGOT (500 nM during 20 s). As it was working remarkably well, I decided that I would do a pharmacological characterization on slices. Indeed, the only published characterizations were done on cultured cells ([Ino et al., 2022](#); [Qian et al., 2023](#)).

The idea was to characterize the fluorescence increase of the Grab_{OT} in response to various concentrations of OT, AVP and TGOT.

4.2.1 Oxytocin

The application of exogenous OT at 50 and 100 nM did not induce a significant increase in fluorescence (aCSF: 4432 ± 1232 ; 50 nM: 14479 ± 4190 , $p = 0.8347$; 100 nM: 30954 ± 13937 , $p = 0.3102$; **Figure 26 D₃**). On the contrary, both 500 and 1000 nM significantly increased the fluorescence emitted by the Grab_{OT} (aCSF: 4432 ± 1232 ; 500 nM: 198327 ± 66752 , $p = 0.001$; 100 nM: 119994 ± 39293 , $p = 0.002$; **Figure 26 D₃**) and the response at 500 nM was completely blocked by the pre-incubation in 1 μ M atosiban (8778 ± 2318 , $p > 0.9999$; **Figure 26 D₃**). Even if the number of tested concentrations is low, it seems that at 500 nM, the plateau is already reached, and the dose-responses curve gives an approximate EC₅₀ value of 116.3 nM (**Figure 26 D₂**).

4.2.2 Vasopressin

Concerning the AVP, we again did not have any response at 50 and 100 nM (aCSF: 4432 ± 1232 ; 50 nM: 11654 ± 2281 , $p > 0.9999$; 100 nM: 16497 ± 3231 , $p = 0.6283$; **Figure 26 E₃**). As for OT, both higher concentrations induced a response (aCSF: 4432 ± 1232 ; 500 nM: 48872 ± 6297 , $p = 0.0118$; 100 nM: 102857 ± 19790 , $p = 0.0005$; **Figure 26 E₃**), and the response at 500 nM was completely blocked by the co-application of atosiban (5259 ± 2588 , $p > 0.9999$; **Figure 26 E₃**). Interestingly, this time the dose-response curve did not reach a plateau at 500 nM and an EC₅₀ could thus not be estimated (**Figure 26 E₂**). This means that to complete it and have an estimation of the EC₅₀ it would be necessary to try even higher doses.

4.2.3 TGOT

Finally, when using the OTR agonist TGOT, as it was chronologically the first molecule I tested, I managed to try even more concentrations. To make it brief, all the concentrations below 250 nM did not have any significant effect (aCSF: 4432 ± 1232 ; 0.1 nM: 4563 ± 1610 , $p > 0.9999$; 1 nM: 4022 ± 827.1 , $p > 0.9999$; 10 nM: 10414 ± 4938 , $p > 0.9999$; 50 nM: 13756 ± 2062 , $p = 0.8677$; 100 nM: 17234 ± 2950 , $p = 0.5087$; **Figure 26 F₃**). The 250, 500 and 1000 nM concentrations produced a significant increase of the fluorescence (aCSF: 4432 ± 1232 ; 250 nM: 44041 ± 5044 , $p = 0.0352$; 500 nM: 151279 ± 30199 , $p = 0.0012$; 1000 nM: 173565 ± 27728 , $p = 0.0009$; **Figure 26 F₃**) and the response at 500 nM was completely blocked by the co-application of atosiban (10395 ± 6006 , $p > 0.9999$; **Figure 26 F₃**). Thanks to all these conditions, the dose-response curve for the TGOT is quite complete, with the plateau reached at 500 nM and an EC₅₀ calculated at 337 nM (**Figure 26 F₂**).

4.2.4 Conclusion

The Grab_{OT} is a recently developed powerful tool to detect the presence of OT in the extracellular space. Here I did its pharmacological characterization and showed that this fluorescent receptor responds similarly to the OT and the TGOT. However, vasopressin also activates this receptor, although it seems that the response at similar doses is lower suggesting that it requires higher doses to produce the same effect. Regarding the dose-response, because some concentrations are missing, it is hard to conclude on the EC₅₀ of both OT and vasopressin, whereas for the TGOT, it has been estimated at 337 nM, indicating that Grab_{OT} is efficient to detect OT in the range of 300 nM in slices.

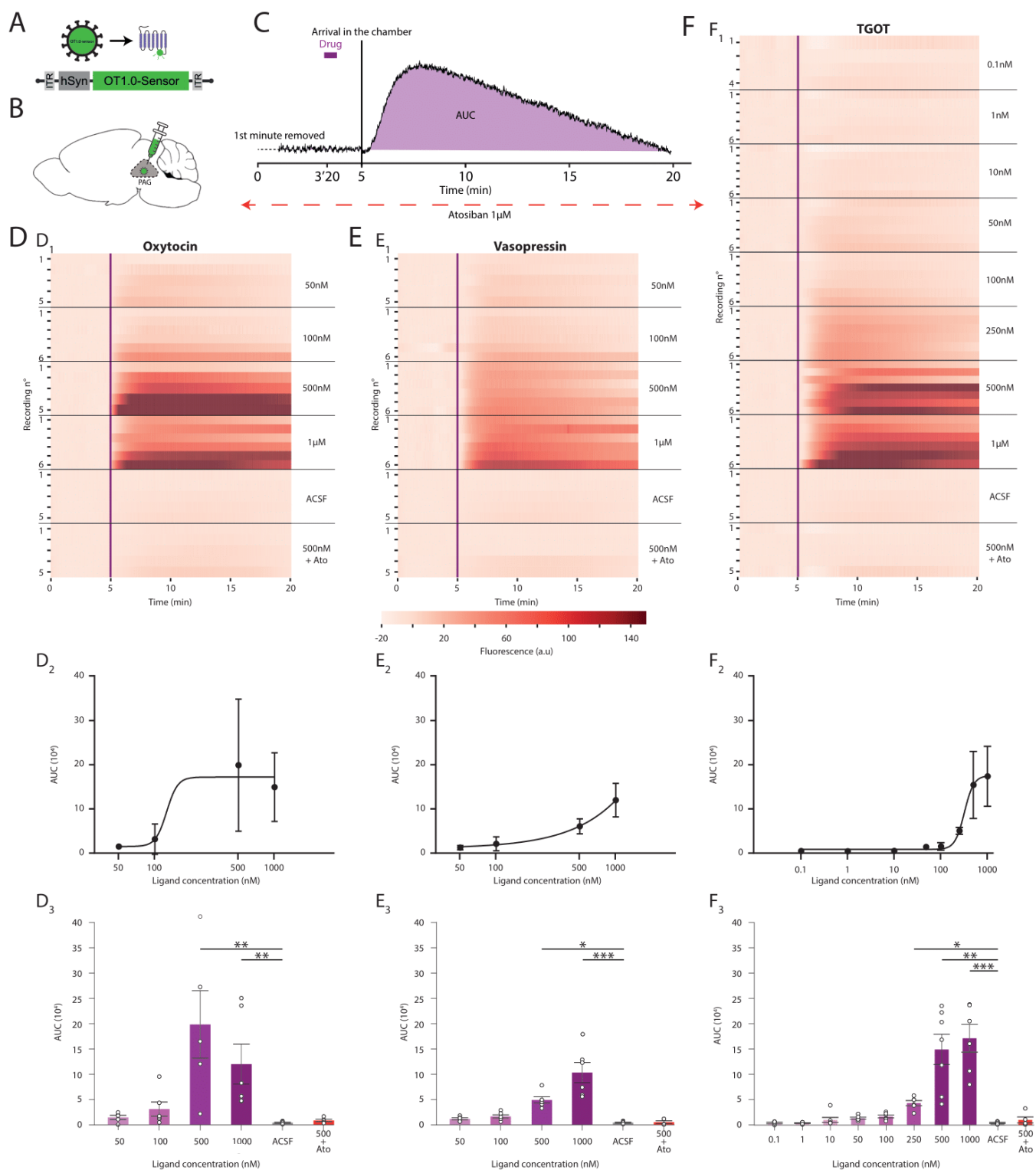


Figure 26 A. Schematic representation of the viral construction used to express the Grab_{OT}. **B.** This virus was injected in the PAG of Wistar rats. **C.** Example recording illustrating the protocol and analysis: the recording lasted 20min, the molecule applied at 3min20s for an expected arrival at 5min. For the analysis, the first minute is removed and the AUC is measured from 5 minutes until the end of the recording. **D-F.** Results obtained for oxytocin (**D**), vasopressin (**E**) and TGOT (**F**). **D1-F1.** Heatmaps representing the fluorescence over time for each recording of all conditions tested. **D2-F2.** Dose-response curves obtained for the OT, AVP and TGOT. **D3-F3.** AUC quantifications for all three tested molecules. All data are expressed as mean \pm SEM; for the detailed statistics, please see [Statistic table](#). * $p < 0.05$, ** $p < 0.001$, *** $p < 0.0001$

4.3 Article: An analgesic pathway from parvocellular oxytocin neurons to the periaqueductal gray in rats

4.3.1 Introduction

Oxytocin is a hypothalamic neuropeptide exerting a variety of functions, with one of them being the induction of antinociception. This effect is mediated by two modes of action: either the oxytocin is released in the blood circulation and acts on the periphery of the central nervous system, or it is directly released in the spinal cord or supraspinal structures. Oxytocinergic fibers and the oxytocin receptor are found in the periaqueductal gray, a structure essential for the descending control of pain. In this study, we explored a circuit between oxytocinergic parvocellular neurons of the paraventricular nucleus of the hypothalamus and the ventrolateral periaqueductal gray (vIPAG) that could mediate antinociception.

4.3.2 Results

To identify the neurons expressing the oxytocin (OT) receptor (OTR), we developed a transgenic rats line expressing the Cre recombinase under the OTR promotor. Using these rats combined with *ex vivo* electrophysiology, we confirmed the presence of functional OTR in GABAergic neurons of the vIPAG that induces upon activation an increase in action potential firing in these neurons. They represent about 20% of the total neurons of the vIPAG.

Using retrograde tracing, we also showed that a small population of parvocellular oxytocinergic neurons of the paraventricular nucleus of the hypothalamus (PVN) project to the vIPAG. These neurons are also glutamatergic and their axons are in close contact with OTR neurons, forming synaptic and non-synaptic contacts.

Using viral injections to express opsins under the OT promotor in the PVN, we were able to stimulate OT fibers in the vIPAG. Firstly, we made sure that the optogenetic stimulation of PVN OT fibers induces the release of OT by using the Grab_{OT} *ex vivo*. Then, we recorded *in vivo* the activity of the vIPAG neurons and found that stimulating the oxytocinergic fibers activate 25% of these neurons.

We then investigated whether this activation of the vIPAG neurons by the OT could modulate the neurons of the spinal cord, which is the first integration center of the

nociceptive message. We thus recorded *in vivo* the activity of lamina V wide dynamic range neurons in the spinal cord in response to the stimulation of the oxytocinergic fibers in the vIPAG. The activation of the PVN-to-vIPAG circuit decreases a type of short-term plasticity (*i.e.* the wind up) of the recorded spinal neurons, and this decrease was blocked by the application of an OTR antagonist in the vIPAG.

Finally, we tested the effect of the PVN-to-vIPAG pathway activation in a mechanical nociceptive test using two models of pain:

- an inflammatory pain model based on the injection of CFA in the paw
- a neuropathic pain model based on the chronic constriction of the sciatic nerve

We found that stimulating the release of oxytocin in the vIPAG increases the mechanical threshold in both model for 1 to 3 hours, and this effect was blocked by the application of an OTR antagonist in the vIPAG.

To confirm these results, we expressed a chemogenetic G_q receptor in OTR-expressing neurons of the vIPAG to mimic the activation of the OTR. We observed that the activation of this receptor induces a mechanical and thermal antinociception in an inflammatory pain model, in both females and males rats.

In conclusion, this study describes an antinociceptive pathway of the OT, which activates vIPAG neurons to inhibit the plasticity of spinal cord neurons, hence decreasing nociception in rats.

4.3.3 Personal contribution

My contribution to this project is the demonstration, using the GrabOT tool, that the optogenetic stimulation of oxytocinergic fibers originating from the PVN triggers the release of oxytocin in the vIPAG. This was a complementary experiment asked during the second round of reviewing, in which I also actively participated in redoing the statistical analysis of many experiments.

An analgesic pathway from parvocellular oxytocin neurons to the periaqueductal gray in rats

Received: 25 February 2022

Accepted: 8 February 2023

Published online: 24 February 2023

 Check for updates

Mai Iwasaki^{1,12}, Arthur Lefevre  ^{1,2,11,12}, Ferdinand Althammer^{2,3,4,12}, Etienne Clauss Creusot^{1,12}, Olga Łapieś  ¹, Hugues Petitjean¹, Louis Hilfiger  ¹, Damien Kerspenn¹, Meggane Melchior¹, Stephanie Küppers  ², Quirin Krabichler  ², Ryan Patwell  ², Alan Kania  ², Tim Gruber⁵, Matthew K. Kirchner  ³, Moritz Wimmer⁴, Henning Fröhlich⁴, Laura Dötsch⁴, Jonas Schimmer², Sabine C. Herpertz⁶, Beate Ditzen^{7,8}, Christian P. Schaaf^{4,8}, Kai Schönig⁹, Dusan Bartsch⁹, Anna Gugula  ¹⁰, Aleksandra Trenk  ¹⁰, Anna Blasiak  ¹⁰, Javier E. Stern³, Pascal Darbon¹, Valery Grinevich  ^{2,3,13}  & Alexandre Charlet  ^{1,13} 

The hypothalamic neuropeptide oxytocin (OT) exerts prominent analgesic effects via central and peripheral action. However, the precise analgesic pathways recruited by OT are largely elusive. Here we discovered a subset of OT neurons whose projections preferentially terminate on OT receptor (OTR)-expressing neurons in the ventrolateral periaqueductal gray (vlPAG). Using a newly generated line of transgenic rats (OTR-IRES-Cre), we determined that most of the vlPAG OTR expressing cells targeted by OT projections are GABAergic. Ex vivo stimulation of parvocellular OT axons in the vlPAG induced local OT release, as measured with OT sensor GRAB. In vivo, optogenetically-evoked axonal OT release in the vlPAG or as well as chemogenetic activation of OTR vlPAG neurons resulted in a long-lasting increase of vlPAG neuronal activity. This lead to an indirect suppression of sensory neuron activity in the spinal cord and strong analgesia in both female and male rats. Altogether, we describe an OT-vlPAG-spinal cord circuit that is critical for analgesia in both inflammatory and neuropathic pain models.

The hypothalamic neuropeptide oxytocin (OT) modulates several key neurophysiological functions, including pain¹. OT is produced in the hypothalamic supraoptic (SON) and paraventricular (PVN) nuclei by two major types of neurons: magnocellular (magnOT) and parvocellular (parvOT) neurons. MagnOT neurons of the SON and PVN are large cells that release OT into the bloodstream via axonal projections to the posterior pituitary. In contrast, parvOT neurons are smaller cells located exclusively in the PVN and project to the brainstem and spinal cord, but not the posterior pituitary². It has been previously demonstrated that a small population of PVN parvOT neurons attenuates pain

perception via two pathways: (1) through coordinated OT release into the bloodstream from magnOT neurons leading to the modulation of peripheral nociceptor activity in the dorsal root ganglion and skin and (2) by inhibiting sensory neurons in the spinal cord^{3–5}.

The periaqueductal gray (PAG) plays a pivotal role in descending analgesic pathways⁶. Indeed, physiological suppression of pain seems to be primarily modulated by a top-down system comprised of the PAG, rostral ventromedial medulla (RVM), and dorsal horn of the spinal cord (SC)⁷. For example, electrical stimulation of the PAG inhibits the firing rate of neurons in the dorsal horn of the spinal cord^{8,9}. In

A full list of affiliations appears at the end of the paper.  e-mail: valery.grinevich@zi-mannheim.de; acharlet@unistra.fr

addition, both OT axons and OT receptors (OTR) have been reported in the PAG of mice^{10,11}, where the administration of exogenous OT enhances neuronal firing rates¹² and blocking of OTRs decreases pain threshold¹³.

Altogether, these studies suggest that OT may promote analgesia through the OT-mediated activation of PAG neurons. It is therefore tempting to hypothesize two independent, yet complementary mechanisms of OT-mediated analgesia wherein OT attenuates nociceptive signals at the level of peripheral nociceptors and/or the spinal cord^{3,14}. This would additionally act within the PAG to fine-tune additional descending pain-related pathways.

However, neither the cellular circuitry nor the analgesic effects of endogenous OT signaling in the PAG have been studied. To address this gap, we first generated a Cre knock-in rat line to label and manipulate OTR neurons in the PAG, wherein we observed both synaptic and non-synaptic contacts of OTergic axon terminals with somata and dendrites of OTR-positive PAG neurons. Next, we employed cell-type-specific viral vectors to identify a subpopulation of parvOT neurons projecting to the ventrolateral subregion of the PAG (vIPAG). We then used *in vivo* electrophysiology combined with optogenetics in the vIPAG to reveal that activation of OTR neurons leads to inhibition of sensory wide dynamic range (WDR) neurons in the spinal cord (SC_{WDR}) of anesthetized rats. Finally, we found that optogenetically-evoked OT release in the vIPAG produces analgesia and this effect was recapitulated by chemogenetic activation of vIPAG OTR neurons (vIPAG_{OTR}).

In this work, we identified an independent parvOT→vIPAG_{OTR}→SC_{WDR} pathway that is distinct from the previously described direct parvOT→SC_{WDR} pathway³ and is capable of promoting analgesia in the context of both inflammatory and chronic neuropathic pain.

Results

vIPAG OTR-expressing neurons are GABAergic

To study OTR-expressing neurons in the vIPAG, we generated a transgenic line of rats with Cre recombinase expression controlled by the endogenous OTR gene locus (OTR-IRES-Cre line, see "Methods" for details) (Fig. 1a, Supplementary Fig. 1a–g). To label OTR neurons, we injected the PAG of OTR-IRES-Cre female rats with a rAAV carrying a Cre-dependent GFP expression cassette (rAAV_{1/2}-EF1α-DIO-GFP) ($n=4$). We found a clustering of OTR neurons along the anteroposterior axis of the vIPAG (Supplementary Fig. 1d–g). To further assess the specificity of Cre localization in OTR-IRES-Cre rats, we performed RNA-Scope using probes against both OTR and Cre mRNAs ($n=3$ rats) and found that 91.38% of Cre-positive cells were also positive for OTR mRNAs and 90.81% of OTR-positive cells also expressed Cre mRNAs (Fig. 1b, Supplementary Fig. 2a, b). We further validated the OTR-IRES-Cre rats by injecting rAAV_{1/2}-EF1α-DIO-GFP into the vIPAG combined with an antibody staining against Cre recombinase and found a 98.6% overlap between GFP and Cre signals (Supplementary Fig. 2c, d). In addition, we performed a western blot using the same Cre antibody and found the specific Cre band (35 kDa) only in OTR-IRES-Cre, but not wild-type rats (Supplementary Fig. 2e, f).

Ex vivo electrophysiology in acute brain slices of PAG showed that application of the selective OTR agonist, [³H⁴Gly⁷]oxytocin (TGOT), induced a significant increase in firing of GFP+ OTR neurons which disappeared after washout (Baseline 0.573 ± 0.295 Hz vs TGOT 1.045 ± 0.388 Hz vs Wash 0.514 ± 0.298 Hz; $n=11$; Fig. 1c–g). There was no response to TGOT in recorded GFP- neurons (Baseline 0.119 ± 0.046 Hz vs TGOT 0.108 ± 0.049 Hz vs Wash 0.122 ± 0.064 Hz, $n=9$, Supplementary Fig. 1h, i). In addition, TGOT incubation induces a significant decrease of the first spike latency (FSL) only in GFP+ OTR neurons ($n=8/10$, Baseline 129.31 ± 28.04 ms vs TGOT 41.42 ± 12.37 ms, *** $p=0.0041$ (paired two-tailed t test, $n=10$, Fig. 1h–j) and has no global effect on the FSL of GFP-OTR neurons (Baseline 31.95 ± 9.44 ms

vs TGOT 37.08 ± 14.89 ms, $p=0.788$ (paired two-tailed t test), $n=7$, Supplementary Fig. 1j–m).

This result shows that OTR-IRES-Cre rats correctly express functional OTRs and Cre within the same cells and that the pharmacological activation of OTRs induces a significant change in the intrinsic excitability properties of GFP+ OTR neurons.

We then quantified the number of vIPAG neurons expressing GFP and found that 396 out of 2135 (18.6%) cells were GFP-positive (Fig. 1k, l), indicating that about a fifth of all vIPAG cells express OTR. Histochemical analysis of vIPAG slices further revealed that the vast majority of GFP+ cells stained positive for GAD-67, a marker of GABAergic neurons. This result indicates that virtually all of the vIPAG OTR neurons are GABAergic in nature (94.7%, $n=174$ cells, Fig. 1m, n).

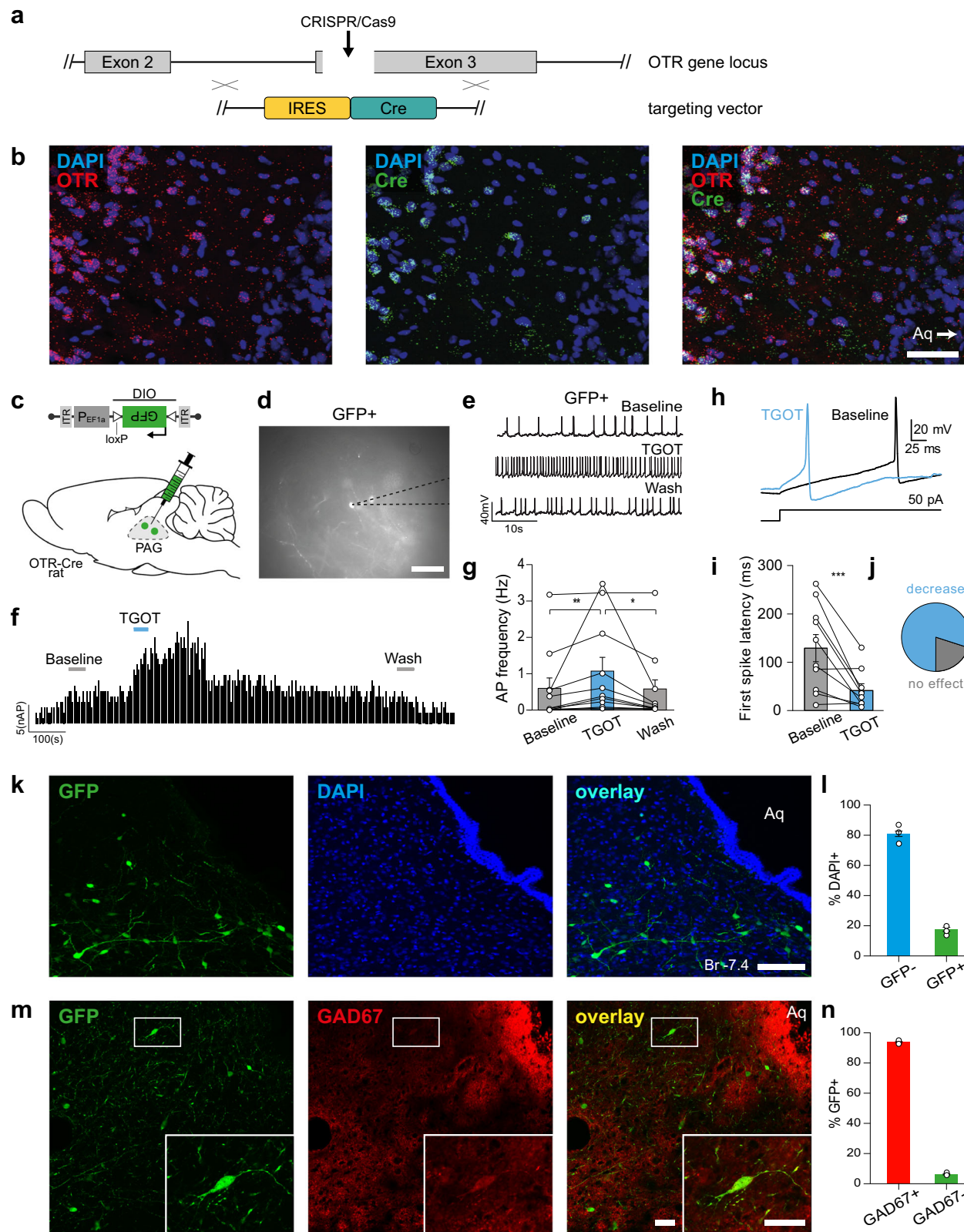
A projection from PVN parvOT neurons to the vIPAG

To determine the origin of OT projections activating vIPAG OTR neurons, we injected a rAAV expressing mCherry under the control of the OT promotor (rAAV_{1/2}-OTp-mCherry¹⁵, into either the PVN or SON in addition to a Cre-dependent rAAV expressing GFP (rAAV_{1/2}-EF1α-DIO-GFP) into the vIPAG of OTR-IRES-Cre female rats ($n=4$; Fig. 2a). A schematic depiction of viral injections, expression time, treatment allocation and performed experiments can be found on Supplementary Fig. 3. We found mCherry+ axons in close proximity to GFP+ OTR cells in the vIPAG after injection into the PVN (Fig. 2b–e). This indicates that axons from OT neurons within the vIPAG originate exclusively from the PVN. To further investigate a potential laterality of PVN→vIPAG fibers and to confirm injection sites, we injected additional rats ($n=3$ male and $n=3$ female) unilaterally into the PVN and SON with rAAV_{1/2}-OTp-GFP and rAAV_{1/2}-OTp-mCherry, respectively (Supplementary Fig. 4). Interestingly, we found that unilateral injections of the PVN resulted in robust OT fiber labeling in both hemispheres of the vIPAG, thus indicating that each PVN innervates both the left and right vIPAG. Here again, no red fibers were detected indicating that SON OT neurons do not project to the vIPAG.

We confirmed these results with retrograde tracing by injecting wild-type female rats ($n=4$) with CAV2-CMV-Cre into the vIPAG and rAAV_{1/2}-OTp-DIO-GFP into the PVN (Fig. 2f). We found that only a few, relatively small ($n=21$ cells, 10 to 20 μm diameter) OT neurons were labeled in the PVN (Fig. 2g–i). Furthermore, the retro-labeled cells were predominantly located at the latero-ventral edge of the PVN, although some GFP+ neurons were found in the caudal medio-dorsal region of the PVN.

Because this discrete population resembled the morphology of parvOT neurons (e.g. small size and spindle-like shape), we injected wild type female rats ($n=3$) with a marker of magnOT cells, Fluorogold (FG, Santa Cruz Biotechnology, Dallas, 15 mg/kg, i.p.), to specifically label magnOT, but not parvOT neurons². In parallel, the same rats received an injection of green latex Retrobeads (Lumafluor Inc., Durham, NC, USA) into the vIPAG (Supplementary Fig. 5a) to retro-label only the OT neurons projecting to vIPAG. The histological analysis revealed that Fluorogold labeled PVN neurons did not contain the green puncta of Retrobeads in their cytoplasm (Supplementary Fig. 5b), indicating that the OT cell projections to the vIPAG represent parvOT neurons, but not magnOT neurons.

Next, we asked whether these ParvOT→vIPAG_{OTR} neurons belonged to the same population of parvOT neurons we previously described³ as projecting to the SON and spinal cord (SC). We first injected wild-type female rats ($n=3$) with green Retrobeads into the vIPAG and red Retrobeads into the SC and found no OT+ neurons in the PVN containing beads of both colors within the same cells (Supplementary Fig. 5c–f). We then analyzed whether ParvOT→vIPAG_{OTR} neurons, identified in Fig. 2b, are projecting axons to the SC or SON



and found no detectable GFP+ axons in the cervical, thoracic or lumbar segments of the SC, nor in the SON (Supplementary Fig. 5g, h). Finally, we injected another cohort of wild-type female rats ($n=3$ per group) with CAV2-CMV-Cre into the SON (Supplementary Fig. 5i) or the SC (Supplementary Fig. 5l) and rAAV_{1/2}-OTp-DIO-GFP into the PVN. Here, we found that PVN neurons projecting to the SON also send axons to the SC, but not to the vIPAG (Supplementary Fig. 5j). Similarly,

PVN neurons projecting to the SC also send axons to the SON, but not to the vIPAG (Supplementary Fig. 5k, l). Altogether, our results indicate the existence of two distinct populations of parvOT neurons that project either to the vIPAG (present study) or to the SC³. A schematic distribution map highlighting the relative contributions of ParvOT neurons projecting to the vIPAG and spinal cord can be found on Supplementary Fig. 6.

Fig. 1 | Generation of KI OTR-Cre rats and identification of vIPAG OTR neurons. **a, b** Generation of knock-in OTR-Cre rats; **a** Schema of the OTR gene locus and the insertion site of the IRES-Cre sequence. **b** RNA-scope *in situ* hybridization signal from Cre ($n_{cells} = 47$ cells) and OTR ($n_{cells} = 42$) probes. Scale bar = 200 μ m. **c–g** TGOT-induced increase of AP frequency of OTR neurons in the PAG of female rats. **c** Schema of rAAV_{1/2}-pEF1 α -DIO-GFP injection in the PAG of OTR-Cre rats. **d** Example image showing a GFP-positive cell during patch-clamp recordings. Scale bar = 20 μ m. **e** Example traces from a GFP-positive cell under baseline, TGOT application, and wash out conditions. **f** Time course of GFP-positive cell activity (frequency distribution) upon TGOT application. **g** Quantification of TGOT effect on AP frequency of GFP-positive cells. Friedmann test, $F = 14.97$, $p < 0.0001$, $n_{cells} = 11$, $n_{rats} = 4$ followed by Dunn's multiple corrections: Baseline 0.573 ± 0.295 Hz vs TGOT 1.045 ± 0.388 Hz vs Wash 0.514 ± 0.298 Hz; ** $p = 0.0029$, * $p = 0.0168$ (two-sided). **h–j** TGOT-induced change in first spike latency (FSL) of OTR neurons in the PAG. **h** Representative evoked currents in a GFP-positive

neuron in response to a square current step (50 pA) in baseline (black line) and after TGOT application (blue line). **i** FSL quantification for GFP-positive neurons showing the difference between baseline (129.31 ± 28.04 ms) and TGOT (41.42 ± 12.37 ms) conditions, *** $p = 0.0041$ (paired two-tailed t test, $n_{cells} = 10$, $n_{rats} = 4$). **j** Proportion of neurons after TGOT incubation with a decrease of the FSL superior to 10 ms ((blue) $n = 8/10$) or with a variation of the FSL < 10 ms ((gray) $n = 2/10$). **k, l** Quantitative analysis of OTR cells in the PAG. **k** Images showing GFP (green) and DAPI (blue) staining of the vIPAG from OTR-Cre rats injected with rAAV_{1/2}-pEF1 α -DIO-GFP virus. Scale bar = 100 μ m. Aq = Aqueduct. **l** Bar plot showing the percentage of vIPAG cells expressing GFP \pm SEM ($n_{cells} = 417$, $n_{rats} = 3$). **m, n** GAD67 staining of OTR cells in the vIPAG. **m** Image of a vIPAG brain slice stained for GFP (green) and GAD67 (red). Scale bar = 100 μ m, inset scale bar = 20 μ m. **n** Bar plot showing the percentage of GFP-positive neurons \pm SEM ($n_{cells} = 338$, $n_{rats} = 2$) in the vIPAG stained and not stained by GAD67 antibody. Data are represented as mean \pm SEM and as individual paired points. Source data are provided as a Source data file.

PVN parvOT axons form somatic and dendritic contacts with vIPAG OTR neurons

Our next aim was to identify synaptic-like contacts between OT axons and OTR + neurons in the vIPAG. First, we counted the number of OT fibers in close proximity to OTR + neurons, relative to Bregma (Fig. 3a–c), and found a positive correlation between the two parameters ($R^2 = 0.575$, $p < 0.0001$, Fig. 3d), indicating that OT fibers specifically target OTR neurons in the vIPAG.

Next, we injected rAAV_{1/2}-pEF1 α -DIO-GFP into the vIPAG of OTR-IRES-Cre female rats to label OTR neurons and then stained for OT, DAPI and the presynaptic marker synaptophysin (SYN, Fig. 3a, e, f). These sections were analyzed using Imaris software to quantify the OT innervation of GFP+ (37%) and GFP- (4%) cells (Fig. 3g) as well as the percentage of synaptophysin-positive contacts between OT axons and GFP+ somas (7%) or dendrites (56%) (Fig. 3h, Supplemental Fig. 7a–e). The latter indicated that the majority of OT axons predominantly form typical synaptic contacts on dendrites of PAG OTR + neurons similar to the OT-containing synapses previously demonstrated in the brainstem and SC¹⁶. When we quantified the proportion of SYN+ OT fibers, we found that 80% of OTergic fibers at Bregma -6.5 mm, 90% of OTergic fibers at Bregma -7.5 mm and virtually 100% of OTergic fibers at Bregma -8.5 mm were positive for SYN+, thus essentially ruling out that these fibers further project to the spinal cord (Supplemental Fig. 7f).

Several reports have shown that OT is produced and released concomitantly with the conventional neurotransmitter, glutamate^{15,17}. Therefore, we next tested whether OT-immunoreactive axons in the vIPAG also contained the glutamate transporter, vGluT2 (Fig. 3i, j). This analysis revealed that only 12.64% of OT fibers were also positive for vGluT2z (Fig. 3j). Importantly, we found synaptic-like contacts between GFP+ dendrites and both vGluT2+ (Fig. 3k) and vGluT2- OT fibers (Fig. 3l). These findings suggest that a small percentage of direct PVN OT \rightarrow vIPAG contacts are glutamatergic, although the precise role of glutamate in these putative synapses remains unclear.

Evoked OT release in the vIPAG increases neuronal activity *in vivo*

Next we wanted to characterize the function of the PVN_{OT} \rightarrow vIPAG circuit in vivo by expressing channelrhodopsin2 (ChR2) fused with mCherry (rAAV_{1/2}-OTp-ChR2-mCherry; Fig. 4g) specifically in OT neurons of the PVN^{3,15}. Firstly, we wanted to assess whether optogenetic stimulation of the OTergic axons arising from the PVN triggers release of OT within the vIPAG. To this end, we injected a modified channelrhodopsin2 (C1V1) fused with mCherry (rAAV_{1/2}-OTp-C1V1-mCherry), or mCherry alone as a control (rAAV_{1/2}-OTp-mCherry), in the PVN, and an OT biosensor named GRAB_{OT}¹⁸ (rAAV_{2/9}-hSyn-OT1.0-sensor) in the vIPAG (Fig. 4a). The GRAB_{OT} is a modified OTR with a fused cpGFP which becomes more fluorescent upon binding of OT to the receptor

(Fig. 4b). Next, vIPAG GRAB_{OT} fluorescence was recorded in female rats ex vivo while stimulating the PVN OT fibers (30 s at 20 Hz, 30 ms pulse width) in presence or absence of atosiban, here used as an antagonist of GRAB_{OT}¹⁸. Overall, the stimulation of the PVN OTergic fibers within the vIPAG induced a significant increase of GRAB_{OT} fluorescence (Fig. 4c, d), as shown by the increase of the maximum fluorescence value (mean \pm SEM, control: 1.151 ± 0.352 , C1V1: 7.987 ± 2.470 , C1V1 + atosiban: 0.5843 ± 0.2279 , $p = 0.0143$, $n = 16$; Fig. 4e) and the increase of the area under the curve (mean \pm SEM, control: 635.6 ± 150.2 , C1V1: 2664 ± 632 , C1V1 + atosiban: 409.7 ± 57.57 , $p = 0.0045$, $n = 16$; Fig. 4f).

In vivo PAG neuronal firing was then recorded in anesthetized female rats using silicone tetrodes coupled with a blue light (BL) that was used to stimulate PVN_{OT} axons in the vIPAG (20 s at 30 Hz, 10 ms pulse width; Fig. 4g, Supplementary Fig. 8). Out of 82 recorded neurons, 21 showed an increase in firing rate (mean \pm SEM; from 1.05 ± 0.39 to 17.65 ± 6.45 Hz, $p = 0.0133$; Fig. 4h–k). In contrast, two neurons, whose spontaneous activity prior to BL onset was high, showed a decreased firing rate within 300 s after the onset of BL (one cell from 25.83 to 6.95 Hz, another from 40.20 to 0.19 Hz; Fig. 4h, i). The remaining 59 neurons did not react to BL (Fig. 4h, i). We found the normalized mean activity of the excited neuronal population remained elevated for at least 300 s following the onset of BL (Fig. 4j). Notably, the time course of spike increase was diverse, as shown by the latency (1st quantile, median, 3rd quantile) for onset (1, 4, 40.25 s), peak activity (116.25, 155, 280.25 s) and offset (147.75, 296, 300) (Supplementary Fig. 8d). However, the total number of active neurons was maintained throughout the 300 s period following BL stimulation (Supplementary Fig. 8e). Therefore, we conclude that BL-evoked OT release in the vIPAG leads to an overall excitation of putative OTR + vIPAG neurons.

Evoked OT release in vIPAG inhibits spinal cord WDR neurons activity *in vivo*

Next, we explored the downstream target of the PVN_{OT} \rightarrow vIPAG_{OTR} circuit by performing in vivo BL stimulation of PVN_{OT} axons in vIPAG (vIPAG-BL) while simultaneously recording sensory wide dynamic range (WDR) neuronal responses to electrical stimulation of the hind paw receptive field of female rats (Fig. 5a; Supplementary Fig. 9a). We focused on WDR neurons in the spinal cord (SC_{WDR}) because they are modulated by vIPAG inputs and have also been identified as an important cell population for integrating pain-related signals¹⁹. Indeed, peripheral sensory information converges from both fast (A β and A δ type) and slow-conducting (C-type) primary afferent fibers, which are then integrated through WDR neurons in the deep laminae of the SC. Following repetitive electric stimulation to the hind paw WDR neuron receptive field, a short-term potentiation (wind-up; WU) occurs on the synapse made by C-type fibers onto WDR neurons that causes the spike rate of the cell to reach a plateau of maximal activity (Fig. 5b; time

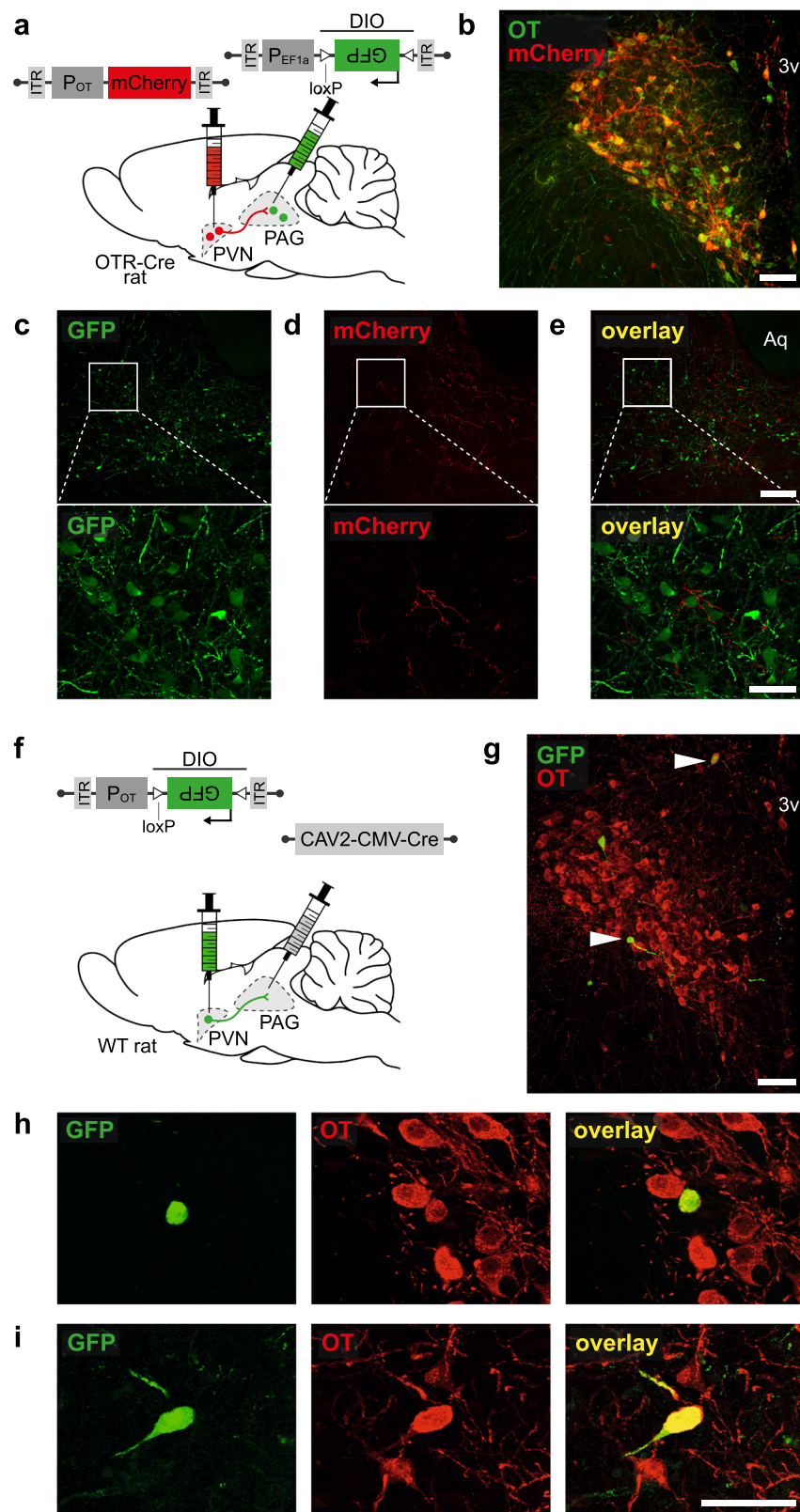


Fig. 2 | PVN ParvOT neurons send axonal projections to vIPAG of female rats. a–e Anterograde tracing of projections from PVN OT-neurons to the vIPAG.

a Schema of viral injection showing injection of rAAV_{1/2}pOT-mCherry in the PVN and rAAV_{1/2}pEF1α-DIO-GFP in the PAG of OTR-Cre rats ($n = 4$ female rats). **b** Image showing co-localization of rAAV_{1/2}pOT-mCherry and OT in the PVN. Scale bar = 200 μm. 3v = third ventricle. **c–e** Images of GFP (green, c) and mCherry (red, d) staining in the vIPAG showing PVN OT fibers surrounding vIPAG GFP neurons (e). Scale bar = 300 μm, zoom scale bar = 40 μm. Aq = Aqueduct. **f–i** Retrograde tracing

of projections from PVN OT-neurons to the vIPAG. **f** Schema of viral injection showing injection of rAAV_{1/2}pOT-DIO-GFP in the PVN and rAAV_{1/2}CAV2-Cre in the vIPAG of WT rats ($n = 4$ female rats). **g** Image of the PVN from a rat injected with CAV2-Cre into the vIPAG and rAAV_{1/2}OTp-DIO-GFP into PVN, with OT stained in red. White arrows indicate co-localization of GFP and OT. Scale bar = 200 μm.

h, i Magnified insets of the cells indicated by white arrows in the wide field image. Scale bar = 40 μm.

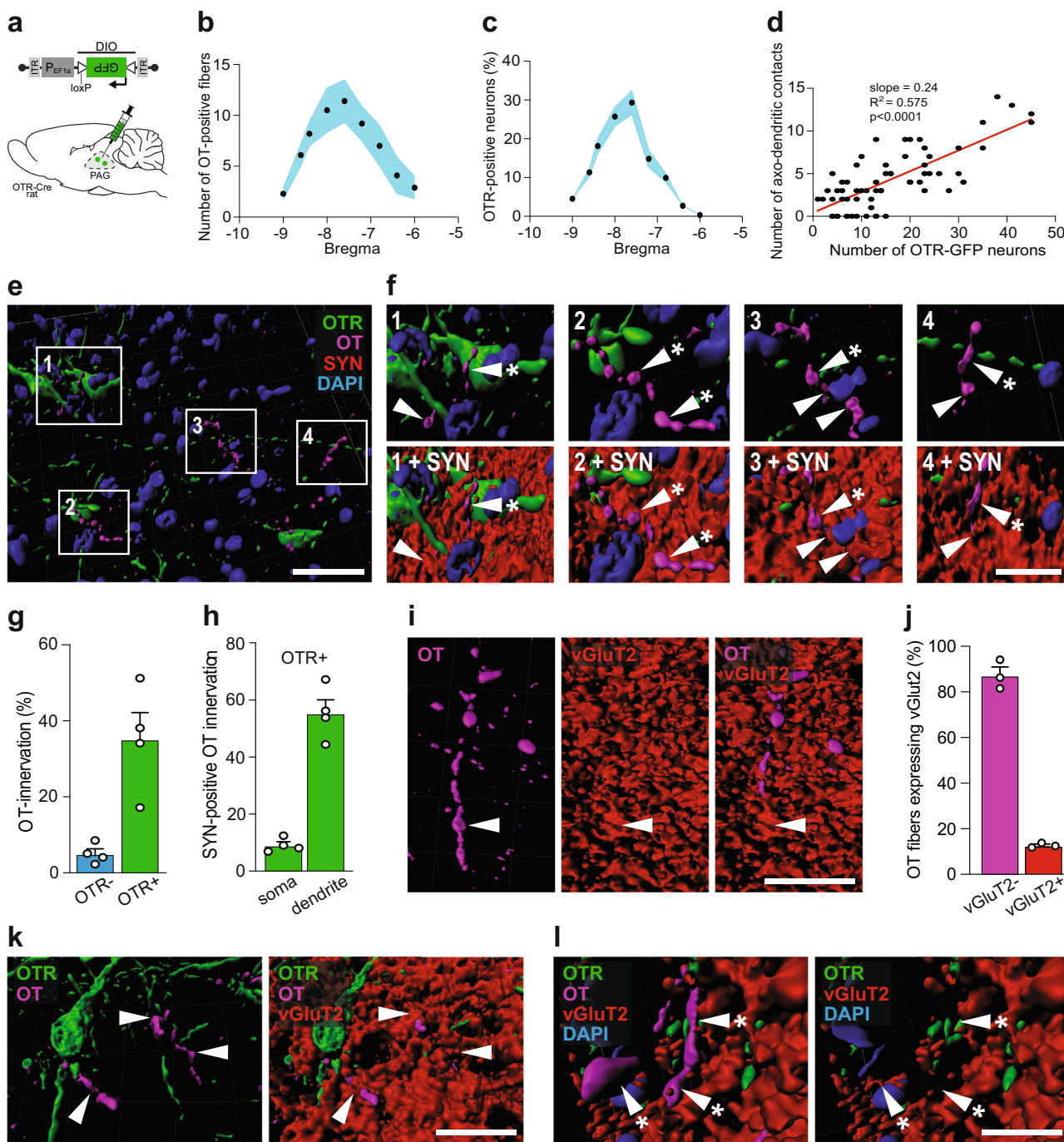


Fig. 3 | OT fibers form synaptic and non-synaptic contacts with vIPAG OTR neurons of female rats. **a** Schema of rAAV_{1/2}-pEF1α-DIO-GFP injection in the PAG of OTR-Cre rats. **b** Graph showing the relation between the number of OT fibers in the vIPAG and the bregma level. Blue area represents SEM. $n_{fibers} = 290$, $n_{rats} = 4$. **c** Graph showing the relation between the percentage of OTR neurons in the vIPAG and the bregma level. Blue area represents SEM. $n_{cells} = 528$, $n_{rats} = 4$. **d** Correlation between the numbers of OTR neurons and OT fibers within the same slice ($n_{slice} = 64$). Each dot represents one analyzed brain section. Pearson r correlation, $R^2 = 0.5745$, $p < 0.0001$ (two-sided), slope = 0.2438. **e** 3D reconstruction of OTRergic contacts with vIPAG OTR neurons. **f** Overview image showing OTR-neurons (green), OT-fibers (magenta), synaptophysin (SYN, red), and DAPI (blue). **g** Bar graph showing the percentage of OTR positive ($n = 496$) and negative ($n = 3840$) cells receiving OT innervation (<1 μm distance between fibers and cells). $n_{rats} = 4$, 8 images per animal, $p = 0.0055$ (two-sided). **h** Bar graph showing the percentage of contacts between OT and OTR-positive neurons at somatic and dendritic locations. $n_{rats} = 4$, 8 images per animal, $p < 0.0001$ (two-sided). **i** Reconstruction of a vGluT2-positive (red) OT fiber (magenta) within the vIPAG. **j** Bar graph showing that the vast majority of OT fibers within the vIPAG are vGluT2-negative (92.4%). $n = 4$. **k** 3D reconstruction of contacts between an OTR dendrite and OT fibers. **l** Co-localization of OT (magenta) and vGluT2 (red) are indicated by white arrowheads. Mismatch of OT (magenta) and vGluT2 (red) are indicated by white arrowheads with an asterisk. DAPI = blue, OTR = green. $n = 4$ female rats. Scale bars in order of appearance: 50, 10, 10, 20, and 20 μm. Results are expressed as the mean ± SEM and the individual points of each condition are represented as white circle. Source data are provided as a Source data file.

g Bar graph showing the percentage of OTR positive ($n = 496$) and negative ($n = 3840$) cells receiving OT innervation (<1 μm distance between fibers and cells). $n_{rats} = 4$, 8 images per animal, $p = 0.0055$ (two-sided).

h Bar graph showing the percentage of contacts between OT and OTR-positive neurons at somatic and dendritic locations. $n_{rats} = 4$, 8 images per animal, $p < 0.0001$ (two-sided).

i Reconstruction of a vGluT2-positive (red) OT fiber (magenta) within the vIPAG.

j Bar graph showing that the vast majority of OT fibers within the vIPAG are vGluT2-negative (92.4%). $n = 4$.

k 3D reconstruction of contacts between an OTR dendrite and OT fibers.

l Co-localization of OT (magenta) and vGluT2 (red) are indicated by white arrowheads. Mismatch of OT (magenta) and vGluT2 (red) are indicated by white arrowheads with an asterisk. DAPI = blue, OTR = green. Scale bars in order of appearance: 50, 10, 10, 20, and 20 μm. Results are expressed as the mean ± SEM and the individual points of each condition are represented as white circle. Source data are provided as a Source data file.

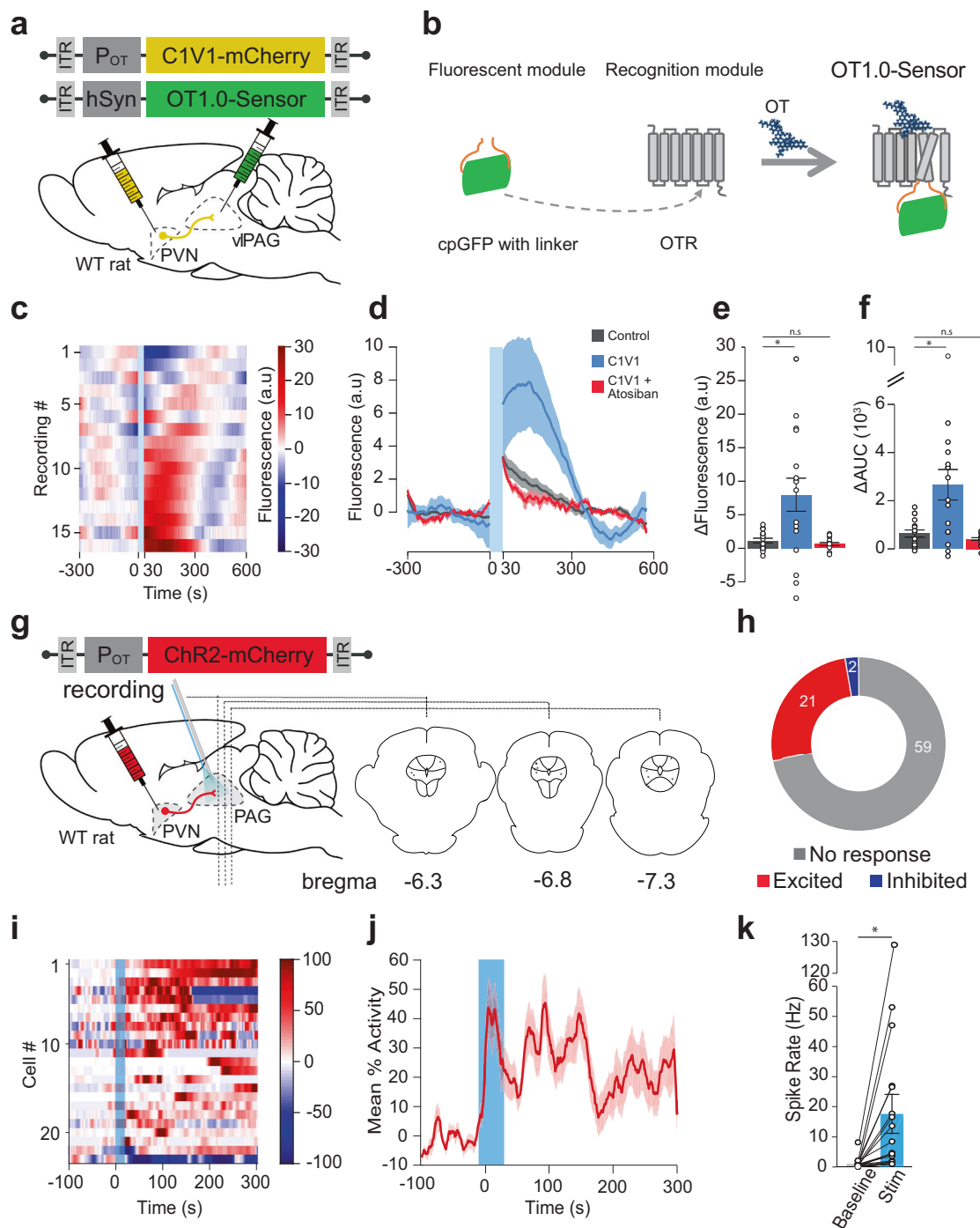
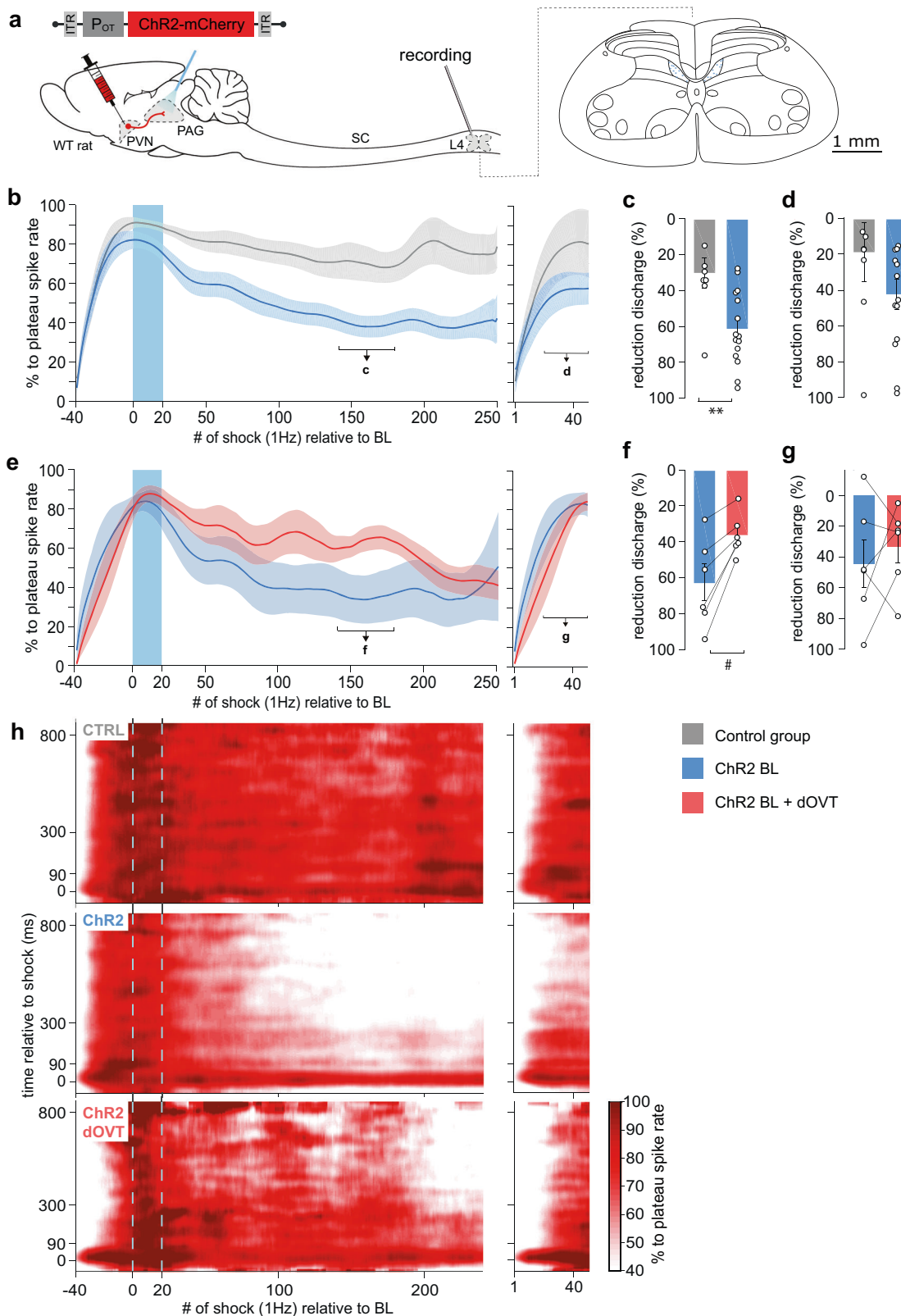


Fig. 4 | Endogenous OT release in the vIPAG increases vIPAG neuron activity in female rats. **a** Schema of injections of rAAV_{1/2}-pOT-C1V1-mCherry in the PVN and rAAV_{1/2}-hSyn-OT1.0-sensor in the vIPAG. **b** Schema depicting the principle behind the GRAB_{OT} sensor¹⁸. **c** Fluorescence signal of the C1V1 condition in the vIPAG ($n_{\text{recordings}} = 16$; $n_{\text{slices}} = 7$; $n_{\text{rats}} = 3$). Blue band at 0 s correspond to the yellow stimulation (30 ms pulse at 20 Hz for 30 s). **d** Mean fluorescence (line) \pm SEM (shaded) of the control (gray), C1V1 (blue), and C1V1 + atosiban (red) recordings in the vIPAG. **e** Delta of the max fluorescence value between the period before the light stimulation (-300 to 0 s) and the period following the light stimulation (0 to 300 s). The delta of the three conditions are represented. Welch's ANOVA test ($W = 6.934$, $p = 0.0045$, $n = 16$) followed by Dunnett's T3 multiple comparison post hoc test (two-sided): Control vs C1V1: $*p_{\text{adj}} = 0.0272$; Control vs C1V1 + Atosiban: $p_{\text{adj}} = 0.3133$. **f** Delta of the mean Area Under the Curve (AUC) between the period before the light stimulation (-300 to 0 s) and the period following the light stimulation (0 to 300 s). The delta of the three conditions are represented. Welch's ANOVA test ($W = 6.934$, $p = 0.0045$, $n = 16$) followed by Dunnett's T3 multiple

comparison post hoc test (two-sided): Control vs C1V1: $*p_{\text{adj}} = 0.0118$; Control vs C1V1 + atosiban: $p_{\text{adj}} = 0.2939$. **g** Schema of rAAV_{1/2}-pOT-ChR2-mCherry injection in the PVN and setup for in vivo electrophysiological recordings (gray electrode), together with blue light (BL) stimulation (blue optic fiber) in the PAG. Recording site is shown on coronal drawings from anterior to posterior. **h** Recorded units' responsiveness. **i** Normalized firing rate of each vIPAG neuron ($n_{\text{cells}} = 23$; $n_{\text{rats}} = 12$) that responded to BL in the vIPAG. 473 nm of BL was added as a 10 ms pulse at 30 Hz for 20 s, $100 \mu\text{W/mm}^2$. Dotted lines = BL stimulation. **j** Mean percent activity (line) \pm SEM (shaded) calculated from panel (i). **k** Difference in mean firing rate between the period before BL (-100 to 0 s) and the maximum activity period following BL stimulation (highest value among moving means with a time window of 21 s, between 0 to +300 s after the start of BL). Paired t-test, $*p = 0.0133$ (two-sided), $n = 17$. Results are expressed as the mean \pm SEM and the individual points of each conditions are represented as white circle. Source data are provided as a Source data file.



from -40 to 0 s). This WU effect is typically enhanced during pain perception in animals with inflammation²⁰, which suggests that WU can serve as an index of ongoing nociceptive processing (i.e., a measure of how sensitive the body is to nociceptive stimuli at a given moment). Therefore, we used WU (represented as the percentage of maximal spiking activity following electrical stimulation (1 Hz) to the hind paw receptive field) as our outcome measure for the effect of

vIPAG-BL stimulation on WDR discharge, specifically from primary afferent C-fibers (Supplementary Fig. 9a).

Prior to any vIPAG-BL stimulation, all cells exhibited the maximal WU effect 30 s after the onset of electrical stimulation (Fig. 5b). In control animals (CTRL) that received vIPAG-BL in the absence of ChR2 expression, the WU remained stable up to 250 s after the plateau, despite a gradual reduction over time that was not statistically

Fig. 5 | Endogenous OT release in vIPAG reduces WDR spinal cord neuronal activity in female rats. **a** Schema of rAAV_{1/2}-OTp-ChR2-mCherry injection in the PVN and setup for in vivo electrophysiological recordings (gray electrode) of WDR neurons in the rat spinal cord (SC) at the lumbar 4 (L4) level during optogenetic BL stimulation (blue optic fiber) in the vIPAG. Recording sites in layer 5 are shown in the coronal drawing of L4. **b-d** vIPAG BL effect on the spike rate of WDR's C-fiber discharge. **b** Mean time course observed after vIPAG BL in control rats (gray, $n_{cells} = 8$; $n_{rats} = 4$) and OT ChR2-expressing rats (blue, $n_{cells} = 14$; $n_{rats} = 6$). Left and right panels show two consecutive recordings separated by 300 s. Line shadows represent SEM. **c** Percentage of reduction expressed as the minimum level activity observed after a wind-up plateau phase, 140–180 s; Unpaired Wilcoxon rank sum test (two-sided); CTRL ($n_{cells} = 8$) 30.12 ± 8.60 vs ChR2 ($n_{cells} = 14$) $61.28 \pm 5.37\%$, $U = 18$, $p = 0.0053$, and **d** 570–600 s after BL onset. Unpaired Wilcoxon rank sum test; CTRL ($n_{cells} = 8$) 18.73 ± 16.45 vs ChR2 ($n_{cells} = 14$) $42.23 \pm 8.45\%$, $U = 34$, $p = 0.1450$. **e-g** PAG OTR contribution to the vIPAG BL effect on the spike rate of

WDR's C-fiber discharge. **e** Mean time course observed after vIPAG BL in OT ChR2-expressing rats (blue, $n_{cells} = 6$; $n_{rats} = 4$), and in the same recordings after dOVT injection in the vIPAG (red, $n_{cells} = 6$; $n_{rats} = 4$). Left and right panels show two consecutive recordings separated by 300 s. Line shadows represent SEM. **f** Percentage of reduction expressed as the minimum level activity observed after a wind-up plateau phase, 140–180 s; Paired Wilcoxon signed-rank test (two-sided); ChR2 63.16 ± 10.07 vs dOVT $36.27 \pm 4.8\%$, $W = 0$, $#p = 0.0313$, $n_{cells} = 6$ and **g** 570–600 s after BL onset. Paired Wilcoxon signed-rank test; ChR2 44.51 ± 15.61 vs dOVT $33.16 \pm 10.89\%$, $W = 8$, $p = 0.6875$, $n_{cells} = 6$. **h** Mean smoothed raster plot of WDR discharge level along the relative timing to each single electric shock on the hind paw (vertical axis) and along the accumulating trials of electric shock (horizontal axis), in CTRL animals (top, $n = 8$), ChR2 animals (middle, $n = 14$), and ChR2 animals after dOVT injection in PAG (bottom, $n = 6$). Results are expressed as the mean \pm SEM and the individual points of each conditions are represented as white circle. Source data are provided as a Source data file.

significant. In contrast, vIPAG-BL stimulation in animals expressing ChR2 in OT neurons showed a significant decrease in C-fiber discharge compared to control animals (Fig. 5c, CTRL ($n = 8$) 30.12 ± 8.60 vs ChR2 ($n = 15$) $61.28 \pm 5.37\%$, $p = 0.0053$). This trend was maintained up to 600 s after the end of vIPAG-BL stimulation, as seen in a second series of recordings of the same neurons (Fig. 5d, CTRL ($n = 8$) 18.73 ± 16.45 vs ChR2 ($n = 15$) $42.23 \pm 8.45\%$, $p = 0.1450$). A similar effect was found for fast-conducting fibers A8- (CTRL ($n = 8$) 34.08 ± 4.73 vs ChR2 ($n = 15$) $51.26 \pm 4.1\%$, $p = 0.0337$; Supplementary Fig. 9c-h), but not for non-nociceptive, fast-conducting A β - fibers (CTRL ($n = 8$) 24.44 ± 10.14 vs ChR2 ($n = 15$) $27.39 \pm 7.91\%$, $p = 0.7763$; Supplementary Fig. 9i-n). While the magnitude of WU reduction was significantly larger in ChR2 animals than CTRL animals, there was no difference in the “inflection” timing of WU dynamics. Specifically, there was no significant difference between CTRL and ChR2 animals for latency (s) to reach the maximum WU (Supplementary Fig. 9b). Importantly, all recorded WDR neurons were impacted by vIPAG-BL, highlighting the effectiveness of this circuit in gating the nociceptive signal at the spinal cord level.

In order to confirm that the recorded effect on WU was due to OT release in the vIPAG, we ran a second series of experiments in which we allowed the WU effect to dissipate over a 10 min interval following the initial stimulation protocols in the ChR2 group. We then infused the specific OTR antagonist, [d(CH2)5,Tyr(Me)2,Orn8]-vasotocin (dOVT), into the vIPAG prior to repeating the same protocol described above. We found that dOVT infusion significantly impaired the vIPAG-BL's ability to reduce WU (ChR2 63.16 ± 10.07 vs dOVT $36.27 \pm 4.80\%$, $p = 0.0313$, $n = 6$; Fig. 5e, f). After the period of maximum WU reduction (from 140 to 180 s), dOVT lost its effectiveness possibly due to diffusion out of the PAG region (ChR2 44.51 ± 15.61 vs dOVT $33.16 \pm 10.89\%$, $p = 0.6875$, $n = 6$; Fig. 5g). The average raster plots shown in Fig. 5h summarize the vIPAG-BL effect in the different groups.

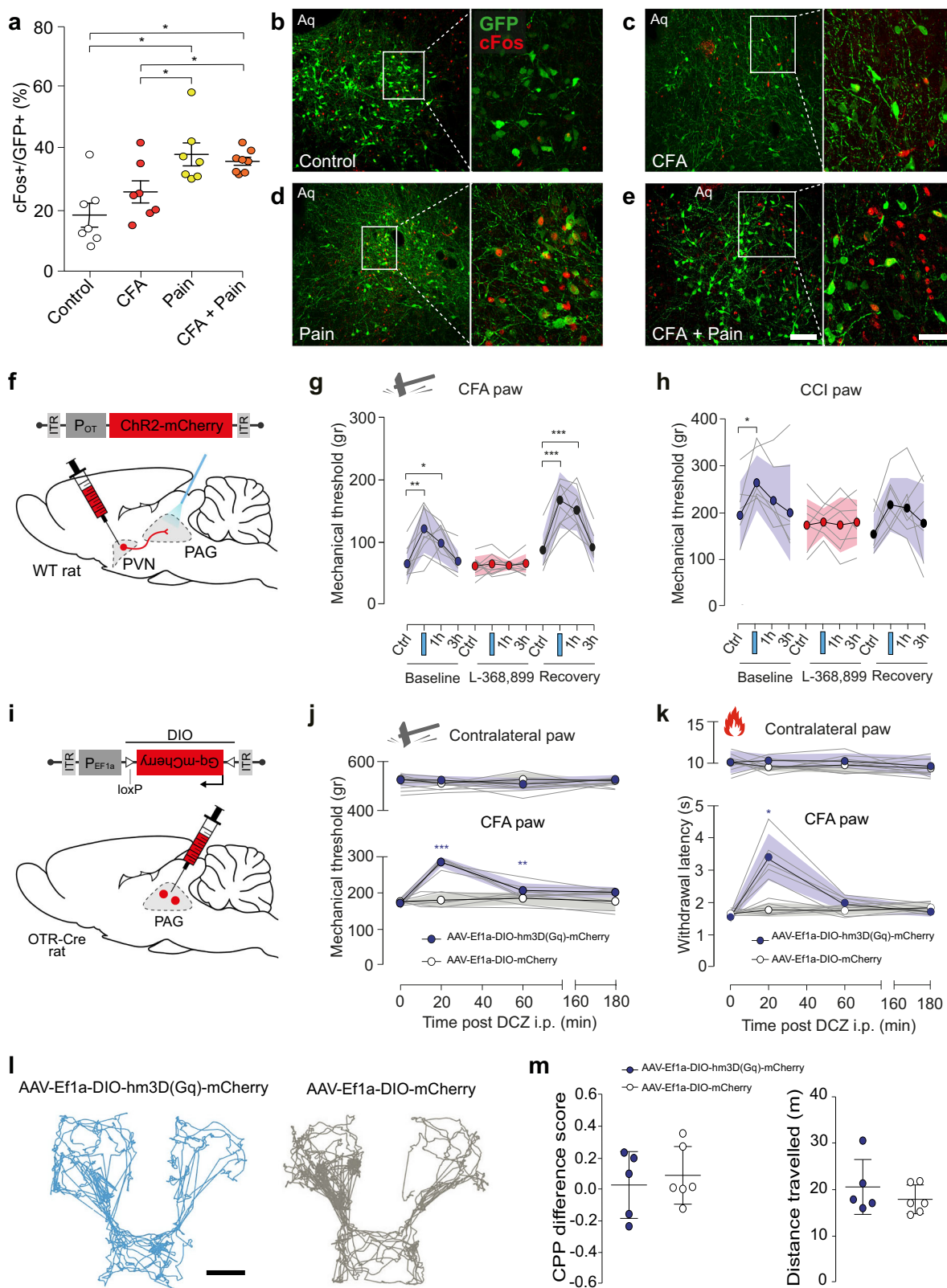
OT in the vIPAG induces analgesia in both inflammatory and neuropathic pain

Because the vIPAG is known to be a key component of an important descending pain modulatory system, and OT is known to exert an analgesic effect¹³, we hypothesized that OTR+ neurons in the vIPAG are involved in pain processing. To test this hypothesis, we injected rAAV_{1/2}-EF1 α -DIO-GFP into the vIPAG of male OTR-IRES-Cre rats. The rats were subdivided into four groups ($n = 7$ –8 per group): (1) no manipulation (Control), (2) inflammatory-induced pain sensitization after complete Freund adjuvant injection in the posterior right paw (CFA), (3) acute mechanical nociception (Pain), (4) mechanical nociception 24 h following hind paw CFA injection (CFA + Pain). Rats were euthanized 30 min following each manipulation and brain sections containing vIPAG were collected. We next used c-Fos staining to compare the number of recently activated OTR (GFP+) expressing cells across the groups (Fig. 6a-e). We found that rats exposed to either

painful stimuli or painful stimuli following CFA injection had significantly more activated OTR neurons in the vIPAG ($38.1 \pm 9.2\%$ and $35.9 \pm 3.4\%$, respectively; $p < 0.01$) than rats not exposed to nociceptive stimulation ($18.4 \pm 9.6\%$). There was no statistically significant difference between the CFA group ($26.0 \pm 6.8\%$) and the control group (Fig. 6a).

To verify the functional significance of vIPAG projecting OT neurons in the processing of inflammatory pain-like behaviors, a separate cohort of female wild-type rats received PVN injections of rAAV_{1/2}-OTp-ChR2-mCherry (Fig. 6f). We then compared the within-subject effect of optogenetically-evoked OT release in the vIPAG (vIPAG-BL) on mechanical pain-like behavior sensitivity both with and without the presence of CFA-induced inflammatory hyperalgesia (Fig. 6g) and in the chronic constriction injury of the sciatic nerve (CCI) model of neuropathic pain. We found that vIPAG-BL stimulation significantly, but not entirely, alleviated CFA-induced hyperalgesia as indicated by an increase in the mechanical pain-like behaviors threshold from 64.01 ± 8.059 g to 120.73 ± 11.98 g (mean \pm SEM; Fig. 6g; $p = 0.0019$, $n = 10$). Injection of the blood-brain barrier (BBB)-permeable OTR antagonist, L-368,899, completely blocked the effect of BL in the vIPAG (from 60.5 ± 4.82 g to 63.81 ± 5.12 g, Fig. 6g; $p = 0.8788$, $n = 10$). After complete wash out of L-368,899, the effect of vIPAG-BL returned to its baseline level (from 86.31 ± 7.95 g to 167.29 ± 14.36 g; Fig. 6g; $p = 0.0001$, $n = 10$). Finally, we found that vIPAG-BL had no effect on mechanical sensitivity in the absence of any peripheral sensitization when testing the contralateral paw (Supplementary Fig. 10a, d). We next sought to test if this PVN_{OT} \rightarrow vIPAG_{OTR} circuit is involved in neuropathic pain, given that other pain-related OT pathways fail to affect such symptoms^{3,21}. To address this, we performed vIPAG-BL stimulation in the CCI model of neuropathic pain²². We found the vIPAG-BL stimulation significantly increases the mechanical pain-like behaviors threshold (mean \pm SEM; 195.68 ± 27.33 g to 265.27 ± 22.26 g, Fig. 6h; $p = 0.0363$, $n = 7$). Again, the effect of the stimulation is completely blocked by the L-368,899 (from 174.6 ± 21.32 g to 181.19 ± 11.21 g; Fig. 6h; $p = 0.9478$, $n = 7$). This time, the effect of vIPAG-BL does not significantly return to its baseline level after complete washout of L-368,899 (from 155.49 ± 16.3 g to 218.286 ± 21.75 g; Fig. 6h; $p = 0.0977$, $n = 7$). Another time, the vIPAG-BL stimulation had no effect when testing the contralateral paw (Supplementary Fig. 10a-c).

To confirm that this effect was driven by vIPAG OTR neurons, we injected male and female OTR-Cre rats with viruses containing either an excitatory chemogenetic receptor, rAAV_{1/2}-EF1 α -DIO-hm3D(Gq)-mCherry, or a control virus rAAV_{1/2}-EF1 α -DIO-mCherry ($n = 5$ –6 per group) (Fig. 6i, Supplementary Fig. 10d, e). We then repeated the CFA-induced inflammatory hyperalgesia experiments described above and found that chemogenetic excitation of vIPAG OTR neurons by i.p deschloroclozapine (DCZ) induced a significant increase in mechanical pain-like behaviors threshold from 171.27 ± 5.59 g to 285.53 ± 6.36 g ($p = 0.0006$, $n = 5$ –6; Fig. 6j). This effect was not



observed in the contralateral paw of the same animals nor in the control virus group that received DCZ injection (Fig. 6j). A similar effect was found in the hot plate test of thermal pain-like behaviors sensitivity, where DCZ increased the latency of response to thermal stimuli from 1.56 ± 0.06 s to 3.41 ± 0.32 s ($p = 0.0108$, $n = 5-6$; Fig. 6k), this was again not found in the contralateral paw of the same animals nor in the control group (Fig. 6l). Finally, we repeated these

experiments in male rats and found the same results (Supplementary Fig. 10f, g, $n = 6$ per group), ruling out a potential sexual dimorphism of this circuit.

Finally, to understand whether the analgesia was caused by a modulation of the sensory and/or affective component of pain²³, we performed a conditioned place preference (CPP) test using the same cohort from the chemogenetic experiments above (Supplementary

Fig. 6 | Evoked OT release in vIPAG reduces mechanical hyperalgesia.

a Percentage of c-Fos positive vIPAG OTR neurons under the control condition, painful stimulation, CFA inflammation, and painful stimulation combined with CFA. $n = 7-8$ per group, Kruskall Wallis test $H = 12.01$, $p = 0.00733$, CTRL vs pain, CTRL vs pain + CFA, CFA vs pain, CFA vs pain + CFA $p < 0.05$, CTRL vs CFA $p > 0.05$.

b–e Examples of images showing c-Fos (red) and GFP (green) staining of vIPAG under the different experimental conditions (**b–e**). Scale bar = 200 μm , inset scale bar = 75 μm . Aq = aqueduct. **f** Schema of rAAV_{1/2}-OTp-ChR2-mCherry injection in the PVN and optic fiber implantation in the PAG. **g, h** Threshold of mechanical pain-like behaviors was raised by PAG-BL. The effect of vIPAG-BL was measured at 5 min, 1 h, and 3 h after vIPAG-BL for: **g** the CFA-injected paw, 2-way RM ANOVA test ($F_{\text{interaction}} = 9.555$; $p < 0.0001$; $n_{\text{rats}} = 10$), followed by multiple comparison post hoc test with Dunnett correction: Baseline Ctrl vs BL: $*p_{\text{adj.}} = 0.0019$; Ctrl vs 1 h: $*p_{\text{adj.}} = 0.0269$; Recovery, Ctrl vs BL: $***p_{\text{adj.}} = 0.0001$; Ctrl vs 1 h: $***p_{\text{adj.}} = 0.0005$. **h** the CCI-treated paw, 2-way RM ANOVA test ($F_{\text{time}} = 6.452$; $p = 0.0012$; $n_{\text{rats}} = 7$), followed by multiple comparison post hoc test with Dunnett correction: Baseline Ctrl vs BL:

$*p_{\text{adj.}} = 0.0363$. **i** Schema of the injection of rAAV_{1/2}-EF1 α -DIO-Gq-mCherry in the PAG. **j** Mechanical pain threshold after DCZ administration in the CFA and contralateral paw of female rats expressing Gq-mCherry (blue) or mCherry only (gray) in vIPAG OTR neurons. 2-way RM ANOVA test ($F_{\text{interaction}} = 21.41$; $p < 0.0001$; $n_{\text{rats}} = 5-6$), followed by multiple comparison post hoc test with Dunnett correction: Gq-mCherry, 0 vs 20: $***p_{\text{adj.}} = 0.0006$; 0 vs 60: $**p_{\text{adj.}} = 0.0089$. **k** Thermal pain threshold of female rats expressing Gq-mCherry (red) or mCherry only (gray) in vIPAG OTR neurons after DCZ administration during normal or inflammation (CFA) conditions. 2-way RM ANOVA test ($F_{\text{interaction}} = 28.29$; $p < 0.0001$; $n_{\text{rats}} = 5-6$), followed by multiple comparison post hoc test with Dunnett correction: Gq-mCherry, 0 vs 20: $*p_{\text{adj.}} = 0.0108$. **l** Representative activity traces during the CPP test. Scale bar = 20 cm. **m** Graphs showing the Δ CPP score (left) and total distance traveled (right) for the test and control groups. Unpaired t-test (two-sided): $p = 0.6185$ (left) and $p = 0.3587$ (right); $n = 6$ per group. All results are expressed as average \pm SEM and individual animals are represented with the lines, or individual points represented as blue or white circle. Source data are provided as a Source data file.

Fig. 10h). The animals' baseline chamber preference was determined during habituation (see "Methods" for details) and used as the saline-paired control chamber. In contrast, the innately non-preferred chamber was paired with DCZ in order to stimulate vIPAG OTR cells expressing hm3D(Gq) (Fig. 6i). Analysis of the rats' behavior on test day revealed no significant change in preference for the DCZ-paired chamber (Fig. 6l, m), rejecting the assumption of the PVN_{OT} \rightarrow vIPAG_{OTR} circuit contribution to affective component of pain. Importantly, this was not due to an effect on locomotion as there were no differences between the test and the control group in the total distance travel during the experiment (Fig. 6m).

Discussion

Here we describe an analgesic pathway recruited by parvOT neurons projecting to the vIPAG (Figs. 1–2), where they release OT to activate GABAergic OTR expressing neurons (Figs. 3–4), which then leads to a decreased response to nociceptive stimuli in spinal cord WDR neurons (Fig. 5). We further showed that activation of this circuit specifically reduces pain-like behaviors (Fig. 6), without alteration of the affective component of pain, in both female and male rats (Fig. 6 and Supplementary Fig. 10).

Past work has shown that OT exerts analgesic effects by acting on various targets of pain-associated areas in the central and peripheral nervous systems^{3,24}. The contribution of OT to analgesia is generally attributed to two pathways. The first is an ascending OT pathway that modulates the activity of brain regions processing the affective and cognitive components of pain, such as the amygdala, in which OT alleviates anxiety, especially in the context of chronic pain in rodents^{15,17,21}. In humans, OT was found to decrease neural activity in the anterior insula with repeated thermal pain stimulation, thereby facilitating habituation to the cognitive component of the painful stimuli¹⁴. The second is a descending OT pathway that indirectly promotes analgesia by reducing the activity of SC WDR neurons, which relay nociception in response to painful stimuli^{3,25}. While this specific descending OT pathway is effective, it is restricted to inflammatory pain model³. In contrast, here we described a powerful descending OT pathway that is effective for both inflammatory and neuropathic pain models across thermal and mechanical modalities.

We identified a population of parvOT neurons that projects to the vIPAG, but not the SON nor the SC. Furthermore, we found that these neurons form synapses with little contribution of glutamate, thus supporting the idea of local axonal delivery of OT, as opposed to volume transmission^{26–28}. Of note, we did not decipher the functional involvement of a putative OT/glutamate co-release in this region, a mechanism of general interest for cellular network modulation that remains to be elucidated.

Consistent with previous reports showing that electrical stimulation of the PAG inhibits the firing of dorsal horn neurons in the SC⁹

and generates analgesia⁸, we found that nociceptive transmission from C-type primary afferents to WDR neurons in the SC was effectively repressed by endogenous OT release in the vIPAG. Notably, this effect peaked 250 s after OT release and was still observed 10 min after the cessation of blue light. This finding suggests that OT triggers a lasting activation of OTR expressing cells in the vIPAG, which then continually drives the regulation of SC WDR neurons for several minutes after initial OT release. Indeed, in a separate set of experiments, we showed that exogenously applied OTR agonist as well as endogenously evoked OT release excites neurons of the vIPAG and induces analgesia in an inflammatory pain model. Notably, optogenetic release of OT in the vIPAG led to activation of individual neurons at various times, mostly within the first 40 seconds after the onset of blue light stimulation. The neurons' offset timings were also diverse and usually lasted for several minutes after the offset of blue light stimulation. The reason for such variability in the offset times is still unclear. One possibility may stem from the G-protein coupled metabotropic receptor nature of OTRs, which typically produce "slow" post synaptic currents lasting on the order of minutes²⁹. Furthermore, although OT axons in the midbrain make synapses^{16,30}, direct release of OT into the synaptic cleft has never been demonstrated. Thus, it is more likely that OT diffuses from axonal terminals or axonal varicosities *en passant* in the vicinity of OTR neurons²⁶. In that case, the action of OT could be synergized across multiple OTR expressing cells, resulting in long-lasting excitation driven by the sum of different active timings. This idea leads to another possible mechanism in which the OT-induced modulation of this pathway relies on the influence of additional non-neuronal cell types within the network, such as astrocytes, as was previously shown in the amygdala²¹. While the specific mechanisms behind the lasting analgesic effect of OT release in the vIPAG are unclear, they would certainly play a critical role in its development as a potential therapeutic target and, therefore, warrant future research.

Importantly, we confirmed the uniqueness of this parvOT pathway by showing that the previously identified parvOT \rightarrow SC_{WDR} and parvOT \rightarrow SON pathways do not project to vIPAG. Interestingly, the level of reduction in nociception caused by optogenetic stimulation of parvOT neurons projecting to SON³ resembled the effect of stimulating vIPAG OT axons. Redundant, parallel circuits that play identical roles in the brain have been previously described (e.g. for feeding behavior³¹). Therefore, the direct projections from parvOT neurons to the SC and the indirect influence of parvOT neurons on sensory WDR neurons via the vIPAG can be interpreted as parallel circuits capable of independently promoting analgesia, particularly in an inflammatory pain model. Although activation of both circuits results in similar electrophysiological inhibition of WDR neurons, they could be triggered by different situations, at different time points, or in different painful contexts. Indeed, we found that the

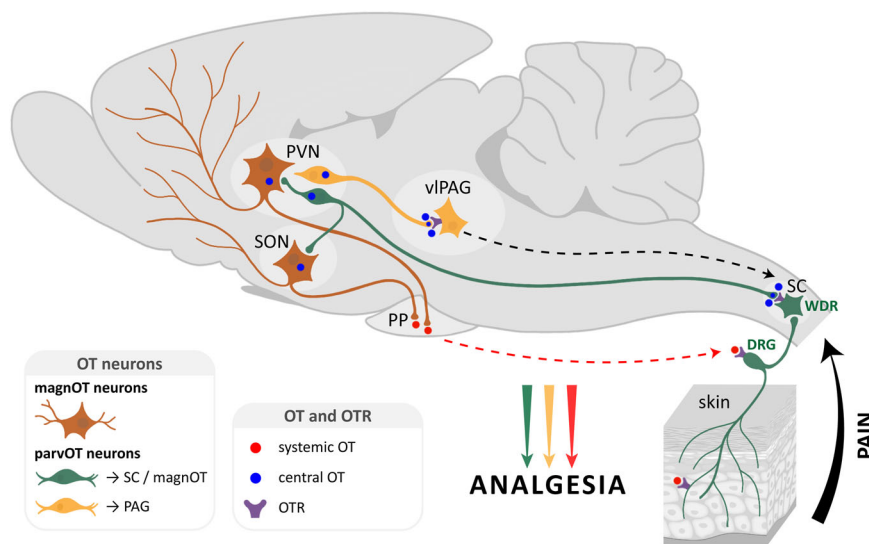


Fig. 7 | Two distinct ParvOT neuronal populations promote analgesia via release of OT in the vIPAG and in the blood and spinal cord. We hypothesize that two parallel parvOT pathways are activated by pathological, painful stimuli.

Both pathways release OT in various brain regions and the periphery which then leads to a reduction in nociception.

$\text{PVN}_{\text{OT}} \rightarrow \text{vIPAG}_{\text{OTR}}$ circuit promotes analgesia in the chronic neuropathic pain model condition and in both male and female rats, whereas previous work found that the parvOT \rightarrow SC_{WDR} circuit does not³. Moreover, considering that the vIPAG is an important area for the regulation of various defensive behaviors³², and that OT can mediate defensive behaviors, it will be important for future research to determine if vIPAG OTR neurons might be involved in other functions beyond nociception.

Local vIPAG GABAergic circuit recruited by OT

It has been previously shown that electric stimulation of PAG inhibits the firing of dorsal horn neurons in SC⁹, resulting in analgesia⁸. However, although these studies did not explore the role of neuronal inputs to the PAG such as the OTergic ones. Because this analgesic effect was interrupted by lesions of the RVM³³, the RVM is currently considered an essential link between PAG and SC. Furthermore, analgesic projections from the PAG to the RVM are glutamatergic³⁴ and tonically inhibited by local PAG GABAergic neurons³⁵. Interestingly, local OT infusion increases the spontaneous activity of PAG neurons¹². In the current study, we confirm this by showing that endogenous OT release in PAG triggered not only excitation of some neurons whose spontaneous spike rates were low, but also caused inhibition of other neurons whose spontaneous spike rates were high (Fig. 4i). We also show that OTR neurons in the vIPAG are GABAergic and that TGOT application increases their electrical activity. Thus, an interesting hypothesis could be that the OT-excited neurons are local GABAergic interneurons³⁵ while the OT-inhibited neurons might correspond to the glutamatergic projection neurons³⁴. Stimulating the endogenous release of OT leads then to the increase of GABAergic interneurons, decreasing the activity of the glutamatergic projection neurons, decreasing also RVM activity, and promoting analgesia. However, further investigations are needed to determine the exact nature of those OT-modulated neuronal populations.

vIPAG OTR neurons reduce pain sensation, but not its affective component

We further found that painful stimulation increased c-Fos levels in vIPAG OTR neurons, indicating that these neurons are endogenously recruited in the context of pain processing. These findings confirm and expand on previous work demonstrating that PAG OTR neurons in mice express c-Fos after noxious stimulation³⁶.

By using our newly generated OTR-IRES-Cre transgenic rats, we were able to specifically activate OTR neurons in the vIPAG. We found that this activation led to a decrease in nociception in both inflammatory and neuropathic pain models, but failed to alter place preference. This suggests the circuit we dissected here is not involved in the affective, memory component of pain²³. Interestingly, the opposite effect of OT on affective valence, but not on physical pain-like behaviors has been demonstrated in the central nucleus of amygdala²¹. In addition, OT was reported to modulate pain-like behaviors at the level of the insular cortex by enhancing GABAergic transmission and causing downstream effects leading to reduced nociceptive signaling in the spinal cord³⁷. Taken together, these findings further emphasize the sheer variety of effects mediated by OT and highlight the need for continued efforts to dissect the precise anatomical and functional characteristics of the central OT system.

Sex (absence of) difference in OT vIPAG induced analgesia

Interestingly, clinical literature, as well as some animal research³⁸, mention a sex relevance in OT-induced analgesia. However, one might consider that clinical studies mostly rely on intra-nasal or intra-venous administration of exogenous OT, thus flooding any brain-area specific effect of OT, while most of sex differences reported in animal studies at the level of the spinal cord were performed via release of endogenous OT. In the present study, we mainly focus on female animals, extensively demonstrating the analgesic action of the specific $\text{PVN}_{\text{OT}} \rightarrow \text{vIPAG}_{\text{OTR}}$ circuit in both inflammatory and neuropathic pain conditions. Interestingly, this analgesic effect was confirmed in male animals (Supplementary Fig. 10), pointing to similar analgesic mechanisms of the $\text{PVN}_{\text{OT}} \rightarrow \text{vIPAG}_{\text{OTR}}$ circuit regardless of sex differences³⁹. This is in accordance with recent anatomical analysis that reveal limited, if any, differences of OT neurons projections between female and male rodents⁴⁰. Given that increasing evidence points toward major sex differences in pain processing, results from our group and others on OT circuits highlight an important, well-conserved OTergic analgesic mechanism.

In conclusion, we identified a subpopulation of parvocellular OT neurons that mediate analgesia by recruiting the PAG-controlled descending pain modulatory system (Fig. 7). This study further describes and supports the role of OT as an analgesic molecule and points to the OTR as a potential therapeutic target. To this end, we generated the

OTR-IRES-Cre line of rat, which will greatly enhance our ability to research this therapeutically relevant receptor. Finally, it should be noted that the inconsistent results regarding sex differences and subjective pain ratings⁴¹ found in human clinical studies of OT effects on pain²⁴ may be due to the limitations of intranasal OT administration⁴². Therefore, future research should be oriented toward developing synthetic OT agonists with the ability to cross the blood–brain barrier more efficiently than OT itself^{43–46}.

Methods

Animals

Adult female (all figures) and male (Supplementary Figs. 4 and 10) Wistar wild type and Wistar OTR-IRES-Cre rats (>8 weeks old; 250–350 g; Chronobiotron, Strasbourg, France) were used for this study. All animals were tattooed, sexed and genotyped (Kapa2G Robust HotStart PCR Kit, Kapa Biosystems; Hoffman La Roche) one week after birth. Animals were housed by sex, in groups of three under standard conditions (room temperature, 22 °C; 12/12 h light/dark cycle) with ad libitum access to food, water and behavioral enrichment. All animals that underwent behavioral testing were handled and habituated to the experimenter two weeks before stereotaxic surgery. After one week of post-surgical recovery, the rats were habituated to the applicable behavioral testing room and handling routines for an additional two weeks prior to the start of experiments. All behavioral tests were conducted during the light period (i.e., between 7:00 and 19:00). All experiments were conducted in accordance with European law, under French Ministry license 3668-2016011815445431 and 15541-2018061412017327, and German Animal Ethics Committee of the Baden Württemberg license G-102/17.

Viral cloning and packaging

Recombinant Adeno-associated virus (serotype 1/2) carrying either a conserved region of the OT promoter or EF1α promoter and genes of interest in direct or “DIO” orientations were cloned and produced as reported previously¹⁵. Briefly, HEK293T cells (#240073, Addgene, USA) were used for viral production. rAAV produced included: rAAV_{1/2}-OTp-mCherry (or Venus), rAAV_{1/2}-OTp-ChR2-mCherry, rAAV_{1/2}-EF1α-DIO-GFP (or mCherry), and rAAV_{1/2}-EF1α-DIO-hM3Dq-mCherry, rAAV_{1/2}-OTp-C1v1-mCherry, rAAV_{1/2}-hSyn-OT1.0. The canine adenovirus serotype 2 (CAV2-CMV-Cre) was purchased from the Institute of Molecular Genetics in Montpellier CNRS, France. rAAV genomic titers were determined with QuickTiter AAV Quantitation Kit (Cell Biolabs, Inc., San Diego, California, USA) and RT-PCR using the ABI 7700 cycler (Applied Biosystems, California, USA). rAAV titers were between 10⁹ and 10¹⁰ genomic copies/μl.

Stereotaxic injections

All surgeries were performed on rats anesthetized with 2.5% isoflurane and receiving Bupivacaine (s.c., 2 mg/kg) or carprofen (i.p., 5 mg/kg) and lidocaine applied locally⁴⁷. rAAV were injected into the PVN, SON, and vIPAG in different combinations, as needed by each experiment, and allowed to express for four weeks. The coordinates were chosen using the Paxinos rat brain atlas⁴⁸ (PVN: ML: +/−0.3 mm; AP: −1.4 mm; DV: −8.0 mm; SON: ML: +/−1.8 mm; AP: −1.2 mm; DV: −9.25 mm; PAG: ML: +/−0.5 mm; AP: −7.0 mm; DV: −5.9/−5.0 mm). Each site was injected with a total of 300 nL of viral solution via a glass pipette at a rate of 150 nL/min using a syringe pump. Verification of injection and implantation sites, as well as expression of genes of interest were confirmed in all rats post hoc (see “Histology” section). Rhodamine conjugated Retrobeads (Lumafluor Inc., Durham, NC, USA) were diluted 1:10 with 1x PBS and injected at a volume of 150 nL. Spinal cord Retrobeads injections was performed during the same surgery as virus injection (see “In vivo extracellular recording of WDR SC neurons” for details on the spinal cord surgery).

Generation of OTR-IRES-Cre rats

Cloning of the rat OXTR-Cre targeting vector. The OXTR-Cre targeting vector was cloned by modifying the plasmid Snap25-IRES2-Cre (Allen Institute for Brain Science⁴⁹) The final vector contained the IRES2-Cre sequences, followed by a bovine growth hormone polyadenylation site, and homology arms for targeted integration of the oxytocin receptor locus, comprised of 1.3 kb and 1.4 kb genomic sequences. Homology arms were generated by PCR on genomic DNA from Sprague Dawley rats using the following primer pairs: OXTR_fwd_upper (5'-GTCGACAGAAAATGGTGGGTTGCC-3') together with OXTR_rev_upper (5'-GCTGCTAGCGAAGACTGGACTCACACCACC-3') and OXTR_fwd_lower (5'-ACCCGGAATTCTGTGCATGAAGCTGCATTAGG-3') together with OXTR_rev_lower (5'-TAGTTAACGTCATTCTGTATGTTGTCTATCC-3'). The upper homology arm was inserted using the restriction enzymes Sall and NheI, while the lower arm was inserted using XmaI and PmeI. Vector sequences can be obtained upon request.

Design of gRNAs and functional testing. We used the online tool CRISPOR (<http://crispor.org>) for selection of the guide RNA (gRNA) target sites in the OXTR gene⁵⁰. Three gRNA target sites were chosen with high specificity scores (>83⁵¹) for binding in the OXTR 3' UTR site where we aimed to introduce the IRES-Cre coding sequences.

For identification of the most effective gRNA, dual expression vectors based on px330 were cloned, harboring an expression cassette for the selected gRNAs and Cas9. In addition, the OXTR 3' UTR gRNA target regions were inserted into a nuclease reporter plasmid (pTAL-Rep⁵²) in between a partly duplicated, nonfunctional β-galactosidase gene. Hela cells were transfected with a combination of one of the px330 plasmids and the OXTR-specific reporter vector. After transfection, the Cas9-nuclease-induced double-strand breaks stimulated the repair of the lacZ gene segments into a functional reporter gene, the activity of which was determined in cell lysates using an o-nitrophenyl-β-D-galactopyranosid (ONPG) assay. A luciferase expression vector was also added to the transfection mix and luciferase activity was measured for normalization. The most effective gRNA target site including PAM was determined as 5'-ACTCCAGTCTTCCCCCGTGGTGG-3'.

Specificity of the CRISPR/Cas induced genomic modification. The CRISPOR program was used to identify potential off-target sites for the selected OXTR gRNA (5'-ACTCCAGTCTTCCCCCGTGGTGG-3'). No off-target sites were detected in an exonic sequence or on the same chromosome. In addition, only two potential target sites harboring at least four mismatches in the 12 bp adjacent to the PAM could be identified by the software.

Generation of transgenic rats. Sprague Dawley (SD) rats (Charles River) were bred in standard cages (Tecniplast) under a 12-h light/dark cycle in a temperature-controlled environment with free access to food and water at the Central Institute of Mental Health, Mannheim. All animal protocols were approved by the Regierungspräsidium Karlsruhe. SD single-cell embryos were injected using standard microinjection procedure⁵³. In brief, microinjections were performed in the cytoplasm and male pronuclei of zygotes with a mixture of Cas9 mRNA (10 ng/μl), sgRNA expression vector (6 ng/μl) and the OXTR-Cre targeting vector (2 ng/μl) as the repair substrate. The injected embryos were cultured in M2 Medium at 37 °C in 5% CO₂ and 95% humidified air until the time of injection. Surviving oocytes were transferred to the oviducts of pseudo pregnant Sprague Dawley rats. Transgenic animals were identified by polymerase chain reaction of tail DNA (DNeasy kit, Qiagen, Hilden, Germany) using primers for Cre⁵⁴.

DNA of Cre-positive animals was further used for detection of homologous recombination at the OXTR locus. For this purpose, the

targeted region was amplified by PCR using the Q5 polymerase (NEB) with 100–200 ng of genomic DNA as a template. Primers were selected which bind both up and downstream of the insertion site (outside of the homology arms), and were each combined with a primer located within the IRES2-Cre construct. For the 5' insertion site, the primers OXTR_check (5'-CAGCAAGAAGACAACTCATCC-3') together with Cre_rev (5'-CATCACTCGTTGCATCGAC-3') and, for the 3' site, CRISPR_bGH_fwd (5'-GACAATAGCAGGCATGCTGG-3') together with OXTR_rev_check (5' AGCCAGGTCCAAGAGTCC-3') were used.

Western blot for the detection of Cre protein in OTR-IRES-Cre rats

Total protein lysates were isolated from frozen rat tissue samples using RIPA buffer with Halt Protease- und Phosphatase-Inhibitor-Cocktail (100X) (ThermoFisher Scientific, Waltham, MA, USA). Concentration was measured using Pierce™ BCA Protein Assay Kit (ThermoFisher Scientific, Waltham, MA, USA). Proteins (40–60 µg) were separated on a NuPAGE 4–12% w/v Bis-Tris 1.0-mm minigel (Invitrogen, Carlsbad, CA) and detected by primary antibody anti-Cre polyclonal rabbit Antibody (NB100-56135) according to the manufacturer's instructions (dilution 1:1000). An anti-Gapdh mouse monoclonal antibody was used as a control (dilution 1:5000). IRDye 800CW and IRDye 680 (LICOR Bioscience, Lincoln, NE, USA) were used as secondary antibodies (Dilution 1:10,000). Protein bands were visualized using the Odyssey Infrared Imaging System and quantified using Image Studio Lite 4.0 software (both LI-COR Biosciences, Lincoln, NE, USA).

Histology

After transcardial perfusion with 4% paraformaldehyde (PFA) and post fixation overnight, brain sections (50 µm) were collected by vibratome slicing and immunohistochemistry was performed as previously described¹⁵. The list of primary antibodies used is available in the key resource table. For secondary antibodies, signal was enhanced by Alexa488-conjugated IgGs (1:1000) or CY3-conjugated or CY5-conjugated antibodies (1:500; Jackson Immuno-Research Laboratories). All images were acquired on a confocal Leica TCS microscope. Digitized images were processed with Fiji and analyzed using Adobe Photoshop. For the visualization of OTergic axonal projections within the PAG, we analyzed brain sections ranging from bregma -6.0 to -8.4 mm.

RNAScope in situ hybridization

RNAScope reagents (Advanced Cell Diagnostics, Inc., PN320881) and probes (OTR: 483671-C2 RNAscope Probe and Cre: 312281 RNAscope Probe) were used to detect the presence of specific mRNA expression using in situ hybridization. Brains were processed as described above using nuclease-free PBS, water, PBS, and sucrose. We followed the manufacturer's protocol with a few modifications: (1) immediately after cryosectioning, slices were washed in nuclease-free PBS to remove residual sucrose and OCT compound. (2) Hydrogen peroxide treatment was performed with free-floating sections prior to slice mounting. (3) Sections were mounted in nuclease-free PBS at room temperature. (4) Pretreatment with Protease III was performed for 20 min at room temperature. (5) No target retrieval step was performed.

To determine the percentage of PAG neurons co-expressing Cre and OTR mRNA, in situ hybridization using the RNAscope™ HiPlex Assay (Advanced Cell Diagnostics (ACD), Hayward, CA, USA; in a version for AF488, Atto550 and Atto647 detection) was performed. All procedures were conducted using fresh frozen 16 µm brain sections (3 PAG-containing slices per brain). During the initial hybridization step Cre (CRE-T2, cat. no. 312281-T2, ACD) and OTR (Rn-Oxtr-T6, cat. no. 483671-T6, ACD) probes were applied. Images were acquired and processed using an Axio Imager M2 fluorescent microscope (Zeiss, Gottingen, Germany) with an automatic z-stage and Axiocam 503 mono camera (Zeiss), and subsequently with Zen (3.1 blue edition and

3.0 SR black edition, Zeiss), CorelDraw 2020 (Corel Corporation, Ottawa, Canada), ImageJ and HiPlex Image Registration Software v1.0 (ACD). OTR and Cre mRNA-expressing cells in the PAG region from one brain hemisphere per section, were counted with an ImageJ Cell Counter plugin. Neurons were identified by the presence of a DAPI-stained nucleus and/or an unambiguous cell-like distribution of fluorescent mRNA dots.

Three-dimensional reconstruction and analysis of OT-OTR contacts in the PAG

Confocal images were obtained using a Zeiss LSM 780 confocal microscope (1024 × 1024 pixel, 16-bit depth, pixel size 0.63-micron, zoom 0.7). For the three-dimensional reconstruction, 40-µm-thick z-stacks were acquired using 1 µm-steps. Imaris-assisted reconstruction was performed as previously described^{21,47,55}. In brief, surface reconstructions were created based on the four individual channels (DAPI, OT, OTR-GFP, SYN/vGlut2). Co-localization of OT signal with SYN or vGlut2 was confirmed both manually and through the association/overlap function of IHC-labeled puncta in the Imaris software. IHC intensity of vGlut2 and SYN were assessed by creating spheres that precisely engulfed somata or dendrites as previously described⁴⁷.

Ex vivo imaging of oxytocin endogenous release

Slice preparation. To confirm the endogenous release of oxytocin following the light stimulation of the PVN fibers, 5–6 weeks old female Wistar Han rats ($n = 3$) received injections of the OT1-sensor virus into the vIPAG and the C1V1 virus into the PVN. Following a 2 weeks recovery period, rats were anesthetized by administering i.p. ketamine (Imalgene 300 mg/kg) and paxman (Rompun, 60 mg/kg). Transcardial perfusions were performed using an ice-cold, NMDG-based aCSF was used containing (in mM): NMDG (93), KCl (2.5), NaH₂PO₄ (1.25), NaHCO₃ (30), MgSO₄ (10), CaCl₂ (0.5), HEPES (20), D-Glucose (25), L-ascorbic acid (5), Thiourea (2), Sodium pyruvate (3), N-acetyl-L-cysteine (10) and Kynurenic acid (2.5). The pH was adjusted to 7.3–7.4 using HCl, after bubbling in a gas comprised of 95% O₂ and 5% CO₂. Rats were then decapitated, brains were removed and 350 µm thick coronal slices containing the vIPAG were obtained using a Leica VT1000s vibratome. Slices were placed in a recuperation chamber filled with normal aCSF at room temperature for at least 1 h. Normal aCSF was composed of (in mM): NaCl (124), KCl (2.5), NaH₂PO₄ (1.25), NaHCO₃ (26), MgSO₄ (2), CaCl₂ (2), D-Glucose (15), at pH 7.3–7.4 and continuously bubbled in 95% O₂–5% CO₂ gas. Osmolarity of all aCSF solutions were controlled to be between 290–310 mOsm. Finally, slices were transferred from the holding chamber to an immersion-recording chamber and superfused at a rate of 2 ml/min.

OT1.O-sensor imaging. The spinning disk confocal microscope used to perform OT1.O-sensor imaging was composed of a Zeiss Axio examiner microscope with a ×40 water immersion objective (numerical aperture of 1.0), mounted with a X-Light Confocal Unit–CRESTOPT spinning disk. Images were acquired at 2 Hz with an optiMOS sCMOS camera (Qimaging). The fluorescent focal planes were illuminated for 30 ms (OGB1: 475 nm) in bright-field mode using a Spectra 7 LUMEN-COR. The different hardware elements were synchronized through the MetaFluor 7.8.8.0 software (Molecular Devices). The fibers were stimulated using a 575 nm wavelength illuminated for 30 ms at 20 Hz for 30 s after 5 min of a baseline period. Using the Fiji software, the brightness and contrast parameters were automatically adjusted. As no cell could be clearly identified, the variations of fluorescence were measured on the whole plane recorded. Further offline data analysis was performed using a custom-written Python-based script available on the editorial website. Briefly, an inverted exponential fit was estimated to compensate the photobleaching of the recordings. Recordings in which the stimulation-induced artifact disrupted the fitting were discarded. Endogenous release of oxytocin was estimated as

changes in the fluorescence signal expressed as a change in the maximum value of fluorescence or in the Area Under the Curve (AUC) after the light stimulation. For this, a delta of the maximum value of fluorescence and the AUC is obtained by subtracting the value measured during the 300 s period after the stimulation to the value obtained during the 300 s period before the stimulation. Slices were incubated for at least 1 h in 1 μ M atosiban before being recorded. All recordings were performed at room temperature (25 °C).

Ex vivo patch-clamp recording of vIPAG-OTR neurons

Slice preparation. To validate the functionality of vIPAG OTR neurons in OTR-IRES-Cre rats using electrophysiology, 12–13-week-old female OTR-IRES-Cre rats ($n=4$) received injections of the Cre-dependent reporter virus, rAAV_{1/2}-pEF1 α -DIO-GFP, into the vIPAG. Following a 4–8 week recovery period, rats were anesthetized by administering i.p. ketamine (Imalgene 300 mg/kg) and paxman (Rompun, 60 mg/kg). Transcardial perfusions were performed using an ice-cold, NMDG-based aCSF was used containing (in mM): NMDG (93), KCl (2.5), NaH₂PO₄ (1.25), NaHCO₃ (30), MgSO₄ (10), CaCl₂ (0.5), HEPES (20), D-Glucose (25), L-ascorbic acid (5), Thiourea (2), Sodium pyruvate (3), N-acetyl-L-cysteine (10), and Kynurenic acid (2). The pH was adjusted to 7.4 using either NaOH or HCl, after bubbling in a gas comprised of 95% O₂ and 5% CO₂. Rats were then decapitated, brains were removed and 350 μ m thick coronal slices containing the hypothalamus were obtained using a Leica VT1000s vibratome. Slices were warmed for 10 min in 35 °C NMDG aCSF then placed in a room temperature holding chamber filled with normal aCSF for at least 1 h. Normal aCSF was composed of (in mM): NaCl (124), KCl (2.5), NaH₂PO₄ (1.25), NaHCO₃ (26), MgSO₄ (2), CaCl₂ (2), D-Glucose (15), adjusted to pH 7.4 with HCl or NaOH and continuously bubbled in 95%-O₂ 5%-CO₂ gas. Osmolarity of all aCSF solutions were maintained between 290 and 310 mOsm/L. Finally, slices were transferred from the holding chamber to an immersion-recording chamber and superfused at a rate of 2 ml/min.

Patch clamp recording. We targeted GFP+ or GFP- neurons in the vIPAG for whole-cell patch-clamp recording. The recording pipettes were visually guided by infrared oblique light video microscopy (DM-LFS; Leica). We used 4–9 M Ω borosilicate pipettes filled with a K-gluconate-based solution composed of (in mM): KMeSO₄ (135), NaCl (8), HEPES (10), ATPNa₂ (2), GTPNa (0.3). The pH was adjusted to 7.3–7.4 with KOH and osmolality was adjusted with sucrose to 290–310 mOsm/L, as needed. Data were acquired with an Axopatch 200B (Axon Instruments) amplifier and digitized with a Digidata 1440 A (Molecular Devices, CA, USA). Data were sampled at 20 kHz and lowpass filtered at 5 kHz using the pClamp10 software (Axon Instruments). Further analysis was performed using Clampfit 10.7 (Molecular Devices; CA, USA) and Mini analysis 6 software (Synaptosoft, NJ, USA) in a semi-automated fashion (automatic detection of events with chosen parameters followed by a visual validation). First spike latency quantification is measured as the duration preceding the first spike of a neuron submitted to a super-threshold stimulus of 50 pA.

TGOT stimulation. Finally, to validate the functionality of the putative OTR-Cre expressing cells in the vIPAG, we recorded GFP+ neurons in gap free (current clamp mode). Following a 5 min baseline recording period, a solution containing the OTR agonist, [Thr⁴Gly⁷]-oxytocin (TGOT, 0.4 μ M), was pumped into the bath for 20 s. The recording continued for a total of 20 min while the frequency of action potentials (APs) was quantified as the measure of neuronal activity. As a control, we repeated this procedure while patching GFP-neurons in the same vicinity. Neurons were held at -50 mV throughout the recording and all ex vivo experiments were conducted at room temperature.

In vivo extracellular recording of vIPAG neurons

To test the effects of endogenous OT release on OTR cells of the vIPAG in vivo, female Wistar rats ($n=11$) were injected with rAAV_{1/2}-pOT-ChR2-mCherry into the PVN. After a 4–8 week recovery period, rats were anaesthetized with 4% isoflurane and placed in a stereotaxic frame before reducing the isoflurane level to 2%. A silicone tetrode coupled with an optical fiber (Neuronexus, USA) was inserted into the PAG to allow for stimulation of the ChR2-expressing axons of PVN-OT neurons projecting to vIPAG while recording the activity of putative OTR expressing neurons in the vicinity. Optical stimulation was delivered using a blue laser (λ 473 nm, output of 3 mW, Dream Lasers, Shanghai, China) for 20 s at 1 Hz, with a pulse width of 5 ms. Extracellular neuronal activity was recorded using a silicone tetrode coupled with an optic fiber (Q1x1-tet-10mm-121-OAQ4LP; Neuronexus, USA). Data were acquired on an MC Rack recording unit (Multi Channel Systems), and spikes were sorted by Wave Clus⁵⁶. Spike data was analyzed with custom MATLAB (MathWorks) scripts and the MLIB toolbox (Stüttgen Maik, Matlab Central File Exchange).

The firing rate of each recording unit was smoothed by convolution of Gaussian distribution, whose width was 10 s and standard deviation was 5. The mean firing rate of the baseline period (BSmean) was defined as 0% activity and subtracted from the firing rates (FR) of the whole period (FR- BSmean). Maximum absolute activity (max(FR- BSmean)) was found using the highest absolute value among moving means of (FR- BSmean) with a time window of 21 s. When maximum absolute activity was found to exceed the BSmean, it was defined as 100% activity (cell#1-21), whereas when maximum absolute activity was found to be below BSmean, it was defined as -100% activity (cell#22-23).

In vivo extracellular recording of WDR SC neurons

Adult female Wistar rats ($n=22$) were anesthetized with 4% isoflurane and then maintained at 2% after being placed in a stereotaxic frame. A laminectomy was performed to expose the L4-L5 SC segments, which were then fixed in place by two clamps positioned on the apophysis of the rostral and caudal intact vertebrae. The dura matter was then removed. To record wide-dynamic-range neurons (WDR), a silicone tetrode (Q1x1-tet-5mm-121-Q4; Neuronexus, USA) was lowered into the medial part of the dorsal horn of the SC, at a depth of around 500–1100 μ m from the dorsal surface (see Fig. 5a for localization of recorded WDRs). We recorded WDR neurons of lamina V as they received both noxious and non-noxious stimulus information from the ipsilateral hind paw.

We measured the action potentials of WDR neurons triggered by electrical stimulation of the hind paw. Such stimulation induced the activation of primary fibers, whose identities can be distinguished by their spike onset following each electrical stimuli (A β -fibers at 0–20 ms, A δ -fibers at 20–90 ms, C-fibers at 90–300 ms and C-fiber post discharge at 300 to 800 ms). When the WDR peripheral tactile receptive fields are stimulated with an intensity corresponding to 3 times the C-fiber threshold (1 ms pulse duration, frequency 1 Hz), a short-term potentiation effect, known as wind-up (WU), occurs that leads to an increased firing rate of WDR neurons^{57,58}. Because the value of WU intensity was highly variable among recorded neurons within and across animals, we averaged the raster plots two dimensionally across neurons within each group of rats. We further normalized these data so that the plateau phase of the maximal WU effect was represented as 100 percent activity. As WU is dependent on C-fiber activation, it can be used as a tool to assess nociceptive information in the SC and, in our case, the anti-nociceptive properties of OT acting in the vIPAG. We recorded WDR neuronal activity using the following protocol: 40 s of hind paw electric stimulation to induce maximal WU followed by continued electrical stimulation to maintain WU while simultaneously delivering 20 s of vIPAG blue light stimulation (30 Hz, 10 ms pulse width, output ~3 mW), followed by another 230 s of

electrical stimulation alone to observe the indirect effects of OT on WU in WDR neurons. Electrical stimulation was ceased after the 290 s recording session to allow the WU effect to dissipate. Following a 300 s period of no stimulation, the ability of the WU effect to recover was assessed by resuming electrical stimulation of the hind paw for 60 s of WU. After another 10 min period without stimulation, we sought to confirm the effects of vIPAG OT activity on WU intensity by injecting 600 nl of the OTR antagonist, dOTV, (d(CH2)5-Tyr(Me)-[Orn8]-vasotocine; 1 μM, Bachem, Germany) into the vIPAG of the rats expressing ChR2, and repeated the protocol described above.

The spikes of each recording unit were collected as raster plots with the vertical axis showing the time relative to electric shock, and the horizontal axis showing the number of electric shocks. Next, the raster plots were smoothed by convolution of the Gaussian distribution (horizontal width = 100 ms, vertical width = 20 ms, standard deviation = 20). The total number of C fiber derived spikes occurring between 90 and 800 ms after each electric shock was counted. The spike counts were smoothed with a moving average window of 21 s and the window containing the maximal activity was defined as '100% activity', which was then used to normalize the activity of each recording unit. Finally, the normalized percent activity from each recording unit was averaged for each experimental condition and plotted in Fig. 5.

Determination of the phase of estrous cycle

To ensure consistency across studies (Eliava et al., 2016), all *in vivo* electrophysiological recordings were conducted during the diestrus phase of the ovarian cycle, which we determined using vaginal smear cytology³⁹. Briefly, a micropipette filled with 100 μL of saline solution (NaCl 0.9%) was placed in the rats' vagina and cells were dissociated by pipetting up and down at least three times. A drop of the smear was placed on a glass slide and observed using a light microscope with a 40x or 100x objective lens. Ovarian phase was determined based on the proportion of leukocytes, nucleated epithelial cells, and anucleate cornified cells. Animals in metestus, proestrus and estrus phases were excluded from experiments and reintroduced once they reached diestrus.

Behavioral tests

Optogenetics. For *in vivo* optogenetic behavioral experiments, we used a blue laser (λ 473 nm, 100 mW/mm², DreamLasers, Shanghai, China) coupled to optical fiber patch cables (BFL37-200-CUSTOM, EndA=FC/PC, EndB=Ceramic Ferrule; ThorLabs, USA). Optical fiber probes (CFMC12L10, Thorlabs, USA) were bilaterally implanted into the vIPAG (Coordinates relative to bregma: ML = ± 2.0 mm, AP = -6.7 mm, DV = -7.0 mm, medio-lateral angle=10°) under isoflurane anesthesia (4% induction, 2% maintenance), and then stabilized with dental cement. Following a two-week recovery period, all animals received special handling to habituate them to the fiber connection routine. Optical stimulation to the vIPAG was delivered using a series of pulse trains (intensity = -3 mW, frequency = 30 Hz, pulse width = 10 ms, duration = 20 s) during all applicable behavioral experiments.

Chronic constriction of the sciatic nerve. To produce the model of chronic neuropathic pain, we surgically implanted a cuff around the sciatic nerve to induce a chronic constriction injury as previously described⁴⁰. Briefly, under isoflurane anesthesia (5%) via a facemask, an incision was made 3–4 mm below the femur on the right hind limb and 10 mm of the sciatic nerve was exposed. A sterile cuff (2 mm section of split PE-20 polyethylene tubing; 0.38 mm ID/1.09 mm OD) was positioned and then closed around the sciatic nerve. The skin was then sutured shut to enclose the cuff and allow chronic constriction to occur.

Mechanical hyperalgesia. Mechanical sensitivity was assessed using calibrated digital forceps (Bioseb®, France) as previously described²⁰. Briefly, the habituated rat is loosely restrained with a towel masking the eyes in order to limit environmental stressors. The tips of the forceps are placed at each side of the paw and gradual force is applied. The pressure required to produce a withdrawal of the paw was used as the nociceptive threshold value. This manipulation was performed three times for each hind paw and the values were averaged. After each trial, the device was cleaned with a disinfectant (Surfa'Safe, Anios laboratory®).

Inflammatory hyperalgesia. In order to induce peripheral inflammation, 100 μL of complete Freund adjuvant (CFA; Sigma, St. Louis, MO), was injected into the right hind paw of the rat. All CFA injections were performed under light isoflurane anesthesia (3%). Edema was quantified by using a caliper to measure the width of the dorsoplantar aspect of the hind paw before and after the injection of CFA. In effort to reduce the number of animals used, we did not include an NaCl-injected group, as it has already been shown that the contralateral hind paw sensitivity is not altered by CFA injection⁴⁵.

Thermal hyperalgesia. To test the animal thermal pain sensitivity threshold, we used the Plantar test with the Hargreaves method (Ugo Basile®, Comerio, Italy) to compare the response of each hind paw of animals having received unilateral intraplantar CFA injection. The habituated rat is placed in a small box and we wait until the animal is calmed. We then exposed the hind paw to radiant heat and the latency time of paw withdrawal was measured. This manipulation was performed three times for each hind paw and the values were averaged. After each trial, the device was cleaned with a disinfectant (Surfa'Safe, Anios laboratory).

Conditioned place preference. The device is composed of two opaque conditioning boxes (rats: 30 × 32 cm; mice: 22 × 22 cm) and one clear neutral box (30 × 20 cm). Animals were tracked using a video-tracking system (Anymaze, Stoelting Europe, Ireland) and apparatus was cleaned with disinfectant (Surfa'Safe, Anios laboratory) after each trial. The animals underwent CPP as previously described²¹. Briefly, all rats underwent a three-day habituation period during which they were able to freely explore the entire apparatus for 30 min. On the 3rd habituation day, exploration behavior was recorded for 15 min to determine the animals' innate side preference. On the 4th day, animals were injected with saline (i.p, 1 mL/kg) and placed in their innately preferred chamber (unpaired box) for 15 min. Four hours later, animals were injected with DCZ (i.p, 100 μg/kg at 1 mL/kg⁴¹) to stimulate vIPAG OTR neurons expressing hM3D(Gq), and then placed in the innately non-preferred chamber (paired box) for 15 min. On the 5th day, the animals were placed in the neutral chamber and allowed to explore the entire apparatus for 15 min. To control for potential locomotor effects, the total distance traveled during the test period was quantified and compared between all groups.

c-Fos expression after painful stimulation. For the c-Fos experiment (Fig. 6), rats were pinched on the right hind paw (with or without CFA) three times using the same forceps as for the mechanical pain threshold procedure. Progressive pressure was applied until the rat exhibited pain-like behaviors by either retracting its paw or squeaking. The control groups were handled in the same way but no pressure was applied. Rats were perfused 90 min later as described previously.

Drugs

All drugs used in this study are listed in the reagents and resource table.

REAGENT OR RESOURCE	SOURCE	IDENTIFIER		
Antibodies				
Chicken anti-GFP primary antibody	Abcam	ab13970		
Mouse NeuN primary antibody	Millipore	MAB377		
Rabbit vGluT2 primary antibody	Synaptic systems	135 103		
Rabbit anti-dsRed primary antibody	Living Colors	632496		
GAD67	Millipore	MAB5406		
Guinea-pig anti-Fluorogold primary antibody	Protos Biotech Corp	NM-101		
Mouse c-Fos polyclonal primary antibody	Santa-Cruz	sc-8047		
Mouse monoclonal anti-OT primary antibody	Provided by Dr. Harold Gainer	PS 38		
DAPI	Vector Laboratories	H-1200-10		
Synaptophysin	Abcam	Ab32127		
Rabbit polyclonal anti-vGluT2 primary antibody	SYSY	135403		
Bacterial and virus strains				
rAAV1/2-OTp-Venus	Lab made	N/A		
rAAV1/2-OTp-mCherry	Lab made	N/A		
rAAV1/2-OTp-FLEX-GFP	Lab made	N/A		
CAV2-CMVp-Cre	Montpellier Vectorology Platform	N/A		
rAAV1/2-OTp-ChR2-mCherry	Lab made	N/A		
rAAV1/2-OTp-C1V1-mCherry	Lab made	N/A		
rAAV1/2-EF1 α p-FLEX-GFP	Lab made	N/A		
rAAV1/2-EF1 α p-FLEX-mCherry	Lab made	N/A		
rAAV1/2-EF1 α p-FLEX-hM3D(Gq)-mCherry	Lab made	N/A		
rAAV2/9-hSyn-OT1.0-sensor	Lab made	N/A		
Chemicals, peptides, and recombinant proteins				
Fluorogold TM	Santa-Cruz	sc-358883		
Oxytocin Receptor Antagonist	Merck	L-368,899		
Deschloroclozapine	MedChemExpress	1977-07-7		
TGOT	Bachem [®]	50-260-164		
CFA	Sigma	32160405		
dOVT	Bachem	d(CH2)5-Tyr(Me)-[Orn8]-vasotocine		
Retrobeads TM	Lumafluor	N/A		
RNAscope reagents and materials				
RNAscope HiPlex12 detection Reagents (488, 550, 647)	ACD	324106		
RNAscope HiPlex Probe Diluent	ACD	324301		
RNAscope Wash Buffer Reagents	ACD	310091		
RNAscope Protease III & IV Reagents	ACD	322340		
RNAscope HiPlex Cleaving Stock Solution	ACD	324136		
RNAscope HiPlex CRE-T2 Probe	ACD	312281-T2		
RNAscope HiPlex Rn-Oxtr-T6 Probe	ACD	483671-T6		
RNAscope HiPlex12 Positive Control Probe – Rn	ACD	324331		
RNAscope HiPlex12 Negative Control Probe	ACD	324341		
UltraPure 20X SSC Buffer	invitrogen	15557-044		
ProLong Gold antifade reagent				
ImmEdge Hydrophobic Barrier Pen	VECTOR LABORATORIES	H-40000		
Tween 20	Sigma-Aldrich	P1379		
Experimental Models: Organisms/Strains				
Rattus Norvegicus (Wistar HAN)	Janvier	N/A		
Rattus Norvegicus (Sprague Dawleys)	Charles River	N/A		
OTR-IRES-Cre (Wistar HAN)	Lab made	N/A		
Software and Algorithms				
Graphpad prism 7.05	www.graphpad.com	N/A		
Fiji	www.imagej.net/Fiji	N/A		
Adobe Photoshop CS5	www.adobe.com	N/A		
Adobe Illustrator 16.05	www.adobe.com	N/A		
CorelDraw 2020	www.coreldraw.com	N/A		
HiPlex Image Registration Software v1.0	ACD	300065		
Matlab	Mathworks	N/A		
Python	Open-source	N/A		
Zen (3.1 blue edition and 3.0 SR black edition)	Zeiss	N/A		
Other				
Optic fiber implants	www.thorlabs.com	CFMC12L10		
473 nm Blue Laser Generator	www.dreamlasers.com	SDL-473-XXXT		
Programmable Pulse Stimulator (A.M.P.I.)	www.ampi.co.il	Master-9		

Statistics and reproducibility

All individual observations (Cre expression, anatomical qualitative observations) were repeated at least 5 times.

For ex vivo electrophysiology data, a nonparametric Friedman test followed by Dunn's post hoc multiple comparisons test was used to compare the mean AP frequencies across the three conditions (Baseline vs TGOT vs wash) (Supplementary Fig. 1). A two-tailed paired t-test was used to test the difference of the first spike latency before and after TGOT application (Fig. 1). Differences were considered significant at $p < 0.05$.

For ex vivo imaging of OT release, a Welch's ANOVA test followed by a Dunnett's T3 multiple comparison was used to compare the change in the fluorescence (max fluorescence and AUC) after stimulating the C1V1 (with or without atosiban) to the change observed in the control condition (Fig. 4). The analysis of the recordings were performed using a custom-written Python-based script available on the editorial website. Statistical tests were then performed with GraphPad Prism 7.05 (GraphPad Software, San Diego, California, USA). Differences were considered significant at $p < 0.05$.

For in vivo electrophysiology data analysis, a paired-sample t-test was used to compare the average spike rates between the baseline and peak activity of PAG neurons in response to BL stimulation (Fig. 4). A nonparametric, unpaired Wilcoxon rank sum test was used to compare the reduction in discharge of SC neurons between the wild type and the ChR2-expressing animals (Fig. 5). A paired Wilcoxon signed-rank test was used to compare the reduction discharge of SC neurons in the ChR2-expressing animals, between the "without dOVT" and "with dOVT" conditions (Fig. 5). Unpaired Wilcoxon rank sum tests were used to compare the latencies to reach the maximum, minimum, and the half value between the wild type and the ChR2-expressing rats (Supplementary Fig. 9).

A Kruskall Wallis test with Dunn's post hoc test was used to compare the percent co-localization of c-Fos+ and GFP+ cells across

pain conditions (Fig. 6). Behavioral data are expressed as mean \pm standard deviation (SD). Statistical tests were performed with GraphPad Prism 7.05 (GraphPad Software, San Diego, California, USA) and MATLAB. For CFA and CCI (Fig. 6 and Supplementary Fig. 10) animals, a two-way ANOVA with repeated measure followed by multiple comparisons post hoc tests with Dunnett correction was used. The multiple comparisons were done within each condition (baseline, antagonist, recovery) by comparing each time point (blue light, 1 h, 3 h) to its own control. The same statistical procedure was used for CFA animals after DCZ administration (Fig. 6 and Supplementary Fig. 10). The Δ CPP score was calculated with the following formula in order to control for time spent in the neutral chamber: Δ CPP score = (paired_{postcond} - unpaired_{postcond}) - (paired_{hab} - unpaired_{hab}). An unpaired two-tailed t-test was used to compare the effect of DCZ on CPP difference score across the two groups as well as the distance traveled by the two groups (Fig. 6). All rats with off-target viral injection sites were removed from analysis. Differences were considered significant at $p < 0.05$.

Asterisks are used to indicate the significance level: * $0.01 \leq p < 0.05$, ** $0.001 \leq p < 0.01$, *** $p < 0.001$.

Reporting summary

Further information on research design is available in the Nature Portfolio Reporting Summary linked to this article.

Data availability

The raw data generated in this study have been deposited in the Zenodo database under accession code 10.5281/zenodo.7473865. The data generated in this study are provided in the Source data file. In addition, all data that support the findings of this study are available from the corresponding authors upon request. Source data are provided with this paper.

Code availability

Python code for ex vivo GRAB analysis can be found at the following address: https://github.com/Etienneclcr/GRAB_PAG; Matlab code for in vivo electrophysiological recordings can be found at the following address: <https://github.com/Etienneclcr/ephy-in-vivo-PAG>.

References

- Poisbeau, P., Grinevich, V. & Charlet, A. Oxytocin signaling in pain: cellular, circuit, system, and behavioral levels. *Curr. Top. Behav. Neurosci.* **35**, 193–211 (2018).
- Althammer, F. & Grinevich, V. Diversity of oxytocin neurons: beyond magno- and parvocellular cell types? *J. Neuroendocrinol.* **30**, e12549 (2018).
- Eliava, M. et al. A new population of parvocellular oxytocin neurons controlling magnocellular neuron activity and inflammatory pain processing. *Neuron* **89**, 1291–1304 (2016).
- Gonzalez-Hernandez, A. et al. Peripheral oxytocin receptors inhibit the nociceptive input signal to spinal dorsal horn wide-dynamic-range neurons. *Pain* **158**, 2117–2128 (2017).
- Moreno-Lopez, Y., Martinez-Lorenzana, G., Condes-Lara, M. & Rojas-Piloni, G. Identification of oxytocin receptor in the dorsal horn and nociceptive dorsal root ganglion neurons. *Neuropeptides* **47**, 117–123 (2013).
- Melzack, R. Prolonged relief of pain by brief, intense transcutaneous somatic stimulation. *Pain* **1**, 357–373 (1975).
- Fields, H. L. Pain modulation: expectation, opioid analgesia and virtual pain. *Prog. Brain Res.* **122**, 245–253 (2000).
- Basbaum, A. I., Marley, N. J. E., O'Keefe, J. & Clanton, C. H. Reversal of morphine and stimulus-produced analgesia by subtotal spinal cord lesions. *Pain* **3**, 43–56 (1977).
- Liebeskind, J. C., Guilbaud, G., Besson, J. M. & Oliveras, J. L. Analgesia from electrical stimulation of the periaqueductal gray matter in the cat: behavioral observations and inhibitory effects on spinal cord interneurons. *Brain Res.* **50**, 441–446 (1973).
- Campbell, P., Ophir, A. G. & Phelps, S. M. Central vasopressin and oxytocin receptor distributions in two species of singing mice. *J. Comp. Neurol.* **516**, 321–333 (2009).
- Nasanbuyan, N. et al. Oxytocin-oxytocin receptor systems facilitate social defeat posture in male mice. *Endocrinology* **159**, 763–775 (2018).
- Ogawa, S., Kow, L. M. & Pfaff, D. W. Effects of lordosis-relevant neuropeptides on midbrain periaqueductal gray neuronal activity in vitro. *Peptides* **13**, 965–975 (1992).
- Yang, J. et al. Oxytocin in the periaqueductal grey regulates nociception in the rat. *Regul. Pept.* **169**, 39–42 (2011).
- Herpertz, S. C. et al. Oxytocin effects on pain perception and pain anticipation. *J. Pain.* **20**, 1187–1198 (2019).
- Knobloch, H. S. et al. Evoked axonal oxytocin release in the central amygdala attenuates fear response. *Neuron* **73**, 553–566 (2012).
- Buijs, R. M. Vasopressin and oxytocin—their role in neurotransmission. *Pharm. Ther.* **22**, 127–141 (1983).
- Hasan, M. T. et al. A fear memory engram and its plasticity in the hypothalamic oxytocin system. *Neuron* **103**, 133–146 e138 (2019).
- Qian, T. et al. A genetically encoded sensor measures temporal oxytocin release from different neuronal compartments. *Nat. Biotechnol.* <https://doi.org/10.1038/s41587-022-01561-2> (2023).
- Ritz, L. A. & Greenspan, J. D. Morphological features of lamina V neurons receiving nociceptive input in cat sacrocaudal spinal cord. *J. Comp. Neurol.* **238**, 440–452 (1985).
- Herrero, J. F., Laird, J. M. & Lopez-Garcia, J. A. Wind-up of spinal cord neurones and pain sensation: much ado about something? *Prog. Neurobiol.* **61**, 169–203 (2000).
- Wahis, J. et al. Astrocytes mediate the effect of oxytocin in the central amygdala on neuronal activity and affective states in rodents. *Nat. Neurosci.* **24**, 529–541 (2021).
- Austin, P. J., Wu, A. & Moalem-Taylor, G. Chronic constriction of the sciatic nerve and pain hypersensitivity testing in rats. *J. Vis. Exp.* **13**, 3393 (2012).
- King, T. et al. Unmasking the tonic-aversive state in neuropathic pain. *Nat. Neurosci.* **12**, 1364–1366 (2009).
- Boll, S., Almeida de Minas, A. C., Raftogianni, A., Herpertz, S. C. & Grinevich, V. Oxytocin and pain perception: From animal models to human research. *Neuroscience* **387**, 149–161 (2017).
- DeLaTorre, S. et al. Paraventricular oxytocinergic hypothalamic prevention or interruption of long-term potentiation in dorsal horn nociceptive neurons: electrophysiological and behavioral evidence. *Pain* **144**, 320–328 (2009).
- Chini, B., Verhage, M. & Grinevich, V. The action radius of oxytocin release in the mammalian CNS: from single vesicles to behavior. *Trends Pharm. Sci.* **38**, 982–991 (2017).
- Landgraf, R. & Neumann, I. D. Vasopressin and oxytocin release within the brain: a dynamic concept of multiple and variable modes of neuropeptide communication. *Front. Neuroendocrinol.* **25**, 150–176 (2004).
- van den Pol, A. N. Neuropeptide transmission in brain circuits. *Neuron* **76**, 98–115 (2012).
- Knobloch, H. S., Charlet, A., Stoop, R. & Grinevich, V. Viral vectors for optogenetics of hypothalamic neuropeptides. *Springer Protocols* (2014).
- Buijs, R. M. Intra- and extrahypothalamic vasopressin and oxytocin pathways in the rat. Pathways to the limbic system, medulla oblongata and spinal cord. *Cell Tissue Res.* **192**, 423–435 (1978).
- Bettley, J. N., Cao, Z. F., Ritola, K. D. & Sternson, S. M. Parallel, redundant circuit organization for homeostatic control of feeding behavior. *Cell* **155**, 1337–1350 (2013).
- Tovote, P., Fadok, J. P. & Luthi, A. Neuronal circuits for fear and anxiety. *Nat. Rev. Neurosci.* **16**, 317–331 (2015).

33. Prieto, G. J., Cannon, J. T. & Liebeskind, J. C. N. raphe magnus lesions disrupt stimulation-produced analgesia from ventral but not dorsal midbrain areas in the rat. *Brain Res.* **261**, 53–57 (1983).
34. Taylor, N. E. et al. The role of glutamatergic and dopaminergic neurons in the periaqueductal gray/dorsal raphe: separating analgesia and anxiety. *eNeuro* **6**, ENEURO.0018–18.2019 (2019).
35. Lau, B. K. & Vaughan, C. W. Descending modulation of pain: the GABA disinhibition hypothesis of analgesia. *Curr. Opin. Neurobiol.* **29**, 159–164 (2014).
36. Saito, H. et al. Effects of oxytocin on responses to nociceptive and non-nociceptive stimulation in the upper central nervous system. *Biochem. Biophys. Res. Commun.* **574**, 8–13 (2021).
37. Gamal-Eltrably, M. et al. The rostral agranular insular cortex, a new site of oxytocin to induce antinociception. *J. Neurosci.* **40**, 5669–5680 (2020).
38. Chow, L. H., Chen, Y. H., Wu, W. C., Chang, E. P. & Huang, E. Y. Sex difference in oxytocin-induced anti-hyperalgesia at the spinal level in rats with intraplantar carrageenan-induced inflammation. *PLoS ONE* **11**, e0162218 (2016).
39. Mogil, J. S. Qualitative sex differences in pain processing: emerging evidence of a biased literature. *Nat. Rev. Neurosci.* **21**, 353–365 (2020).
40. Freda, S. N. et al. Brainwide input-output architecture of paraventricular oxytocin and vasopressin neurons. Preprint at *bioRxiv* <https://doi.org/10.1101/2022.01.17.476652> (2022).
41. Pfeifer, A. C. et al. Oxytocin and positive couple interaction affect the perception of wound pain in everyday life. *Mol. Pain.* **16**, 1744806920918692 (2020).
42. Leng, G. & Ludwig, M. Intranasal oxytocin: myths and delusions. *Biol. Psychiatry* **79**, 243–250 (2016).
43. Busnelli, M. & Chini, B. Molecular basis of oxytocin receptor signalling in the brain: what we know and what we need to know. *Curr. Top. Behav. Neurosci.* **35**, 3–29 (2018).
44. Busnelli, M. et al. Design and characterization of superpotent bivalent ligands targeting oxytocin receptor dimers via a channel-like structure. *J. Med. Chem.* **59**, 7152–7166 (2016).
45. Hilfiger, L. et al. A nonpeptide oxytocin receptor agonist for a durable relief of inflammatory pain. *Sci. Rep.* **10**, 3017 (2020).
46. Muttenthaler, M. et al. Subtle modifications to oxytocin produce ligands that retain potency and improved selectivity across species. *Sci. Signal* **10**, eaan3398 (2017).
47. Tang, Y. et al. Social touch promotes interfemal communication via activation of parvocellular oxytocin neurons. *Nat. Neurosci.* **23**, 1125–1137 (2020).
48. Paxinos, G., Watson, C., Pennisi, M. & Topple, A. Bregma, lambda and the interaural midpoint in stereotaxic surgery with rats of different sex, strain and weight. *J. Neurosci. Methods* **13**, 139–143 (1985).
49. Harris, J. A. et al. Anatomical characterization of Cre driver mice for neural circuit mapping and manipulation. *Front Neural Circuits* **8**, 76 (2014).
50. Haeussler, M. et al. Evaluation of off-target and on-target scoring algorithms and integration into the guide RNA selection tool CRISPOR. *Genome Biol.* **17**, 148 (2016).
51. Hsu, P. D. et al. DNA targeting specificity of RNA-guided Cas9 nucleases. *Nat. Biotechnol.* **31**, 827–832 (2013).
52. Wefers, B. et al. Direct production of mouse disease models by embryo microinjection of TALENs and oligodeoxynucleotides. *Proc. Natl Acad. Sci. USA* **110**, 3782–3787 (2013).
53. Shao, Y. et al. CRISPR/Cas-mediated genome editing in the rat via direct injection of one-cell embryos. *Nat. Protoc.* **9**, 2493–2512 (2014).
54. Schonig, K., Schwenk, F., Rajewsky, K. & Bujard, H. Stringent doxycycline dependent control of CRE recombinase in vivo. *Nucleic Acids Res* **30**, e134 (2002).
55. Althammer, F. et al. Three-dimensional morphometric analysis reveals time-dependent structural changes in microglia and astrocytes in the central amygdala and hypothalamic paraventricular nucleus of heart failure rats. *J. Neuroinflammation* **17**, 221 (2020).
56. Chaure, F. J., Rey, H. G. & Quian Quiroga, R. A novel and fully automatic spike-sorting implementation with variable number of features. *J. Neurophysiol.* **120**, 1859–1871 (2018).
57. Mendell, L. M. & Wall, P. D. Responses of single dorsal cord cells to peripheral cutaneous unmyelinated fibres. *Nature* **206**, 97–99 (1965).
58. Schouenborg, J. Functional and topographical properties of field potentials evoked in rat dorsal horn by cutaneous C-fibre stimulation. *J. Physiol.* **356**, 169–192 (1984).
59. Marcondes, F. K., Bianchi, F. J. & Tanno, A. P. Determination of the estrous cycle phases of rats: some helpful considerations. *Braz. J. Biol.* **62**, 609–614 (2002).
60. Yalcin, I. et al. The sciatic nerve cuffing model of neuropathic pain in mice. *J. Vis. Exp.* **16**, 51608 (2014).
61. Nagai, Y. et al. Deschloroclozapine, a potent and selective chemogenetic actuator enables rapid neuronal and behavioral modulations in mice and monkeys. *Nat. Neurosci.* **23**, 1157–1167 (2020).

Acknowledgements

This work was supported by the Centre National de la Recherche Scientifique contract UPR3212, the Université de Strasbourg contract UPR3212; the University of Strasbourg Institute for Advanced Study (USIAS) fellowship 2014–15, Fyssen Foundation research grant 2015, NARSAD Young Investigator Grant 24821, Agence Nationale de la Recherche (ANR, French Research Foundation) grants n° 19-CE16-0011-0, 19-CE37-0019, and 20-CE18-0031 (to A.C.); the Graduate School of Pain EURIDOL, ANR-17-EURE-0022 (to A.C. and E.C.C.); ANR-DFG grant GR 3619/701, PHC PROCOPE and PICOS07882 grants (to A.C. and V.G.); Deutsche Forschungsgemeinschaft (DFG, German Research Foundation) grants GR 3619/15-1, GR 3619/16-1 (to V.G.); SFB Consortium 1158-2 (to V.G., S.H., and B.D.); French Japanese governments fellowship B-16012 JM/NH and Subsidy from Nukada Institute for Medical and Biological Research (to M.I.); Fyssen Foundation fellowship (to A.L.); Région Grand Est fellowship (to D.K.); DFG Postdoc Fellowship AL 2466/1-1 (to F.A.); the Foundation of Prader-Willi Research post-doctoral fellowship (to C.P.S. and F.A.); DAAD Postdoc Short term research grant 57552337 (to R.P.); DFG Walter Benjamin Position – Projektnummer 459051339 (to Q.K.). National Heart, Lung, and Blood Institute Grant NIH HL090948, National Institute of Neurological Disorders and Stroke Grant NIH NS094640, and funding provided by the Center for Neuroinflammation and Cardiometabolic Diseases (CNCD) at Georgia State University (to J.E.S.). The authors thank Prof. Yulong Li for providing the GRAB_{OTR} plasmid, Drs. Romain Goutagny and Vincent Douchamps for in vivo electrophysiology advices, the Chronobiotron UMS 3415 for all animal care and the technical plateau ComptOpt UPR 3212 for behavior technical assistance.

Author contributions

Conceptualization: A.C.; methodology: A.B., A.C., A.L., C.P.S., D.K., E.C.C., F.A., J.E.S., L.H., M.I., M.M., O.Ł., Q.K., and V.G.; in situ hybridization: A.G., A.K., A.T., and F.A.; immunohistochemistry: A.L., F.A., M.K.K., and S.K.; ex vivo patch-clamp electrophysiology: D.K., E.C.C., H.P., and L.H.; in vivo electrophysiology: M.I., M.M., and O.Ł.; GRAB monitoring: E.C.C.; behavior: L.H. and M.I.; transgenic rats line generation: K.S. and D.B.; transgenic rats line validation: A.K., H.F., J.S., L.D., and M.W.; writing: A.C., A.L., B.D., E.C.C., F.A., J.E.S., M.I., M.K.K., O.Ł., P.D., R.P., S.H., S.K., and V.G.; funding acquisition: A.C. and V.G.; supervision: A.C. and V.G.; project administration: A.C.

Competing interests

The authors declare no competing interests.

Additional information

Supplementary information The online version contains supplementary material available at <https://doi.org/10.1038/s41467-023-36641-7>.

Correspondence and requests for materials should be addressed to Valery Grinevich or Alexandre Charlet.

Peer review information *Nature Communications* thanks Patrick Sheets, Jun Yang and the other, anonymous, reviewer(s) for their contribution to the peer review of this work. Peer reviewer reports are available.

Reprints and permissions information is available at <http://www.nature.com/reprints>

Publisher's note Springer Nature remains neutral with regard to jurisdictional claims in published maps and institutional affiliations.

Open Access This article is licensed under a Creative Commons Attribution 4.0 International License, which permits use, sharing, adaptation, distribution and reproduction in any medium or format, as long as you give appropriate credit to the original author(s) and the source, provide a link to the Creative Commons license, and indicate if changes were made. The images or other third party material in this article are included in the article's Creative Commons license, unless indicated otherwise in a credit line to the material. If material is not included in the article's Creative Commons license and your intended use is not permitted by statutory regulation or exceeds the permitted use, you will need to obtain permission directly from the copyright holder. To view a copy of this license, visit <http://creativecommons.org/licenses/by/4.0/>.

© The Author(s) 2023

¹Centre National de la Recherche Scientifique and University of Strasbourg, Institute of Cellular and Integrative Neuroscience, 67000 Strasbourg, France.

²Department of Neuropeptide Research in Psychiatry, Central Institute of Mental Health, University of Heidelberg, Mannheim 68159, Germany. ³Center for Neuroinflammation and Cardiometabolic Diseases, Georgia State University, Atlanta, USA. ⁴Institute of Human Genetics, University Hospital Heidelberg, Heidelberg, Germany. ⁵Van Andel Institute, Grand Rapids, MI, USA. ⁶Department of General Psychiatry, Center of Psychosocial Medicine, University of Heidelberg, 69115 Heidelberg, Germany. ⁷Institute of Medical Psychology, Heidelberg University Hospital, 69115 Heidelberg, Germany. ⁸Ruprecht-Karls University Heidelberg, Heidelberg, Germany. ⁹Department of Molecular Biology, Central Institute of Mental Health, University of Heidelberg, Mannheim 68159, Germany. ¹⁰Department of Neurophysiology and Chronobiology, Institute of Zoology and Biomedical Research, Faculty of Biology, Jagiellonian University, Krakow 30-387, Poland. ¹¹Present address: Cortical Systems and Behavior Laboratory, University of California, San Diego, La Jolla, CA 92093, USA.

¹²These authors contributed equally: Mai Iwasaki, Arthur Lefevre, Ferdinand Althammer, Etienne Clauss Creusot. ¹³These authors jointly supervised this work: Valery Grinevich, Alexandre Charlet.  e-mail: valery.grinevich@zi-mannheim.de; acharlet@unistra.fr

An analgesic pathway from parvocellular oxytocin neurons to the periaqueductal gray in rats

Supplementary Information

Mai Iwasaki^{1,#}, Arthur Lefevre^{1,2,+,#}, Ferdinand Althammer^{2,3,4,#}, Etienne Clauss Creusot^{1,#}, Olga Łapieś¹, Hugues Petitjean¹, Louis Hilfiger¹, Damien Kerspern¹, Meggane Melchior¹, Stephanie Küppers², Quirin Krablicher², Ryan Patwell², Alan Kania², Tim Gruber⁵, Matthew K. Kirchner³, Moritz Wimmer⁴, Henning Fröhlich⁴, Laura Dötsch⁴, Jonas Schimmer², Sabine C. Herpertz⁶, Beate Ditzen^{7,8}, Christian P. Schaaf^{4,8}, Kai Schönig⁹, Dusan Bartsch⁹, Anna Gugula¹⁰, Aleksandra Trenk¹⁰, Anna Blasiak¹⁰, Javier E. Stern³, Pascal Darbon¹, Valery Grinevich^{2,3,§,*}, Alexandre Charlet^{1,§,*}

¹ Centre National de la Recherche Scientifique and University of Strasbourg, Institute of Cellular and Integrative Neuroscience, 67000 Strasbourg, France

² Department of Neuropeptide Research in Psychiatry, Central Institute of Mental Health, University of Heidelberg, Mannheim 68159, Germany

³ Center for Neuroinflammation and Cardiometabolic Diseases, Georgia State University, Atlanta, GA, USA

⁴ Institute of Human Genetics, University Hospital Heidelberg, Heidelberg, Germany

⁵ Van Andel Institute, Grand Rapids, MI, USA

⁶ Department of General Psychiatry, Center of Psychosocial Medicine, University of Heidelberg, 69115, Heidelberg, Germany

⁷ Institute of Medical Psychology, Heidelberg University Hospital, 69115, Heidelberg, Germany

⁸ Ruprecht-Karls University Heidelberg, Heidelberg, Germany

⁹ Department of Molecular Biology, Central Institute of Mental Health, University of Heidelberg, Mannheim 68159, Germany

¹⁰ Department of Neurophysiology and Chronobiology, Institute of Zoology and Biomedical Research, Faculty of Biology, Jagiellonian University, Krakow, 30-387, Poland

+ Present address: Cortical Systems and Behavior Laboratory, University of California, San Diego, La Jolla, CA 92093, USA

These authors contributed equally

§ These authors jointly supervised this work

Supplementary Figure 1

a, Schema of the generation of knock-in OTR-Cre rats.

b, As a further control, DNAs of Cre positive animals were used for detection of homologous recombination at the OT locus. For this purpose, the targeted region was amplified by PCR using the Q5 polymerase (NEB) with 100 -200ng of genomic DNA as template. Primers were selected which bind up- and downstream of the insertion site (outside of the homology arms) and were each combined with a primer located within the IRES2-Cre construct. We used for the 5' insertion site the primers OT_upper_check (5' CTCCCAGGGAAGATCTGTACC 3') together with IRES2_rev (5' GCTTCGGCCAGTAACGTTAGG 3') and for the 3' site the primers CRISPR_bGH_for (5' gacaatagcaggcatgctgg3') together with OT_rev_hom (5' GGGTTTCCCAGAACTCAGC 3').

c, Injection schema for the labelling of OTR neurons in the OTR-Cre rats. The rAAV_{1/2}-EF1α-DIO-GFP is injected into the PAG.

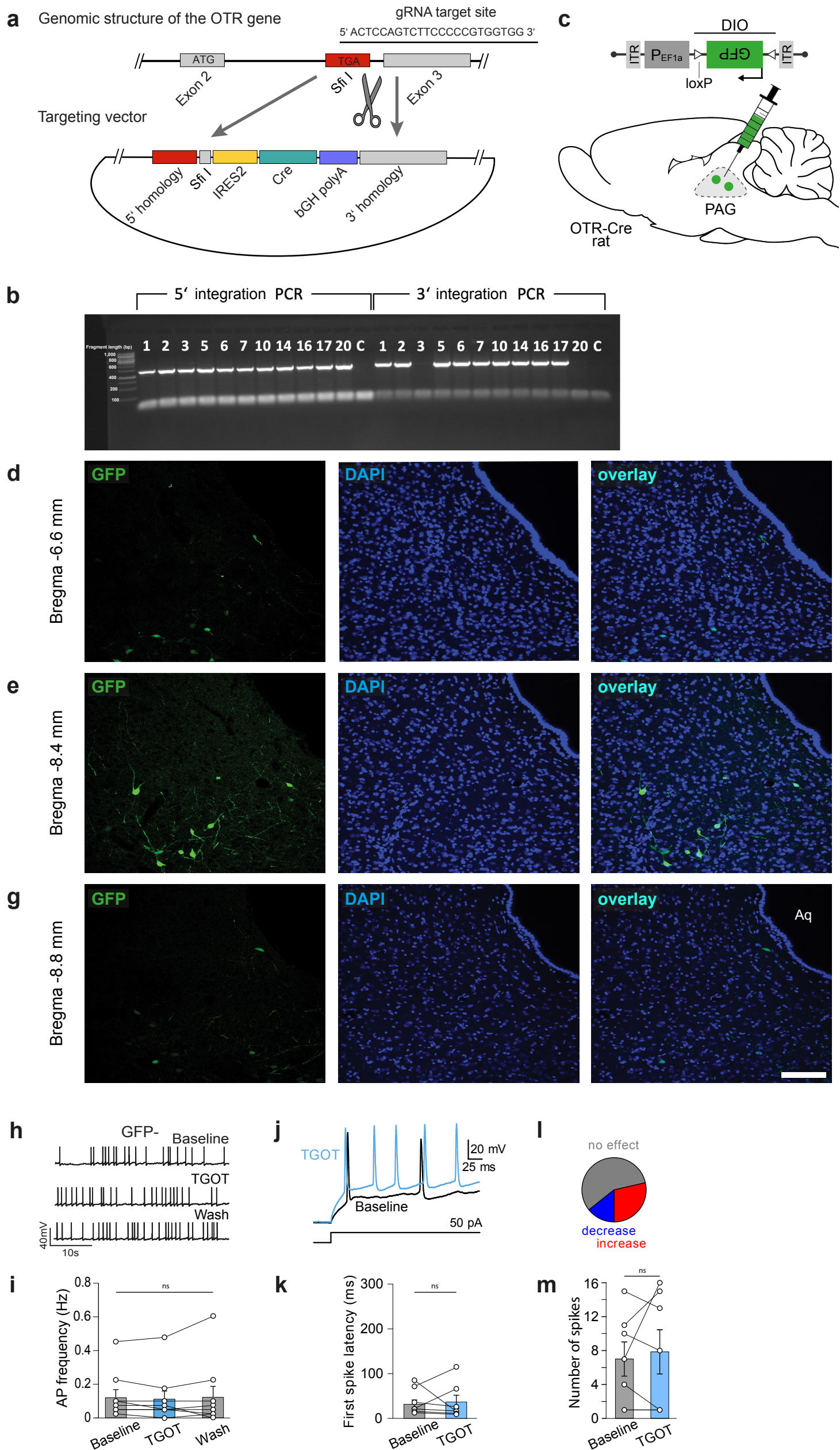
d-f, Images showing GFP (green) and DAPI (blue) staining, at various distances from Bregma, in the vIPAG of OTR-Cre rats injected with the EF1α-DIO-GFP rAAV. Scale bar = 100μm. Aq = Aqueduct.

h-i, TGOT-induced increase of AP frequency of GFP-negative neurons in the PAG of female rats. **h**, Example traces from a GFP-negative cell under baseline, TGOT application, and wash out conditions. **i**, Quantification of TGOT effect on AP frequency of GFP-negative neurons (Baseline 0.119 ± 0.046 Hz vs TGOT 0.108 ± 0.049 Hz vs Wash 0.122 ± 0.064 Hz; Friedman's test = 1.6, p = 0.48, n_{cells} = 9).

j-m, TGOT-induced change in first spike latency (FSL) of GFP-negative neurons in the PAG of female rats. **j**, Representative evoked currents in a GFP-negative neuron in response to a square current step (50 pA; 800 ms) in baseline (black line) and oxytocin (blue line) conditions. **k**, FSL quantification for GFP-negative neurons (OTR⁻) during a square current step: no differences were found between the baseline condition (31.95 ± 9.44 ms) and after the TGOT incubation 37.08 ± 14.89 ms, non significative (n.s.) p = 0.788 (paired two-tailed t test, n_{cells} = 7). **l**, Proportion of neuron after TGOT incubation with a decrease of the FSL (n = 1/7, blue); an increase (n = 2/7, red) or without a variation of ± 10 ms (no effect, gray (n = 4/7). **m**, Quantification of TGOT effect on AP frequency of GFP-negative neurons during a square current step (Baseline 7 ± 2.012 spikes vs TGOT 7.857 ± 2.604 spikes; Wilcoxon signed-rank test = 6, p = 0.6845 (two-sided), n_{cells} = 7.

Data are represented as mean ± sem and as individual paired points. Source data are provided as a Source Data file.

Figure S1



Supplementary Figure 2

a, RNAscope for OTR and Cre mRNA probes. Enlarged insets highlight co-localization of OTR and Cre probe signals. Aq=aqueduct, DR=dorsal raphe nucleus, vIPAG=ventrolateral periaqueductal gray.

b, Quantification of OTR/Cre and Cre/OTR probe signals from n = 3 rats (3 sections each). Results are expressed as the mean ± SEM and the individual points of each conditions are represented as white circle.

c, Confocal images show the vIPAG of a OTR-IRES-Cre rat injected with a cre-dependent rAAV expressing GFP that was counterstained with a cre antibody. High magnification images highlight co-localization of cre protein and GFP signals.

d, Quantification of cre+ GFP-expressing cells in vIPAG (GFP/Cre). Results are expressed as the mean ± SEM and the individual points of each conditions are represented as white circle.

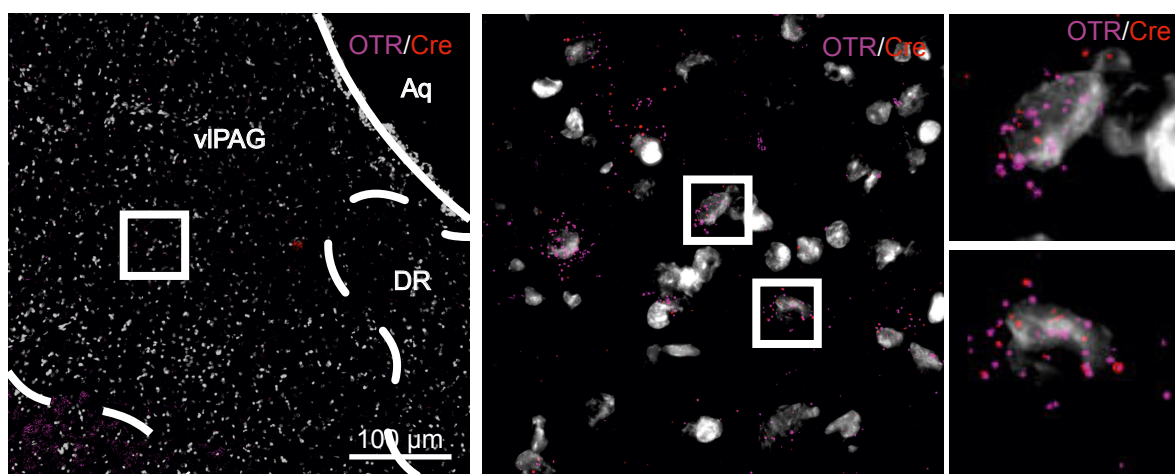
e, Uncut western blot of WT and OTR-IRES-Cre (KI) rats using a cre antibody.

f, Enlarged inset shows presence of specific cre band (35kDa) in a KI, but not WT rat.

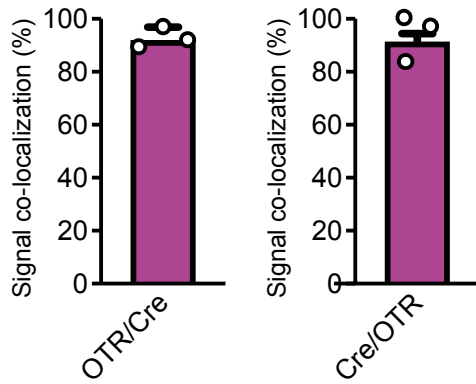
Source data are provided as a Source Data file.

Figure S2

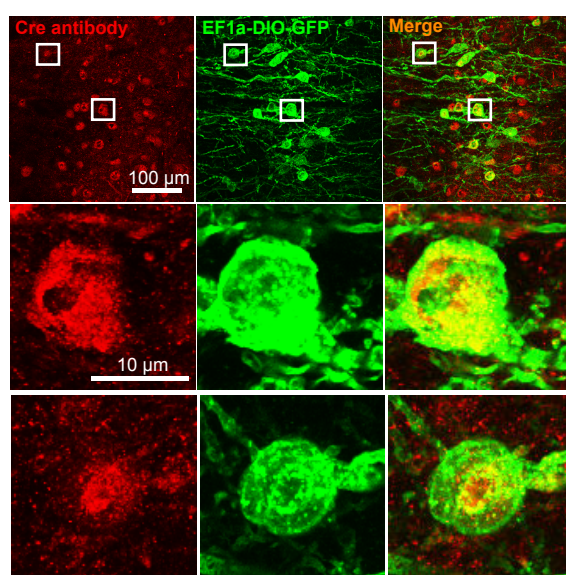
a



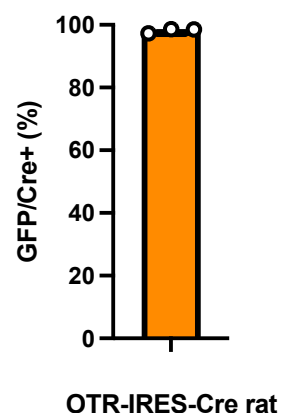
b



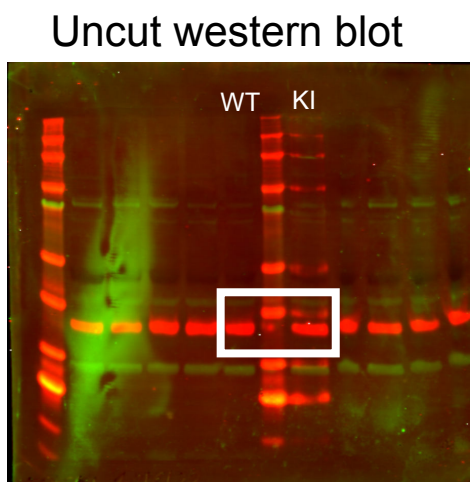
c



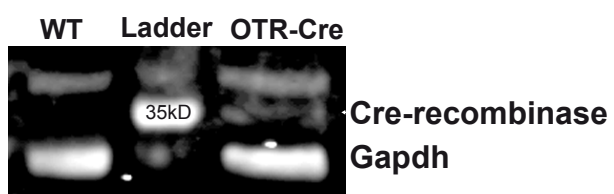
d



e

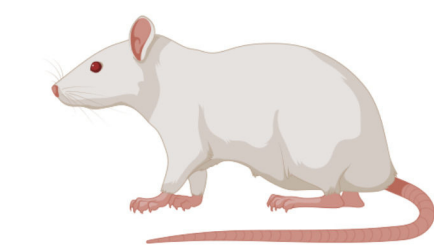


f

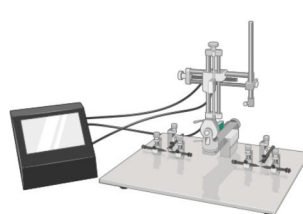


Supplementary Figure 3

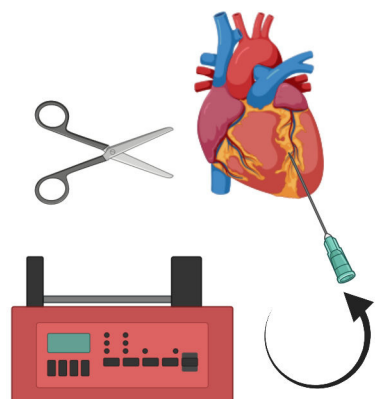
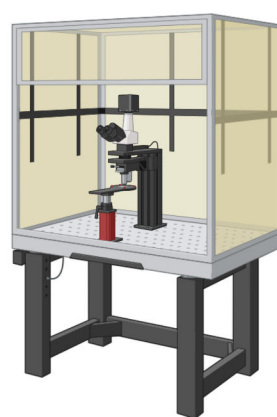
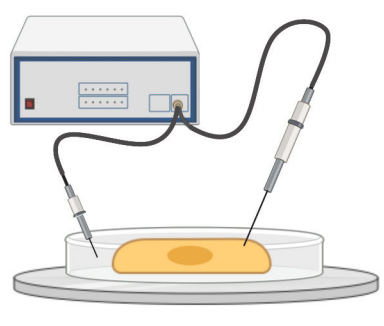
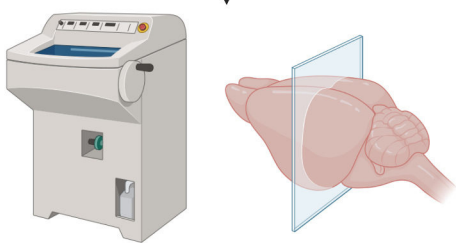
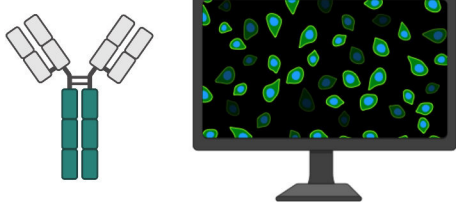
Schematic depiction of experimental procedures. WT and OTR-IRES-Cre rats were subjected to stereotaxic injection of various viral vectors at 10-12 weeks of age. Rats were then allocated to either neuroanatomical or physiological studies and processed accordingly. Images were created using BioRender.

Figure S3**Schematic depiction of experimental procedures**

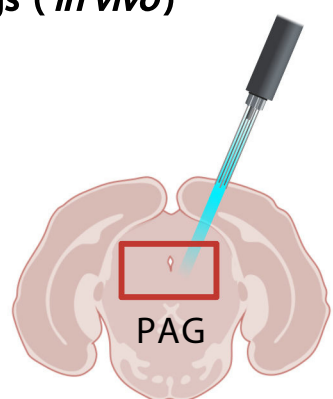
WT and OTR-Cre knockin rats

Stereotaxic injection of viral vectors
10-12 weeks old

3-4 weeks of virus expression

**Anatomical experiments**Perfusion and tissue collection
13-15 weeks old**Recordings (*ex vivo*)**Electrophysiology
13 - 15 weeks old**Recordings (*in vivo*)**

Tissue processing and immunohistochemistry

Optogenetic stimulation and
electrophysiological recordings
within PAG

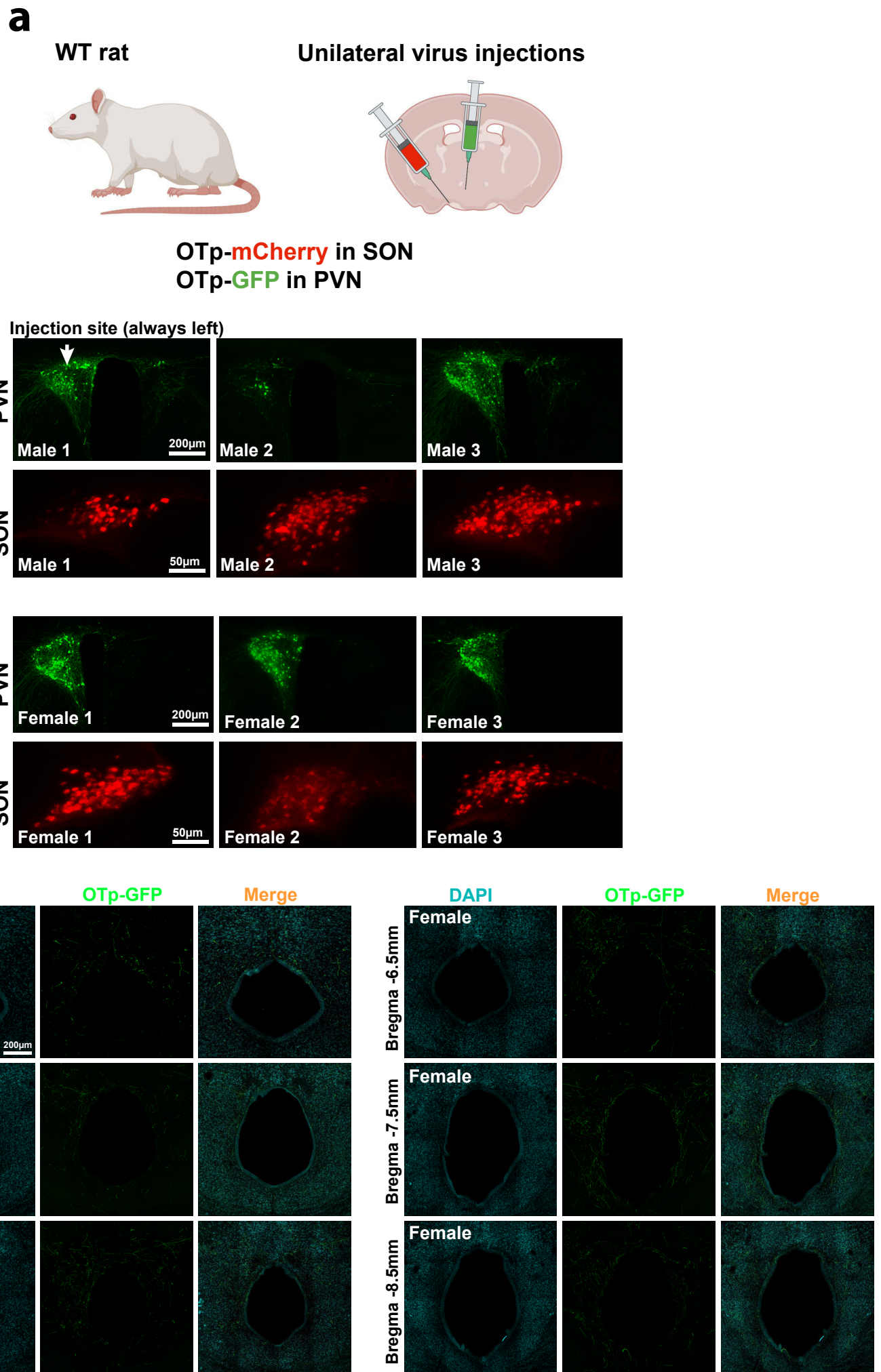
Supplementary Figure 4

a, Unilateral stereotaxic injection of WT rats (n=3 male and n=3 female) into the SON and PVN using rAAV_{1/2}-EF1α-mCherry or rAAV_{1/2}-EF1α-GFP, respectively.

b, Verification of injection sites and correct expressing of viral fluorescent proteins in the respective nuclei.

c, Analysis of OTergic fiber laterality within the vIPAG of male and female rats and various Brema levels. Note that OT fibers are prominently labeled in both hemispheres (i.e. left and right vIPAG) following unilateral injections into the PVN.

Figure S4



Supplementary Figure 5

a-b, Distinction of parvocellular (parvOT) and magnocellular (magnOT) OT-neuron populations. **a**, Schema for the identification of magnOT and parvOT neurons: injection of green retrobeads into the PAG, staining for OT (red) and central application of fluorogold (FG, blue), which labels only magnOT neurons. **b**, Image of retrolabeled neurons containing fluorescent beads (green) as well as staining for Fluorogold (blue) and OT (red). White arrows indicate the co-localization of OT and FG (magnOT neuron) and the white asterisk indicates the co-localization of retrobeads and OT. Scale bars = 25 µm. n = 3 female rats.

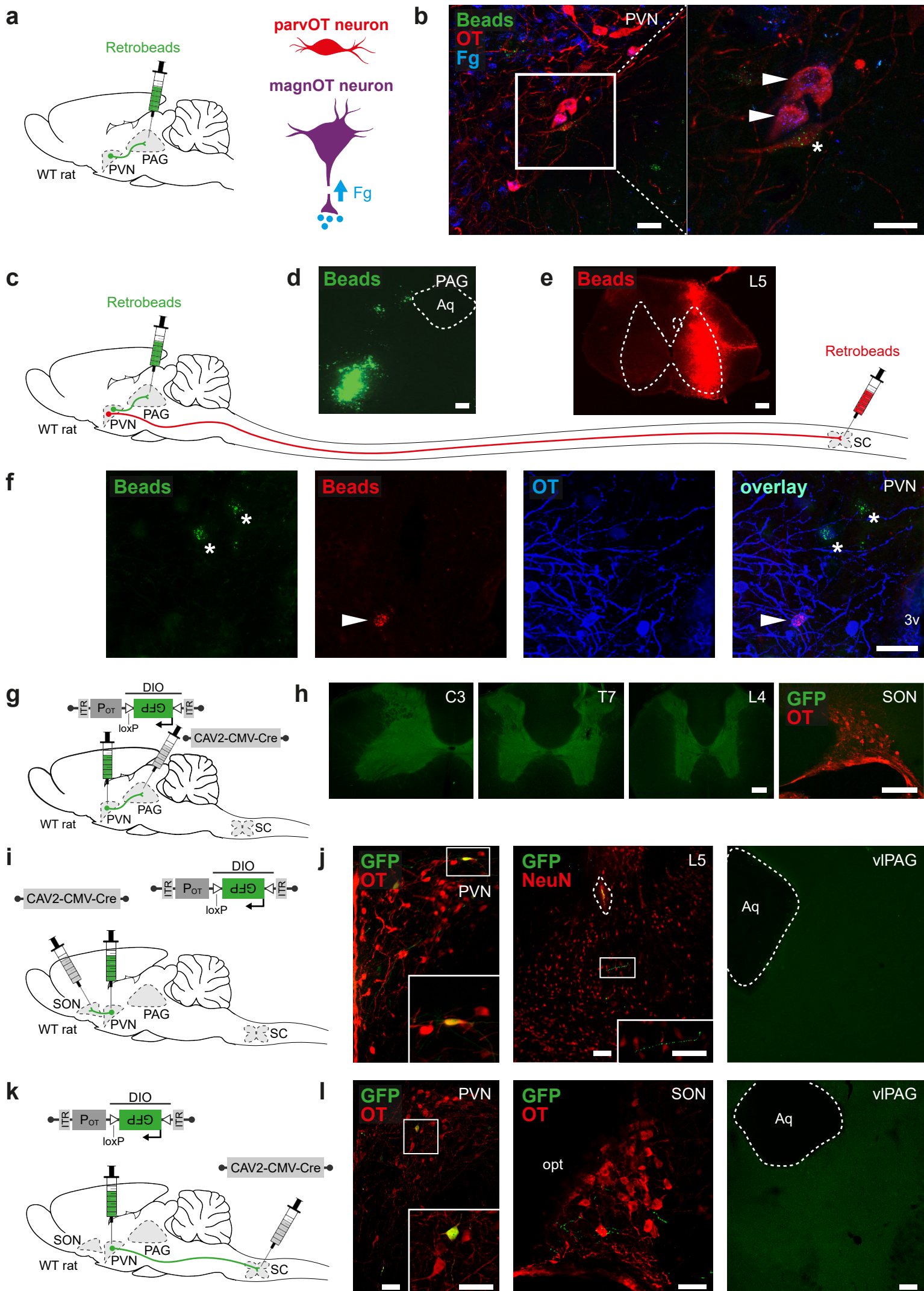
c-f, Retrograde labelling of projections from PVN OT-neurons to the vIPAG and SC. **c**, Schema of the experimental design with injection site of green retrobeads in the vIPAG (**d**) and red retrobeads in the SC (L5, **e**). Scale bars = 200 µm. **f**, Image of PVN OT-neurons (blue) projecting either to the vIPAG (green, white asterisk) or to the SC (red, white arrow). No OT neuron containing both red and green retrobeads was found. Aq = Aqueduct. 3v = third ventricle. Scale bar = 50µm. n = 4 female rats.

g-h, PAG-projecting PVN OT-neurons from Figure 2B do not target the SC or SON. **g**, Schema of viral injection showing injection of rAAV_{1/2}-OTp-DIO-GFP in the PVN and rAAV-CAV2-Cre in the vIPAG of WT rats. **h**, Images of slices from the spinal cord at different levels (cervical, C3; thoracic, T7; lumbar, L4) and from the SON. No GFP fibers were found. Scale bars = 200 µm. n = 2 female rats.

i-j, SON-projecting PVN OT-neurons target the SC but not the vIPAG. **i**, Schema of viral injection showing injection of rAAV_{1/2}-OTp-DIO-GFP in the PVN and rAAV-CAV2-Cre in the SON of WT rats. **j, Left** Images of PVN OT-neurons (red) expressing GFP (green) projecting fibers to the SC (L5, NeuN in red, scale bars = 100 µm). **Right** Image of the vIPAG showing no GFP positive fibers. Scale bar = 100 µm. n = 4 female rats.

k-l, SC-projecting PVN OT-neurons target the SON but not the vIPAG. **k**, Schema of viral injection showing injection of rAAV_{1/2}-OTp-DIO-GFP in the PVN and rAAV-CAV2-Cre in the SC of WT rats. **l** **Left** Images of PVN (scale bars = 40 µm) OT-neurons (red) expressing GFP (green) projecting fibers to the SON (scale bar = 100 µm). opt = optic tract. **Right** Image of the vIPAG showing no GFP positive fibers. Aq = aqueduct. Scale bar = 100 µm. n = 4 female rats.

Figure S5

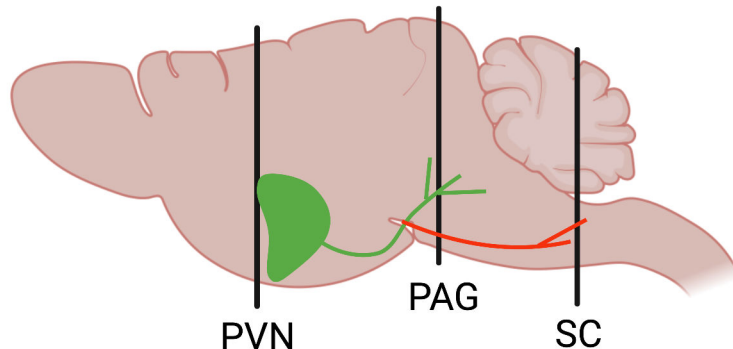


Supplementary Figure 6

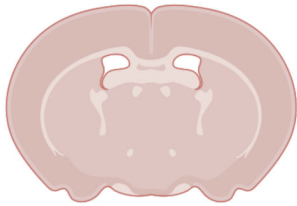
Scheme depicting the respective projections of the two different neuronal populations of parvOT and their projections to spinal cord (Eliava et al., 2016) and to vIPAG (present manuscript). Given that the oxytocinergic innervation of the PAG appears to be higher by roughly 2-3-fold, we speculate that approximately 50-70 parvocellular OT cells might project to the vIPAG compared to the approximately 30 parvocellular OT cells that we previously reported for the spinal cord.

Figure S6

Distribution map of distinct parvocellular oxytocinergic projections from PVN to PAG and SC



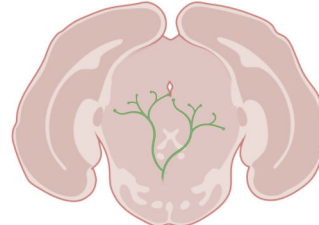
Bregma -2.0mm



PVN

2400 OT cells total
70-200 parvOT cells

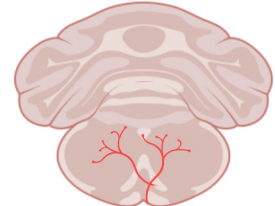
Bregma -8.0mm



PAG

Projections of 50-70?
parvOT cells

Bregma -11.0mm



SC

Projections of 30 parvOT
cells

Supplementary Figure 7

a, Pipeline for Imaris-assisted 3D reconstruction based on raw IHC images.

b-c, Confocal images showing OT fibers and OTR-positive neurons in the vIPAG. **b**, Images of OTR neurons (green), OT fibers (magenta), vGluT2 (red) and DAPI (blue). Scale bar = 100 μ m. **c**, Overlay. Scale bar = 100 μ m.

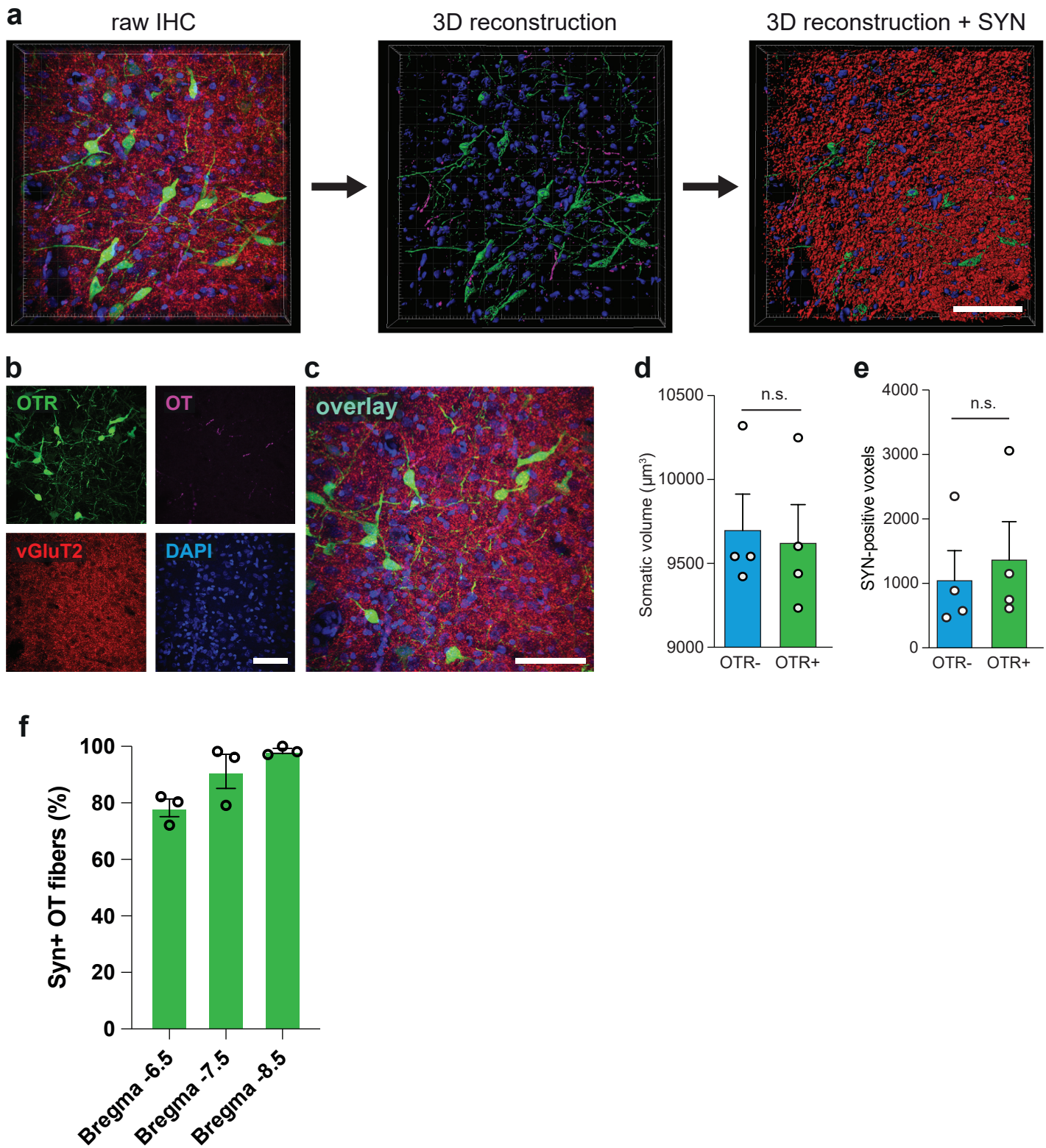
d, Automated quantification of the number of SYN positive voxels in GFP-positive and negative neurons reveals no difference in overall synaptic input. n = 4 rats, 8 images per animal, p=0.6689, two-tailed student t-test. Results are expressed as the mean \pm SEM and the individual points of each conditions are represented as white circle.

e, Analysis of somatic volume reveals no difference between OTR-positive (n = 496) and OTR-negative (n = 3840) soma sizes. n = 4 rats, 8 images per animal, p = 0.8104, two-tailed student t-test. Results are expressed as the mean \pm SEM and the individual points of each conditions are represented as white circle.

f, Quantification of Syn+ OTergic fibers in vIPAG at various Bregma levels.

Individual data and statistics are presented in Source Data File. Results are expressed as the mean \pm SEM and the individual points of each conditions are represented as white circle.

Source data are provided as a Source Data file.

Figure S7

Supplementary Figure 8

a, Visualization of the last step of spike sorting- superparamagnetic clustering (ascription of spikes to their corresponding neurons). This step is preceded by 1) automatic spike detection based on amplitude threshold and feature extraction – wavelets coefficients. From left to right: superimposed clusters, cluster separation and unassigned spikes based on spike shapes

b, Spike shapes represented in each channel of the tetrode.

c, Cluster 3 (from B) detailed profile, depicting (from left to right, and up to down) spikes' waveforms, baseline & peak voltages, spikes waveform variability over time, spikes parameters, stability presented as spikes count/time, activity during interspikes intervals of different length, density plots, waveform of selected spikes, PSTH, waveforms detected around an event and spikes distribution.

d, Onset, peak and offset of BL-induced excitation in the vIPAG. Onset is defined as the first time point when the spike rate exceeded the threshold ($BS_{mean} + 4BS_{SD}$); BS_{mean} represents the mean firing rate of the baseline period, and BS_{SD} is the standard deviation of firing rate during the baseline period. Offset is defined as the last time point when the spike rate fell below the threshold for more than 20 s during the 300 s following BL ($n_{cells} = 21$).

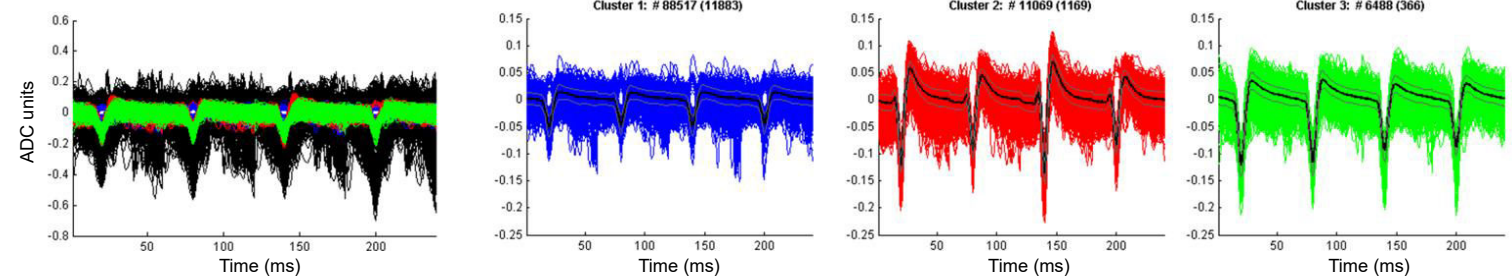
e, Number of active cells in each single second. “Active” defined by a spike rate above the threshold ($BS_{mean} + 4BS_{SD}$) ($n = 21$).

f, Image showing a representative recording site in the vIPAG. Dotted line indicates placement of the optic fiber. Aq = aqueduct. Scale bar = 100 μ m.

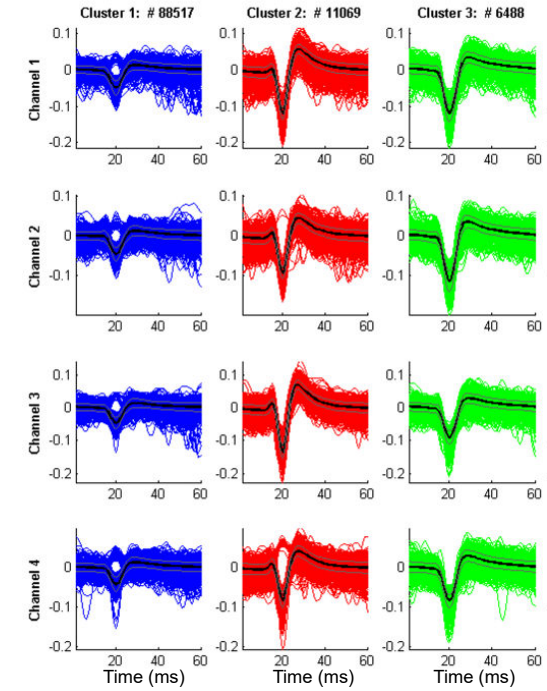
Source data are provided as a Source Data file.

Figure S8

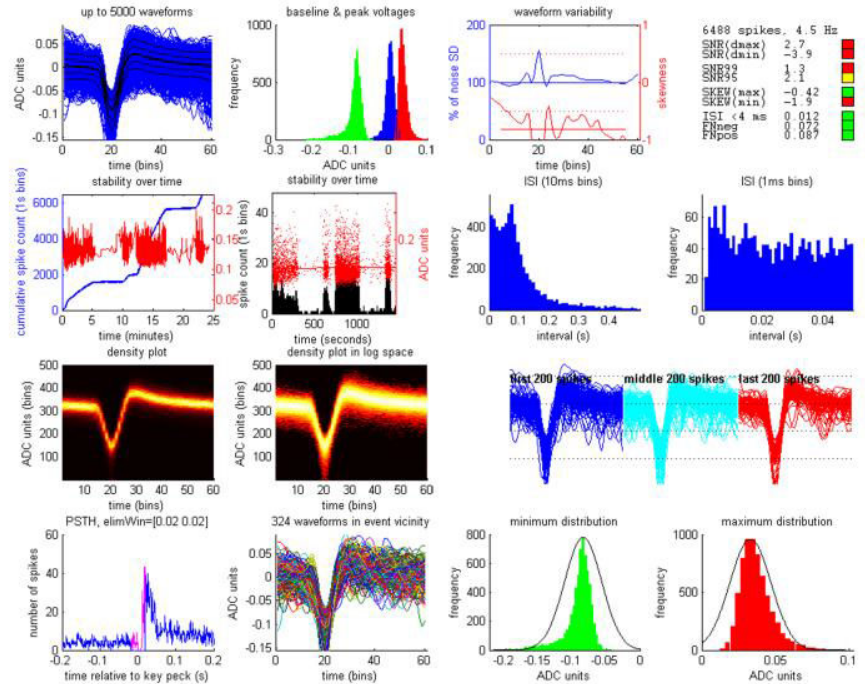
a



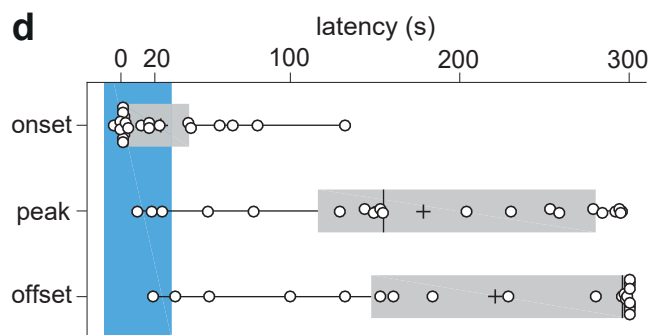
b



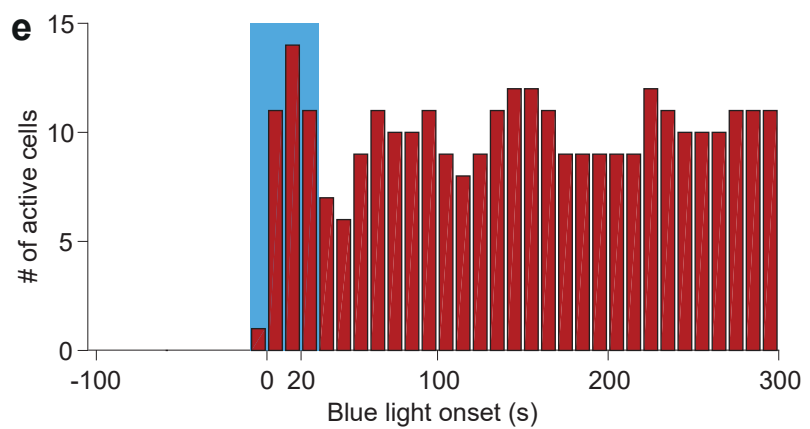
C



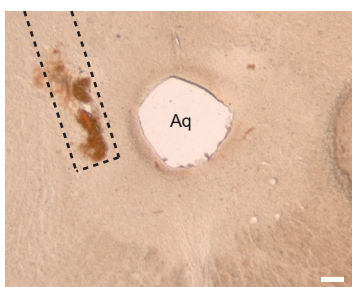
d



e



f



Supplementary Figure 9

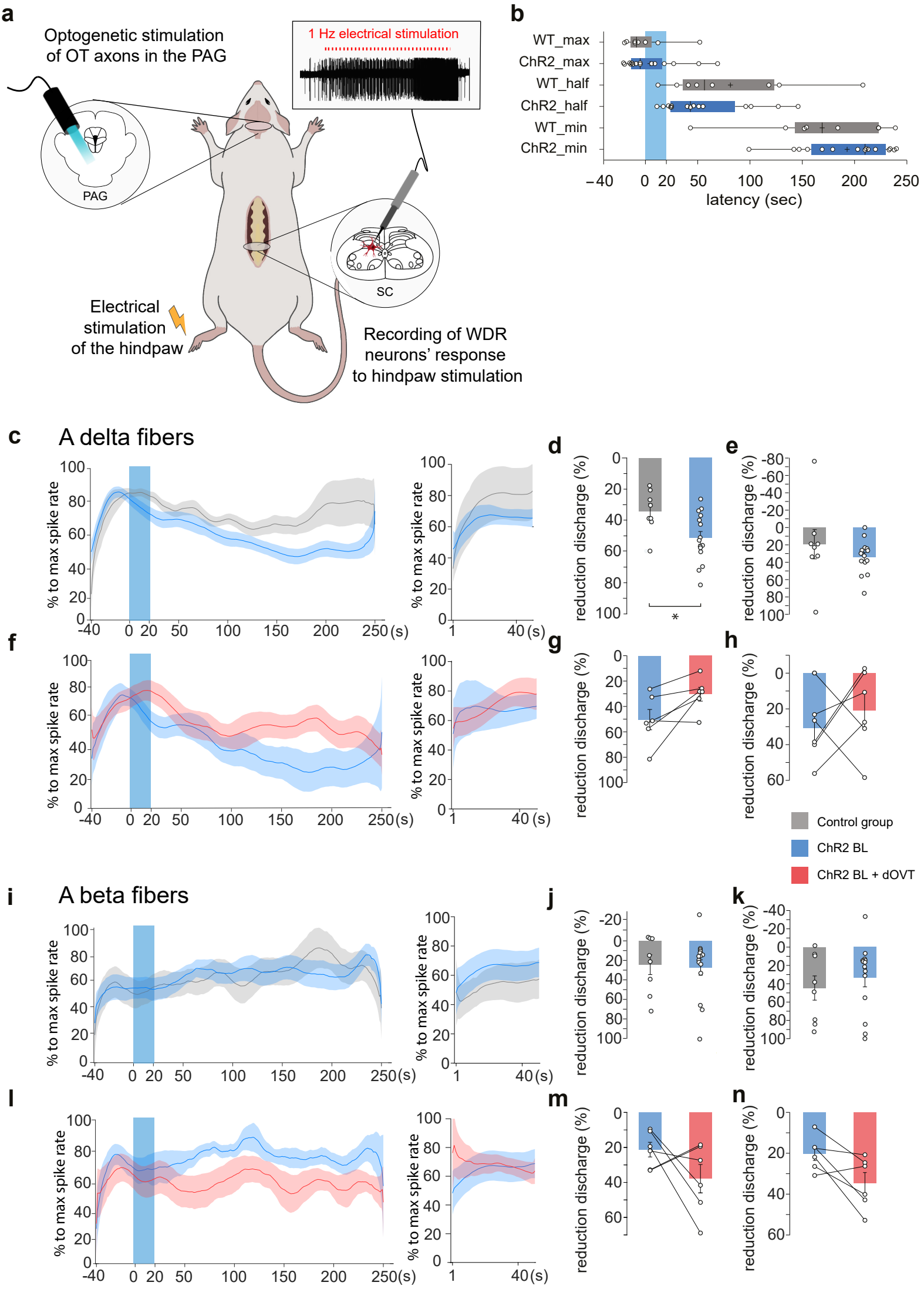
a, Scheme of electrophysiological recordings from SC in female rats.

b, Box plot showing maximum activity, minimum activity, and half activity latencies. Whiskers indicate the minimum and maximum latency. Colored box shows the range between 1st and 3rd quantile, median is depicted as vertical line. Unpaired Wilcoxon rank sum tests were performed. WT n=8, ChR2 n=15 (1st quartile, median, 3rd quartile); Latency to reach the maximum WU (s) [WT:(26.00, 31.50, 46.00), ChR2: (26.25, 35.00, 55.75)] not significant ($p = 0.85$); latency to reach the half reduction of WU (s) [WT: (75.50, 96.50, 163.00), ChR2 (64.25, 83.00, 125.75)] not significant ($p = 0.32$); or latency to reach the maximum reduction of WU (s) [WT (183.00, 209.00, 263.00), ChR2 (198.50, 250, 269.75)] not significant ($p=0.50$).

c-h, vIPAG BL effect on the spike rate of WDR's A δ -fiber discharge. **c**, Mean time course observed after vIPAG BL in control rats (gray, $n_{cells} = 8$) and OT ChR2-expressing rats (blue, $n_{cells} = 14$). Left and right panels show two consecutive recordings separated by 300 s. Line shadows represent SEM. **d**, Percentage of reduction expressed as the minimum level activity observed after a wind-up plateau phase, 140 – 180 s; Unpaired Wilcoxon rank sum test (two-sided); Ctrl ($n_{cells} = 8$) 34.08 ± 4.73 vs ChR2 ($n_{cells} = 14$) $51.26 \pm 4.1\%$, $U = 27$, $p = 0.0337$ and **e** 570 – 600 s after BL onset. Unpaired Wilcoxon rank sum test (two-sided); CTRL ($n_{cells} = 8$) 19.26 ± 16.88 vs ChR2 ($n_{cells} = 14$) $33.88 \pm 5.12\%$, $U = 37$, $p = 0.2119$. **f**, Mean time course observed after vIPAG BL in OT ChR2-expressing rats (blue, $n_{cells} = 6$), and in the same recordings after dOVT injection in the vIPAG (red, $n_{cells} = 6$). Left and right panels show two consecutive recordings separated by 300 s. Line shadows represent SEM. **g**, Percentage of reduction expressed as the minimum level activity observed after a wind-up plateau phase, 140 – 180 s; Paired Wilcoxon signed rank test (two-sided); ChR2 50.38 ± 8 vs dOVT $30.36 \pm 5.46\%$, $W = -19$, $p = 0.0625$, $n_{cells} = 6$ and **h** 570 – 600 s after BL onset. Paired Wilcoxon signed rank test (two-sided); ChR2 30.66 ± 7.78 vs dOVT $20.78 \pm 9.41\%$, $W = -7$ $p = 0.5625$, $n_{cells} = 6$.

i-n, vIPAG BL effect on the spike rate of WDR's A β -fiber discharge. **i**, Mean time course observed after vIPAG BL in control rats (gray, $n = 8$) and OT ChR2-expressing rats (blue, $n = 14$). Left and right panels show two consecutive recordings separated by 300 s. Line shadows represent SEM. **j** Percentage of reduction expressed as the minimum level activity observed after a wind-up plateau phase, 140 – 180 s; Unpaired Wilcoxon rank sum test (two-sided); Ctrl ($n=8$) 24.44 ± 10.14 vs ChR2 ($n=15$) $27.39 \pm 7.91\%$, $U = 55$, $p = 0.7763$, and **k** 570 – 600 s after BL onset. Unpaired Wilcoxon rank sum test (two-sided); CTRL ($n=8$) 44.7 ± 13.23 vs ChR2 ($n=14$) $33.43 \pm 10\%$, $U = 53$, $p = 0.8676$. **l** Mean time course observed after vIPAG BL in OT ChR2-expressing rats (blue, $n_{cells} = 6$), and in the same recordings after dOVT injection in the vIPAG (red, $n_{cells} = 6$). Left and right panels show two consecutive recordings separated by 300 s. Line shadows represent SEM. **m** Percentage of reduction expressed as the minimum level activity observed after a wind-up plateau phase, 140 – 180 s; Paired Wilcoxon signed rank test (two-sided); ChR2 21.28 ± 10.25 vs dOVT $37.89 \pm 8.12\%$, $W = 11$, $p = 0.3125$, $n = 6$ and **n** 570 – 600 s after BL onset. Paired Wilcoxon signed rank test (two-sided); ChR2 20.14 ± 3.39 vs dOVT $34.58 \pm 5.13\%$, $W = 17$, $p = 0.0938$, $n_{cells} = 6$.

Results are expressed as the mean \pm SEM and the individual points of each conditions are represented as white circle. Source data are provided as a Source Data file.

Figure S9

Supplementary Figure 10

a-c, Optogenetic stimulation of the vIPAG in the chronic constriction of the sciatic nerve (CCI) model of neuropathic pain in female rats. **a**, Schema of the injection of rAAV_{1/2}-OTp-ChR2-mCherry in the PVN and optic fiber implantation in the PAG. **b-c** Graphs showing the threshold response to mechanical stimuli in female rats optogenetically stimulated in vIPAG (as in Figure 6C and 6D). The effect of vIPAG-BL was measured at 5 min, 1 h and 3 h after vIPAG-BL on the CFA contralateral side (**b**) as well as CCI contralateral side (**c**). All results are expressed as average ± SEM. (**b**) 2-way RM ANOVA, $F_{\text{treatment}} = 8.391$; $p = 0.178$, $n_{\text{rats}} = 10$. (**c**) 2-way RM ANOVA, $F_{\text{treatment}} = 9.319$; $p = 0.2331$, $n_{\text{rats}} = 10$.

d-e, Verification for the expression of Gq-mCherry in the vIPAG. **d**, Schema of the injection of rAAV_{1/2}-EF1α-DIO-Gq-mCherry in the PAG. **e**, Image showing the expression of rAAV_{1/2}-EF1α-DIO-Gq-mCherry (red) with staining for DAPI (blue). Scale bar = 100 μm. Aq = aqueduct.

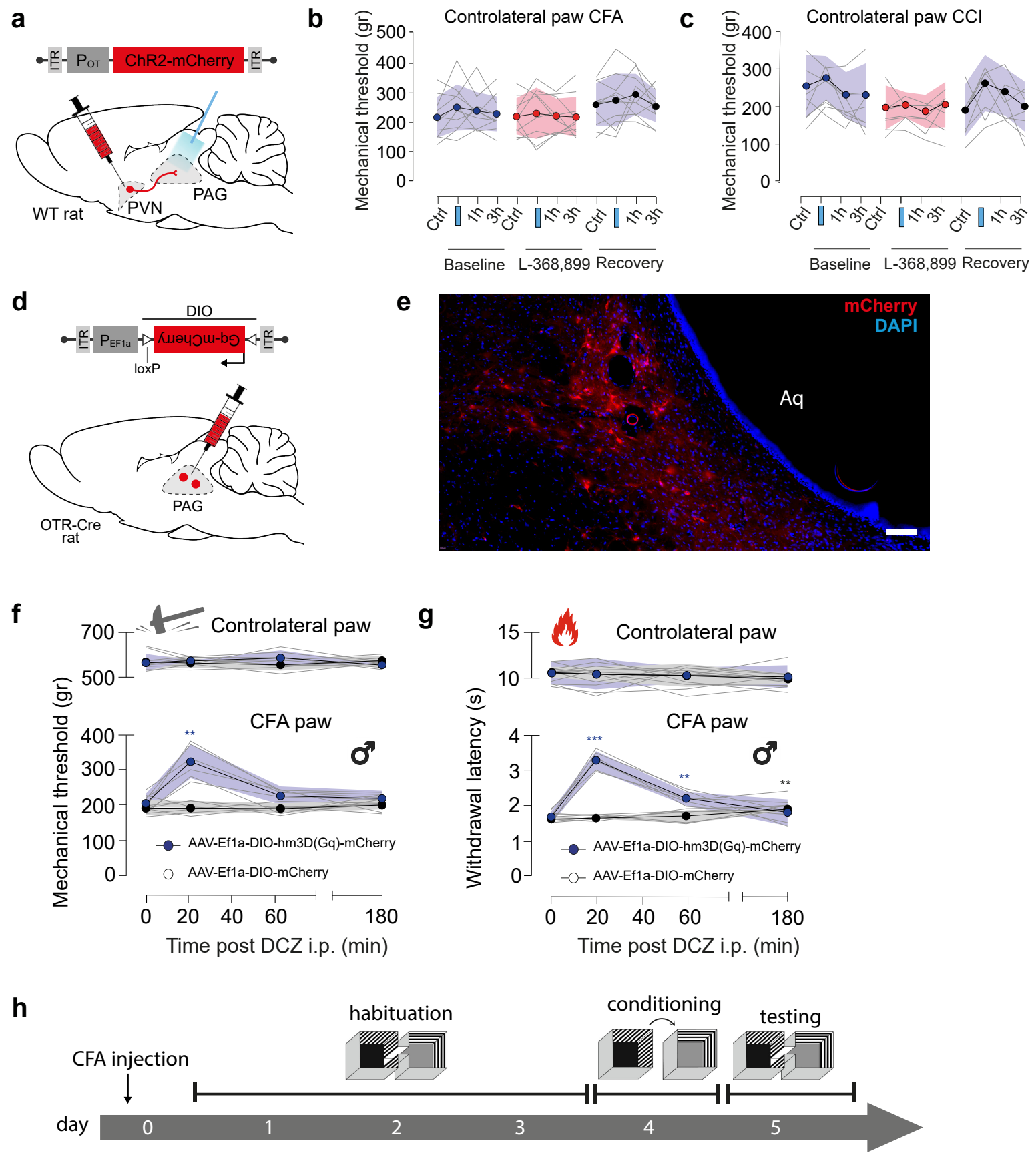
f-g, Thermal pain threshold of male rats expressing Gq-mCherry (red) or mCherry only (gray) in vIPAG OTR neurons after DCZ administration during normal or inflammation (CFA) conditions.

f, Mechanical pain threshold after DCZ administration in the CFA paw of male rats expressing Gq-mCherry (blue) or mCherry only (gray) in vIPAG OTR neurons. 2-way RM ANOVA test ($F_{\text{interaction}} = 17.79$; $p < 0.0001$; $n_{\text{rats}} = 6$), followed by multiple comparison post-hoc test with Dunnett correction: Gq-mCherry, 0 vs 20: ** $p_{\text{adj}} = 0.0033$. **g**, Thermal pain threshold after DCZ administration in the CFA paw of male rats expressing Gq-mCherry (red) or mCherry only (gray) in vIPAG OTR neurons. 2-way RM ANOVA test ($F_{\text{interaction}} = 40.40$; $p < 0.0001$; $n_{\text{rats}} = 6$), followed by multiple comparison post-hoc test with Dunnett correction: Gq-mCherry, 0 vs 20: *** $p_{\text{adj}} = 0.0003$; 0 vs 60: ** $p_{\text{adj}} = 0.0077$; mCherry, 0 vs 180: ** $p = 0.0058$. Blue asterisks correspond to the statistic done on the Gq-mCherry group while black asterisks to the mCherry group.

h, Schema depicting the experimental timeline of the CPP protocol.

All results are expressed as average ± SEM. Source data are provided as a Source Data file.

Figure S10



5 Discussion

5.1 Relaxin-3 discussion

During the first 2/3 of my Ph.D, I studied the relaxin-3/RXFP3 system in the amygdala and mainly its basal part. We based this project on preliminary data that suggested an antinociceptive effect of the activation of RXFP3 in this structure. The goal was to decipher and characterize the circuitry of the BA recruited by the relaxin-3 in response to pain. To do so, we used the patch-clamp technic to record the electrophysiological activity of the different neuronal populations in response to the application of an RXFP3 agonist on brain slices of naïve mice. Overall, we did not find any effect, be it in the BA or CeA, suggesting that the activation of RXFP3 does not change the electrical activity of the neurons in these structures.

5.1.1 Mice models

The behavioural tests assessing the antinociceptive effect of the relaxin-3 were done on mice and rats, both giving similar results. Because we wanted to identify the neurons we would be recording, we decided to use mice as a model because of the genetic lines available (Gad65-GFP, SOM-Cre). However, the only electrophysiological studies on relaxin-3 effect were done on rats (Blasiak et al., 2013; Kania et al., 2017). It would thus be interesting to verify whether the relaxin-3 also has an inhibitory effect on the same structures as (Blasiak et al., 2013; Kania et al., 2017) in mice.

5.1.1.1 Gad65

We started using the Gad65-GFP mice because of their availability at the lab. These mice are supposed to express the fluorescent protein GFP in GABAergic neurons, as shown in the cortex (Lopez-Bendito, 2004). We were mainly interested in labelling SOM interneurons, and because this mice line does not discriminate between the different interneurons, we used immunohistochemistry on the recorded slices to identify the marker of the cells recorded after the recordings were made. However, out of the four slices

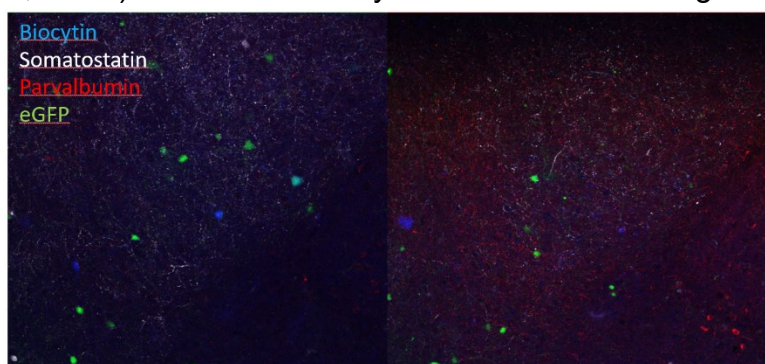


Figure 27 Example pictures of immunohistochemistry where we cannot see any SOM cells colocalized with GFP.

used for setting up the immunohistochemistry, I could not find a single GFP-expressing neuron co-expressing SOM (**Figure 27**). This is in fact not surprising since Wierenga and colleagues used this Gad65-GFP mice line to characterize molecularly and electrophysiologically the CA1 interneurons and found almost no SOM interneurons expressing GFP (Wierenga et al., 2010). In addition, when looking at the original paper describing this line, they show that 20 to 40% of the GFP-positive neurons of the layer IV and V respectively in the cortex express SOM. However, in their example picture, it is surprising to note that there is not a single SOM interneuron expressing GFP (Figure 6 K-M in (Lopez-Bendito, 2004)) suggesting that they either could not find SOM interneurons co-expressing the GFP (and thus had a problem in their quantification), or they did not choose the best example picture. In any case, this mice line does not seem to be adapted for labelling SOM interneurons, even more since there is another mice line expressing the Cre recombinase under the SOM promotor (Taniguchi et al., 2011), which we used later on.

5.1.1.2 *Male vs female*

In this study, we used both males and females mice. Indeed, we wanted to determine whether the effect was sex-dependent or not. Although, we did not tested the cycle period of the females before using them. We now know that the cycle can affect the relaxin-3 modulation, as it has been shown that the relaxin-3 mRNA expression in the *nucleus incertus* decrease during the proestrus, and the RXFP3 mRNA increases in structures such as the bed nucleus of the stria terminalis or the medial preoptic area of the hypothalamus (de Ávila et al., 2020). In addition, it has been shown that the inhibitory activity in the BA is different depending on the period of the cycle the animal is on (Pidoplichko et al., 2021). As a result, not testing the estrous cycle adds a bias for the female part of the study.

5.1.1.3 *Naïve vs painful mice*

During this study, we only used naïve animal in order to first characterize the basal effect of RXFP3 activation on amygdala neurons. Indeed, even if the behavioural experiments showed an effect of the agonist only in the CFA animals, but not in the

naïve ones, there is no difference in RXFP3 mRNA expression pattern between naïve and inflammatory mice (*i.e.* the CFA mice) (*Data from Marc Landry's lab, Figure 28*). However, the quantification shows the percentage of interneurons type (SOM, PV, etc.) in function of the RXFP3-expressing cells. Therefore, this indicates that there is no novel expression of the mRNA in another interneuron type, but does not indicate the number of SOM cells expressing the RXFP3 mRNA. Furthermore, even if the proportion of SOM interneurons expressing RXFP3 mRNA would not change, the mRNA is not yet a protein. It is conceivable that in basal conditions, RXFP3 mRNA in the amygdala is not or poorly translated, and that this translation is triggered when the animal is in pain. This could explain that in our conditions (*i.e.* in naïve animals) we could not see any effect of the agonist application on the electrical activity of the BA neurons.

5.1.2 Technical considerations

5.1.2.1 Electrophysiology as the only method

During this study, I only used electrophysiology to try to understand how the injection of an RXFP3 agonist in the amygdala could lead to antinociception. Despite being really adapted to characterize a change in electrical activity of neurons, I think that we persisted in using only this technic for too long. At some point, we should have tried other technics assessing the activity of a neuron. For example, we could have done some calcium imaging or c-Fos labelling in response to the application of the agonist. One might argue however that these two technics are mainly usable to observe an increase in the activity of a cell, whereas we are expecting to see a decrease in the activity of RXFP3-expressing neurons. Nevertheless, if the GABAergic interneurons expressing this receptor are themselves inhibited, it might increase the activity of the

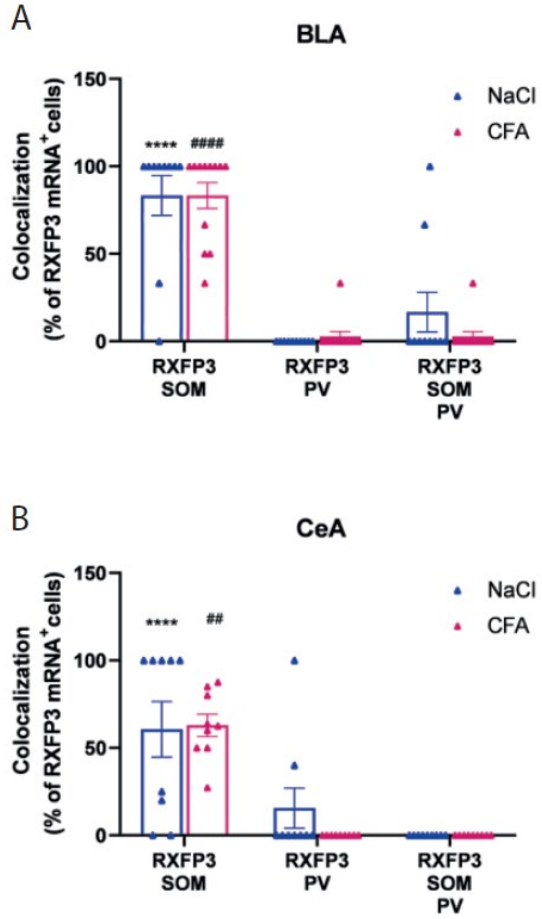


Figure 28 Proportion of RXFP3 mRNA-positive neurons colocalized with SOM and/or PV in the basolateral amygdala (A) or the CeA (B)

neurons they are projecting to. Therefore, we could have tried these technics without targeting specific cells, but only to see whether something happen on the global activity of neurons in the amygdala. In addition, Yang and colleagues identified that the phosphorylation of the pyruvate dehydrogenase is a marker of neuronal inhibition (Yang et al., 2023). We could have thus labels both c-Fos and the pyruvate dehydrogenase to have a complete view on the neuronal activity in the amygdala in response to a RXFP3 agonist.

5.1.2.2 Protocol and analysis

When performing the experiments, we used to do everything in whole-cell configuration, for postsynaptic current or action potential recordings. The idea was to always use the same protocol, meaning a 20 minutes recording in gap-free (*i.e.* recording of the spontaneous activity of the cell), with a bath application of the molecule at 5 minutes. However, when recording

in current clamp (in order to record action potential), I noticed that the majority of the cell had a decrease in their firing frequency over time that would not come back to basal level even after 1 hour of recording (**Figure 29**). One explanation could be that after 20 min of recording, the dialysis of the intracellular medium has impacted the capacity of the neurons action potential by diluting the second messenger, which might, for example, reduce the ions reuptake and thus change the ions concentrations. It thus seems that the current clamp mode is not suited for long recordings of action potential. This is why I started to record the putative RXFP3-expressing neurons in cell-attached mode. I also decided, whenever possible, to apply the molecule by puff application. Indeed, the bath application of agonists has multiple caveats, related to the fact that we cannot control the diffusion in the tubes that bring the aCSF to the chamber. In our case, this has two major problems:

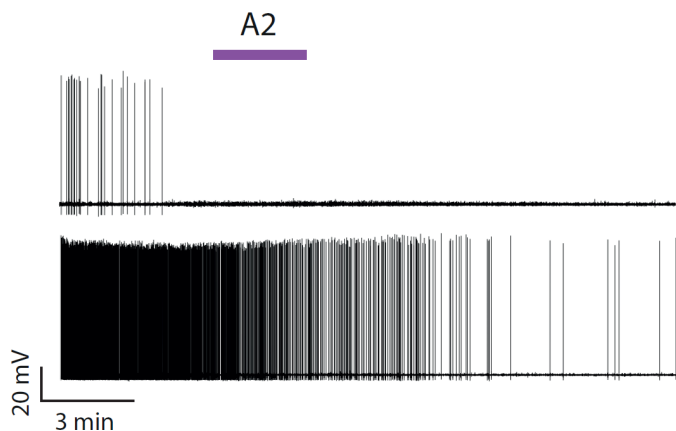


Figure 29 Example recordings of neurons recorded in whole-cell current clamp, showing a strong decrease in action potential that does not come back to basal level even after 1 hour recording.

- Even if we calculate the time it takes for the aCSF to reach the recording chamber, we cannot really evaluate the diffusion of the peptide in the solution, hence, we cannot know with precision when the molecule reach the slice.

- When we started the project (this apply to the Gad65-GFP recordings only), we applied the molecule during 40 seconds, with the idea in mind that applying too much peptide might trigger the desensitization of the receptor. However, by applying during such a short period and because of the dilution in the circuit, it is impossible to control the concentration reaching the recording chamber.

These two points and the long duration of the recordings are also a source to another issue related to the analysis. Indeed, there is no clear response similar to the ones we can see when applying glutamate or GABA on a neuron. As a result, it is not evident to determine a quantification window for a 40 seconds application out of a 20 minutes recording. To overcome the dilution issue, we started to apply the agonist during 3 minutes to be sure to reach the wanted concentration. Regarding the quantification window issue, we used the results of another experiment in which we applied bicuculline on CeM neurons to determine when the molecule reached the slice. Indeed, in this experiment, we had a very strong effect that was reproducible between all recordings. We thus used these results to determine when the molecule we used would reach the slice and start having an effect. This gave me the starting point of the quantification window of the agonist application, which explain the choice of starting quantifying at 6 min and 40 s.

5.1.2.3 Recordings of BA projection neurons

When recording BA projection neurons, we used a K-gluconate solution that mimics the normal ions concentrations gradients. This allow us to record the excitatory inputs but not the inhibitory ones as the chlorine equilibrium potential is close to the membrane potential. The idea to record those neurons was to see the neuron that would be connected with a RXFP3-expressing neuron. However, one could argue that RXFP3-expressing neurons are supposed to be GABAergic, and thus, recording inhibitory currents would be more interesting than the excitatory ones. And one would be right as the use of the K-gluconate was initially a mistake. However, SOM interneurons target the distal dendrites, hence, a decrease in their activity might not result in such a strong decrease in IPSC. In addition, the dendrites receive many excitatory inputs from other structures. Therefore, the inhibition of the SOM interneurons would prevent the shunt inhibition and result in stronger excitatory transmission (*i.e.* an increased amplitude of the EPSC received by the projection neurons). So even if we meant to use KCl intrapipette solution, I am not entirely sure that using K-gluconate prevented us to see a potential effect.

5.1.3 Conclusion & perspective

In this study, I showed that the relaxin-3/RXFP3 system does not modulate the electrical activity of the basal and central amygdala in naïve mice. Since an anti-allodynia effect has only been shown in inflammatory condition, it could then be interesting to redo these experiments under inflammatory condition. If RXFP3's antibodies are developed someday, we could also measure if RXFP3's expression is changed between naïve and painful conditions. Finally, investigating the activity of neuronal circuit of the amygdala during nociceptive assays *in vivo* could also confirm or infirm if the antinociception is associated with a change in the electrical activity of amygdala's neurons.

5.2 Oxytocin discussion

During the last part of my Ph.D, I set up and characterize the newly developed Grab_{OT}. This modified version of the OTR is linked to a GFP, and when a molecule of OT binds to this receptor, the GFP fluorescence intensity increases. My goal was to characterize this tool *ex vivo* in response to different doses of OT, AVP and TGOT. I found that all three molecules increases Grab_{OT} fluorescence, with OT and TGOT triggering a stronger one than AVP. In addition, I estimated the EC₅₀ for TGOT at 337 nM. For OT, I got an approximate value of 116 nM and I could not estimate any for the AVP.

I also had the opportunity to use this Grab_{OT} in a study interested in characterizing an analgesic pathway from the OTergic neurons of the PVN. In this study, we showed that these neurons release OT in the vIPAG, activating a population of the vIPAG neurons. This activation leads to the inhibition of WDR neurons plasticity in the lumbar section of the spinal cord. We finally showed that the activation of this pathway triggers a mechanical and thermal antinociception in both males and females rats.

5.2.1 Technical considerations on the Grab_{OT}

5.2.1.1 *Oxytocin and Vasopressin*

When I started the pharmacological characterization of the Grab_{OT}, I only used TGOT, and we then thought it would be interesting to test also OT and AVP. But because of a lack of time, I could not complete the doses for these two molecules. As a result, I cannot estimate an EC₅₀ for AVP and the one estimated for OT is probably not precise. Still, the maximum is not reached for AVP and seems to start at higher doses compared to OT or TGOT. This suggest a lower affinity of the Grab_{OT} receptor for AVP. On the other hand, both OT and TGOT dose-response curves seems similar suggesting a similar affinity. The fact that both OT and TGOT act on the OTR with a similar affinity is in accordance with previous studies (Jurek and Neumann, 2018; Taylor et al., 2020).

5.2.1.2 *Ex vivo vs culture EC₅₀*

When applying TGOT and OT on slices, I found that the EC₅₀ for the Grab_{OT} is 337 nM for TGOT and a rough estimation of 116 nM for OT. However, in culture the EC₅₀ has been estimated at about 3 nM. This would mean that between the culture and the slice there is a 100-fold difference in the EC₅₀. But, for this pharmacological characterization, I performed a 20 minutes recordings during which I bath applied the molecules at 5 minutes for 20 seconds. One might wonder why did I not take into account the problems related to applying a molecule for such a short time in the bath seen in the

previous part (see [Protocol and analysis](#)). The answer is that when I did my first trials using this Grab_{OT} with the application of 500 nM TGOT, I had such strong and reproducible responses that I did not think it necessary to increase the application time. However, the dilution of the molecule in the circuit might explain this difference obtained in slices compared to cultured cells as the real concentration on the slice was probably much lower. Again, it would have been preferable to apply the molecules for 3 minutes (or more) to make sure to reach the maximum effect possible at a certain dose. One could argue that applying an OTR agonist for so long could cause the receptor to desensitize, as it is known to do so in the matter of minutes (Busnelli and Chini, 2018). However, Qian and colleagues showed that the Grab_{OT} does not desensitize, as even after being incubated in 100 nM OT for 120 minutes, they observed no decrease in fluorescence and the receptor was still present at the cell membrane (Qian et al., 2023).

[5.2.1.3 OT1.0, OT3.0 or OT42.0?](#)

Here the Grab_{OT} we used is the OT1.0 sensor described by Qian and colleagues (Qian et al., 2023). However, in the same time, Ino and colleagues developed their own OT sensor. They got OT1.0, 2.0 and 3.0 sensors, with the latter being the most efficient. Note that the OT1.0 sensor from both studies are different, and thus, the comparison performed in Ino et al., does not concern the sensor developed by Qian and colleagues. Still, OT3.0 sensor has a maximum fluorescence almost two times stronger than the one of the Grab_{OT}. Nonetheless, the EC₅₀ is 10 times higher for the OT3.0 sensor (Ino et al., 2022; Qian et al., 2023). This would mean that OT3.0 sensor response to OT release is stronger than the Grab_{OT} but not as precise when concerning low concentrations. It could then be interesting to use and compare both sensors and use the more appropriate one depending on the OT concentrations present in the structure of interest.

[5.2.2 Scientific considerations on the vIPAG article](#)

[5.2.2.1 What circuit for the OT-dependent antinociception?](#)

The PAG is one of the main actor in the descending control of pain. However, it does not project to the spinal cord. To exert its effect, the PAG projects to the RVM. There, there are ON- and OFF-cells. Their names were given according to their electrical activity following a nociceptive stimulus: the ON-cells' activity increases, while the OFF-cells' activity decreases. It is often assumed that ON-cells could inhibit OFF-cells, and so the ON-cells' increase in activity may result in OFF-cells' inhibition. Regarding

how this PAG-to-RVM circuit produces antinociception, there are two hypotheses on the circuit involved:

- The disinhibition hypothesis (also called ‘lateral inhibition’) states that the PAG neurons projecting to the RVM are, in basal condition, inhibited by the GABAergic interneurons of the PAG. Decreasing the activity of these neurons creates a disinhibition of PAG-to-RVM projection neuron that results in activating the descending pain control pathway, ultimately triggering an antinociception (**Figure 30**). This hypothesis is based on the fact that, in the PAG, the injection of glutamate or an electrical stimulation produces an antinociception (respectively (Behbehani and Fields, 1979; Vanegas et al., 1984)), whereas the injection of opioids that have a direct inhibitory effect on neurons also produces an antinociception (Yeung et al., 1977). Therefore, we would have the following circuit: GABAergic interneurons tonically inhibiting the glutamatergic neurons projecting to the RVM (for more detail, see (Lau and Vaughan, 2014)) (**Figure 30**).

- The parallel inhibition/excitation hypothesis is mainly based on one study from Cleary and colleagues showing that during a nociceptive assay, the OFF-cells’ inhibition actually occurs prior to the activation of the ON-cells (Cleary et al., 2008). The hypothesis stating that the ON-cells are the cause of the OFF-cells’ decrease in activity is thus invalidated. As a result, the inhibition of the OFF-cells should come from outside the RVM (**Figure 30**).

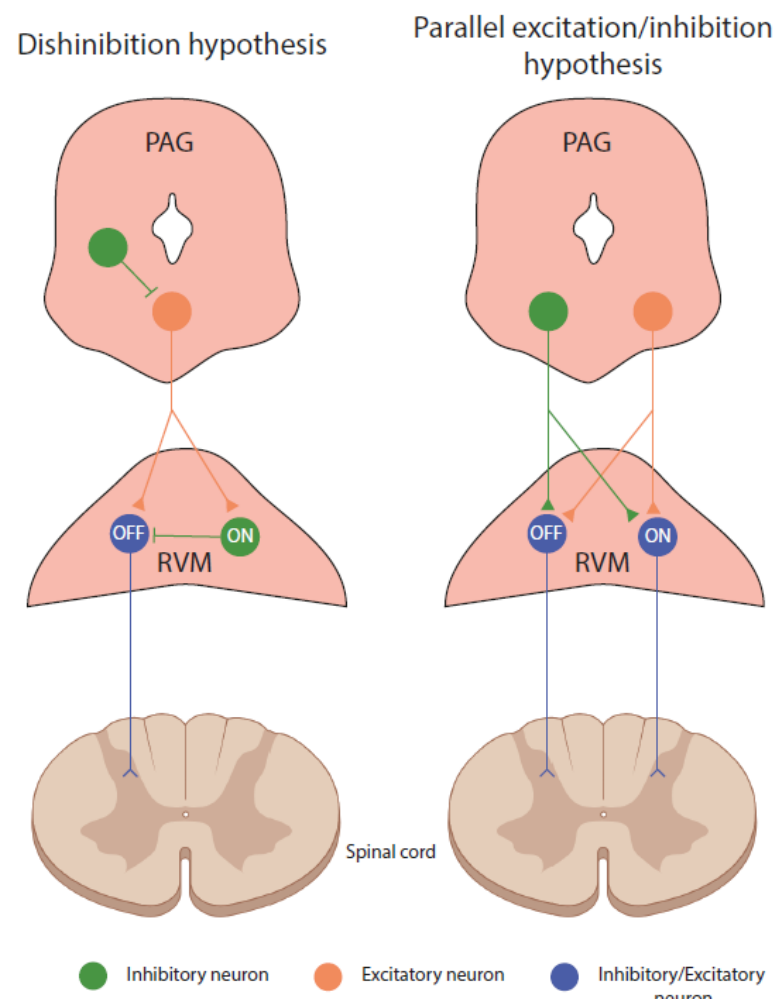


Figure 30 Schematic representation of the disinhibition hypothesis (left panel) and the parallel excitation/inhibition hypothesis (right panel).

In my point of view, the dishinibition hypothesis is mainly based on the assumption of a cortical-like histoarchitecture of the PAG, with GABAergic interneurons and glutamatergic projection neurons. However, Morgan and colleagues showed that PAG neurons projecting to the RVM are more often GABAergic and not glutamatergic. Therefore, I think that the parallel inhibition/excitation hypothesis is closer to reality than the dishinibition one. In addition, here we showed that the release of OT in the vIPAG increased the activity of OTR-expressing neurons, which are in the vast majority GABAergic. Furthermore, this OT release induces an antinociception. It thus seems that activating the GABAergic neurons from the vIPAG induces antinociception. This strengthen the parallel inhibition/excitation hypothesis. However, recent studies showed using chemogenetic that activating the GABAergic neurons of the PAG is pronociceptive while inhibiting them is antinociceptive (Samineni et al., 2017; Xie et al., 2023). On the other hand, activating the glutamatergic neurons of the PAG is antinociceptive and inhibiting them is pronociceptive (Samineni et al., 2017). One explanation could be that the OTR-expressing neurons population is a subpopulation of the GABAergic neurons of the vIPAG projecting directly to the RVM. To test this, we could do retrograde tracing in the OTR-Cre rats we used in (Iwasaki et al., 2023) to see whether vIPAG OTR neurons directly project to the RVM.

5.2.2.2 Sexual dimorphism in the vIPAG

We showed that the release of OT in the vIPAG induces an antinociception and mimicking this effect by activating DREADD G_q receptors in OTR-expressing neurons in the vIPAG induces the same type of antinociception in both males and females rats. The vIPAG has been described to be sexually dimorphic. Indeed, there are more vIPAG neurons projecting to the RVM in females than males (Loyd and Murphy, 2006). In addition, in an inflammatory pain model, morphine produces a stronger antinociception in males compared to females (Wang et al., 2006), but not when the females are in diestrus (Loyd et al., 2008). Finally, the application of bicuculline induces a stronger antinociception in males (Moreau and Fields, 1986). These studies suggest that the antinociception mediated by the vIPAG is stronger in males than females. However, we did not observe such a difference between females and males. One could argue that no comparison was done between the sexes, but the effect induced is similar (**Figure 31**).

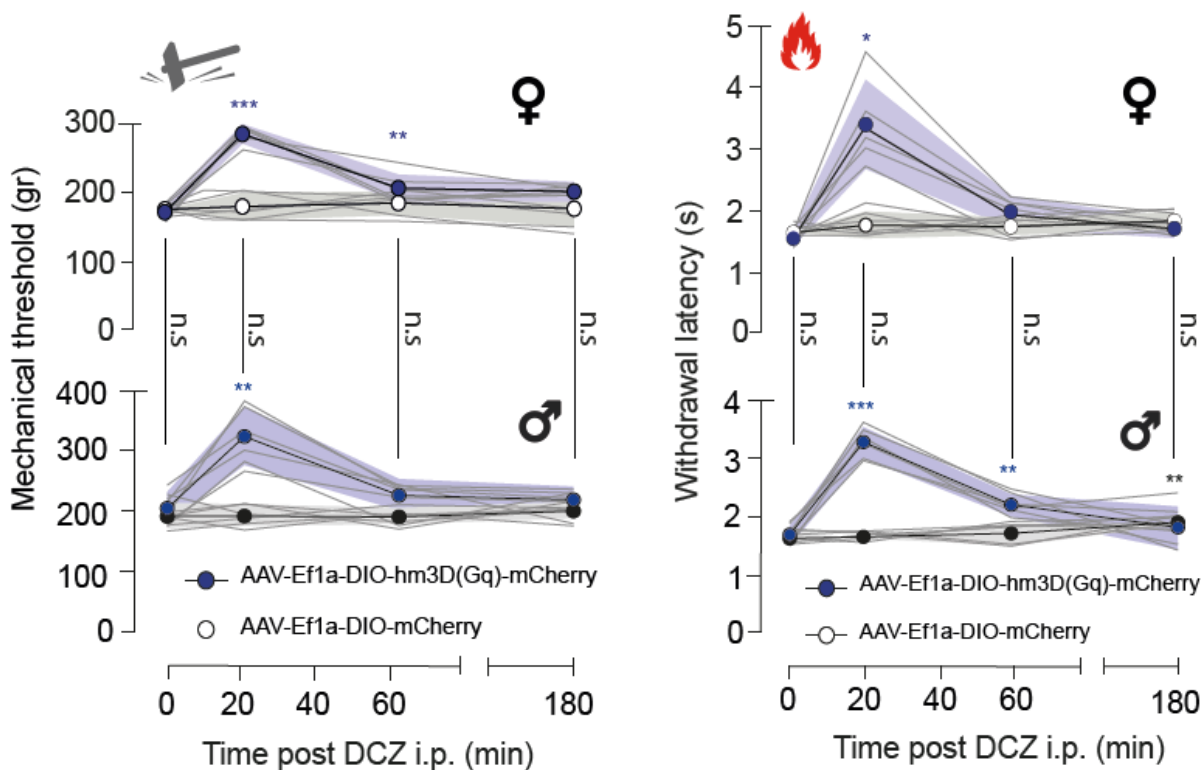


Figure 31 No differences are observed between females and males in the antinociception triggered by the activation of a G_q DREADD in OTR neurons. See [Statistic table](#) for the detailed statistics.

One explanation could come from the fact that the estrous cycle of the female rats was not tested before the behavioural assay. Knowing that the rats in diestrus have similar

antinociception compared with males rats (Loyd et al., 2008) then if the rats were to be synchronized and all in diestrus, it could explain that no differences were seen. Anyway, because estradiol enhances the synthesis of OT (Lee et al., 2009), testing the estrous cycle would have been essential in this study.

Finally, the conclusion of the article is that this antinociception-induced by the OT released in the vIPAG is similar in both males and females. However, the nociceptive assays were done in male only after DREADD G_q receptor activation in OTR-expressing neurons and not after endogenous release of OT. As a result, if we truly wanted to conclude on the release of OT inducing a similar antinociception in both females and males rats, we should have tested both sexes when optogenetically stimulating the OTergic fibres.

5.2.1 Conclusion

Here, I showed that the GrabOT can detect OT and TGOT at equivalent dose and AVP but with higher doses. In addition, atosiban acts as an antagonist and completely block the response to the application of all three molecules at any doses.

I also participated in showing that a population of OTergic neurons of the PVN project to the vIPAG, and I confirmed their OT-releasing ability using the GrabOT. This release triggers the activation of about a quarter of the vIPAG neurons. In the spinal cord, the stimulation of the OTergic fibres in the vIPAG decreases the neuronal plasticity of the wide dynamic range neurons, and it produces a transitory antinociception.

6 Appendix

6.1 Statistic table

Figure	Experiment	Molecule	Parameter analysed	Sample size (n)	Statistical test	Statistical value & p-value	Multiple comparisons (Dunn's multiple comparison in each case)
19	Whole-cell Gad65 neurons BA	A2 (600 nM)	Action potential frequency	n _{mice} = 6 n _{cell} = 16	Friedman test	S = 3.170 p = 0.2050	///
20	Cell-attached SOM neurons BA	A2 (1 μM)	Action potential frequency	n _{mice} = 4 n _{cell} = 19	Friedman test	S = 1.368 p = 0.5045	///
21	Whole-cell BA to CeA neurons	A2 (1 μM)	EPSC frequency	n _{mice} = 3 n _{cell} = 8	RM one-way ANOVA	F = 2.009 p = 0.1813	///
21	Whole-cell BA to CeA neurons	A2 (1 μM)	EPSC amplitude	n _{mice} = 3 n _{cell} = 8	RM one-way ANOVA	F = 2.960 p = 0.1235	///
22	Cell-attached SOM neurons CeL	A2 (1 μM)	Action potential frequency	n _{mice} = 4 n _{cell} = 10	Friedman test	S = 1.867 p = 0.4320	///
23	Whole-cell CeM neurons	A2 (1 μM)	IPSC frequency	n _{mice} = 4 n _{cell} = 15	RM one-way ANOVA	F = 0.6537 p = 0.4739	///
23	Whole-cell CeM neurons	A2 (1 μM)	IPSC amplitude	n _{mice} = 4 n _{cell} = 15	Friedman test	S = 6.400 p = 0.0408	Basal vs ln3: p > 0.9999 Basal vs wash: p = 0.0569
23	Whole-cell CeM neurons	Relaxin-3 (1 μM)	IPSC frequency	n _{mice} = 2 n _{cell} = 6	RM one-way ANOVA	F = 0.2002 p = 0.6945	///
23	Whole-cell CeM neurons	Relaxin-3 (1 μM)	IPSC amplitude	n _{mice} = 2 n _{cell} = 6	Friedman test	S = 1.000 p = 0.7402	///
25	Grab _{OT} OT	OT (50 nM)	AUC	n _{rats} = 1-2 n _{recordings} = 5-6	Kruskal-Wallis test	H = 22.63 p = 0.0004	ACSF vs 50 nM: p = 0.8347 ACSF vs 100 nM: p = 0.3102 ACSF vs 500 nM: p = 0.0010** ACSF vs 1 μM: p = 0.0020** ACSF vs Atosiban: p > 0.9999
25	Grab _{OT} AVP	AVP (50 nM)	AUC	n _{rats} = 1-2 n _{recordings} = 5-6	Kruskal-Wallis test	H = 27.06 p < 0.001	ACSF vs 50 nM: p > 0.9999 ACSF vs 100 nM: p = 0.6283 ACSF vs 500 nM: p = 0.0118* ACSF vs 1 μM: p = 0.0005*** ACSF vs Atosiban: p > 0.9999
25	Grab _{OT} TGOT	TGOT (0.1 nM)	AUC	n _{rats} = 1-3 n _{recordings} = 4-6	Kruskal-Wallis test	H = 46.57 p < 0.001	ACSF vs 0.1 nM: p > 0.9999 ACSF vs 1 nM: p > 0.9999 ACSF vs 10 nM: p > 0.9999 ACSF vs 50 nM: p = 0.8677 ACSF vs 100 nM: p = 0.5087 ACSF vs 250 nM: p = 0.0352* ACSF vs 500 nM: p = 0.0012** ACSF vs 1 μM: p = 0.0009*** ACSF vs Atosiban: p > 0.9999
30	DREADD Gq mechanical nociception	DCZ	Paw withdrawal threshold	n _{females} = 4 n _{males} = 4	2-way ANOVA	P _{interaction} = 0.6796 P _{sex} = 0.0243	0 _{female} vs 0 _{male} : p = 0.0954 20 _{female} vs 20 _{male} : p = 0.3950 60 _{female} vs 60 _{male} : p = 0.5512 180 _{female} vs 180 _{male} : p = 0.4359

	test females vs males						
30	DREADD Gq thermal nociception test females vs males	DCZ	Paw withdrawal threshold	n _{females} = 4 n _{males} = 4	2-way ANOVA	P _{interaction} = 0.5204 P _{sex} = 0.4223	///

Table 6 Statistic table.

6.2 List of publications

(*equal contribution)

Baudon A.*, **Clauss Creusot E.***, Althammer F., Schaaf C.P., Charlet A., 2022. Emerging role of astrocytes in oxytocin-mediated control of neural circuits and brain functions. *Progress in Neurobiology* 217, 102328. doi:10.1016/j.pneurobio.2022.102328

Baudon A.*, **Clauss Creusot E.***, Charlet A., 2022. Rôle émergent des astrocytes dans le contrôle des circuits neuronaux et des fonctions cérébrales modulées par l'ocytocine. *Biologie Aujourd'hui* 216, 155–165. doi:10.1051/jbio/2022022

Baudon A.*, **Clauss-Creusot E.***, Darbon P., Patwell R., Grinevich V., Charlet A., 2022. Calcium imaging and BAPTA loading of amygdala astrocytes in mouse brain slices. *STAR Protocols* 3, 101159. doi:10.1016/j.xpro.2022.101159

Iwasaki M*, Lefevre A*, Althammer F*, **Clauss Creusot E***, Łapieś O, Petitjean H, Hilfiger L, Kerspern D, Melchior M, Küppers S, Krabichler Q, Patwell R, Kania A, Gruber T, Kirchner MK, Wimmer M, Fröhlich H, Dötsch L, Schimmer J, Herpertz SC, Ditzen B, Schaaf CP, Schönig K, Bartsch D, Gugula A, Trenk A, Blasiak A, Stern JE, Darbon P, Grinevich V, Charlet A. An analgesic pathway from parvocellular oxytocin neurons to the periaqueductal gray in rats. *Nat Commun.* 2023 Feb 24;14(1):1066. doi: 10.1038/s41467-023-36641-7

Vivot K., Meszaros G., Pangou E., Zhang Z., Qu M., Erbs E., Yeghiazaryan G., Quiñones M., Grandgirard E., Schneider A., **Clauss--Creusot E.**, Charlet A., Faour M., Martin C., Berditchevski F., Sumara I., Luquet S., Kloppenburg P., Nogueiras R., Ricci R. CaMK1D signalling in AgRP neurons promotes ghrelin-mediated food intake. *Nat Metabo.* 2023 June 05. doi: 10.1038/s42255-023-00814-x

Clauss Creusot E., Darbon P., Charlet A. La grande traversée de l'ocytocine dans le système nerveux pour calmer les douleurs. *Médecine Science. Soumis.*

Baudon A., Althammer F., Grelot V., Wang KY., **Clauss Creusot E.**, Rouach N., Breton R., Darbon P., Charlet A. Astrocytes oxytocin receptor in mice central amygdala mediates behavioral fear adaptation through Gα_i proteins. *En préparation.*

6.3 List of communications

Oral presentations

Modulation by the relaxin3/RXFP3 system of the basal amygdala neuronal network. E. Clauss--Creusot, 1st year Ph.D presentation, INCI, 02 Février 2021.

RXFP3-induced modulation of basal amygdala neuronal network activity. E. Clauss--Creusot, ED Days, 1er Avril 2021.

Relaxin-3 meeting. E. Clauss--Creusot, online, 18 Juin 2021.

Restitution sondage Master. E. Clauss--Creusot, ITI Neurostra, online, 03 Septembre 2022.

GRABing the oxytocin until the pain goes away. E. Clauss--Creusot, Sex differences in pain experiences and management symposium, 24 Octobre 2022.

Grab_{OT}: the first *ex vivo* results. E. Clauss--Creusot, X-Mas Symposium of Oxytocin Friends, 5 Décembre 2022, Mannheim.

Grab_{OT}. E. Clauss--Creusot, Neurotech, 01 Mars 2023.

Survey feedback Ph.D. E. Clauss--Creusot, ITI Neurostra, 19 Avril 2023.

Survey feedback Ph.D pour le LNCA. E. Clauss--Creusot, LNCA, 02 Mai 2023.

Survey feedback Ph.D pour l'INCI. E. Clauss--Creusot, INCI, 05 Mai 2023.

Posters

RXFP3-induced modulation of basal amygdala neuronal network activity. **E. Clauss--Creusot**, A. Baudon, M. Landry, A. Gundlach, P. Darbon, A. Charlet. NeuroFrance, 19-21 mai 2021, forum dématérialisé.

RXFP3-induced modulation of basal amygdala neuronal network activity. **E. Clauss--Creusot**, A. Baudon, M. Landry, A. Gundlach, P. Darbon, A. Charlet. Journée Euridol, 1er Octobre 2021.

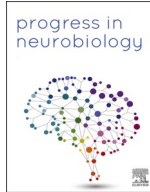
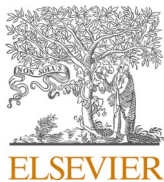
RXFP3-induced (no) modulation of basal amygdala neuronal network activity. **E. Clauss--Creusot**, V. Grelot, M. Landry, P. Darbon, A. Charlet. Federation of European Neuroscience Societies, 09-13 Juillet 2022.

A novel analgesic pathway from parvocellular oxytocin neurons to the periaqueductal gray. **E. Clauss--Creusot**, M. Iwasaki, A. Lefevre, F. Althammer, P. Darbon, V. Grinevich, A. Charlet. Neurofrance 2023, 24-26 Mai 2023.

6.4 Emerging role of astrocytes in oxytocin-mediated control of neural circuits and brain functions

Baudon A.*, **Clauss Creusot E.***, Althammer F., Schaaf C.P., Charlet A., 2022.

Progress in Neurobiology, 217.



Review article

Emerging role of astrocytes in oxytocin-mediated control of neural circuits and brain functions



Angel Baudon^{a,1}, Etienne Clauss Creusot^{a,1}, Ferdinand Althammer^b, Christian P. Schaaf^b, Alexandre Charlet^{a,*}

^a Centre National de la Recherche Scientifique and University of Strasbourg, Institute of Cellular and Integrative Neuroscience, Strasbourg 67000 France

^b Institute of Human Genetics, Heidelberg University, Heidelberg, Germany

ARTICLE INFO

Keywords:

Astrocytes
Oxytocin
Amygdala
Hypothalamus
Neuropeptide

ABSTRACT

The neuropeptide oxytocin has been in the focus of scientists for decades due to its profound and pleiotropic effects on physiology, activity of neuronal circuits and behaviors, among which sociality. Until recently, it was believed that oxytocinergic action exclusively occurs through direct activation of neuronal oxytocin receptors. However, several studies demonstrated the existence and functional relevance of astroglial oxytocin receptors in various brain regions in the mouse and rat brain. Astrocytic signaling and activity is critical for many important physiological processes including metabolism, neurotransmitter clearance from the synaptic cleft and integrated brain functions. While it can be speculated that oxytocinergic action on astrocytes predominantly facilitates neuromodulation via the release of specific gliotransmitters, the precise role of astrocytic oxytocin receptors remains elusive. In this review, we discuss the latest studies on the interaction between the oxytocinergic system and astrocytes, including detailed information about intracellular cascades, and speculate about future research directions on astrocytic oxytocin signaling.

1. Introduction

The hypothalamic neuropeptide oxytocin (OT) has been in the focus of researchers for several decades, ever since it was first described by Sir Henry H. Dale (Dale, 1906). Due to its prosocial and trust-enhancing effects, the popular press even coined the term *love hormone*. In fact, OT is involved in a plethora of social interactions and emotional processes and is pivotal for pair bonding (Young and Wang, 2004) and attachment (Insel and Young, 2001). Current data suggest that OT first emerged around 600 million years ago (Gwee et al., 2009) and evolved with its sister peptide arginine-vasopressin (AVP) from a common ancestor peptide, namely vasotocin (Gwee et al., 2009; Theofanopoulou et al., 2021). Its function is the regulation of osmolarity, one of the crucial homeostasis parameters. It is assumed that over time, the vasotocin gene duplicated and gave rise to two distinct neuropeptides with different properties and physiological functions. While the first evolutionary lineage leads to AVP, which can be found in all vertebrates and is still critical for osmoregulation and control of blood pressure, the alternate path is at the origin of oxytocin-like peptides whose structures

are dependent on the species: Isotocin can be found in fish, mesotocin is present in amphibia and reptiles, and OT is synthesized in all mammals (Gimpl and Fahrenholz, 2001; Jurek and Neumann, 2018; Theofanopoulou et al., 2021). It has been recently proposed to standardize the nomenclature of these two peptides across species to OT for all oxytocin-like peptides and VT for all AVP-like ones (Theofanopoulou et al., 2021).

In mammals, the gene encoding OT (*Oxt*) is transcribed in the hypothalamus, and its mRNA is one of the most prevalent hypothalamic-specific mRNAs (Gautvik et al., 1996; Gimpl and Fahrenholz, 2001). Like many other peptides, OT mRNA is translated into an inactive precursor, which is then cleaved into smaller fragments, ultimately resulting in the active oxytocin peptide. Following synthesis, OT is stored in large dense-core vesicles (Leng and Ludwig, 2008), released via calcium-dependent exocytosis (Leng and Ludwig, 2008; Ludwig and Stern, 2015; Maicas-Royo et al., 2018; Tobin et al., 2012) and acts on the membrane-bound, G-protein-coupled oxytocin receptor (OTR) (Jurek and Neumann, 2018). To date, two distinct intracellular signaling cascades have been identified following OTR activation: $G\alpha_{i/o}$ - and

* Correspondence to: Institute of Cellular and Integrative Neuroscience, INCI CNRS UPR32128, Allée du Général Rouvillois, 67000 Strasbourg, France.

E-mail address: acharlet@unistra.fr (A. Charlet).

¹ Equally contributing authors.

<https://doi.org/10.1016/j.pneurobio.2022.102328>

Received 7 April 2022; Received in revised form 1 July 2022; Accepted 18 July 2022

Available online 21 July 2022

0301-0082/© 2022 The Author(s). Published by Elsevier Ltd. This is an open access article under the CC BY-NC-ND license (<http://creativecommons.org/licenses/by-nc-nd/4.0/>).

$\text{G}\alpha_q$ -dependent pathways (Jurek and Neumann, 2018).

Different modes of OT release in the central nervous system have been described including axonal release (Grinevich et al., 2016; Knebloch et al., 2012), somato-dendritic release (Ludwig and Leng, 2006) and en passant release (Bakos et al., 2018; Fuxe et al., 2012; Ludwig and Leng, 2006). OT is also released into the portal circulation through the neurohypophysis in the posterior pituitary and reaches a variety of peripheral targets via the blood stream. Targeted, local release of OT within different brain regions that express OTR allows the peptide to act both as a neurotransmitter (Althammer et al., 2021; Buijs, 1983; Landgraf and Neumann, 2004; Leng and Ludwig, 2008; Stoop, 2012) and a neuromodulator (Mitre et al., 2018; Owen et al., 2013; Stoop, 2012; Tirko et al., 2018), thus affecting a wide range of behaviors (Froemke and Young, 2021; Grinevich and Neumann, 2020). Past research on OT was solely focused on its direct effects on neural circuits. As a result, the prevailing hypothesis was that OTergic actions are exclusively mediated by neurons and this view has not been challenged until recently (Wahis et al., 2021). Moreover, a growing body of evidence suggests that oxytocin also acts directly on non-neuronal cells (Havranek et al., 2017; Mairesse et al., 2019; Tasker et al., 2012; Wang and Hatton, 2009).

Recent studies suggest that neuronal and glial cells in the brain exist in a 1:1 ratio in the human brain, albeit the individual proportions strongly depend on brain regions and species (von Bartheld et al., 2016). Glial cells are composed of several types including astrocytes, microglia or oligodendrocytes. Per definition, they are non-electrically excitable. Thus, for a long time it was believed that they are merely passive cells and do not actively participate in sensory processing and signal transduction. While, to our knowledge, there is currently no evidence suggesting OTergic action on oligodendrocytes, it has been shown that oxytocin influences microglia activity (Inoue et al., 2019; Panaro et al., 2020), neural progenitor differentiation (Palanisamy et al., 2018) and pituicyte stellation (Rosso et al., 2002). Importantly, evidence has been accumulating to demonstrate an action of oxytocin on astrocytes (Di Scala-Guenot et al., 1994; Panatier et al., 2006; Wahis et al., 2021).

Astrocytes are paramount for brain homeostasis, nutrient supply and metabolism. They account for ~20–40 % of all glial cells, depending on the species and brain region (Augusto-Oliveira et al., 2020). Within the last two decades astrocytes emerged as key players involved in neuromodulation and neuroinflammation both in the healthy and diseased brain. It is particularly intriguing how astrocytes mediate the function of local neurocircuits. Neurons and astrocytes are fundamentally different in their morphology and activity kinetics: neurons have characteristic dendrites and axons allowing the formation of long-range projections, while astrocytes possess a myriad of tiny filaments to infiltrate the local environment and can respond to many signaling cues; neurons have a millisecond-range electrical activity, whereas the duration of astrocytic calcium transients can range from minutes to hours (Bazargani and Attwell, 2016). This drastic temporal dynamic difference between the two cell types could affect the way that different neuromodulators operate within these microcircuits. Thus, it is imperative to understand the interplay of neurons and glial cells in response to neuromodulators to fully decipher their respective role in brain function. In this review, we explore the current literature on the action of OT on astrocytes, and we propose new models that could explain several observed phenomena.

2. Oxytocin effects on astrocytes

2.1. The oxytocin receptor is expressed in astrocytes

In the brain, OT is mainly synthesized in three distinct hypothalamic nuclear formations: the paraventricular nucleus, supraoptic nucleus and scattered accessory nuclei. A feature of OTergic neurons is the somato-dendritic release, which prompted researchers to explore the role of OT in the hypothalamus. In the mid-80 s, it was shown that following high secretion/infusion of OT in this structure, active changes in the morphology of astrocytes occur *in vivo* (Salm et al., 1985; Theodosis

et al., 1986a; Theodosis et al., 1986b). Thus, Di Scala-Guenot and Strosser performed binding studies to investigate whether cultured astrocytes from the hypothalamus express the OTR. Using autoradiography of radioactive ligands, they found that the OTR is distributed all over the soma and processes of cells morphologically similar to those expressing the glial fibrillary acidic protein (GFAP), suggesting their astrocytic identity (Di Scala-Guenot and Strosser, 1992). In addition, using the same methods, OTR have been found in GFAP-expressing cells in primary cultures of spinal astrocytes (Ervard et al., 1997). With the help of *in situ* hybridization or immunolabeling, recent studies detected OTR expression in rodent astrocytes in the supraoptic nucleus of the hypothalamus (Wang and Hatton, 2006), the auditory cortex (Mitre et al., 2016), the central amygdala (Wahis et al., 2021), the ventral striatum (Amato et al., 2022), the hippocampus (Althammer et al., 2022b) and even in the frontal cortex of humans (McKay et al., 2019) (Fig. 1A). Moreover, OTR can be co-immunoprecipitated with GFAP in supraoptic nucleus (SON) lysates, indicating that the receptor is bound to the astrocytic cytoskeleton (Wang et al., 2017). While each of these results suffer from inherent technical limitation, inviting to prudence when interpreting the presented data, OTR seems widely expressed in astrocytes of several brain structures.

In all cases, this evidence does not provide proof of the receptor functionality. It must be noted here that albeit OTR expression in neurons is observed in a myriad of species and brain regions (Gould and Zingg, 2003; Mitre et al., 2016; Newmaster et al., 2020; Young and Song, 2020), these studies did not investigate actual OTR expression levels in neurons on a quantitative, single cell basis. To the best of our knowledge, no studies have been published yet that directly assessed and compared neuronal and astrocytic OTR expression levels. However, a reanalysis of published *in situ* hybridization data for OTR mRNA suggest that astrocytic OTR levels could be 2–3-fold lower in the amygdala (Althammer et al., 2022a; Wahis et al., 2021) and dorsal CA2 region (Althammer et al., 2022b) (Fig. 1B). This constitutes an experimental challenge for scientists willing to study the cell-type specific OTR. Thus, a combination of single cell RNA sequencing or cell-type specific western blots together with precise pharmacological experiments would be needed to unequivocally demonstrate the presence and function of astrocytic OTR. In addition, a new generation novel genetic models could help to provide a deeper insight into cell-type specific OTR expression and function.

2.2. Astrocytic oxytocin receptors are functional

The first indication of a direct action of OT on glial cells dates back to the mid-90 s, when Di Scala-Guenot and colleagues performed calcium imaging on cultured hypothalamic astrocytes. They observed that OT or [Thr^4Gly^7]-oxytocin (TGOT, a selective OTR agonist) application triggers monophasic calcium responses in the majority of recorded astrocytes, but also calcium oscillation in ~15 % of them (Di Scala-Guenot et al., 1994). Such observation done in pure astrocytic culture suggests that astrocyte directly react to oxytocin. However, cultured astrocytes are known to be really different from those found *in situ*, both in term of morphology, protein expression and calcium signaling (Foo et al., 2011; Shigetomi et al., 2010a, 2010b).

More recently, it has been showed that optogenetic photostimulation and subsequent release of OT from axonal terminals within the central amygdala triggers calcium transients in local astrocytes *ex vivo* (Wahis et al., 2021). This strongly suggests that endogenous OT release is sufficient to induce astrocyte calcium signaling. Yet, this effect could result indirectly from the activation of OTR on neighboring neuron terminals/fibers. Using a Cre/Lox approach, we knock out the OTR in GFAP expressing cells and observed a decrease of OTR-induced calcium responses in astrocytes. Despite the potential issue regarding a putative Cre leakage from GFAP positive cells (Hu et al., 2020b; Stifter and Greter, 2020) this experiment corroborates the hypothesis that OT-mediated astrocyte activity might be dependent on astrocytic OTR

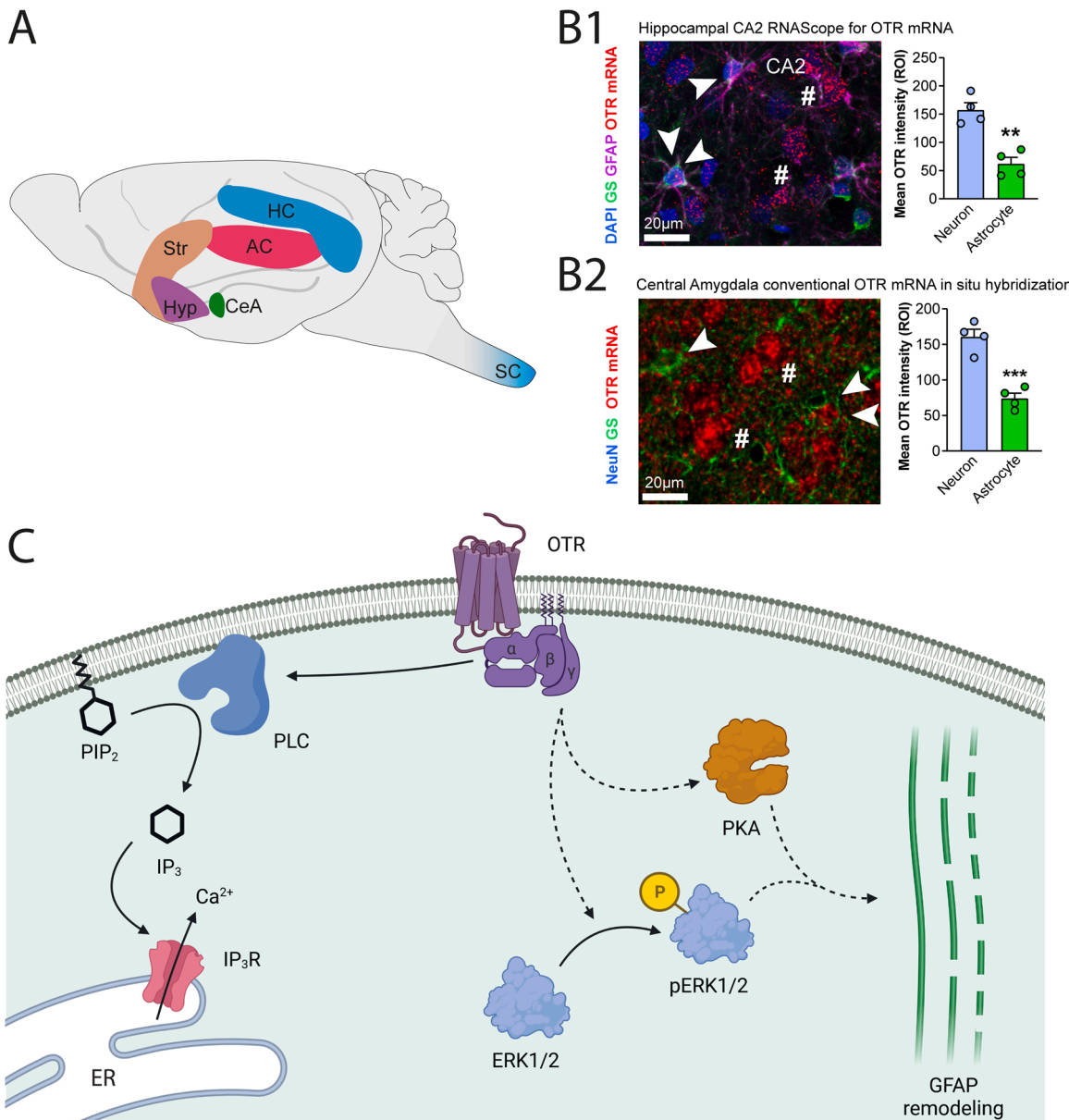


Fig. 1. Astrocytic oxytocin receptor distribution in the brain. A. Known localization of astrocytic oxytocin receptor (OTR) in the rodent brain. Described in situ: Striatum (Str), Hypothalamus (Hyp), Central Amygdala (CeA), Auditory Cortex (AC). Described in culture: Spinal Cord (SC). B1. Combined RNAscope for OTR mRNA and immunohistochemical staining against glutamine synthetase and GFAP in dorsal CA2 of a wistar rat. Single white arrowhead highlights OTR-negative astrocyte, double arrowhead highlights OTR-positive astrocyte and hashtags highlight OTR-positive, GS-negative neurons. Bar graph shows that respective OTR mRNA transcript levels in astrocytes are significantly lower than neuronal OTR mRNA levels ($n = 4$ rats per group, 70–120 cells analyzed per animal, $**p < 0.01$). Recreated from Wahis et al., 2021. B2. Combined approach of conventional in situ hybridization for OTR mRNA and immunohistochemical staining against glutamine synthetase in the central amygdala of a wistar rat. Single white arrowhead highlights OTR-negative astrocyte, double arrowhead highlights OTR-positive astrocyte and hashtags highlight OTR-positive, GS-negative neurons. Bar graph shows that respective OTR mRNA transcript levels in astrocytes are significantly lower than neuronal OTR mRNA levels ($n = 4$ rats per group, 70–120 cells analyzed per animal, $***p < 0.001$). Recreated from Althammer et al. (2022b). C. Intracellular pathways triggered by the activation of astrocytic OTR. Left: activation of the $G_{\alpha}q$ protein triggers the activation of the PLC-IP₃ pathway that results in a calcium release from the endoplasmic reticulum (ER). Right: dissociation of the $\beta\gamma$ complex is suggested to mediate the sequential activation of ERK1/2 and PKA that ultimately results in a reorganization of the GFAP cytoskeleton.

(Wahis et al., 2021). However, even if this GFAP OTR KO model highlights the involvement of OTR in astrocyte activity, it does not rule out a potential participation of a neurotransmitter co-released together with OT from OTergic axon terminals.

Based on these observations, it seems plausible that functional OTR could be expressed in astrocytes in several regions of the central nervous system. To fully understand the precise effect of OT on astrocytes, it is important to have a close look at the intracellular pathway triggered by binding of OT to astrocytic OTR.

2.3. Oxytocin receptor-dependent signaling in astrocytes

The oxytocin receptor (OTR) is a member of the class A G-protein coupled receptors (GPCR) family, composed of seven transmembrane domains. In mammals, the OTR is encoded by a single gene, however, its intracellular coupling is complex. The intracellular loops and the intracellular C-terminal domain link heterotrimeric G protein complexes. Each of them is composed of three subunits: G_{α} , G_{β} , G_{γ} . Upon binding of their ligands, conformational changes of the receptor lead to

the replacement of the guanine diphosphate bound to the G_{α} by a guanine triphosphate. G_{α} then dissociate from the $G_{\beta\gamma}$ complex and act on various enzymes that produce second messengers. Interestingly, the OTR is functionally coupled to G_q and/or $G_{i/o}$ proteins and its activation can produce a calcium surge from intracellular calcium stores (Busnelli and Chini, 2018; Gimpl and Fahrenholz, 2001; Jurek and Neumann, 2018; Phaneuf et al., 1993). Apart from its effect on calcium signaling, the activation of OTR can activate various intracellular pathways second messengers, including cAMP, phospholipase C (PLC) and protein kinase C (PKC) (Chatterjee et al., 2016) (Fig. 1C).

In astrocytes, OT-induced intracellular pathways are currently unclear, with yet few studies raising different hypothesis. Indeed, application of OT or an OTR agonist on astrocyte cell cultures seems to trigger calcium transients via a mechanism that is independent of extracellular calcium influx but depends on endoplasmic reticulum stores (Di Scala-Guenot et al., 1994). These seminal data suggest are in accordance with the recruitment of the classical PLC-dependent G_q pathway in cultured hypothalamic astrocytes.

In addition, OT application on SON slices increased the quantity of phosphorylated extracellular signal-regulated kinase 1/2 (ERK 1/2), strengthening the hypothesis that OTR activation in astrocytes affects the MAPK pathway in astrocytes (Wang and Hatton, 2007). Wang and colleagues further showed that OT decreases the expression of GFAP in SON astrocytes (Wang et al., 2017). This effect seems to be mediated by the $G_{\beta\gamma}$ subunits of the G protein coupled to the OTR, which triggers the sequential activation of ERK1/2 and protein kinase A (PKA) (Wang et al., 2017). It is noteworthy that activation of ERK1/2 and PKA seems to have antagonistic effects on GFAP stability and that the consecutive action of ERK and PKA is needed: PKA initially provokes the breakdown of GFAP filament and then ERK1/2 stabilizes newly synthesized filaments (Wang et al., 2017). Recently, a study in astrocyte-like cells from astrocytoma showed that knockdown of OTR prevented OT-induced phosphorylation of ERK and interfered with the proliferation and anti-oxidant effects of OTR activation (Alanazi et al., 2020), thereby strengthening the idea of an OTR-mediated regulation of the MAPK pathway (Fig. 1C).

As previously mentioned, OTR can also couple $G_{i/o}$ proteins (Busnelli and Chini, 2018; Busnelli et al., 2012; Hoare et al., 1999; Phaneuf et al., 1993; Strakova et al., 1998) but to our knowledge, no evidence has shown that stimulation of astrocytic OTR can trigger the activity of $G_{i/o}$ proteins in astrocytes. It is also possible that the OTR couples different G-protein in the same cell type as shown in neuron-like cells (Gravati et al., 2010). This coupling might also depend on OTR localization in different microdomains of the plasma membrane (Rimoldi et al., 2003).

3. Oxytocin-induced modulation of astrocyte morphology and functions

Knowing that functional OTR are expressed in astrocytes, one can investigate the effect of OTR activation in those cells. Several studies indicate that binding of OT to astrocytic OTR triggers astrocyte calcium transients (Kuo et al., 2009; Wahis et al., 2021; Zatkova et al., 2018). However, the downstream targets and ultimate consequences of astrocytic OTR signaling remain somewhat elusive. In this chapter we summarize the consequences of OTR activation on astrocyte morphology and neuronal network activity.

3.1. Morphological consequences of astrocytic oxytocin receptor activation

Hypothalamic OT neurons release the peptide locally, a phenomenon known as somato-dendritic release (Ludwig and Leng, 2006). This form of peptide release is thought to facilitate a local feedback mechanism, as well as to prime the neuroendocrine cells during challenging physiological situations such as parturition, lactation or other homeostatic challenges (Brown et al., 2013, 2020).

Already in the mid 80's it was reported that these conditions induce a strong OT release and lead to an important decrease in GFAP staining density within SON (Salm et al., 1985; Wang and Hatton, 2009). Furthermore, OT infusion in the SON resulted in an increase of neuronal somata contacts (Langle et al., 2003; Theodosis et al., 1986a, 1986b). This strongly suggests that OT can modify astrocyte morphology. This hypothesis was further confirmed in hypothalamic SON slices. Indeed, under normal conditions, there is almost no neuronal juxtaposition, as astrocytic processes separate them, but OT application triggers the retraction of astrocytic processes, leaving OTergic neurons in close contact. This modification of the astrocytic cytoarchitecture appears to be calcium-dependent (Langle et al., 2003). While authors did not provide an explanation for this interesting observation, it can be speculated that activation of astrocytic OTR alters the astrocytic cytoskeleton by interfering with microtubule/actin dynamics. Indeed, it has been shown that calcium transients in astrocytes can regulate actin-remodeling proteins, such as cofilin. This has been demonstrated in the hippocampus where long term potentiation triggers withdrawal of peridendritic astrocyte processes from potentiated synapses (Henneberger et al., 2020). Interestingly, such OT-mediated reorganization of the actin cytoskeleton has been observed in SON neurons, and probably in nearby astrocytes following OT application (Wang and Hatton, 2007) (Fig. 2).

These morphological changes of hypothalamic astrocytes could potentially have many drastic and long-lasting consequences on the overall network activity. First, astrocytes maintain homeostasis for ions like potassium, which is known to be strongly implicated in neuronal excitability (Verkhratsky and Nedergaard, 2018). Thus, a reduction in astrocytic coverage could lead to important changes of the membrane potential of neighboring neurons. Second, astrocytes are important mediators of neurotransmitter clearance from the synaptic cleft. For example, GLT-1 and GAT transporters are present on the astrocytic processes and facilitate clearing of extracellular glutamate and GABA, respectively. Thus, a reduction in the clearance rate inevitably results in an increased extracellular concentration of neurotransmitters, which ultimately results in an amplification of post-synaptic currents. Moreover, the neurotransmitters can spill over the synaptic cleft and activate presynaptic (e.g. mGluRs) or extrasynaptic (e.g. NMDA) receptors to promote a feedback regulatory effect or to modulate the efficiency/potency of neighboring synapses (Oliet et al., 2008). Third, the retraction of astrocytic processes may declutter the extracellular space, allowing the formation of new synapses, as suggested for the hypothalamus (Hatton et al., 1984) (For a more general review on the effects of astrocytes morphological modification, see Lawal et al., 2022).

In addition, astrocytes are known to release neuroactive molecules described as gliotransmitters. By retracting astrocytic processes, it is plausible that less gliotransmitters reach their receptors expressed by the surrounding neurons, leading to a change in the transmission of information.

3.2. Astrocytic oxytocin receptor functions in gliotransmission

The concept of communication from astrocytes to neurons by the release of gliotransmitters was first introduced in the 90's (Grandes et al., 1991) but the first demonstration of a direct communication between astrocytes and neurons was done by Parpura and colleagues, when they observed that glutamate released from astrocytes caused an increase in calcium activity of nearby neurons (Parpura et al., 1994). Later, adenosine triphosphate (ATP) was also shown to act on neuronal P2X receptors after being released by astrocytes (Zhang et al., 2003). It is important to note, however, that the mechanism underlying gliotransmission is still somewhat controversial (Fiacco and McCarthy, 2018; Sloan and Barres, 2014), albeit the majority of researchers in the field seem to acknowledge its existence (Araque et al., 2014; Savtchouk and Volterra, 2018).

In the SON, Panatier and colleagues showed that astrocytes express the serine racemase, an enzyme that converts L-serine to D-serine and

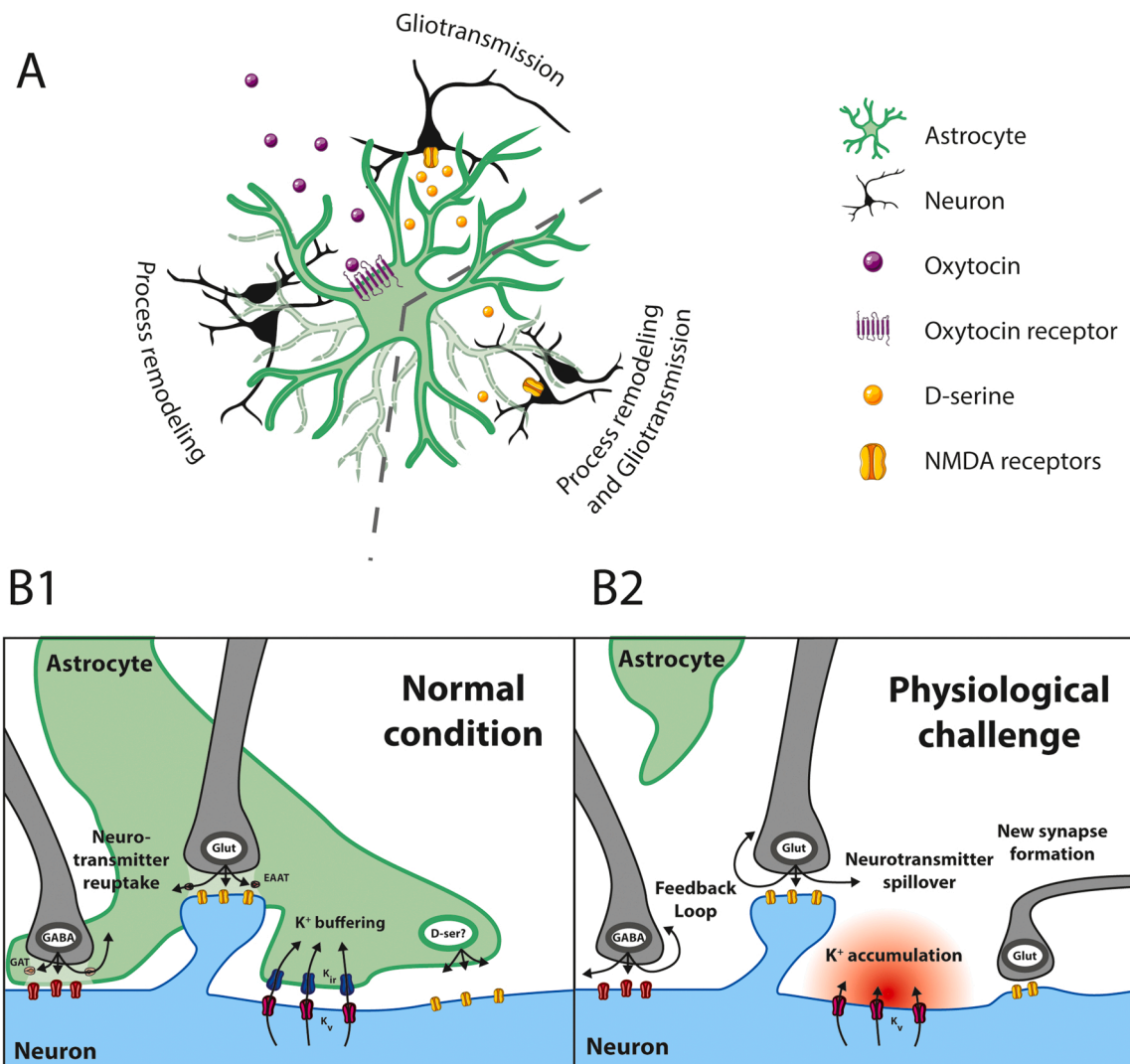


Fig. 2. Effects of OTR activation on astrocytes. **A. Top:** OTR activation modulates astroneuronal communication. This gliotransmission has been seen in the hypothalamus where OT stimulation decreases the amount of available D-serine, and in the central amygdala where the opposite action has been observed. **Bottom left:** astrocytic OTR activation triggers the remodeling of astrocytic processes, as seen by their retraction in the hypothalamus and their length increased in cultured astrocytes. **Bottom right:** suggested hypothesis in which both mechanisms could occur at the same time. For instance, a retraction astrocytic processes could explain the decrease in D-serine availability observed in the hypothalamus. **B.** Proposed astrocyte-neuron interactions under normal conditions (astrocyte process extension, B1) and during physiological challenge (astrocyte process retraction, B2) based on our own experimental data.

that this D-serine is the endogenous ligand of the glycine site on NMDAR in the SON (Panatier et al., 2006). Furthermore, they demonstrated that NMDA currents are strongly impaired in D-amino acid oxidase (DAAO)-treated SON slices, an enzyme that breaks down extracellular D-serine. This impairment is rescued by the acute application of exogenous D-serine. These results suggest that astrocytes synthesize and release D-serine to induce an NMDA-dependent signal. Panatier and colleagues also performed *ex vivo* recordings of NMDA currents in SON neurons from virgin or lactating rats. They showed that in lactating rats, the AMPA/NMDA ratio was similar compared to virgin animal slices treated with DAAO and could also be rescued when applying D-serine. Given that NMDAR activation appeared to be essential for the establishment of long-term potentiation (LTP), they investigated the involvement of this receptor using several LTP protocols in neurons of the SON of virgin or lactating animals. In virgin animals, they observed a normal establishment of LTP compared to lactating rats in which no LTP occurred unless they supplied the slice with D-serine. Hence, it seems that D-serine supply from astrocytes is essential for neuronal plasticity in the SON (Panatier et al., 2006). However, it is noteworthy that the astrocytic

origin of D-serine is still under debate (Coyle et al., 2020; Ivanov and Mothet, 2019; Papouin et al., 2017).

More recently, we studied the implication of astrocytes in the lateral part of the central amygdala (CeL) in the regulation of neuronal activity in response to OT. In this structure, a population of CeL astrocytes seems to express the OTR and its activation triggers an increase in their calcium activity (Wahis et al., 2021). Furthermore, these changes in calcium activity seem to be linked to an increase in the electrical activity of neighboring CeL neurons. This increase is dependent on NMDAR and sensitive to the D-serine degrading enzyme DAAO, suggesting that astrocytes modulate the activity of CeL neurons by releasing D-serine (Fig. 2). At a behavioral level, this neuronal network modulation seems to reduce negative emotional values such as anxiety. This demonstrates that CeA astrocytes are actively involved in the OT-induced modulation of a neuronal network (Wahis et al., 2021).

Another circuit where astrocytes have been involved in the regulation of neuronal circuits can be found in the medial basal hypothalamus (Parent et al., 2008). In this structure, authors found no OTR *in vivo* on GnRH neurons, but on neighboring cells thought to be astrocytes, as

suggested by OTR expression in astrocytes in vitro (Parent et al., 2008). Interestingly, intraperitoneal injection of OT reduced the GnRH interpulse interval known to be involved in sexual maturation. Suggesting that only astrocytes express the OTR in this structure, one can wonder how OT modulates GnRH release in the blood (ie. GnRH neuron activity). Given that OT induce the Prostaglandin E₂ (PGE₂) release (Strakova et al., 1998), they hypothesized that it might mediate the communication between astrocytes and GnRH neurons. Indeed, they found that PGE₂ mimicked the OT effect by decreasing the GnRH interpulse interval. This study suggests that OT acts directly on astrocytes of the medial basal hypothalamus to trigger PGE₂ release, which then acts on GnRH neurons to modulate the pulsatile neuronal secretion of GnRH and, ultimately, the sexual maturation.

Based on these observations, OT-activated astrocytes could communicate with neighboring neurons by releasing several gliotransmitters, such as D-serine or PGE₂.

4. Oxytocin and astrocytes: a glimpse into future research directions

Within the last years, OTergic signaling in astrocytes emerged as an important mechanism involved in the regulation of astrocyte morphology, calcium signaling and even affects physiological regulation and emotional processing. However, several key questions about OTR-expressing astrocytes and their interaction with nearby neural cells remain.

4.1. Can an astrocytic relay explain the pleiotropic effects of oxytocin?

One of the biggest enigmas in OTergic research is that one neuropeptide seems to facilitate a seemingly endless list of behaviors (Froemke and Young, 2021; Jurek and Neumann, 2018; Mitre et al., 2018). To exert these functions, OTergic fibers and OTR are found in various brain regions such as the cortices, amygdala, hippocampus, hypothalamic nuclei, septum and thalamus (Knobloch et al., 2012; Mitre et al., 2016; Zhang et al., 2020). However, astrocytic OTR have been identified in only a few of them (see section *The oxytocin receptor is expressed in astrocytes*). In addition, their functions are even less studied, with evidences of functional OTR existing only in the hypothalamic astrocyte cultures (Di Scula Guenot et al., 1994) and in the amygdala (Wahis et al., 2021) (see section *Astrocytic oxytocin receptors are functional*).

Intriguingly, OT occasionally seems to elicit opposing behaviors depending on the involved brain regions or social context (De Dreu et al., 2011; Jurek and Meyer, 2020; Ma et al., 2015; Neumann and Slattery, 2016). Thus, it is important to note that astrocytes are known to be more than simple relays to neurotransmitters, even reversing the excitation/inhibition polarity of an input. This mechanism, called “incongruent”, has been demonstrated in several models such as the CA3-CA1 synapse where a GABA input is transformed into glutamate release (Caudal et al., 2020). However, if and how astrocytes are involved in the contradictory effects of OT on neural circuits and behavior, is currently unclear.

Furthermore, neuropeptidergic cells co-express and co-release various neurotransmitters (Nusbaum et al., 2001; Svensson et al., 2018; van den Pol, 2012). In hypothalamic OT neurons, several studies showed co-release of both glutamate and OT (Althammer et al., 2021; Eliava et al., 2016; Grinevich and Ludwig, 2021; Hasan et al., 2019; Hrabovszky and Liposits, 2008; van den Pol, 2012). There are several potential cross-talks between the glutamatergic and the oxytocinergic system, which could explain some of the pleiotropic context-, experience- and brain region-dependent effects of OT release (Froemke and Young, 2021; Grinevich and Stoop, 2018; Jurek and Neumann, 2018; Lee et al., 2009; Mitre et al., 2018). For instance, varying degrees of OT and glutamate could be released from the same axonal terminal, and potentially act on different postsynaptic elements, thus providing

fine-tuning of neural circuits. Moreover, OT-induced calcium transients can be blocked with an mGluR1a antagonist and promoted by an agonist (Kuo et al., 2009). This suggests that mGluR1a can form functional heteromers with OTR, thus adding a new level of complexity to the OTR intracellular pathways. However, no physical interaction has been demonstrated to date.

Since OT has been shown to suggestively modulate the activity of TRPV1 channel (Nersesyan et al., 2017), and given that astrocytes also express these channels in various species and brain regions (reviewed in (Kong et al., 2017)) it is also possible that some OT actions on astrocytes may be mediated through these channels. Aside, there is currently no evidence that OT can directly activate TRPV1 channels in astrocytes (Gonzalez-hernandez and Charlet, 2018). Finally, it has recently been shown that OTR can physically heteromerize with the A2A adenosine receptor in the striatum. The functional effect of this association has been tested in striatal gliosomes and it was observed that OT prevents evoked glutamate release only if the A2A is not activated (Amato et al., 2022). In future studies, it will be interesting to evaluate the effect of the concomitant activation of these receptors in a basal condition. Moreover, it has been shown that OTR can heteromerize with D2R in the striatum (Romero-Fernandez 2013). Given the intricate cooperation of the oxytocin and the dopamine systems in social behaviors such as partner preference (Young and Wang, 2004), it can be interesting to assess the presence of such heteromers in astrocytes.

Therefore, the study of astrocytes involvement in OT-induced modulation of brain functions, in all its complexity, might be the key to unravel how OT exert its pleiotropic functions through modulation of numerous brain regions. However, this should be completed by considering the whole brain environment, from physiology to pathology.

4.2. Do astrocytes-mediated oxytocinergic functions vary in a brain region or pathophysiological state manner?

To date, the functions of putatively OT-activated astrocytic have only been studied in exceptional physiological conditions such as lactation and parturition in the SON (Panatier et al., 2006), sexual maturation in the medial basal hypothalamus (Parent et al., 2008) and chronic pain in the CeA (Wahis et al., 2021). However, the default role of OT-activated astrocytic subpopulation also remains unclear. This can be explained by a confounding factor inherent of biological studies. Indeed, it is easier to study mechanisms that involve strong changes in physiological processes rather than small, everyday challenges that slightly modify the activity of neuronal circuits. There might be physiological processes during which OTergic activation of OT-sensitive astrocytes is not critical and where activation of OTR-expressing neurons is sufficient.

One can also imagine that OT can trigger different effects according to the targeted region. For instance, it has been shown in the hypothalamus that OT triggers retraction of astrocytic processes during high-demanding OT situations, which is linked to a reduction in D-serine release by the astrocytes (Panatier et al., 2006). Conversely, OTR activation in the CeL seems to trigger the release of D-serine by the astrocytes (Wahis et al., 2021), suggesting morphological effect different than the retraction observed in the SON. This hypothesis is supported by in vitro assessment of OT action on glial morphology that reveal an unforeseen OT-mediated increase in astrocytes-like U-87 MG cells processes length (Zatkova et al., 2018). Thus, OT effects on astrocyte morphology and functions could be region-dependent.

Therefore, it will not be surprising to discover that OT effects on astrocyte morphology is region- and function-specific, paving the way to a better understanding of the plural OT functions in pathophysiological conditions.

4.3. What are the relative contributions of astrocytes and neurons to OT functions?

Given that OTR has been shown to be expressed in both astrocytes and neurons, it is coherent to interrogate their respective contribution to OT functions. At first sight, one may suggest that OT acts on neuronal OTR to trigger a rapid, short lasting neuromodulation. On the other side, OT action on astrocytes may result in slower and longer mechanisms such as the metabolic regulation, release of lactate or gene regulation.

However, CeA ablation of astrocytic OTR impaired the OT-induced neuromodulation of the local microcircuit (Wahis et al., 2021). This absence of OT-evoked neuromodulation despite the presence of neuronal OTR raises two hypotheses: i) OT only needs to act on astrocytes to exert its neuromodulatory effect, ii) OT needs to activate simultaneously astrocytic and neuronal OTR. In the first scenario, OT initially acts on astrocytes to trigger the release of gliotransmitters which, in turn, increases neuronal excitability. However, this seems less probable since a higher portion of CeA neurons express OTR compared to astrocytes. The alternative scenario involves the concomitant activation of both cell types: OT could act on OTR-expressing neurons to increase membrane potential, thus priming CeA neurons and enabling an astrocyte-driven long-lasting, sustained activation of the neural network. In fact, besides its intracellular calcium releasing action by the G_q-PLC-IP₃R pathway, OT was shown to inhibit Na⁺-activated K⁺ leak channels in the myometrium (Ferreira et al., 2019) and spinal cord (Breton et al., 2009). These mechanisms can keep neurons closer to their firing threshold potential, thus making them more likely to respond to incoming stimuli. At the same time, OT can bind to astrocytic OTR to triggers calcium transients and ultimately, the release of gliotransmitters such as D-serine. Knowing the role of OT signaling in synaptic plasticity (Rajamani et al., 2018) and LTP formation (Lin et al., 2012), it seems plausible that coordinated dual activation of both NMDA and OTR could result in a potentiated neural response.

In addition, OT can act directly on OTR-expressing neurons and indirectly on other neurons. For instance, CeA neurons can be broadly divided into SOM-expressing and PKCδ-expressing neurons (Haubensak et al., 2010; Hunt et al., 2017), which are thought to have antagonistic functions, at least in fear, anxiety (Janak and Tye, 2015) and pain expression (Wilson and Murphy, 2009). Haubensak and colleagues have shown that OTR expressing cells are more likely to be PKCδ, congruently with the fear-OFF function of those cells (Haubensak et al., 2010). In this context, one can imagine that OT directly activates PKCδ-positive neurons and indirectly inhibits PKCδ negative neurons, thus favoring a disinhibition of PKCδ-expressing neurons.

To decide between those hypotheses, it will be interesting to specifically ablate neuronal, but not astrocytic, OTR and to evaluate the effect of OT on those cells.

4.4. Are intracellular pathways recruited downstream of the OTR different between astrocytes and neurons?

As mentioned before, the OTR has the surprising feature to couple both the G_{i/o} and the G_q pathways (Busnelli and Chini, 2018). This point is of crucial importance given that activation of G_q and G_{i/o} proteins have opposite functions on neuronal excitability, with the former favoring neuronal spiking and the latter preventing it. To our knowledge, all published studies investigating the effect of OT on neuronal firing found an activity increase, suggesting no G_{i/o} coupling in neurons (Alberi et al., 1997; Barrett et al., 2021; Crane et al., 2020; Eliava et al., 2016; Hu et al., 2020a; Knobloch et al., 2012; Ryan et al., 2017; Wang and Hatton, 2004, 2007). However, since the recruitment of both pathways in astrocytes was shown, independently of OTR, to trigger calcium transients (Durkee et al., 2019; Mehina et al., 2017), differentiating the pathway recruited cannot be done based on their calcium activity. To overcome this issue, biased agonists have been developed to trigger preferentially the recruitment of G_{i/o} proteins (e.g. Atosiban) or

G_q proteins (e.g. Carbetocin) (Busnelli et al., 2012). It will be interesting for the next studies to investigate the recruitment of one pathway or the other in astrocytes and neurons.

5. Conclusions

Research in the last two decades has shown that astrocytes are much more than passive cells needed for neuronal support. It has become evident that astrocytes play a major role in metabolism, homeostasis, sensory information processing and cognitive functions. Many neuromodulators that influence these functions also modulate astrocytic calcium activity, suggesting that astrocytes may be involved in the regulation of neuronal circuit activity. Among these neuromodulators, OT has been shown to trigger calcium transients in astrocytes, highlighting a way of integrating OTergic information in the central nervous system. The difference in the temporal dynamic between astrocytes and neurons allows for an intricate interplay between the two cell types and could drastically influence the function of neuromodulators.

The finding that OT induces morphological changes in hypothalamic astrocytes and thus directly affects neuronal transmission gives rise to a series of interesting hypotheses. OT could potentially gate a precise and temporally restricted enhancement of neurotransmission in local microcircuits during important physiological situations. Retraction of astrocytic processes does not only make room for more extracellular signaling, but also impedes astrocytic clearing of transmitters via specific transporters. Thus, OTergic priming of astrocytes could potentially have long-lasting effects on neural network activity. This would be in line with the idea that astrocytes can integrate, process and transmit information as part of an astro-neuronal network. Future studies are needed to precisely assess the role of neuronal OTR in these astrocyte-neuron networks. It seems plausible that activation of astrocytes by OT precedes OTR-mediated activation of neurons and that OTergic signaling in neurons enables sustained activity of the astrocyte-neuronal networks. Finally, it remains unknown how OTergic signaling in astrocytes affects various behavioral paradigms and diseases, in which a compromised OT has been identified as an underlying cause such as autism spectrum disorder (Anagnostou et al., 2014; Domes et al., 2013; Ford and Young, 2021; Gordon et al., 2013; Guastella et al., 2010), Prader-Willi syndrome (Swaab, 1997; Swaab et al., 1995; Tauber et al., 2017, 2011) or PTSD (Anagnostou et al., 2014; Domes et al., 2013; Ford and Young, 2021; Frijling, 2017; Frijling et al., 2014; Gordon et al., 2013; Guastella et al., 2010; Meyer-Lindenberg et al., 2011; Olff et al., 2010; Swaab, 1997; Swaab et al., 1995; Tauber et al., 2017).

Acknowledgement

This work was supported by the Centre National de la Recherche Scientifique contract UPR3212, the Université de Strasbourg contract UPR3212, and the Agence Nationale de la Recherche (ANR) Jeune Chercheuse Jeune Chercheur (JCJC) grant n° 19-CE16-0011-0 (to AC), the Graduate School of Pain EURIDOL, ANR-17-EURE-0022 (to AC and ECC), and the Foundation of Prader-Willi Research post-doctoral fellowship (to CPS and FA).

Author contributions

All authors discussed and elaborated the ideas, wrote the first draft and corrected it until the final version was obtained. All authors contributed to the article and approved the submitted version.

References

- Alanazi, M.M., Havranek, T., Bakos, J., Cubeddu, L.X., Castejon, A.M., 2020. Cell proliferation and anti-oxidant effects of oxytocin and oxytocin receptors: role of extracellular signal-regulating kinase in astrocyte-like cells. *Endocr. Regul.* 54, 172–182.

- Alberi, S., Dreifuss, J.J., Raggenbass, M., 1997. The oxytocin-induced inward current in vagal neurons of the rat is mediated by G protein activation but not by an increase in the intracellular calcium concentration. *Eur. J. Neurosci.* 9, 2605–2612.
- Althammer, F., Eliava, M., Grinevich, V., 2021. Central and peripheral release of oxytocin: relevance of neuroendocrine and neurotransmitter actions for physiology and behavior. *Handb. Clin. Neurol.* 180, 25–44.
- Althammer, F., Krause, E.G., de Kloet, A.D., Smith, J., Grinevich, V., Charlet, A., Stern, J.E., 2022a. Identification and three-dimensional reconstruction of oxytocin receptor expressing astrocytes in the rat and mouse brain. *STAR Protoc.* 3, 101160.
- Althammer, F., Roy, R.K., Lefevre, A., Najjar, R.S., Schoenig, K., Bartsch, D., Eliava, M., Feresin, R., Hammock, E.A.D., Murphy, A.Z., Charlet, A., Grinevich, V., Stern, J.E., 2022b. Altered PVN-to-CA2 hippocampal oxytocin pathway and reduced number of oxytocin-receptor expressing astrocytes in heart failure rats. *J. Neuroendocr.*
- Amato, S., Averna, M., Guidolin, D., Pedrazzi, M., Pelassa, S., Capraro, M., Passalacqua, M., Bozzo, M., Gatta, E., Anderlini, D., Maura, G., Agnati, L.F., Cervetto, C., Marcoli, M., 2022. Heterodimer of A2A and oxytocin receptors regulating glutamate release in adult striatal astrocytes. *Int. J. Mol. Sci.* 23.
- Anagnostou, E., Soorya, L., Brian, J., Dupuis, A., Mankad, D., Smile, S., Jacob, S., 2014. Intranasal oxytocin in the treatment of autism spectrum disorders: a review of literature and early safety and efficacy data in youth. *Brain Res.* 1580, 188–198.
- Araque, A., Carmignoto, G., Haydon, P.G., Oliet, S.H., Robitaille, R., Volterra, A., 2014. Gliotransmitters travel in time and space. *Neuron* 81, 728–739.
- Augusto-Oliveira, M., Arrifano, G.P., Takeda, P.Y., Lopes-Araujo, A., Santos-Sacramento, L., Anthony, D.C., Verkhratsky, A., Crespo-Lopez, M.E., 2020. Astroglia-specific contributions to the regulation of synapses, cognition and behaviour. *Neurosci. Biobehav. Rev.* 118, 331–357.
- Bakos, J., Srancikova, A., Havranek, T., Bacova, Z., 2018. Molecular mechanisms of oxytocin signaling at the synaptic connection. *Neural Plast.* 2018, 4864107.
- Barrett, L.R., Nuniez, J., Zhang, X., 2021. Oxytocin activation of paraventricular thalamic neurons promotes feeding motivation to attenuate stress-induced hypophagia. *Neuropsychopharmacology* 46, 1045–1056.
- Bazargani, N., Attwell, D., 2016. Astrocyte calcium signaling: the third wave. *Nat. Neurosci.* 19, 182–189.
- Breton, J.D., Poisbeau, P., Darbon, P., 2009. Antinociceptive action of oxytocin involves inhibition of potassium channel currents in lamina II neurons of the rat spinal cord. *Mol. Pain.* 5, 63.
- Brown, C.H., Bains, J.S., Ludwig, M., Stern, J.E., 2013. Physiological regulation of magnocellular neurosecretory cell activity: integration of intrinsic, local and afferent mechanisms. *J. Neuroendocr.* 25, 678–710.
- Brown, C.H., Ludwig, M., Tasker, J.G., Stern, J.E., 2020. Somato-dendritic vasopressin and oxytocin secretion in endocrine and autonomic regulation. *J. Neuroendocr.* 32, e12856.
- Buijs, R.M., 1983. Vasopressin and oxytocin—their role in neurotransmission. *Pharm. Ther.* 22, 127–141.
- Busnelli, M., Chini, B., 2018. Molecular basis of oxytocin receptor signalling in the brain: what we know and what we need to know. *Curr. Top. Behav. Neurosci.* 35, 3–29.
- Busnelli, M., Sauliere, A., Manning, M., Bouvier, M., Gales, C., Chini, B., 2012. Functional selective oxytocin-derived agonists discriminate between individual G protein family subtypes. *J. Biol. Chem.* 287, 3617–3629.
- Caudal, L.C., Gobbo, D., Scheller, A., Kirchhoff, F., 2020. The paradox of astroglial Ca²⁺) signals at the interface of excitation and inhibition. *Front Cell Neurosci.* 14, 60947.
- Chatterjee, O., Patil, K., Sahu, A., Gopalakrishnan, L., Mol, P., Advani, J., Mukherjee, S., Christopher, R., Prasad, T.S., 2016. An overview of the oxytocin-oxytocin receptor signaling network. *J. Cell Commun. Signal* 10, 355–360.
- Coyle, J.T., Balu, D., Wolosker, H., 2020. D-Serine, the shape-shifting NMDA receptor Co-agonist. *Neurochem Res* 45, 1344–1353.
- Crane, J.W., Holmes, N.M., Fam, J., Westbrook, R.F., Delaney, A.J., 2020. Oxytocin increases inhibitory synaptic transmission and blocks development of long-term potentiation in the lateral amygdala. *J. Neurophysiol.* 123, 587–599.
- Dale, H.H., 1906. On some physiological actions of ergot. *J. Physiol.* 34, 163–206.
- De Dreu, C.K., Greer, L.L., Van Kleef, G.A., Shalvi, S., Handgraaf, M.J., 2011. Oxytocin promotes human ethnocentrism. *Proc. Natl. Acad. Sci. USA* 108, 1262–1266.
- van den Pol, A.N., 2012. Neuropeptide transmission in brain circuits. *Neuron* 76, 98–115.
- Di Scala-Guenot, D., Strosser, M.T., 1992. Oxytocin receptors on cultured astroglial cells. Kinetic and pharmacological characterization of oxytocin-binding sites on intact hypothalamic and hippocampic cells from foetal rat brain. *Biochem J.* 284 (Pt 2), 491–497.
- Di Scala-Guenot, D., Mouginot, D., Strosser, M.T., 1994. Increase of intracellular calcium induced by oxytocin in hypothalamic cultured astrocytes. *Glia* 11 (3), 269–276. https://doi.org/10.1002/glia.440110308_7960031.
- Domes, G., Heinrichs, M., Kumbier, E., Grossmann, A., Hauenstein, K., Herpertz, S.C., 2013. Effects of intranasal oxytocin on the neural basis of face processing in autism spectrum disorder. *Biol. Psychiatry* 74, 164–171.
- Durkee, C.A., Covelo, A., Lines, J., Kofuji, P., Aguilar, J., Araque, A., 2019. Gi/o protein-coupled receptors inhibit neurons but activate astrocytes and stimulate gliotransmission. *Glia* 67, 1076–1093.
- Eliava, M., Melchior, M., Knobloch-Bollmann, H.S., Wahis, J., da Silva Gouveia, M., Tang, Y., Ciobanu, A.C., Triana del Rio, R., Roth, L.C., Althammer, F., Chavant, V., Goumon, Y., Gruber, T., Petit-Demouliere, N., Busnelli, M., Chini, B., Tan, L.L., Mitre, M., Froemke, R.C., Chao, M.V., Giese, G., Sprengel, R., Kuner, R., Poisbeau, P., Seeburg, P.H., Stoop, R., Charlet, A., Grinevich, V., 2016. A new population of parvocellular oxytocin neurons controlling magnocellular neuron activity and inflammatory pain processing. *Neuron* 89, 1291–1304.
- Evrard, M.E., Strosser, M.T., Di Scala-Guenot, D., 1997. Pharmacological characterization of oxytocin-binding sites in rat spinal cord membranes: comparison with embryonic cultured spinal cord neurones and astrocytes. *J. Neuroendocr.* 9, 553–560.
- Ferreira, J.J., Butler, A., Stewart, R., Gonzalez-Cota, A.L., Lybaert, P., Amazu, C., Reinl, E.L., Wakle-Prabagaran, M., Salkoff, L., England, S.K., Santl, C.M., 2019. Oxytocin can regulate myometrial smooth muscle excitability by inhibiting the Na⁺-activated K⁺ channel, Slo2.1. *J. Physiol.* 597, 137–149.
- Fiacco, T.A., McCarthy, K.D., 2018. Multiple lines of evidence indicate that gliotransmission does not occur under physiological conditions. *J. Neurosci.* 38, 3–13.
- Foo, L.C., Allen, N.J., Bushong, E.A., Ventura, P.B., Chung, W.S., Zhou, L., Cahoy, J.D., Daneman, R., Zong, H., Ellisman, M.H., Barres, B.A., 2011. Development of a method for the purification and culture of rodent astrocytes. *Neuron* 71, 799–811.
- Ford, C.L., Young, L.J., 2021. Refining oxytocin therapy for autism: context is key. *Nat. Rev. Neurol.*
- Frijling, J.L., 2017. Preventing PTSD with oxytocin: effects of oxytocin administration on fear neurocircuitry and PTSD symptom development in recently trauma-exposed individuals. *Eur. J. Psychotraumatol* 8, 1302652.
- Frijling, J.L., van Zuiden, M., Koch, S.B., Nawijn, L., Goslings, J.C., Luitse, J.S., Biesheuvel, T.H., Honig, A., Bakker, F.C., Denys, D., Veltman, D.J., Olff, M., 2014. Efficacy of oxytocin administration early after psychotrauma in preventing the development of PTSD: study protocol of a randomized controlled trial. *BMC Psychiatry* 14, 92.
- Froemke, R.C., Young, L.J., 2021. Oxytocin, neural plasticity, and social behavior. *Annu. Rev. Neurosci.* 44, 359–381.
- Fuxe, K., Borroto-Escuela, D.O., Romero-Fernandez, W., Ciruela, F., Manger, P., Leo, G., Diaz-Cabiale, Z., Agnati, L.F., 2012. On the role of volume transmission and receptor-receptor interactions in social behaviour: focus on central catecholamine and oxytocin neurons. *Brain Res* 1476, 119–131.
- Gautvik, K.M., de Lecea, L., Gautvik, V.T., Danielson, P.E., Tranque, P., Dopazo, A., Bloom, F.E., Sutcliffe, J.G., 1996. Overview of the most prevalent hypothalamus-specific mRNAs, as identified by directional tag PCR subtraction. *Proc. Natl. Acad. Sci. USA* 93, 8733–8738.
- Gimpl, G., Fahrenholz, F., 2001. The oxytocin receptor system: structure, function, and regulation. *Physiol. Rev.* 81, 629–683.
- Gonzalez-Hernandez, A., Charlet, A., 2018. Oxytocin, GABA, and TRPV1, the Analgesic Triad? *Front Mol Neurosci* 11 (398). <https://doi.org/10.3389/fnmol.2018.00398>.
- Gordon, I., Vander Wyk, B.C., Bennett, R.H., Cordeaux, C., Lucas, M.V., Eilbott, J.A., Zagoory-Sharon, O., Leckman, J.F., Feldman, R., Pelphrey, K.A., 2013. Oxytocin enhances brain function in children with autism. *Proc. Natl. Acad. Sci. USA* 110, 20953–20958.
- Gould, B.R., Zingg, H.H., 2003. Mapping oxytocin receptor gene expression in the mouse brain and mammary gland using an oxytocin receptor-LacZ reporter mouse. *Neuroscience* 122, 155–167.
- Grandes, P., Kq, K.Q.D., Morino, P., Cuendet, M., Streit, P., 1991. Homocysteate, an excitatory transmitter candidate localized in glia. *Eur. J. Neurosci.* 3, 1370–1373.
- Gravat, M., Busnelli, M., Bulgheroni, E., Reversi, A., Spaiardi, P., Parenti, M., Toselli, M., Chini, B., 2010. Dual modulation of inward rectifier potassium currents in olfactory neuronal cells by promiscuous G protein coupling of the oxytocin receptor. *J. Neurochem.* 114, 1424–1435.
- Grinevich, V., Stoop, R., 2018. Interplay between oxytocin and sensory systems in the orchestration of socio-emotional behaviors. *Neuron* 99, 887–904.
- Grinevich, V., Neumann, I.D., 2020. Brain oxytocin: how puzzle stones from animal studies translate into psychiatry. *Mol. Psychiatry*.
- Grinevich, V., Ludwig, M., 2021. The multiple faces of the oxytocin and vasopressin systems in the brain. *J. Neuroendocr.* 33, e13004.
- Grinevich, V., Knobloch-Bollmann, H.S., Eliava, M., Busnelli, M., Chini, B., 2016. Assembling the puzzle: pathways of oxytocin signaling in the brain. *Biol. Psychiatry* 79, 155–164.
- Guastella, A.J., Einfeld, S.L., Gray, K.M., Rinehart, N.J., Tonge, B.J., Lambert, T.J., Hickie, I.B., 2010. Intranasal oxytocin improves emotion recognition for youth with autism spectrum disorders. *Biol. Psychiatry* 67, 692–694.
- Gwee, P.C., Tay, B.H., Brenner, S., Venkatesh, B., 2009. Characterization of the neurohypophysis hormone gene loci in elephant shark and the Japanese lamprey: origin of the vertebrate neurohypophysis hormone genes. *BMC Evol. Biol.* 9, 47.
- Hasan, M.T., Althammer, F., Silva da Gouveia, M., Goyon, S., Eliava, M., Lefevre, A., Kerspern, D., Schimmer, J., Raftogianni, A., Wahis, J., Knobloch-Bollmann, H.S., Tang, Y., Liu, X., Jain, A., Chavant, V., Goumon, Y., Weislogel, J.M., Hurlemann, R., Herpertz, S.C., Pitzler, C., Darbon, P., Dogbevia, G.K., Bertocchi, I., Larkum, M.E., Sprengel, R., Bading, H., Charlet, A., Grinevich, V., 2019. A fear memory engram and its plasticity in the hypothalamic oxytocin system. *Neuron* 103 (133–146), e138.
- Hatton, G.I., Perlmuter, L.S., Salm, A.K., Tweedle, C.D., 1984. Dynamic neuronal-glia interactions in hypothalamus and pituitary: implications for control of hormone synthesis and release. *Peptides* 5 (Suppl 1), 121–138.
- Haubensak, W., Kunwar, P.S., Cai, H., Ciocchi, S., Wall, N.R., Ponnusamy, R., Biag, J., Dong, H.W., Deisseroth, K., Callaway, E.M., Fanselow, M.S., Luthi, A., Anderson, D.J., 2010. Genetic dissection of an amygdala microcircuit that gates conditioned fear. *Nature* 468, 270–276.
- Havranek, T., Lestanova, Z., Mravec, B., Strbak, V., Bakos, J., Bacova, Z., 2017. Oxytocin modulates expression of neuron and glial markers in the rat hippocampus. *Folia Biol. (Praha)* 63, 91–97.
- Henneberger, C., Bard, L., Panatier, A., Reynolds, J.P., Kopach, O., Medvedev, N.I., Minge, D., Herde, M.K., Anders, S., Kraev, I., Heller, J.P., Rama, S., Zheng, K., Jensen, T.P., Sanchez-Romero, I., Jackson, C.J., Janovjak, H., Ottersen, O.P.,

- Nagelhus, E.A., Oliet, S.H.R., Stewart, M.G., Nagerl, U.V., Rusakov, D.A., 2020. LTP induction boosts glutamate spillover by driving withdrawal of perisynaptic astroglia. *Neuron* 108 (919–936), e911.
- Hoare, S., Copland, J.A., Strakova, Z., Ives, K., Jeng, Y.J., Hellmich, M.R., Soloff, M.S., 1999. The proximal portion of the COOH terminus of the oxytocin receptor is required for coupling to g(q), but not g(i). Independent mechanisms for elevating intracellular calcium concentrations from intracellular stores. *J. Biol. Chem.* 274, 28682–28689.
- Hrabovszky, E., Liposits, Z., 2008. Novel aspects of glutamatergic signalling in the neuroendocrine system. *J. Neuroendocrin.* 20, 743–751.
- Hu, B., Boyle, C.A., Lei, S., 2020a. Oxytocin receptors excite lateral nucleus of central amygdala by phospholipase Cbeta- and protein kinase C-dependent depression of inwardly rectifying K(+) channels. *J. Physiol.* 598, 3501–3520.
- Hu, N.Y., Chen, Y.T., Wang, Q., Jie, W., Liu, Y.S., You, Q.L., Li, Z.L., Li, X.W., Reibel, S., Priefer, F.W., Yang, J.M., Gao, T.M., 2020b. Expression patterns of inducible cre recombinase driven by differential astrocyte-specific promoters in transgenic mouse lines. *Neurosci. Bull.* 36, 530–544.
- Hunt, S., Sun, Y., Kucukdereli, H., Klein, R., Sah, P., 2017. Intrinsic circuits in the lateral central amygdala. *eNeuro* 4.
- Inoue, T., Yamakage, H., Tanaka, M., Kusakabe, T., Shimatsu, A., Satoh-Asahara, N., 2019. Oxytocin Suppresses inflammatory responses induced by lipopolysaccharide through inhibition of the eIF2-ATF4 pathway in mouse microglia. *Cells* 8.
- Insel, T.R., Young, L.J., 2001. The neurobiology of attachment. *Nat. Rev. Neurosci.* 2, 129–136.
- Ivanov, A.D., Mothet, J.P., 2019. The plastic d-serine signaling pathway: sliding from neurons to glia and vice-versa. *Neurosci. Lett.* 689, 21–25.
- Janak, P.H., Tye, K.M., 2015. From circuits to behaviour in the amygdala. *Nature* 517, 284–292.
- Jurek, B., Neumann, I.D., 2018. The oxytocin receptor: from intracellular signaling to behavior. *Physiol. Rev.* 98, 1805–1908.
- Jurek, B., Meyer, M., 2020. Anxiolytic and anxiogenic? how the transcription factor MEF2 might explain the manifold behavioral effects of oxytocin. *Front Endocrinol. (Lausanne)* 11, 186.
- Knobloch, H.S., Charlet, A., Hoffmann, L.C., Eliava, M., Khrulev, S., Cetin, A.H., Osten, P., Schwarz, M.K., Seeburg, P.H., Stoop, R., Grinevich, V., 2012. Evoked axonal oxytocin release in the central amygdala attenuates fear response. *Neuron* 73, 553–566.
- Kong, W.L., Peng, Y.Y., Peng, B.W., 2017. Modulation of neuroinflammation: Role and therapeutic potential of TRPV1 in the neuro-immune axis. *Brain Behav. Immun.* 64, 354–366.
- Kuo, J., Hariri, O.R., Micevych, P., 2009. An interaction of oxytocin receptors with metabotropic glutamate receptors in hypothalamic astrocytes. *J. Neuroendocrin.* 21, 1001–1006.
- Landgraf, R., Neumann, I.D., 2004. Vasopressin and oxytocin release within the brain: a dynamic concept of multiple and variable modes of neuropeptide communication. *Front Neuroendocrin.* 25, 150–176.
- Langle, S.L., Poulain, D.A., Theodosis, D.T., 2003. Induction of rapid, activity-dependent neuronal-glial remodelling in the adult rat hypothalamus in vitro. *Eur. J. Neurosci.* 18, 206–214.
- Lawal, O., Ulloa Severino, F.P., Eroglu, C., 2022. The role of astrocyte structural plasticity in regulating neural circuit function and behavior. *Glia* 70 (8), 1467–1483. <https://doi.org/10.1002/glia.24191>.
- Lee, H.J., Macbeth, A.H., Pagani, J.H., Young 3rd, W.S., 2009. Oxytocin: the great facilitator of life. *Prog. Neurobiol.* 88, 127–151.
- Leng, G., Ludwig, M., 2008. Neurotransmitters and peptides: whispered secrets and public announcements. *J. Physiol.* 586, 5625–5632.
- Lin, Y.T., Huang, C.C., Hsu, K.S., 2012. Oxytocin promotes long-term potentiation by enhancing epidermal growth factor receptor-mediated local translation of protein kinase Mzeta. *J. Neurosci.* 32, 15476–15488.
- Ludwig, M., Leng, G., 2006. Dendritic peptide release and peptide-dependent behaviours. *Nat. Rev. Neurosci.* 7, 126–136.
- Ludwig, M., Stern, J., 2015. Multiple signalling modalities mediated by dendritic exocytosis of oxytocin and vasopressin. *Philos. Trans. R. Soc. Lond. B Biol. Sci.* 370.
- Ma, Y., Liu, Y., Rand, D.G., Heatherton, T.F., Han, S., 2015. Opposing oxytocin effects on intergroup cooperative behavior in intuitive and reflective minds. *Neuropsychopharmacology* 40, 2379–2387.
- Maicas-Royo, J., Leng, G., MacGregor, D.J., 2018. A predictive, quantitative model of spiking activity and stimulus-secretion coupling in oxytocin neurons. *Endocrinology*.
- Mairesse, J., Zinni, M., Pansiot, J., Hassan-Abdi, R., Demene, C., Colella, M., Charraut-Marlangue, C., Rideau Batista Novais, A., Tanter, M., Maccari, S., Gressens, P., Vaiman, D., Soussi-Yanicostas, N., Baud, O., 2019. Oxytocin receptor agonist reduces perinatal brain damage by targeting microglia. *Glia* 67, 345–359.
- McKay, E.C., Beck, J.S., Khoo, S.K., Dykema, K.J., Cottingham, S.L., Winn, M.E., Paulson, H.L., Lieberman, A.P., Counts, S.E., 2019. Peri-infarct upregulation of the oxytocin receptor in vascular dementia. *J. Neuropathol. Exp. Neurol.* 78, 436–452.
- Mehina, E.M.F., Murphy-Royal, C., Gordon, G.R., 2017. Steady-State Free Ca(2+) in astrocytes is decreased by experience and impacts arteriole tone. *J. Neurosci.* 37, 8150–8165.
- Meyer-Lindenberg, A., Domes, G., Kirsch, P., Heinrichs, M., 2011. Oxytocin and vasopressin in the human brain: social neuropeptides for translational medicine. *Nat. Rev. Neurosci.* 12, 524–538.
- Mitre, M., Minder, J., Morina, E.X., Chao, M.V., Froemke, R.C., 2018. Oxytocin modulation of neural circuits. *Curr. Top. Behav. Neurosci.* 35, 31–53.
- Mitre, M., Marlin, B.J., Schiavo, J.K., Morina, E., Norden, S.E., Hackett, T.A., Aoki, C.J., Chao, M.V., Froemke, R.C., 2016. A distributed network for social cognition enriched for oxytocin receptors. *J. Neurosci.* 36, 2517–2535.
- Nersesyan, Y., Demirkhanian, L., Cabezas-Bratesco, D., Oakes, V., Kusuda, R., Dawson, T., Sun, X., Cao, C., Cohen, A.M., Chelluboina, B., Veeravalli, K.K., Zimmermann, K., Domene, C., Brauchi, S., Zakharian, E., 2017. Oxytocin modulates nociception as an agonist of pain-sensing TRPV1. *Cell Rep.* 21, 1681–1691.
- Neumann, I.D., Slattery, D.A., 2016. Oxytocin in general anxiety and social fear: a translational approach. *Biol. Psychiatry* 79, 213–221.
- Newmaster, K.T., Nolan, Z.T., Chon, U., Vanselow, D.J., Weit, A.R., Tabbaa, M., Hidema, S., Nishimori, K., Hammock, E.A.D., Kim, Y., 2020. Quantitative cellular-resolution map of the oxytocin receptor in postnatally developing mouse brains. *Nat. Commun.* 11, 1885.
- Nusbaum, M.P., Blitz, D.M., Swensen, A.M., Wood, D., Marder, E., 2001. The roles of co-transmission in neural network modulation. *Trends Neurosci.* 24, 146–154.
- Olff, M., Langeland, W., Witteveen, A., Denys, D., 2010. A psychobiological rationale for oxytocin in the treatment of posttraumatic stress disorder. *CNS Spectr.* 15, 522–530.
- Oliet, S.H., Panatier, A., Piet, R., Mohtet, J.P., Poulain, D.A., Theodosis, D.T., 2008. Neuron-glia interactions in the rat supraoptic nucleus. *Prog. Brain Res.* 170, 109–117.
- Owen, S.F., Tuncdemir, S.N., Bader, P.L., Tirko, N.N., Fishell, G., Tsien, R.W., 2013. Oxytocin enhances hippocampal spike transmission by modulating fast-spiking interneurons. *Nature* 500, 458–462.
- Palanisamy, A., Kannapan, R., Xu, Z., Martino, A., Friese, M.B., Boyd, J.D., Crosby, G., Culley, D.J., 2018. Oxytocin alters cell fate selection of rat neural progenitor cells in vitro. *PLoS One* 13, e0191160.
- Panaro, M.A., Benameur, T., Porro, C., 2020. Hypothalamic neuropeptide brain protection: focus on oxytocin. *J. Clin. Med.* 9.
- Panatier, A., Gentles, S.J., Bourque, C.W., Oliet, S.H., 2006. Activity-dependent synaptic plasticity in the supraoptic nucleus of the rat hypothalamus. *J. Physiol.* 573, 711–721.
- Papouin, T., Henneberger, C., Rusakov, D.A., Oliet, S.H.R., 2017. Astroglial versus neuronal D-serine: fact checking. *Trends Neurosci.* 40, 517–520.
- Parent, A.S., Rasier, G., Matagne, V., Lomniczi, A., Lebrethon, M.C., Gerard, A., Ojeda, S.R., Bourguignon, J.P., 2008. Oxytocin facilitates female sexual maturation through a glia-to-neuron signaling pathway. *Endocrinology* 149, 1358–1365.
- Parpura, V., Basarsky, T.A., Liu, F., Jeftinija, K., Jeftinija, S., Haydon, P.G., 1994. Glutamate-mediated astrocyte-neuron signalling. *Nature* 369, 744–747.
- Phaneuf, S., Europe-Finner, G.N., Varney, M., MacKenzie, I.Z., Watson, S.P., Lopez Bernal, A., 1993. Oxytocin-stimulated phosphoinositide hydrolysis in human myometrial cells: involvement of pertussis toxin-sensitive and -insensitive G-proteins. *J. Endocrinol.* 136, 497–509.
- Rajamani, K.T., Wagner, S., Grinevich, V., Harony-Nicolas, H., 2018. Oxytocin as a modulator of synaptic plasticity: implications for neurodevelopmental disorders. *Front Synaptic Neurosci.* 10, 17.
- Rimoldi, V., Reversi, A., Taverna, E., Rosa, P., Francolini, M., Cassoni, P., Parenti, M., Chini, B., 2003. Oxytocin receptor elicits different EGFR/MAPK activation patterns depending on its localization in caveolin-1 enriched domains. *Oncogene* 22, 6054–6060.
- Romero-Fernandez, W., Borroto-Escuela, D.O., Agnati, L.F., Fuxe, K., 2013. Evidence for the existence of dopamine D2-oxytocin receptor heteromers in the ventral and dorsal striatum with facilitatory receptor-receptor interactions. *Mol Psychiatry* 18 (8), 849–850. <https://doi.org/10.1038/mp.2012.103>.
- Rosso, L., Peteri-Brunback, B., Vuoret-Craviari, V., Deroanne, C., Van Obberghen-Schilling, E., Mienville, J.M., 2002. Vasopressin and oxytocin reverse adenosine-induced pituicyte stellation via calcium-dependent activation of Cdc42. *Eur. J. Neurosci.* 16, 2324–2332.
- Ryan, P.J., Ross, S.I., Campos, C.A., Derkach, V.A., Palmiter, R.D., 2017. Oxytocin-receptor-expressing neurons in the parabrachial nucleus regulate fluid intake. *Nat. Neurosci.* 20, 1722–1733.
- Salm, A.K., Smithson, K.G., Hatton, G.I., 1985. Lactation-associated redistribution of the glial fibrillary acidic protein within the supraoptic nucleus. *Immunocytochemical Study Cell Tissue Res.* 242, 9–15.
- Savtchouk, I., Volterra, A., 2018. Gliotransmission: beyond black-and-white. *J. Neurosci.* 38, 14–25.
- Shigetomi, E., Kracun, S., Khakh, B.S., 2010a. Monitoring astrocyte calcium microdomains with improved membrane targeted GCaMP reporters. *Neuron Glia Biol.* 6, 183–191.
- Shigetomi, E., Kracun, S., Sofroniew, M.V., Khakh, B.S., 2010b. A genetically targeted optical sensor to monitor calcium signals in astrocyte processes. *Nat. Neurosci.* 13, 759–766.
- Sloan, S.A., Barres, B.A., 2014. Looks can be deceiving: reconsidering the evidence for gliotransmission. *Neuron* 84, 1112–1115.
- Stifter, S.A., Greter, M., 2020. STOP floxing around: specificity and leakiness of inducible Cre/loxP systems. *Eur. J. Immunol.* 50, 338–341.
- Stoop, R., 2012. Neuromodulation by oxytocin and vasopressin. *Neuron* 76, 142–159.
- Strakova, Z., Copland, J.A., Lolait, S.J., Soloff, M.S., 1998. ERK2 mediates oxytocin-stimulated PGE2 synthesis. *Am. J. Physiol.* 274, E634–E641.
- Svensson, E., Apergis-Schoule, J., Burnstock, G., Nusbaum, M.P., Parker, D., Schiott, H.B., 2018. General principles of neuronal co-transmission: insights from multiple model systems. *Front Neural Circuits* 12, 117.
- Swaab, D.F., 1997. Prader-Willi syndrome and the hypothalamus. *Acta Paediatr. Suppl.* 423, 50–54.
- Swaab, D.F., Purba, J.S., Hofman, M.A., 1995. Alterations in the hypothalamic paraventricular nucleus and its oxytocin neurons (putative satiety cells) in Prader-Willi syndrome: a study of five cases. *J. Clin. Endocrinol. Metab.* 80, 573–579.
- Tasker, J.G., Oliet, S.H., Bains, J.S., Brown, C.H., Stern, J.E., 2012. Glial regulation of neuronal function: from synapse to systems physiology. *J. Neuroendocrin.* 24, 566–576.

- Tauber, M., Mantoulan, C., Copet, P., Jauregui, J., Demeer, G., Diene, G., Roge, B., Laurier, V., Ehlinger, V., Arnaud, C., Molinas, C., Thuilleaux, D., 2011. Oxytocin may be useful to increase trust in others and decrease disruptive behaviours in patients with Prader-Willi syndrome: a randomised placebo-controlled trial in 24 patients. *Orphanet J. Rare Dis.* 6, 47.
- Tauber, M., Boulanger, K., Diene, G., Cabal-Berthoumieu, S., Ehlinger, V., Fichaux-Bourin, P., Molinas, C., Faye, S., Valette, M., Pourriat, J., Cessans, C., Vieux-Sauvelon, S., Bascul, C., Guedeney, A., Delhanty, P., Geenen, V., Martens, H., Muscatelli, F., Cohen, D., Consoli, A., Payoux, P., Arnaud, C., Salles, J.P., 2017. The use of oxytocin to improve feeding and social skills in infants with prader-willi syndrome. *Pediatrics* 139.
- Theodosis, D.T., Chapman, D.B., Montagnese, C., Poulain, D.A., Morris, J.F., 1986a. Structural plasticity in the hypothalamic supraoptic nucleus at lactation affects oxytocin-, but not vasopressin-secreting neurones. *Neuroscience* 17, 661–678.
- Theodosis, D.T., Montagnese, C., Rodriguez, F., Vincent, J.D., Poulain, D.A., 1986b. Oxytocin induces morphological plasticity in the adult hypothalamo-neurohypophyseal system. *Nature* 322, 738–740.
- Theofanopoulou, C., Gedman, G., Cahill, J.A., Boeckx, C., Jarvis, E.D., 2021. Universal nomenclature for oxytocin-vasotocin ligand and receptor families. *Nature* 592, 747–755.
- Tirko, N.N., Eyring, K.W., Carcea, I., Mitre, M., Chao, M.V., Froemke, R.C., Tsien, R.W., 2018. Oxytocin transforms firing mode of CA2 hippocampal. *Neurons Neuron* 100 (593–608), e593.
- Tobin, V., Leng, G., Ludwig, M., 2012. The involvement of actin, calcium channels and exocytosis proteins in somato-dendritic oxytocin and vasopressin release. *Front Physiol.* 3, 261.
- Verkhratsky, A., Nedergaard, M., 2018. Physiology of astroglia. *Physiol. Rev.* 98, 239–389.
- von Bartheld, C.S., Bahney, J., Herculano-Houzel, S., 2016. The search for true numbers of neurons and glial cells in the human brain: A review of 150 years of cell counting. *J. Comp. Neurol.* 524, 3865–3895.
- Wahis, J., Baudon, A., Althammer, F., Kersperrn, D., Goyon, S., Hagiwara, D., Lefevre, A., Bartczko, L., Boury-Jamot, B., Bellanger, B., Abatis, M., Da Silva Gouveia, M., Benusiglio, D., Eliava, M., Rozov, A., Weinsanto, I., Knobloch-Bollmann, H.S., Kirchner, M.K., Roy, R.K., Wang, H., Pertin, M., Inquimbert, P., Pitzer, C., Siemens, J., Goumon, Y., Bouthrel, B., Lamy, C.M., Decosterd, I., Chatton, J.Y., Rouach, N., Young, W.S., Stern, J.E., Poisbeau, P., Stoop, R., Darbon, P., Grinevich, V., Charlet, A., 2021. Astrocytes mediate the effect of oxytocin in the central amygdala on neuronal activity and affective states in rodents. *Nat. Neurosci.* Wang, P., Qin, D., Wang, Y.F., 2017. Oxytocin rapidly changes astrocytic GFAP plasticity by differentially modulating the expressions of pERK 1/2 and protein kinase A. *Front Mol. Neurosci.* 10, 262.
- Wang, Y.F., Hatton, G.I., 2004. Milk ejection burst-like electrical activity evoked in supraoptic oxytocin neurons in slices from lactating rats. *J. Neurophysiol.* 91, 2312–2321.
- Wang, Y.F., Hatton, G.I., 2006. Mechanisms underlying oxytocin-induced excitation of supraoptic neurons: prostaglandin mediation of actin polymerization. *J. Neurophysiol.* 95, 3933–3947.
- Wang, Y.F., Hatton, G.I., 2007. Interaction of extracellular signal-regulated protein kinase 1/2 with actin cytoskeleton in supraoptic oxytocin neurons and astrocytes: role in burst firing. *J. Neurosci.* 27, 13822–13834.
- Wang, Y.F., Hatton, G.I., 2009. Astrocytic plasticity and patterned oxytocin neuronal activity: dynamic interactions. *J. Neurosci.* 29, 1743–1754.
- Wilson, Y.M., Murphy, M., 2009. A discrete population of neurons in the lateral amygdala is specifically activated by contextual fear conditioning. *Learn Mem.* 16, 357–361.
- Young, L.J., Wang, Z., 2004. The neurobiology of pair bonding. *Nat. Neurosci.* 7, 1048–1054.
- Young, W.S., Song, J., 2020. Characterization of oxytocin receptor expression within various neuronal populations of the mouse dorsal hippocampus. *Front Mol. Neurosci.* 13, 40.
- Zatkova, M., Bacova, Z., Puerta, F., Lestanova, Z., Alanazi, M., Kiss, A., Reichova, A., Castejon, A.M., Ostatnikova, D., Bakos, J., 2018. Projection length stimulated by oxytocin is modulated by the inhibition of calcium signaling in U-87MG cells. *J. Neural Transm. (Vienna)* 125, 1847–1856.
- Zhang, B., Qiu, L., Xiao, W., Ni, H., Chen, L., Wang, F., Mai, W., Wu, J., Bao, A., Hu, H., Gong, H., Duan, S., Li, A., Gao, Z., 2020. Reconstruction of the hypothalamo-neurohypophyseal system and functional dissection of magnocellular oxytocin neurons in the brain. *Neuron*.
- Zhang, J.M., Wang, H.K., Ye, C.Q., Ge, W., Chen, Y., Jiang, Z.L., Wu, C.P., Poo, M.M., Duan, S., 2003. ATP released by astrocytes mediates glutamatergic activity-dependent heterosynaptic suppression. *Neuron* 40, 971–982.

6.1 Rôle émergent des astrocytes dans le contrôle des circuits neuronaux et des fonctions cérébrales modulées par l'ocytocine.

Baudon A.* , **Clauss Creusot E.***, Charlet A., 2022.

Biologie Aujourd'hui 216.

ARTICLE

Rôle émergent des astrocytes dans le contrôle des circuits neuronaux et des fonctions cérébrales modulés par l’ocytocine

Angel Baudon [#], Etienne Clauss Creusot [#], et Alexandre Charlet ^{*} 

Centre National de la Recherche Scientifique et Université de Strasbourg, Institut des Neurosciences Cellulaires et Intégratives, 8 allée du Général Rouvillois, 67000 Strasbourg, France

Reçu le 22 septembre 2022

Résumé - L’ocytocine est un neuropeptide au centre de l’attention des scientifiques depuis des décennies, en raison de ses effets puissants et pléiotropes tant sur le plan physiologique que sur l’activité des circuits neuronaux, modulant ainsi nos comportements. Jusqu’à une date récente, on pensait que l’action de l’ocytocine était induite exclusivement par l’activation directe de ses récepteurs neuronaux. Cependant, plusieurs études ont démontré l’existence et la pertinence fonctionnelle des récepteurs astrogiaux de l’ocytocine dans diverses régions du cerveau de la souris et du rat. La signalisation et l’activité astrocytaires sont essentielles à de nombreux processus physiologiques importants, notamment le métabolisme, l’élimination des neurotransmetteurs de la fente synaptique et les fonctions cérébrales intégrées. Bien que l’on puisse supposer que l’action de l’ocytocine sur les astrocytes facilite principalement la neuromodulation *via* la libération de gliotransmetteurs, le rôle précis des récepteurs astrocytaires de l’ocytocine reste difficile à cerner. Dans cette revue, nous discutons des dernières études sur l’interaction entre le système oxytocinergique et les astrocytes, et décrivons les cascades intracellulaires mises en jeu.

Mots clés : oxytocine, astrocytes, amygdale, hypothalamus

Abstract – Emergent role of astrocytes in oxytocin-mediated modulatory control of neuronal circuits and brain functions. The neuropeptide oxytocin has been in the focus of scientists for decades due to its profound and pleiotropic effects on physiology, activity of neuronal circuits and behaviors. Until recently, it was believed that oxytocinergic action exclusively occurs through direct activation of neuronal oxytocin receptors. However, several studies demonstrated the existence and functional relevance of astrogial oxytocin receptors in various brain regions in the mouse and rat brain. Astrocytic signaling and activity are critical for many important physiological processes including metabolism, neurotransmitter clearance from the synaptic cleft and integrated brain functions. While it can be speculated that oxytocinergic action on astrocytes predominantly facilitates neuromodulation *via* the release of gliotransmitters, the precise role of astrocytic oxytocin receptors remains elusive. In this review, we discuss the latest studies on the interaction between the oxytocinergic system and astrocytes, and give details of underlying intracellular cascades.

Keywords: oxytocin, astrocytes, amygdala, hypothalamus

Abréviations

AMPAR	Récepteur de l’acide α -amino-3-hydroxy-5-méthyl-4-isoxazolepropionique
AMPc	Adénosine monophosphate cyclique
ATP	Adénosine triphosphate
AVP	Arginine-vasopressine

CeL	Amygdale centrale latérale
DAAO	D-aminoacide-oxydase
ERK 1/2	Kinases 1/2 régulées par les signaux extracellulaires
GAT	Transporteur du GABA (acide γ -aminobutyrique)
GFAP	Protéine acide fibrillaire gliale
GLT-1	Transporteur 1 du glutamate
GnRH	Hormone de libération des gonadotropines
LTP	Potentiation à long terme
mGluR	Récepteur métabotropique du glutamate

*Auteur correspondant : acharlet@unistra.fr
#Contribution égale.

MAPK	Protéine kinase activée par les signaux mitochondriens
NMDAR	Récepteur du glutamate liant le N-méthyl D-aspartate
OT	Ocytocine
OTR	Récepteur de l'ocytocine
Oxt	Gène codant l'ocytocine
P2X	Récepteur canal de l'ATP
PGE2	Prostaglandine E2
PKA	Protéine kinase A
PKC	Protéine kinase C
PLC	Phospholipase C
RCPG	Récepteurs couplés aux protéines G
SON	Noyau supraoptique
TGOT	[Thr ₄ Gly ₇]-ocytocine

Introduction

L'ocytocine (OT), un neuropeptide hypothalamique, est au centre de l'attention des chercheurs depuis sa première description par Sir Henry H. Dale (Dale, 1906). En raison de ses effets prosociaux et de renforcement de la confiance, la presse populaire a même inventé le terme d'hormone de l'amour. L'OT est impliquée dans une pléthora de fonctions, tout particulièrement le contrôle des interactions sociales et des processus émotionnels (Lee *et al.*, 2009), et joue un rôle central dans la formation de couples (Young & Wang, 2004) et l'attachement entre les individus (Insel & Young, 2001). Les données actuelles suggèrent que l'OT est apparue il y a environ 600 millions d'années (Gwee *et al.*, 2009) et a évolué avec son peptide frère, l'arginine-vasopressine (AVP), à partir d'un peptide ancêtre commun, la vasotocine (VT) (Gwee *et al.*, 2009 ; Theofanopoulou *et al.*, 2021). Sa fonction était alors la régulation de l'osmolarité, l'un des paramètres cruciaux de l'homéostasie. On suppose qu'au fil du temps, le gène de la vasotocine s'est dupliqué et a donné naissance à deux neuropeptides distincts aux propriétés et fonctions physiologiques différentes. Alors que la première lignée évolutive mène à l'AVP, que l'on trouve chez tous les vertébrés et qui est toujours critique pour l'osmorégulation et le contrôle de la pression sanguine, la voie alternative est à l'origine des peptides de type ocytocine dont les structures varient en fonction des espèces : l'isotocine se retrouve chez les poissons, la mésotocine est présente chez les amphibiens et les reptiles, et l'OT est synthétisée chez tous les mammifères (Gimpl & Fahrenholz, 2001 ; Jurek & Neumann, 2018 ; Theofanopoulou *et al.*, 2021). Il a récemment été proposé de standardiser la nomenclature de ces deux peptides à travers les espèces en OT pour tous les peptides de type ocytocine et VT pour tous ceux de type AVP (Theofanopoulou *et al.*, 2021).

Chez les mammifères, le gène codant l'OT (*Oxt*) est transcrit dans l'hypothalamus, où son ARNm y est l'un des ARNm spécifiques les plus abondants (Gautvik *et al.*, 1996 ; Gimpl & Fahrenholz, 2001). Comme c'est le cas pour de nombreux autres peptides, l'ARNm de l'OT est traduit en un précurseur inactif, qui est ensuite clivé en

fragments plus petits, pour finalement donner le peptide actif. Après sa synthèse, l'OT est stockée dans de grandes vésicules à cœur dense (Leng & Ludwig, 2008), libérée via une exocytose dépendante du calcium (Leng & Ludwig, 2008 ; Tobin *et al.*, 2012 ; Ludwig & Stern, 2015 ; Maicas-Royo *et al.*, 2018) et agit sur le récepteur de l'ocytocine (OTR) couplé aux protéines G (Jurek & Neumann, 2018). À ce jour, deux cascades de signalisation intracellulaires distinctes ont été identifiées après l'activation de l'OTR : les voies G_{αi/o}- et G_{αq}-dépendantes (Jurek & Neumann, 2018).

Différents modes de libération de l'OT dans le système nerveux central ont été décrits, notamment la libération axonale (Knobloch *et al.*, 2012 ; Eliava *et al.*, 2016 ; Grinevich *et al.*, 2016 ; Hasan *et al.*, 2019), la libération somato-dendritique (Ludwig & Leng, 2006) et la libération *en passant* (Ludwig & Leng, 2006 ; Fuxé *et al.*, 2012 ; Bakos *et al.*, 2018). L'OT est également libérée dans la circulation sanguine par la neurohypophyse. La libération ciblée et locale de l'OT au sein de différentes régions du cerveau qui expriment l'OTR permet au peptide d'agir à la fois comme un neurotransmetteur (Buijs, 1983 ; Landgraf & Neumann, 2004 ; Leng & Ludwig, 2008 ; Stoop, 2012 ; Althammer *et al.*, 2021) et comme un neuromodulateur (Stoop, 2012 ; Owen *et al.*, 2013 ; Mitre *et al.*, 2018 ; Tirko *et al.*, 2018), affectant ainsi un large éventail de comportements (Grinevich & Neumann, 2020 ; Froemke & Young, 2021). Jusqu'alors, les recherches sur l'OT étaient uniquement axées sur ses effets directs sur les circuits neuronaux. Par conséquent, selon l'hypothèse dominante, les actions de l'OT devaient être exclusivement médiées par les neurones et ce point de vue a prévalu jusqu'à une date récente (Wahis *et al.*, 2021). En réalité, un nombre croissant de preuves suggère que l'OT agit également directement sur des cellules non neuronales (Wang & Hatton, 2009 ; Tasker *et al.*, 2012 ; Havranek *et al.*, 2017 ; Mairesse *et al.*, 2019).

Les cellules neuronales et gliales existent dans un rapport global 1:1 dans le cerveau humain, mais des variations de ce rapport s'observent d'une région cérébrale à une autre, et des proportions différentes de ces deux populations cellulaires ont été rapportées chez d'autres espèces (von Bartheld *et al.*, 2016). Les cellules gliales sont composées de plusieurs types, dont les astrocytes, les microglies et les oligodendrocytes. Par définition, elles sont non excitables électriquement. Ainsi, pendant longtemps, on a cru qu'elles étaient simplement des cellules passives et qu'elles ne participaient pas activement au traitement de l'information et à la transduction du signal au sein du cerveau. Si, à notre connaissance, il n'existe actuellement aucune preuve suggérant une action de l'OT sur les oligodendrocytes, en revanche il a été démontré qu'elle influence l'activité de la microglie (Inoue *et al.*, 2019 ; Panaro *et al.*, 2020), la différenciation des progéniteurs neuraux (Palanisamy *et al.*, 2018) et la stellation des pituicytes (Rosso *et al.*, 2002). De surcroît, il existe de plus en plus de données démontrant une action de l'OT sur les astrocytes (Di Scala-Guénnot *et al.*, 1994 ; Panatier *et al.*, 2006 ; Wahis *et al.*, 2021).

Les astrocytes jouent un rôle primordial dans l'homéostasie, l'approvisionnement en nutriments et le métabolisme du cerveau. Ils représentent environ 20 à 40 % de toutes les cellules gliales, selon l'espèce et la région du cerveau (Augusto-Oliveira *et al.*, 2020). Au cours des deux dernières décennies, les astrocytes sont devenus des acteurs clés de la neuromodulation et de la neuroinflammation, tant dans le cerveau sain que dans le cerveau malade. La façon dont les astrocytes interviennent dans le fonctionnement des circuits neuronaux est particulièrement intrigante. Les neurones et les astrocytes sont fondamentalement différents dans leur morphologie et leur cinétique d'activité : les neurones sont polarisés fonctionnellement et ont des dendrites et des axones permettant la formation de projections à longue distance, tandis que les astrocytes possèdent une myriade de minuscules excroissances membranaires leur permettant de s'infiltrer dans leur environnement et de répondre à de nombreux signaux. De plus, les neurones ont une activité électrique de l'ordre de la milliseconde, tandis que la durée des événements calciques astrocytaires peut aller de quelques minutes à plusieurs heures (Bazargani & Attwell, 2016). Cette différence de dynamique temporelle drastique entre les deux types de cellules pourrait affecter la façon dont les différents neuromodulateurs opèrent au sein des microcircuits. Ainsi, il est impératif de comprendre comment les neurones et les cellules gliales interagissent en réponse aux neuromodulateurs pour déchiffrer complètement leurs rôles respectifs dans le fonctionnement du cerveau. Dans cette revue, nous résumons la littérature actuelle sur l'action de l'OT sur les astrocytes, et nous proposons de nouveaux modèles qui pourraient expliquer l'implication astrocytaire dans des pathologies associées à des dysfonctionnements du système ocytocinergique.

Effets de l'ocytocine sur les astrocytes

Le récepteur de l'ocytocine est exprimé par les astrocytes

Dans le cerveau, l'OT est principalement synthétisée au sein de trois structures hypothalamiques distinctes : le noyau paraventriculaire, le noyau supraoptique (SON) et les noyaux accessoires. L'une des caractéristiques des neurones OTergiques est la libération somato-dendritique. Au milieu des années 1980, il a été démontré qu'après une sécrétion/infusion d'une quantité importante d'OT dans l'hypothalamus, des modifications de la morphologie des astrocytes s'y produisent *in vivo* (Salm *et al.*, 1985 ; Theodosis *et al.*, 1986a, b). Cette observation a conduit Di Scala-Guénöt & Strosser (1992) à réaliser des études de liaison pour déterminer si les astrocytes hypothalamiques en culture expriment l'OTR. L'utilisation de ligands radiomarqués leur a permis de démontrer que l'OTR est distribué au niveau du soma et des prolongements de cellules morphologiquement similaires à celles exprimant

la protéine acide fibrillaire gliale (GFAP), suggérant leur identité astrocytaire. De plus, en utilisant les mêmes méthodes, des OTR ont été révélés dans des cellules exprimant la GFAP au sein de cultures primaires d'astrocytes spinaux (Evrard *et al.*, 1997). En utilisant l'hybridation *in situ* ou l'immunomarquage, des études récentes ont détecté l'expression des OTR dans les astrocytes de rongeurs au niveau du SON (Wang & Hatton, 2006), du cortex auditif (Mitre *et al.*, 2016), de l'amygdale centrale (Wahis *et al.*, 2021), du striatum ventral (Amato *et al.*, 2022), de l'hippocampe (Althammer *et al.*, 2022b) et même du cortex frontal humain (McKay *et al.*, 2019). En outre, l'OTR peut être co-immunoprécipité avec la GFAP dans des lysats de SON, ce qui indique que le récepteur est lié au cytosquelette astrocytaire (Wang *et al.*, 2017). Si chacun de ces résultats souffre d'une limitation technique inhérente à l'approche utilisée, invitant à la prudence dans l'interprétation des données présentées, leur convergence laisse à penser que l'OTR est effectivement exprimé dans les astrocytes de plusieurs structures cérébrales.

Il faut noter ici que, bien que l'expression de l'OTR dans les neurones soit observée chez une myriade d'espèces et dans de nombreuses régions du cerveau (Gould & Zingg, 2003 ; Mitre *et al.*, 2016 ; Newmaster *et al.*, 2020 ; Young & Song, 2020), les études réalisées jusqu'à présent n'ont pas quantifié les niveaux d'expression réels de l'OTR dans les neurones. À notre connaissance, aucune étude publiée n'a encore évalué et comparé directement les niveaux d'expression d'OTR neuronaux et astrocytaires ; en cause, l'absence d'une approche quantitative et fiable pour la mesure de l'expression de l'OTR, par immunofluorescence par exemple. Cependant, de récentes données d'hybridation *in situ* de l'ARNm de l'OTR suggèrent que les niveaux d'OTR pourraient être 2 à 3 fois plus faibles dans les astrocytes que dans les neurones au niveau de l'amygdale (Wahis *et al.*, 2021 ; Althammer *et al.*, 2022a) et de la région dorsale CA2 (Althammer *et al.*, 2022b).

Les récepteurs ocytocinergiques astrocytaires sont fonctionnels

La première indication d'une action directe de l'OT sur les cellules gliales remonte au milieu des années 1990, lorsque Di Scala-Guénöt *et al.* (1994) ont réalisé de l'imagerie du calcium intracellulaire sur des astrocytes hypothalamiques en culture. Ils ont observé que l'application d'OT ou de [Thr₄Gly₇]-ocytocine (TGOT, un agoniste sélectif de l'OTR) déclenche des réponses calciques monophasiques dans la majorité des astrocytes enregistrés, mais aussi des oscillations calciques dans ~15 % d'entre eux (Di Scala-Guénöt *et al.*, 1994). Ces observations sur des astrocytes *in vitro* suggèrent que ces cellules réagissent directement à l'OT. Cependant, il convient de rappeler que les astrocytes cultivés sont connus pour être très différents de ceux trouvés *in situ*, à la fois en termes de morphologie, d'expression protéique et de signalisation calcique (Shigetomi *et al.*, 2010a, b ; Foo *et al.*, 2011).

Plus récemment, il a été démontré que la libération d'OT évoquée par optogénétique à partir de terminaisons axonales dans l'amygdale centrale déclenche des événements calciques dans les astrocytes *ex vivo* (Wahis *et al.*, 2021). Cela suggère fortement que la libération endogène d'OT est suffisante pour induire une signalisation calcique dans les astrocytes. Pourtant, cet effet pourrait résulter indirectement de l'activation de l'OTR sur les neurones voisins. En utilisant une approche Cre/Lox, les auteurs ont éliminé l'OTR dans les cellules exprimant la GFAP et observé une diminution des réponses calciques induites par l'activation de l'OTR dans les astrocytes. Malgré le problème potentiel concernant une putative fuite de Cre des cellules GFAP positives (Hu *et al.*, 2020; Stifter & Greter, 2020), cette observation corrobore l'hypothèse selon laquelle l'activité astrocytaire médiée par l'OTR pourrait dépendre de l'activation de ce récepteur sur les astrocytes (Wahis *et al.*, 2021). Cependant, même si ce modèle GFAP-OTR KO met en évidence l'implication de l'OTR dans l'activité astrocytaire, il n'exclut pas la participation potentielle d'un neurotransmetteur co-libéré avec l'OT à partir des terminaisons axonales OTergiques.

Sur la base de ces observations, il semble plausible que des OTR fonctionnels puissent être exprimés dans les astrocytes de plusieurs régions du système nerveux central. Pour bien comprendre comment l'OT agit sur les astrocytes, il est important d'examiner de près la voie intracellulaire déclenchée par la liaison de l'OT à l'OTR astrocytaire.

Signalisation intracellulaire recrutée par le récepteur ocytocinergique astrocytaire

L'OTR est un membre de la famille des récepteurs à sept domaines transmembranaires, couplés aux protéines G (RCPG), de classe A. Chez les mammifères, l'OTR est codé par un seul gène, cependant, son couplage intracellulaire est complexe. Les boucles intracellulaires et le domaine C-terminal intracellulaire relient le récepteur aux complexes de protéines G hétérotrimériques. Chacun d'entre eux est composé de trois sous-unités : G_{α} , G_{β} , G_{γ} . Lors de la liaison de l'agoniste, des changements conformationnels du récepteur conduisent au remplacement de la guanine diphosphatée liée à la sous-unité G_{α} par une guanine triphosphatée. La sous-unité G_{α} se dissocie alors du complexe $G_{\beta\gamma}$ et agit sur diverses enzymes qui produisent des seconds messagers. Comme l'OTR est fonctionnellement couplé aux protéines $G_{\alpha q}$ et/ou $G_{\alpha i/o}$, son activation peut produire une signalisation calcique à partir des réserves de calcium intracellulaire (Phaneuf *et al.*, 1993; Gimpl & Fahrenholz, 2001; Busnelli & Chini, 2018; Jurek & Neumann, 2018). Outre cet effet, l'activation de l'OTR peut contrôler diverses voies intracellulaires, notamment celles dépendantes de l'AMPc, de la phospholipase C (PLC) et de la protéine kinase C (PKC) (Chatterjee *et al.*, 2016). De plus, l'application d'OT sur des tranches de SON augmente la phosphorylation des kinases 1/2 régulées par les signaux extracellulaires (ERK1/2), renforçant l'hypothèse selon

laquelle l'activation de l'OTR affecte la voie MAPK dans les astrocytes (Wang & Hatton, 2007). Wang *et al.* (2017) ont en outre montré que l'OT diminue l'expression de la GFAP dans les astrocytes du SON, un effet qui semble médié par les sous-unités $G_{\beta\gamma}$ des protéines G couplées à l'OTR et l'activation séquentielle de ERK1/2 et de la protéine kinase A (PKA) (Wang *et al.*, 2017). Il convient de noter que l'activation de ERK1/2 et de la PKA semble avoir des effets antagonistes sur la stabilité de la GFAP, la PKA provoquant d'abord la dégradation des filaments de GFAP et ERK1/2 stabilisant ensuite les filaments nouvellement synthétisés (Wang *et al.*, 2017). Récemment, une étude menée sur des cellules provenant d'un astrocytome et semblables à des astrocytes a montré que l'ablation de l'OTR empêchait la phosphorylation de ERK1/2 induite par l'OT et interférait avec la prolifération et les effets antioxydants de l'activation de l'OTR (Alanazi *et al.*, 2020), soutenant ainsi l'idée d'une régulation de la voie MAPK médiée par l'OTR.

Comme mentionné précédemment, l'OTR peut également se coupler aux protéines $G_{\alpha i/o}$ (Phaneuf *et al.*, 1993; Strakova *et al.*, 1998; Hoare *et al.*, 1999; Busnelli *et al.*, 2012; Busnelli & Chini, 2018) mais, à notre connaissance, ceci n'a encore jamais été démontré dans les astrocytes. Il est possible que l'OTR puisse être couplé à différentes protéines G dans un même type cellulaire comme cela a été rapporté pour les neurones (Gravati *et al.*, 2010). Ce couplage pourrait également dépendre de la localisation de l'OTR dans différents microdomaines de la membrane plasmique (Rimoldi *et al.*, 2003).

Modulation de la morphologie et des fonctions astrocytaires par l'ocytocine

Sachant que des OTR fonctionnels sont exprimés dans les astrocytes, il est possible d'étudier l'effet de leur activation sur les fonctions de ces cellules. Plusieurs études indiquent que la liaison de l'OT aux OTR des astrocytes déclenche des événements calciques dans ces cellules (Kuo *et al.*, 2009; Zatkova *et al.*, 2018; Wahis *et al.*, 2021). Cependant, les cibles en aval et les conséquences finales de la signalisation de l'OTR astrocytaire ne sont pas encore complètement connues. Dans ce chapitre, nous résumons les conséquences de l'activation de l'OTR sur la morphologie des astrocytes et l'activité du réseau neuronal.

Conséquences morphologiques

Les neurones OT libèrent le peptide localement, un phénomène connu sous le nom de libération somatodendritique (Ludwig & Leng, 2006). Il a été proposé que cette forme de libération facilite un mécanisme de rétroaction locale et permet d'activer les neurones ocytocinergiques lors de situations physiologiques particulières comme la parturition, la lactation ou d'autres défis homéostatiques (Brown *et al.*, 2013, 2020). Dès le milieu

des années 1980, il a été démontré que ces conditions associées à une forte libération d'OT entraînent une diminution importante de la densité de filaments de GFAP dans les SON (Salm *et al.*, 1985 ; Wang & Hatton, 2009). En outre, la perfusion d'OT dans les SON entraîne une augmentation des contacts entre les somas neuronaux (Theodosis *et al.*, 1986a, b ; Langle *et al.*, 2003). Cela suggère fortement que l'OT peut modifier la morphologie des astrocytes dont les extensions membranaires séparent normalement les corps cellulaires des neurones. Cette hypothèse a été confirmée dans des tranches de SON. En effet, alors que dans les conditions basales, les membranes neuronales ne sont presque pas juxtaposées car les prolongements astrocytaires les séparent, l'application d'OT sur les tranches, en déclenchant la rétraction de ces prolongements, augmente les contacts entre les neurones OTergiques. Cette modification de la cytoarchitecture astrocytaire semble être calcium-dépendante (Langle *et al.*, 2003). Bien que les auteurs n'aient pas fourni d'explication à ce phénomène, on peut supposer que l'activation de l'OTR des astrocytes modifie le cytosquelette de ces cellules en affectant la dynamique des microtubules, des filaments intermédiaires et/ou des microfilaments d'actine. De fait, les variations de la concentration calcique intracellulaire dans les astrocytes peuvent influer sur les protéines de remodelage de l'actine, telles que la coiffine. Cela a été démontré dans l'hippocampe où la potentialisation à long terme (LTP) déclenche le retrait des prolongements astrocytaires péridendritiques au niveau des synapses « potentialisées » (Henneberger *et al.*, 2020). Il est intéressant de noter qu'une telle réorganisation du cytosquelette d'actine a été observée dans les neurones du SON, et probablement aussi dans les astrocytes voisins en réponse à l'application d'OT (Wang & Hatton, 2007) (Figure 1).

Ces changements morphologiques des astrocytes hypothalamiques pourraient potentiellement avoir de nombreuses conséquences drastiques et durables sur l'activité globale du réseau. En premier lieu, comme les astrocytes maintiennent l'homéostasie des ions K⁺, connus pour être fortement impliqués dans l'excitabilité neuronale (Verkhratsky & Nedergaard, 2018), une réduction de la couverture astrocytaire pourrait entraîner des modifications importantes du potentiel membranaire des neurones voisins. Deuxièmement, les astrocytes étant des médiateurs importants de la clairance des neurotransmetteurs de la fente synaptique (les transporteurs GLT-1 et GAT sont présents sur les extensions astrocytaires et assurent l'élimination respective du glutamate et du GABA extracellulaires), une réduction de la couverture astrocytaire entraîne inévitablement une augmentation de la concentration extracellulaire des neurotransmetteurs, ce qui se traduit finalement par des modifications de la transmission synaptique. D'ailleurs, les neurotransmetteurs peuvent déborder de la fente synaptique et activer les récepteurs présynaptiques (par exemple, les mGluR) ou extrasynaptiques (par exemple, les NMDAR) afin de promouvoir un effet de régulation par rétroaction ou de moduler l'efficacité et/ou la puissance des synapses voisines

(Oliet *et al.*, 2008). Troisièmement, en désencombrant l'espace extracellulaire, la rétraction des prolongements astrocytaires pourrait permettre la formation de nouvelles synapses, comme cela a été suggéré pour l'hypothalamus (Hatton *et al.*, 1984). Enfin, les astrocytes étant connus pour libérer des molécules neuroactives nommées gliotransmetteurs, la rétraction de leurs prolongements pourrait conduire à une diminution des taux de ces molécules dans l'espace extracellulaire et donc à la réduction de leur capacité à moduler la neurotransmission via les récepteurs de gliotransmetteurs exprimés par les neurones environnants.

Gliotransmission

Le concept de communication directe entre les astrocytes et les neurones par la libération de gliotransmetteurs a été introduit dès le début des années 1990 (Grandes *et al.*, 1991), mais il a fallu attendre les travaux de Parpura *et al.* (1994) pour en apporter la démonstration. En effet, ces auteurs ont été les premiers à rapporter que le glutamate libéré par les astrocytes provoquait une augmentation de l'activité calcique dans les neurones voisins. Plus tard, il a également été démontré que l'ATP agissait sur les récepteurs P2X des neurones après avoir été libéré par les astrocytes (Zhang *et al.*, 2003). Il est important de noter, cependant, que les mécanismes qui sous-tendent la gliotransmission sont encore controversés (Sloan & Barres, 2014 ; Fiacco & McCarthy, 2018), bien que la majorité des chercheurs dans le domaine semble reconnaître son existence (Araque *et al.*, 2014 ; Savtchouk & Volterra, 2018).

Dans le SON, Panatier *et al.* (2006) ont montré que les astrocytes expriment la sérine racémase, une enzyme qui convertit la L-séroline en D-séroline et que cette D-séroline est le co-agoniste endogène des NMDAR (Panatier *et al.*, 2006). En outre, ils ont démontré que les courants induits par l'ouverture des NMDAR sont fortement altérés dans les tranches de SON traitées par la D-aminoacide-oxydase (DAAO), une enzyme qui dégrade la D-séroline extracellulaire. Comme cette altération est corrigée par l'application de D-séroline exogène, ils en déduisent que les astrocytes synthétisent et libèrent la D-séroline pour induire un signal dépendant des NMDAR. Panatier *et al.* (2006) ont également réalisé des enregistrements *ex vivo* de courants déclenchés par l'ouverture des NMDAR dans des neurones du SON de ratten vierges ou en lactation. Ils ont montré que chez les ratten allaitantes, les courants évoqués par l'ouverture des AMPAR et des NMDAR étaient similaires à ceux observés dans des tranches d'animaux vierges traités par DAAO et qu'ils pouvaient également être corrigés par l'application de D-séroline. Étant donné que l'activation des NMDAR semble être essentielle pour l'établissement de la LTP, ils ont étudié l'implication de ces récepteurs dans ce phénomène de plasticité synaptique au niveau du SON. Chez les animaux vierges, ils ont observé un établissement normal de la LTP, alors que chez les ratten allaitantes, cette plasticité ne se produit que si le milieu d'enregistrement est supplémenté en D-séroline.

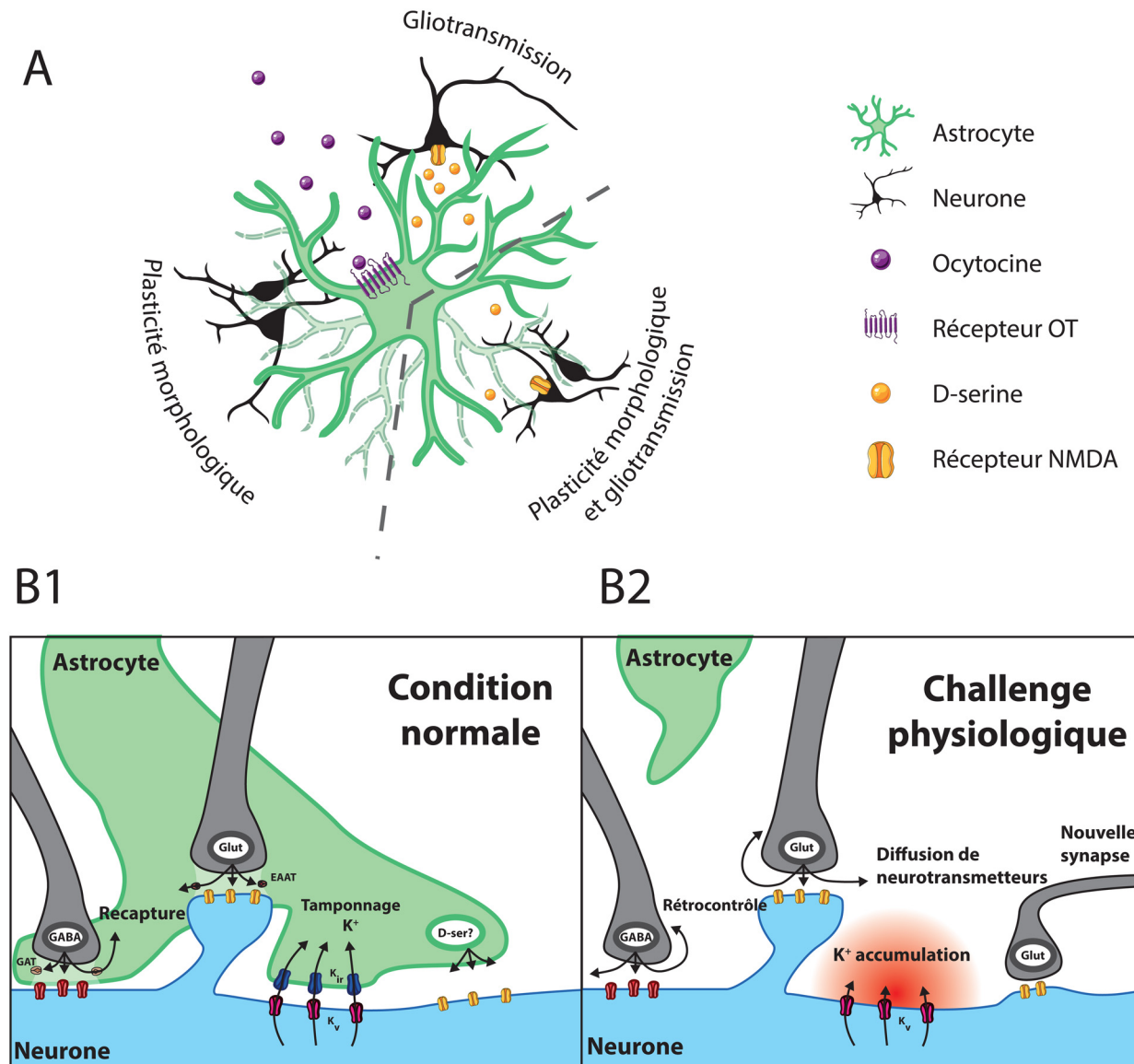


Figure 1. Effets de l'activation du récepteur ocytocinergique astrocytaire. (A) En haut : L'ocytocine module la gliotransmission. En bas à gauche : L'ocytocine induit des changements morphologiques astrocytaires. En bas à droite : Nous émettons l'hypothèse selon laquelle les deux mécanismes pourraient se produire en même temps. (B) Interactions astrocytes-neurones en conditions normales (B1) ou pathologiques (rétraction des prolongements astrocytaires), (B2) (voir le texte pour plus de détails).

Il semble donc que l'apport de D-sérine par les astrocytes soit essentiel à la plasticité synaptique dans le SON (Panatier *et al.*, 2006). Toutefois, il convient de noter que l'origine astrocytaire de la D-sérine fait encore l'objet de débats (Papouin *et al.*, 2017; Ivanov & Mothet, 2019; Coyle *et al.*, 2020).

Plus récemment, Wahis *et al.* (2021) ont étudié l'implication des astrocytes de la partie latérale de l'amygdale centrale (CeL) dans la régulation de l'activité neuronale en réponse à l'OT. Dans cette structure, une population d'astrocytes de la CeL semble exprimer l'OTR et son activation déclenche une augmentation de leur activité calcique (Wahis *et al.*, 2021). De plus, ces changements d'activité calcique astrocytaire sont liés à

une augmentation de l'activité électrique des neurones du CeL voisins. Cette augmentation est dépendante des NMDAR et sensible à l'enzyme de dégradation de la D-sérine, la DAAO, suggérant que les astrocytes modulent l'activité des neurones de CeL en libérant de la D-sérine (Figure 1). Au niveau comportemental, cette modulation du réseau neuronal semble réduire les comportements de type anxieux. Cela démontre que les astrocytes de la CeL participent activement à la modulation du réseau neuronal par l'OT (Wahis *et al.*, 2021).

Un autre circuit impliquant les astrocytes dans la régulation de l'activité neuronale a été mis en évidence au niveau de l'hypothalamus basal médian par Parent *et al.* (2008). Dans cette structure, l'OTR n'est pas exprimé par

les neurones exprimant la GnRH, mais l'est au contraire par les cellules voisines qui seraient des astrocytes, comme le suggère l'expression d'OTR dans ces cellules mises en culture (Parent *et al.*, 2008). De manière intéressante, l'injection intrapéritonéale d'OT réduit l'intervalle entre les pics de sécrétion de la GnRH, connue pour être impliquée dans la maturation sexuelle. Si les astrocytes sont bien les seules cellules qui expriment l'OTR dans l'hypothalamus basal médian, on peut alors se demander comment l'OT module la libération de GnRH dans le sang (c'est-à-dire l'activité des neurones GnRH). Étant donné que l'OT induit la libération de prostaglandine E2 (PGE2) (Strakova *et al.*, 1998), Parent *et al.* (2008) ont émis l'hypothèse selon laquelle celle-ci était le médiateur de la communication entre les astrocytes et les neurones GnRH. De fait, ils ont constaté que la PGE2 reproduisait l'effet de l'OT en diminuant l'intervalle entre les pics de sécrétion de GnRH. *In fine*, l'ensemble de ces données suggère que l'OT active directement les astrocytes de l'hypothalamus basal médian pour déclencher la libération de PGE2, celle-ci agissant ensuite sur les neurones GnRH pour moduler la sécrétion neuronale pulsatile de GnRH et, finalement, la maturation sexuelle (Parent *et al.*, 2008). Ainsi, les astrocytes activés par l'OT pourraient communiquer avec les neurones voisins en libérant plusieurs gliotransmetteurs, tels que la D-sérine ou la PGE2.

Conclusions

Les recherches menées au cours des deux dernières décennies ont montré que les astrocytes sont bien plus que des cellules passives nécessaires au soutien neuronal. Il est devenu évident que les astrocytes jouent un rôle majeur dans le métabolisme, l'homéostasie, le traitement des informations et les fonctions cognitives. De nombreux neuromodulateurs qui influencent ces fonctions agissent également sur l'activité calcique astrocytaire, ce qui suggère que les astrocytes pourraient être impliqués dans la régulation de l'activité des circuits neuronaux. Parmi ces neuromodulateurs, il a été démontré que l'OT déclenche des événements calciques dans les astrocytes, mettant en évidence un mode d'intégration des informations OTergiques dans le système nerveux central. La différence de dynamique temporelle entre les astrocytes et les neurones permet une interaction complexe entre les deux types de cellules et pourrait influencer radicalement la fonction des neuromodulateurs.

Le fait que l'OT induise des changements morphologiques dans les astrocytes hypothalamiques, et affecte ainsi directement la transmission neuronale, donne lieu à une série d'hypothèses intéressantes. L'OT pourrait potentiellement déclencher un ajustement fin et limité dans le temps de la neurotransmission dans les microcircuits pendant des situations physiologiques particulières. La rétraction des prolongements astrocytaires ne fait pas seulement de la place pour plus de signalisation extracellulaire, mais empêche également l'élimination des neurotransmetteurs et des surcharges ioniques générées par l'activité neuronale. Ainsi, l'amorçage OTergique des astrocytes pourrait

potentiellement avoir des effets durables sur l'activité du réseau neuronal. Cela serait en accord avec l'idée que les astrocytes peuvent intégrer, traiter et transmettre des informations dans le cadre d'un réseau astro-neurononal. Des études futures devraient permettre d'évaluer précisément le rôle de l'OTR neuronal dans ces réseaux astrocytes-neurones. Il semble plausible que l'activation des astrocytes par l'OT précède l'activation des neurones médiée par l'OTR et que la signalisation OTergique dans les neurones permette une activité soutenue des réseaux astrocytaires-neuronaux. Enfin, on ne sait toujours pas comment la signalisation OTergique dans les astrocytes affecte divers comportements en conditions physiologiques ou pathologiques, des dysfonctionnements du système OTergique ayant été identifiées comme cause sous-jacente des troubles du spectre autistique (Guastella *et al.*, 2010 ; Domes *et al.*, 2013 ; Gordon *et al.*, 2013 ; Anagnostou *et al.*, 2014 ; Ford & Young, 2022), du syndrome de Prader-Willi (Swaab *et al.*, 1995 ; Swaab, 1997 ; Tauber *et al.*, 2011, 2017) ou des troubles de stress post-traumatiques (Swaab *et al.*, 1995 ; Swaab, 1997 ; Guastella *et al.*, 2010 ; Olff *et al.*, 2010 ; Meyer-Lindenberg *et al.*, 2011 ; Domes *et al.*, 2013 ; Gordon *et al.*, 2013 ; Anagnostou *et al.*, 2014 ; Frijling *et al.*, 2014 ; Frijling, 2017 ; Tauber *et al.*, 2017 ; Ford & Young, 2022).

Remerciements. Ce travail a reçu le support du Centre National de la Recherche Scientifique (UPR3212) et de l'Université de Strasbourg (UPR3212), et les financements de l'ANR (JCJC n°19-CE16-0011-0 à A. Charlet), de la fondation pour la recherche médicale (FDT202204015114 à A. Baudon) et de la Graduate School of Pain (EURIDOL ANR-17-EURE-0022 à A. Charlet et E. Clauss Creusot). Les auteurs remercient les refereees et les relecteurs pour la qualité de leur travail d'édition.

Références

- Alanazi, M.M., Havranek, T., Bakos, J., Cubeddu, L.X., Castejon, A.M. (2020). Cell proliferation and anti-oxidant effects of oxytocin and oxytocin receptors: role of extracellular signal-regulating kinase in astrocyte-like cells. *Endocr Regul*, 54, 172-182.
- Althammer, F., Eliava, M., Grinevich, V. (2021). Central and peripheral release of oxytocin: Relevance of neuroendocrine and neurotransmitter actions for physiology and behavior. *Handb Clin Neurol*, 180, 25-44.
- Althammer, F., Krause, E.G., de Kloet, A.D., Smith, J., Grinevich, V., Charlet, A., Stern, J.E. (2022a). Identification and three-dimensional reconstruction of oxytocin receptor expressing astrocytes in the rat and mouse brain. *STAR Protoc*, 3, 101160.
- Althammer, F., Roy, R.K., Lefevre, A., Najjar, R.S., Schoenig, K., Bartsch, D., Eliava, M., Feresin, R., Hammock, E.A.D., Murphy, A.Z., Charlet, A., Grinevich, V., Stern, J.E. (2022b). Altered PVN-to-CA2 hippocampal oxytocin pathway and reduced number of oxytocin-receptor expressing astrocytes in heart failure rats. *J Neuroendocrinol*, 34, e13166.
- Amato, S., Averna, M., Guidolin, D., Pedrazzini, M., Pelassa, S., Capraro, M., Passalacqua, M., Bozzo, M., Gatta, E., Anderlini, D., Maura, G., Agnati, L.F., Cervetto, C., Marcoli, M. (2022). Heterodimer of A2A and oxytocin receptors regulating glutamate release in adult striatal astrocytes. *Int J Mol Sci*, 23, 2326.

- Anagnostou, E., Soorya, L., Brian, J., Dupuis, A., Mankad, D., Smile, S., Jacob, S. (2014). Intranasal oxytocin in the treatment of autism spectrum disorders: a review of literature and early safety and efficacy data in youth. *Brain Res*, 1580, 188-198.
- Araque, A., Carmignoto, G., Haydon, P.G., Oliet, S.H., Robitaille, R., Volterra, A. (2014). Gliotransmitters travel in time and space. *Neuron*, 81, 728-739.
- Augusto-Oliveira, M., Arrifano, G.P., Takeda, P.Y., Lopes-Araujo, A., Santos-Sacramento, L., Anthony, D.C., Verkhratsky, A., Crespo-Lopez, M.E. (2020). Astroglia-specific contributions to the regulation of synapses, cognition and behaviour. *Neurosci Biobehav Rev*, 118, 331-357.
- Bakos, J., Srancikova, A., Havranek, T., Bacova, Z. (2018). Molecular mechanisms of oxytocin signaling at the synaptic connection. *Neural Plast*, 2018, 4864107.
- Bazargani, N., Attwell, D. (2016). Astrocyte calcium signaling: the third wave. *Nat Neurosci*, 19, 182-189.
- Brown, C.H., Bains, J.S., Ludwig, M., Stern, J.E. (2013). Physiological regulation of magnocellular neurosecretory cell activity: integration of intrinsic, local and afferent mechanisms. *J Neuroendocrinol*, 25, 678-710.
- Brown, C.H., Ludwig, M., Tasker, J.G., Stern, J.E. (2020). Somato-dendritic vasopressin and oxytocin secretion in endocrine and autonomic regulation. *J Neuroendocrinol*, 32, e12856.
- Buijs, R.M. (1983). Vasopressin and oxytocin – Their role in neurotransmission. *Pharmacol Ther*, 22, 127-141.
- Busnelli, M., Chini, B. (2018). Molecular basis of oxytocin receptor signalling in the brain: What we know and what we need to know. *Curr Top Behav Neurosci*, 35, 3-29.
- Busnelli, M., Sauliere, A., Manning, M., Bouvier, M., Gales, C., Chini, B. (2012). Functional selective oxytocin-derived agonists discriminate between individual G protein family subtypes. *J Biol Chem*, 287, 3617-3629.
- Chatterjee, O., Patil, K., Sahu, A., Gopalakrishnan, L., Mol, P., Advani, J., Mukherjee, S., Christopher, R., Prasad, T.S. (2016). An overview of the oxytocin-oxytocin receptor signaling network. *J Cell Commun Signal*, 10, 355-360.
- Coyle, J.T., Balu, D., Wolosker, H. (2020). D-Serine, the shape-shifting NMDA receptor co-agonist. *Neurochem Res*, 45, 1344-1353.
- Dale, H.H. (1906). On some physiological actions of ergot. *J Physiol*, 34, 163-206.
- Di Scala-Guénot, D., Strosser, M.T. (1992). Oxytocin receptors on cultured astroglial cells. Kinetic and pharmacological characterization of oxytocin-binding sites on intact hypothalamic and hippocampic cells from foetal rat brain. *Biochem J*, 284, 491-497.
- Di Scala-Guénot, D., Mouginot, D., Strosser, M.T. (1994). Increase of intracellular calcium induced by oxytocin in hypothalamic cultured astrocytes. *Glia*, 11, 269-276.
- Domes, G., Heinrichs, M., Kumbier, E., Grossmann, A., Hauenstein, K., Herpertz, S.C. (2013). Effects of intranasal oxytocin on the neural basis of face processing in autism spectrum disorder. *Biol Psychiatry*, 74, 164-171.
- Eliava, M., Melchior, M., Knobloch-Bollmann, H.S., Wahis, J., da Silva Gouveia, M., Tang, Y., Ciobanu, A.C., Triana del Rio, R., Roth, L.C., Althammer, F., Chavant, V., Goumon, Y., Gruber, T., Petit-Demoulière, N., Busnelli, M., Chini, B., Tan, L.L., Mitre, M., Froemke, R.C., Chao, M.V., Giese, G., Sprengel, R., Kuner, R., Poisbeau, P., Seeburg, P.H., Stoop, R., Charlet, A., Grinevich, V. (2016). A new population of parvocellular oxytocin neurons controlling magnocellular neuron activity and inflammatory pain processing. *Neuron*, 89, 1291-1304.
- Evrard, M.E., Strosser, M.T., Di Scala-Guénot, D. (1997). Pharmacological characterization of oxytocin-binding sites in rat spinal cord membranes: comparison with embryonic cultured spinal cord neurones and astrocytes. *J Neuroendocrinol*, 9, 553-560.
- Fiacco, T.A., McCarthy, K.D. (2018). Multiple lines of evidence indicate that gliotransmission does not occur under physiological conditions. *J Neurosci*, 38, 3-13.
- Foo, L.C., Allen, N.J., Bushong, E.A., Ventura, P.B., Chung, W. S., Zhou, L., Cahoy, J.D., Daneman, R., Zong, H., Ellisman, M.H., Barres, B.A. (2011). Development of a method for the purification and culture of rodent astrocytes. *Neuron*, 71, 799-811.
- Ford, C.L., Young, L.J. (2022). Refining oxytocin therapy for autism: context is key. *Nat Rev Neuro*, 18, 67-68.
- Frijling, J.L., (2017). Preventing PTSD with oxytocin: effects of oxytocin administration on fear neurocircuitry and PTSD symptom development in recently trauma-exposed individuals. *Eur J Psychotraumatol*, 8, 1302652.
- Frijling, J.L., van Zuiden, M., Koch, S.B., Nawijn, L., Goslings, J.C., Luitse, J.S., Biesheuvel, T.H., Honig, A., Bakker, F.C., Denys, D., Veltman, D.J., Olff, M. (2014). Efficacy of oxytocin administration early after psychotrauma in preventing the development of PTSD: study protocol of a randomized controlled trial. *BMC Psychiatry*, 14, 92.
- Froemke, R.C., Young, L.J. (2021). Oxytocin, neural plasticity, and social behavior. *Annu Rev Neurosci*, 44, 359-381.
- Fuxé, K., Borroto-Escuela, D.O., Romero-Fernandez, W., Ciruela, F., Manger, P., Leo, G., Diaz-Cabiale, Z., Agnati, L.F. (2012). On the role of volume transmission and receptor-receptor interactions in social behaviour: focus on central catecholamine and oxytocin neurons. *Brain Res*, 1476, 119-131.
- Gautvik, K.M., de Lecea, L., Gautvik, V.T., Danielson, P.E., Tranque, P., Dopazo, A., Bloom, F.E., Sutcliffe, J.G. (1996). Overview of the most prevalent hypothalamus-specific mRNAs, as identified by directional tag PCR subtraction. *Proc Natl Acad Sci USA*, 93, 8733-8738.
- Gimpl, G., Fahrenholz, F., (2001). The oxytocin receptor system: structure, function, and regulation. *Physiol Rev*, 81, 629-683.
- Gordon, I., Vander Wyk, B.C., Bennett, R.H., Cordeaux, C., Lucas, M.V., Eilbott, J.A., Zagoory-Sharon, O., Leckman, J. F., Feldman, R., Pelphrey, K.A. (2013). Oxytocin enhances brain function in children with autism. *Proc Natl Acad Sci USA*, 110, 20953-20958.
- Gould, B.R., Zingg, H.H. (2003). Mapping oxytocin receptor gene expression in the mouse brain and mammary gland using an oxytocin receptor-LacZ reporter mouse. *Neuroscience*, 122, 155-167.
- Grandes, P., Kq, K.Q.D., Morino, P., Cuenod, M., Streit, P. (1991). Homocysteate, an excitatory transmitter candidate localized in glia. *Eur J Neurosci*, 3, 1370-1373.
- Gravati, M., Busnelli, M., Bulgheroni, E., Reversi, A., Spaiardi, P., Parenti, M., Toselli, M., Chini, B. (2010). Dual modulation of inward rectifier potassium currents in olfactory neuronal cells by promiscuous G protein coupling of the oxytocin receptor. *J Neurochem*, 114, 1424-1435.
- Grinevich, V., Knobloch-Bollmann, H.S., Eliava, M., Busnelli, M., Chini, B. (2016). Assembling the puzzle: Pathways of oxytocin signaling in the brain. *Biol Psychiatry*, 79, 155-164.
- Grinevich, V., Neumann, I.D. (2020). Brain oxytocin: how puzzle stones from animal studies translate into psychiatry. *Mol Psychiatry*, 26, 265-279.

- Guastella, A.J., Einfeld, S.L., Gray, K.M., Rinehart, N.J., Tonge, B.J., Lambert, T.J., Hickie, I.B., (2010). Intranasal oxytocin improves emotion recognition for youth with autism spectrum disorders. *Biol Psychiatry*, 67, 692-694.
- Gwee, P.C., Tay, B.H., Brenner, S., Venkatesh, B. (2009). Characterization of the neurohypophyseal hormone gene loci in elephant shark and the Japanese lamprey: Origin of the vertebrate neurohypophyseal hormone genes. *BMC Evol Biol*, 9, 47.
- Hasan, M.T., Althammer, F., Silva da Gouveia, M., Goyon, S., Eliava, M., Lefevre, A., Kerspern, D., Schimmer, J., Raftogianni, A., Wahis, J., Knobloch-Bollmann, H.S., Tang, Y., Liu, X., Jain, A., Chavant, V., Goumon, Y., Weislogel, J. M., Hurleman, R., Herpertz, S.C., Pitzer, C., Darbon, P., Dogbevia, G.K., Bertocchi, I., Larkum, M.E., Sprengel, R., Bading, H., Charlet, A., Grinevich, V. (2019). A fear memory engram and its plasticity in the hypothalamic oxytocin system. *Neuron*, 103, 133-146.
- Hatton, G.I., Perlmutter, L.S., Salm, A.K., Tweedle, C.D. (1984). Dynamic neuronal-glial interactions in hypothalamus and pituitary: implications for control of hormone synthesis and release. *Peptides*, 5(Suppl 1), 121-138.
- Havranek, T., Lestanova, Z., Mravec, B., Strbak, V., Bakos, J., Bacova, Z. (2017). Oxytocin modulates expression of neuron and glial markers in the rat hippocampus. *Folia Biol (Praha)*, 63, 91-97.
- Henneberger, C., Bard, L., Panatier, A., Reynolds, J.P., Kopach, O., Medvedev, N.I., Minge, D., Herde, M.K., Anders, S., Kraev, I., Heller, J.P., Rama, S., Zheng, K., Jensen, T.P., Sanchez-Romero, I., Jackson, C.J., Janovjak, H., Ottersen, O. P., Nagelhus, E.A., Oliet, S.H.R., Stewart, M.G., Nagerl, U. V., Rusakov, D.A. (2020). LTP induction boosts glutamate spillover by driving withdrawal of perisynaptic astroglia. *Neuron*, 108, 919-936.
- Hoare, S., Copland, J.A., Strakova, Z., Ives, K., Jeng, Y.J., Hellmich, M.R., Soloff, M.S. (1999). The proximal portion of the COOH terminus of the oxytocin receptor is required for coupling to G(q), but not G(i). Independent mechanisms for elevating intracellular calcium concentrations from intracellular stores. *J Biol Chem*, 274, 28682-28689.
- Hu, N.Y., Chen, Y.T., Wang, Q., Jie, W., Liu, Y.S., You, Q.L., Li, Z.L., Li, X.W., Reibel, S., Pfrieger, F.W., Yang, J.M., Gao, T.M. (2020). Expression patterns of inducible Cre recombinase driven by differential astrocyte-specific promoters in transgenic mouse lines. *Neurosci Bull*, 36, 530-544.
- Inoue, T., Yamakage, H., Tanaka, M., Kusakabe, T., Shimatsu, A., Satoh-Asahara, N. (2019). Oxytocin suppresses inflammatory responses induced by lipopolysaccharide through inhibition of the eIF-2-ATF4 pathway in mouse microglia. *Cells*, 8, 527.
- Insel, T.R., Young, L.J., 2001. The neurobiology of attachment. *Nat Rev Neurosci*, 2, 129-136.
- Ivanov, A.D., Mothet, J.P. (2019). The plastic D-serine signaling pathway: Sliding from neurons to glia and vice-versa. *Neurosci Lett*, 689, 21-25.
- Jurek, B., Neumann, I.D. (2018). The oxytocin receptor: From intracellular signaling to behavior. *Physiol Rev*, 98, 1805-1908.
- Knobloch, H.S., Charlet, A., Hoffmann, L.C., Eliava, M., Khrulev, S., Cetin, A.H., Osten, P., Schwarz, M.K., Seeburg, P.H., Stoop, R., Grinevich, V. (2012). Evoked axonal oxytocin release in the central amygdala attenuates fear response. *Neuron*, 73, 553-566.
- Kuo, J., Hariri, O.R., Micevych, P. (2009). An interaction of oxytocin receptors with metabotropic glutamate receptors in hypothalamic astrocytes. *J Neuroendocrinol*, 21, 1001-1006.
- Landgraf, R., Neumann, I.D. (2004). Vasopressin and oxytocin release within the brain: a dynamic concept of multiple and variable modes of neuropeptide communication. *Front Neuroendocrinol*, 25, 150-176.
- Langle, S.L., Poulain, D.A., Theodosis, D.T. (2003). Induction of rapid, activity-dependent neuronal-glial remodelling in the adult rat hypothalamus in vitro. *Eur J Neurosci*, 18, 206-214.
- Lee, H.J., Macbeth, A.H., Pagani, J.H., Young, W.S., 3rd. (2009). Oxytocin: the great facilitator of life. *Prog Neurobiol*, 88, 127-151.
- Leng, G., Ludwig, M. (2008). Neurotransmitters and peptides: whispered secrets and public announcements. *J Physiol*, 586, 5625-5632.
- Ludwig, M., Leng, G. (2006). Dendritic peptide release and peptide-dependent behaviours. *Nat Rev Neurosci*, 7, 126-136.
- Ludwig, M., Stern, J. (2015). Multiple signalling modalities mediated by dendritic exocytosis of oxytocin and vasopressin. *Philos Trans R Soc Lond B Biol Sci*, 370(1762), 20140182.
- Maicas-Royo, J., Leng, G., MacGregor, D.J. (2018). A predictive, quantitative model of spiking activity and stimulus-secretion coupling in oxytocin neurons. *Endocrinology*, 159, 1433-1452.
- Mairesse, J., Zinni, M., Pansiot, J., Hassan-Abdi, R., Demene, C., Colella, M., Charriaut-Marlangue, C., Rideau Batista Novais, A., Tanter, M., Maccari, S., Gressens, P., Vaiman, D., Soussi-Yanicostas, N., Baud, O. (2019). Oxytocin receptor agonist reduces perinatal brain damage by targeting microglia. *Glia*, 67, 345-359.
- McKay, E.C., Beck, J.S., Khoo, S.K., Dykema, K.J., Cottingham, S.L., Winn, M.E., Paulson, H.L., Lieberman, A.P., Counts, S.E. (2019). Peri-infarct upregulation of the oxytocin receptor in vascular dementia. *J Neuropathol Exp Neurol*, 78, 436-452.
- Meyer-Lindenberg, A., Domes, G., Kirsch, P., Heinrichs, M. (2011). Oxytocin and vasopressin in the human brain: social neuropeptides for translational medicine. *Nat Rev Neurosci*, 12, 524-538.
- Mitre, M., Marlin, B.J., Schiavo, J.K., Morina, E., Norden, S.E., Hackett, T.A., Aoki, C.J., Chao, M.V., Froemke, R.C. (2016). A distributed network for social cognition enriched for oxytocin receptors. *J Neurosci*, 36, 2517-2535.
- Mitre, M., Minder, J., Morina, E.X., Chao, M.V., Froemke, R.C. (2018). Oxytocin modulation of neural circuits. *Curr Top Behav Neurosci*, 35, 31-53.
- Newmaster, K.T., Nolan, Z.T., Chon, U., Vanselow, D.J., Weit, A.R., Tabbaa, M., Hidema, S., Nishimori, K., Hammock, E. A.D., Kim, Y., (2020). Quantitative cellular-resolution map of the oxytocin receptor in postnatally developing mouse brains. *Nat Commun*, 11, 1885.
- Olff, M., Langeland, W., Witteveen, A., Denys, D. (2010). A psychobiological rationale for oxytocin in the treatment of posttraumatic stress disorder. *CNS Spectr*, 15, 522-530.
- Oliet, S.H., Panatier, A., Piet, R., Mothet, J.P., Poulin, D.A., Theodosis, D.T. (2008). Neuron-glia interactions in the rat supraoptic nucleus. *Prog Brain Res*, 170, 109-117.
- Owen, S.F., Tuncdemir, S.N., Bader, P.L., Tirko, N.N., Fishell, G., Tsien, R.W. (2013). Oxytocin enhances hippocampal spike transmission by modulating fast-spiking interneurons. *Nature*, 500, 458-462.
- Palanisamy, A., Kannappan, R., Xu, Z., Martino, A., Friese, M. B., Boyd, J.D., Crosby, G., Culley, D.J. (2018). Oxytocin alters cell fate selection of rat neural progenitor cells in vitro. *PLoS One*, 13, e0191160.
- Panaro, M.A., Benameur, T., Porro, C. (2020). Hypothalamic neuropeptide brain protection: Focus on oxytocin. *J Clin Med*, 9, 1534.

- Panatier, A., Gentles, S.J., Bourque, C.W., Oliet, S.H. (2006). Activity-dependent synaptic plasticity in the supraoptic nucleus of the rat hypothalamus. *J Physiol*, 573, 711-721.
- Papouin, T., Henneberger, C., Rusakov, D.A., Oliet, S.H.R. (2017). Astroglial versus neuronal D-serine: Fact checking. *Trends Neurosci*, 40, 517-520.
- Parent, A.S., Rasier, G., Matagne, V., Lomniczi, A., Lebrethon, M.C., Gerard, A., Ojeda, S.R., Bourguignon, J.P. (2008). Oxytocin facilitates female sexual maturation through a glia-to-neuron signaling pathway. *Endocrinology*, 149, 1358-1365.
- Parpura, V., Basarsky, T.A., Liu, F., Jeftinija, K., Jeftinija, S., Haydon, P.G. (1994). Glutamate-mediated astrocyte-neuron signalling. *Nature*, 369, 744-747.
- Phaneuf, S., Europe-Finner, G.N., Varney, M., MacKenzie, I.Z., Watson, S.P., Lopez Bernal, A. (1993). Oxytocin-stimulated phosphoinositide hydrolysis in human myometrial cells: involvement of pertussis toxin-sensitive and -insensitive G-proteins. *J Endocrinol*, 136, 497-509.
- Rimoldi, V., Reversi, A., Taverna, E., Rosa, P., Francolini, M., Cassoni, P., Parenti, M., Chini, B. (2003). Oxytocin receptor elicits different EGFR/MAPK activation patterns depending on its localization in caveolin-1 enriched domains. *Oncogene*, 22, 6054-6060.
- Rosso, L., Peteri-Brunback, B., Vouret-Craviari, V., Deroanne, C., Van Obberghen-Schilling, E., Mienville, J.M. (2002). Vasopressin and oxytocin reverse adenosine-induced pituitary stellation via calcium-dependent activation of Cdc42. *Eur J Neurosci*, 16, 2324-2332.
- Salm, A.K., Smithson, K.G., Hatton, G.I. (1985). Lactation-associated redistribution of the glial fibrillary acidic protein within the supraoptic nucleus. An immunocytochemical study. *Cell Tissue Res*, 242, 9-15.
- Savtchouk, I., Volterra, A. (2018). Gliotransmission: Beyond black-and-white. *J Neurosci*, 38, 14-25.
- Shigetomi, E., Kracun, S., Khakh, B.S. (2010a). Monitoring astrocyte calcium microdomains with improved membrane targeted GCaMP reporters. *Neuron Glia Biol*, 6, 183-191.
- Shigetomi, E., Kracun, S., Sofroniew, M.V., Khakh, B.S. (2010b). A genetically targeted optical sensor to monitor calcium signals in astrocyte processes. *Nat Neurosci*, 13, 759-766.
- Sloan, S.A., Barres, B.A. (2014). Looks can be deceiving: reconsidering the evidence for gliotransmission. *Neuron*, 84, 1112-1115.
- Stifter, S.A., Greter, M. (2020). STOP floxing around: Specificity and leakiness of inducible Cre/loxP systems. *Eur J Immunol*, 50, 338-341.
- Stoop, R. (2012). Neuromodulation by oxytocin and vasopressin. *Neuron*, 76, 142-159.
- Strakova, Z., Copland, J.A., Lolait, S.J., Soloff, M.S. (1998). ERK2 mediates oxytocin-stimulated PGE2 synthesis. *Am J Physiol*, 274, E634-641.
- Swaab, D.F. (1997). Prader-Willi syndrome and the hypothalamus. *Acta Paediatr Suppl*, 423, 50-54.
- Swaab, D.F., Purba, J.S., Hofman, M.A. (1995). Alterations in the hypothalamic paraventricular nucleus and its oxytocin neurons (putative satiety cells) in Prader-Willi syndrome: a study of five cases. *J Clin Endocrinol Metab*, 80, 573-579.
- Tasker, J.G., Oliet, S.H., Bains, J.S., Brown, C.H., Stern, J.E. (2012). Glial regulation of neuronal function: from synapse to systems physiology. *J Neuroendocrinol*, 24, 566-576.
- Tauber, M., Boulanouar, K., Diene, G., Cabal-Berthoumieu, S., Ehlinger, V., Fichaux-Bourrin, P., Molinas, C., Faye, S., Valette, M., Pourrinet, J., Cessans, C., Viaux-Sauvelon, S., Bascoul, C., Guedeney, A., Delhanty, P., Geenen, V., Martens, H., Muscatelli, F., Cohen, D., Consoli, A., Payoux, P., Arnaud, C., Salles, J.P. (2017). The use of oxytocin to improve feeding and social skills in infants with Prader-Willi syndrome. *Pediatrics*, 139, e20162976.
- Tauber, M., Mantoulan, C., Copet, P., Jauregui, J., Demeer, G., Diene, G., Roge, B., Laurier, V., Ehlinger, V., Arnaud, C., Molinas, C., Thuilleaux, D. (2011). Oxytocin may be useful to increase trust in others and decrease disruptive behaviours in patients with Prader-Willi syndrome: a randomised placebo-controlled trial in 24 patients. *Orphanet J Rare Dis*, 6, 47.
- Theodosis, D.T., Chapman, D.B., Montagnese, C., Poulaïn, D. A., Morris, J.F. (1986a). Structural plasticity in the hypothalamic supraoptic nucleus at lactation affects oxytocin-, but not vasopressin-secreting neurones. *Neuroscience*, 17, 661-678.
- Theodosis, D.T., Montagnese, C., Rodriguez, F., Vincent, J.D., Poulaïn, D.A. (1986b). Oxytocin induces morphological plasticity in the adult hypothalamo-neurohypophysial system. *Nature*, 322, 738-740.
- Theofanopoulou, C., Gedman, G., Cahill, J.A., Boeckx, C., Jarvis, E.D. (2021). Universal nomenclature for oxytocin-vasotocin ligand and receptor families. *Nature*, 592, 747-755.
- Tirko, N.N., Eyring, K.W., Carcea, I., Mitre, M., Chao, M.V., Froemke, R.C., Tsien, R.W. (2018). Oxytocin transforms firing mode of CA2 hippocampal neurons. *Neuron*, 100, 593-608.
- Tobin, V., Leng, G., Ludwig, M. (2012). The involvement of actin, calcium channels and exocytosis proteins in somatodendritic oxytocin and vasopressin release. *Front Physiol*, 3, 261.
- Verkhratsky, A., Nedergaard, M. (2018). Physiology of astroglia. *Physiol Rev*, 98, 239-389.
- von Bartheld, C.S., Bahney, J., Herculano-Houzel, S. (2016). The search for true numbers of neurons and glial cells in the human brain: A review of 150 years of cell counting. *J Comp Neurol*, 524, 3865-3895.
- Wahis, J., Baudon, A., Althammer, F., Kerspenn, D., Goyon, S., Hagiwara, D., Lefevre, A., Bartczko, L., Boury-Jamot, B., Bellanger, B., Abatis, M., Da Silva Gouveia, M., Benusiglio, D., Eliava, M., Rozov, A., Weinsanto, I., Knobloch-Bollmann, H.S., Kirchner, M.K., Roy, R.K., Wang, H., Pertin, M., Inquimbert, P., Pitzer, C., Siemens, J., Goumon, Y., Boutrel, B., Lamy, C.M., Decosterd, I., Chatton, J.Y., Rouach, N., Young, W.S., Stern, J.E., Poisbeau, P., Stoop, R., Darbon, P., Grinevich, V., Charlet, A. (2021). Astrocytes mediate the effect of oxytocin in the central amygdala on neuronal activity and affective states in rodents. *Nat Neurosci*, 24, 529-541.
- Wang, P., Qin, D., Wang, Y.F. (2017). Oxytocin rapidly changes astrocytic GFAP plasticity by differentially modulating the expressions of pERK 1/2 and protein kinase A. *Front Mol Neurosci*, 10, 262.
- Wang, Y.F., Hatton, G.I. (2006). Mechanisms underlying oxytocin-induced excitation of supraoptic neurons: prostaglandin mediation of actin polymerization. *J Neurophysiol*, 95, 3933-3947.
- Wang, Y.F., Hatton, G.I. (2007). Interaction of extracellular signal-regulated protein kinase 1/2 with actin cytoskeleton in supraoptic oxytocin neurons and astrocytes: role in burst firing. *J Neurosci*, 27, 13822-13834.
- Wang, Y.F., Hatton, G.I. (2009). Astrocytic plasticity and patterned oxytocin neuronal activity: dynamic interactions. *J Neurosci*, 29, 1743-1754.
- Young, L.J., Wang, Z. (2004). The neurobiology of pair bonding. *Nat Neurosci*, 7, 1048-1054.
- Young, W.S., Song, J. (2020). Characterization of oxytocin receptor expression within various neuronal populations of the mouse dorsal hippocampus. *Front Mol Neurosci*, 13, 40.

Zatkova, M., Bacova, Z., Puerta, F., Lestanova, Z., Alanazi, M., Kiss, A., Reichova, A., Castejon, A.M., Ostatnikova, D., Bakos, J. (2018). Projection length stimulated by oxytocin is modulated by the inhibition of calcium signaling in U-87MG cells. *J Neural Transm*, 125, 1847-1856.

Zhang, J.M., Wang, H.K., Ye, C.Q., Ge, W., Chen, Y., Jiang, Z.L., Wu, C.P., Poo, M.M., Duan, S. (2003). ATP released by astrocytes mediates glutamatergic activity-dependent heterosynaptic suppression. *Neuron*, 40, 971-982.

Citation de l'article : Baudon, A., Clauss Creusot, E., et Charlet, A. (2022). Rôle émergent des astrocytes dans le contrôle des circuits neuronaux et des fonctions cérébrales modulés par l'oxytocine. *Biologie Aujourd'hui*, **216**, 155-165

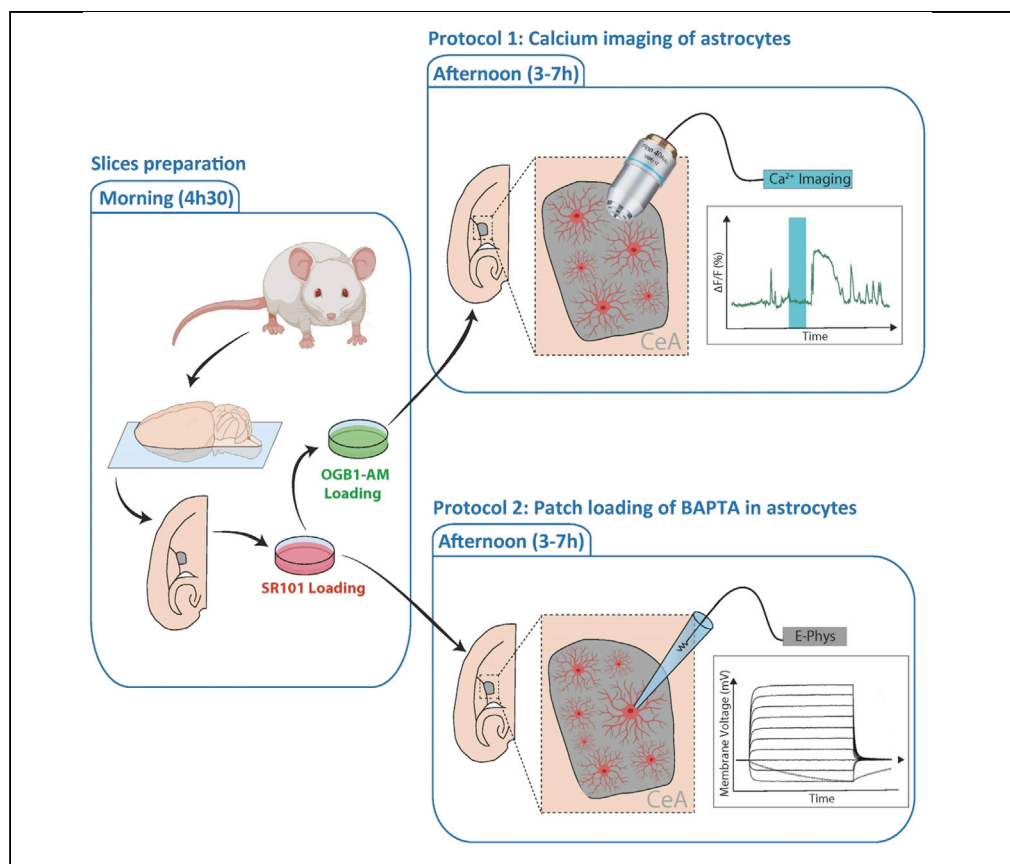
6.2 Star protocol: Calcium imaging and BAPTA loading of amygdala astrocytes in mouse brain slices

Baudon A.*, **Clauss-Creusot E.***, Darbon P., Patwell R., Grinevich V., Charlet A.,
2022.

STAR Protocols 3.

Protocol

Calcium imaging and BAPTA loading of amygdala astrocytes in mouse brain slices



Astrocytes are glial cells that exhibit calcium signaling-mediated activity. Here, we present a protocol to monitor and manipulate astrocyte calcium activity from mouse amygdala slices. In the first part of this protocol, we describe the procedure of astrocyte calcium imaging. In the second part, we detail how to disrupt astrocyte calcium activity by patch-clamp-mediated loading of BAPTA. These two approaches are presented separately but they can also be used simultaneously to monitor the effects of disruption on an astrocyte network.

Angel Baudon,
Etienne
Clauss-Creusot,
Pascal Darbon, Ryan
Patwell, Valery
Grinevich,
Alexandre Charlet
acharlet@unistra.fr

Highlights
Protocol describes calcium imaging and BAPTA loading on astrocytes in mouse brain slices

Calcium imaging is a simple yet reliable tool to study astrocyte activity

Patch-clamp-mediated loading of BAPTA allows the disruption of astrocytic activity

Calcium imaging can assess BAPTA diffusion within the astrocytic network

Baudon et al., STAR Protocols
3, 101159
March 18, 2022 © 2022 The Author(s).
<https://doi.org/10.1016/j.xpro.2022.101159>



Protocol

Calcium imaging and BAPTA loading of amygdala astrocytes in mouse brain slices

Angel Baudon,^{1,3,4} Etienne Clauss-Creusot,^{1,3} Pascal Darbon,¹ Ryan Patwell,² Valery Grinevich,² and Alexandre Charlet^{1,5,*}

¹Centre National de la Recherche Scientifique and University of Strasbourg, Institute of Cellular and Integrative Neuroscience, INCI CNRS UPR3212, 8, Allée du Général Rouvillois, Strasbourg, 67000 France

²Department of Neuropeptide Research in Psychiatry, Central Institute of Mental Health, University of Heidelberg, Mannheim, 68159 Germany

³These authors contributed equally

⁴Technical contact

⁵Lead contact

*Correspondence: acharlet@unistra.fr

<https://doi.org/10.1016/j.xpro.2022.101159>

SUMMARY

Astrocytes are glial cells that exhibit calcium signaling-mediated activity. Here, we present a protocol to monitor and manipulate astrocyte calcium activity from mouse amygdala slices. In the first part of this protocol, we describe the procedure of astrocyte calcium imaging. In the second part, we detail how to disrupt astrocyte calcium activity by patch-clamp-mediated loading of BAPTA. These two approaches are presented separately but they can also be used simultaneously to monitor the effects of disruption on an astrocyte network.

For complete details on the use and execution of this protocol, please refer to Wahis et al. (2021).

BEFORE YOU BEGIN

Calcium imaging requires a confocal fluorescence microscope and an illumination system capable of achieving a high temporal resolution (sampling frequency > 1 Hz). For the calcium indicator, we use Oregon Green BAPTA 1 coupled to an AcetoxyMethyl ester group (OGB1-AM) because it preferentially stains astrocytes, but this protocol can be used with other AM-coupled calcium indicators as well. For example, Rhod2-AM can be used as a red wavelength alternative. However, in our hands, we observe more cell death with Rhod2-AM than with OGB1-AM. One can also use ratiometric calcium indicators such as Fura 2, Fluo-4 or Indo-1. However, while this approach allows for an accurate estimation of the intracellular calcium concentration, it also has the drawback of requiring three wavelengths of light, thereby restricting the use of other fluorescent labeling approaches. The Kd value should also be considered when choosing a calcium indicator. For example, if the goal of the experiment is to monitor small events, then an indicator with a high Kd (e.g., Fluo-4FF) would be ideal, whereas a dye with a lower Kd (e.g., OGB1) would be preferable for monitoring bigger calcium events due to a lower degree of saturation (Delvendahl et al., 2015). Yet another approach that may be used in conjunction with this protocol would be the use of genetically encoded calcium indicators such as GCaMP, or the newly developed Salsa6f ratiometric analogs (for use in astrocytes, see Wakida et al., 2020).

For required tools, please see [key resources table](#) and [materials and equipment](#) for references.

In the present paper, the two protocols were performed in mouse horizontal slices, containing the central nucleus of the amygdala.



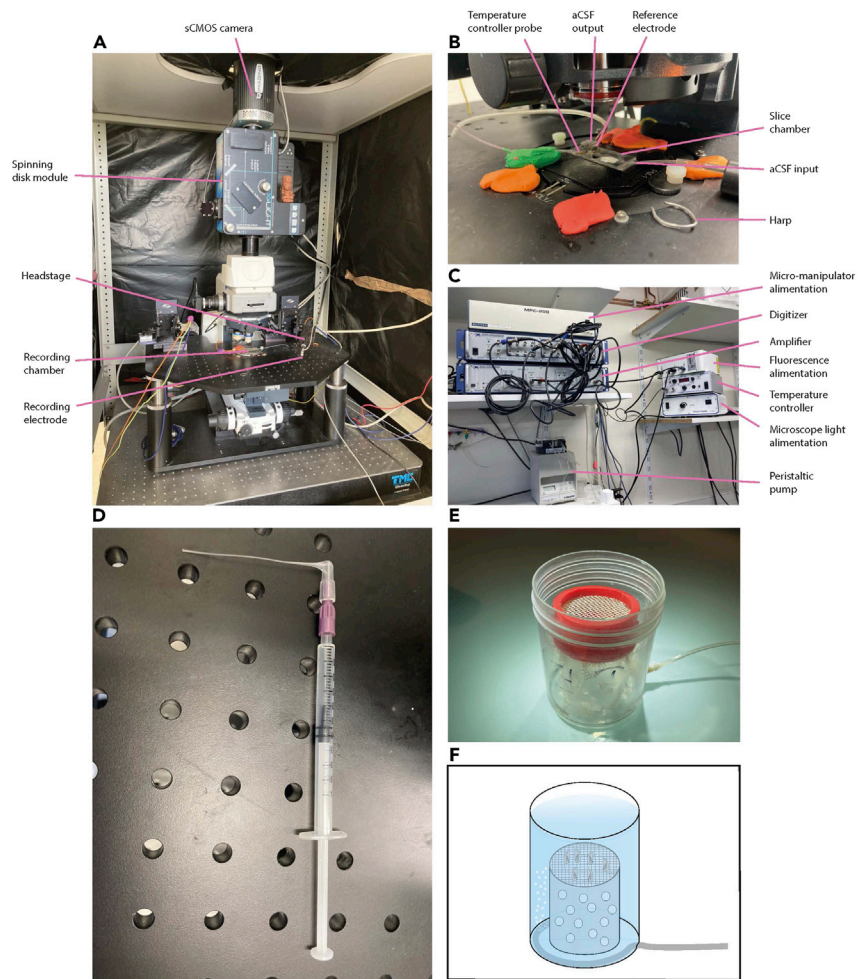


Figure 1. Material for calcium imaging and patching of astrocytes

(A) Microscope equipped with a spinning disk module and a sCMOS camera for calcium imaging. This microscope is placed on a Gibraltar table along with the recording chamber, the headstage and the recording electrode. The assembled instruments are placed on an anti-vibration table.

(B) Magnified photo of a recording chamber divided into 3 parts: one space for the slice and aCSF input, one for the aCSF output and one for the reference electrode. The harp is placed on the slice to avoid any movement during recordings.

(C) All the equipment needed for patch clamp (for more details, see [key resources table](#)).

(D) Example of a manually pulled tip used to fill the pipette in patch-clamp. The tip is mounted on a filter placed on a 1 mL syringe to avoid clogging the tip.

(E) Photo of a recovery chamber.

(F) Scheme of the recovery chamber, a pierced tube is fixed at the bottom of the chamber to bring carbogen in the aCSF of the chamber.

The calcium imaging setup is composed of a Zeiss Axio examiner microscope equipped with a 40× water immersion objective and a mounted X-Light Confocal unit – CRESTOPT spinning disk ([Figure 1A](#)). We use a LED light source for excitation and emission data are acquired at 2 Hz with an optiMOS sCMOS camera ([Figure 1A](#)). All of these hardware elements are interfaced with a computer running MetaFluor (ver. 7.8.8.0) software.

The patch-clamp setup is composed of an Axon MultiClamp 700B amplifier coupled to an ADC Digidata 1440A Digitizer ([Figure 1C](#)). Data are acquired at a sampling rate of 20 kHz and stored on a computer using the pClamp (ver. 10) software suite.

If needed, prepare aCSF, the perfusion solution and the internal solution in advance (see [materials and equipment](#)).

Experiments have to be performed in accordance with ethical rules and approbation from your local institutions.

Slice preparation

⌚ Timing: 2 h

1. Anesthetize the mouse with an *i.p.* injection of ketamine and paxman at 400 mg/kg and 80 mg/kg respectively.

Note: one can also use isoflurane inhalation followed by quick decapitation.

2. Access the heart by performing a laparotomy and a thoracotomy, being careful not to damage the internal organs ([Figures 2A and 2B](#)). Use a 50 mL syringe filled with cold (4°C) perfusion solution (see [materials and equipment](#)), insert the needle into the left ventricle and cut the right atrium. Exsanguinate the animal until there is no more blood flowing from the heart (typically, 10 mL is enough).

Note: Heart perfusion is not essential for young animals (<P30-40) to obtain proper slices.

Note: To perform the exsanguination, you can also use a peristaltic pump to have better control over the flow of the perfusion solution.

Note: Observe the liver during the perfusion. If the perfusion procedure is done properly, its color should change from red to almost white.

3. Once perfusion has finished, decapitate the animal using scissors. Place the head in a Petri dish containing cold oxygenated perfusion solution. Open the scalp using the scalpel and remove the part of the skull covering the brain using scissors and forceps ([Figure 2C](#)). Extract the brain from the skull and place it in another Petri dish filled with clean cold oxygenated perfusion solution.

Note: If you are fast enough (< 3 min), this step can be done outside the perfusion solution to save both time and solution. For the sake of reproducibility, we highly recommend that the first few attempts be done as described here until you get used to it.

⚠ CRITICAL: It is important to transfer the brain into a clean Petri dish immediately after extraction as the first Petri dish will contain blood and parts of the skull that might damage the brain tissue.

4. Using a scalpel, remove the cerebellum and the olfactory bulbs. Separate the two hemispheres by cutting along the sagittal axis ([Figure 2D](#)). Then, slice off a portion of the cortex to flatten the dorsal part of the brain ([Figure 2E](#)).

⚠ CRITICAL: It is important to cut the dorsal part of the brain as flat as possible to fix the brain correctly and have identical slices throughout the days.

5. Put some glue on the vibratome sample holder. Reassemble the brain ([Figure 2F](#)), fix it on its dorsal surface by sliding it from the spoon onto the sample holder, and slice it using a vibratome to obtain 350 µm thick slices. This will allow the slicing of both hemispheres together with the same accuracy ([Figure 2G](#)).

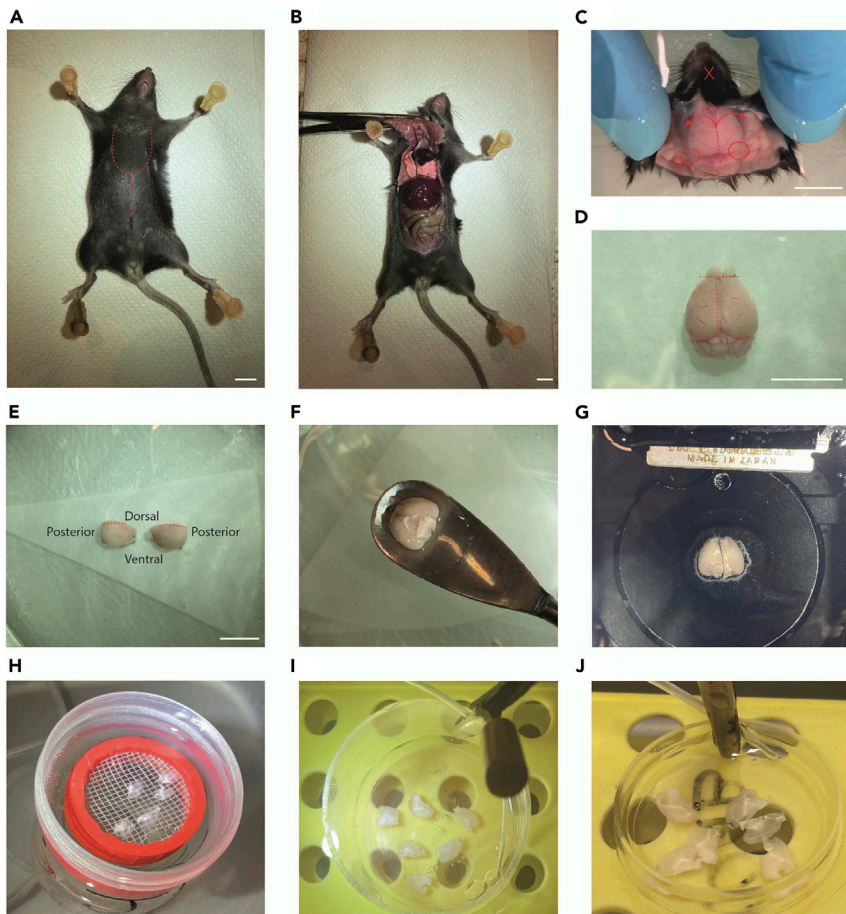


Figure 2. Slice preparation and dye loading

- (A) The mouse is fixed by the paws using syringe needles. The red dotted lines show where to cut for clear access to the heart.
- (B) Photo of the mouse after performing the laparotomy and thoracotomy.
- (C) After opening the scalp, cut the skull following the dotted red line. Then remove the two parts of the skull as indicated by the red arrows. The two red circles show important bones to remove to avoid damaging the brain during the extraction. Stick the tips of closed scissors in the red cross and open them to remove the lateral part of the skull. This last step is optional but facilitates brain extraction.
- (D) Brain after extraction. The red dotted lines show where to cut to remove the cerebellum, olfactory bulbs and hemisect the brain.
- (E) After hemisecting the brain, cut the two parts following the red dotted lines to flatten the dorsal part of the brain. Scale bar A–E = 1 cm.
- (F) Use a spoon-shaped tool to retrieve the brain after re-assembling it. Dry the remaining liquid and fix it on its dorsal surface.
- (G) Fixed brain before slicing.
- (H) Photo of the slices placed in the recovery chamber.
- (I) Photo of the slices placed in the culture well for SR101 staining.
- (J) Photo of the slices placed in the culture well for OGB1-AM loading.

Note: Use a spoon-shaped tool to put the brain on the vibratome sample holder. The glue we use sets when in contact with a liquid. Thus, dry the spoon and the dorsal surface of the brain as much as possible.

Note: We use a Leica VT1000S vibratome with the following parameters: (1) 0° blade angle; (2) 7.5 (75 Hz) vibration frequency; (3) 1 (0.05 mm/s) progression speed.

⚠ CRITICAL: during the slicing, it is essential to keep the solution containing the brain as cold as possible by adding ice around the slicing tank (you can also pour ethanol into the ice to keep it cooler). Failing to keep the solution cold enough will cause the brain to soften, which may cause it to be crushed by the razor blade. Furthermore, keeping the brain cold will reduce both the activity of degradation enzymes and the metabolic activity within the cells.

6. Transfer the slices into a recovery chamber containing aCSF (see [materials and equipment](#)), oxygenated with carbogen for 1 h at 25°C ([Figure 2H](#), for recovery chamber details, see [Figures 1E](#) and [1F](#)).

⚠ CRITICAL: Starting from this point, all manipulations have to be performed in the dark.

Slice incubations for SR101 dye loading

⌚ Timing: 30 min

7. While waiting for the slices to recover in the chamber, pour 10 mL of aCSF into a culture well and add 10 µL of SR101 (1 mM) so the final concentration of SR101 will be 1 µM. Connect a carbogen line to the well to make it bubble at a modest rate (~2–3 bubbles/second). Carefully position the bubbling culture well into the heating bath at 37°C ([Figure 2I](#)).

Note: You can make a platform with a test tube rack so the well will heat properly and not sink.

8. After 1-h recovery (step 6), transfer the slices from the recovery chamber into the culture well containing SR101 using either a brush or a Pasteur pipette and let them incubate for 20–30 min ([Figure 2I](#)).

Note: Make sure that the slices do not overlap with each other and that the carbogen bubbling does not move them around.

Slice incubations for calcium dye loading

⌚ Timing: 1 h

9. The following step is only applicable for calcium imaging.
 - a. During the incubation period of step 8, prepare the OGB1-AM solution. Add 2 µL of PF-127 (20% in DMSO) and 8 µL of Cremophor EL (0.5% in DMSO) in the OGB1-AM vial. Vortex 1 min. Wrap the vial in aluminum foil to avoid photodamage and ultrasonicate it for 10–20 min.

Note: If you do not have a sonication bath, you can use a thermomixer at max speed, 40°C for 10 min.

- b. Centrifuge the aliquot for 5 s to get all the droplets to the bottom of the vial. Carefully add 20 µL of aCSF to the vial and homogenize the solution by gently pipetting up and down without making bubbles.
- c. At the end of the SR101 incubation time, transfer the slices into a small culture well containing 3 mL aCSF. Put a carbogen line in the well and adjust the carbogen flow to produce 1 bubble every 2 s. Carefully position the bubbling culture well into the heating bath at 37°C ([Figure 2J](#)).

Note: Maintain the orientation of the slices such that the same side is loaded with both SR101 and OGB1-AM.

Note: Surfactants tend to produce foam that will desiccate the slices. Try to adjust the carbogen flow in such a way as to keep the bubbles along the well wall and not floating above the slices.

Note: You can also put the carbogen line just above the level of the aCSF such that it oxygenates the solution without producing foam. To do so, pipet 3 mL into the well and make a hand-made hole just above the level of the aCSF.

d. Slowly and carefully, deposit 6–10 μ L of OGB1-AM solubilized into Cremophor and PF-127 directly onto your region of interest to ensure that it will receive exposure to a high concentration of dye. Repeat the operation for all other slices. Incubate for 45 min to 1 h in the dark.

⚠ **CRITICAL:** Cover the incubation well with a lid to avoid evaporation and dehydration of the slices. Leave a tiny space between the lid and the well to allow carbogen to escape from the well.

Recovery

⌚ Timing: 1 h

10. After the incubation period, transfer the slices to a recovery chamber filled with aCSF oxygenated with carbogen. Incubate at 25°C for at least 1 h before starting experiments ([Figure 2H](#)).

Note: At this point, you can take a break to eat.

KEY RESOURCES TABLE

REAGENT or RESOURCE	SOURCE	IDENTIFIER
Chemicals, peptides, and recombinant proteins		
Oregon Green 488 BAPTA-1, AM, cell permeant – Special Packaging	Thermo Fisher Scientific	Cat#O6807
Sulforhodamine 101 (SR101)	Merck	Cat#S7635
NaCl	Sigma-Aldrich	793566
KCl	Carlo Erba	471177
NaH ₂ PO ₄	Sigma-Aldrich	S9638
NaHCO ₃	Sigma-Aldrich	S5761
D-Glucose	Sigma-Aldrich	G8270
MgSO ₄	Merck	63139
CaCl ₂	Carlo Erba	433381
NMDG	Sigma-Aldrich	M2004
HEPES	Sigma-Aldrich	H4034
L-Ascorbic Acid	Sigma-Aldrich	95209
Thiourea	Sigma-Aldrich	T8656
Sodium Pyruvate	Sigma-Aldrich	P2256
N-Acetyl-L-Cysteine	Sigma-Aldrich	A7250
Kynurenic acid	Alomone labs	K-110
BAPTA	Thermo Fisher Scientific	B1204
Na ₂ ATP	Sigma-Aldrich	A2383
Na ₂ GTP	Sigma-Aldrich	51120
MgCl ₂	Sigma-Aldrich	208337
PF-127	Sigma-Aldrich	P2443

(Continued on next page)

Continued

REAGENT or RESOURCE	SOURCE	IDENTIFIER
Cremophor EL	Sigma-Aldrich	238470-1 SET
DMSO	Sigma-Aldrich	D8418
Experimental models: Organisms/strains		
1–2 months old C57BL6/J male or female mice	Chronobiotron UMS3415	n/a
Software and algorithms		
MetaFluor 7.8.8.0	Molecular Devices	n/a
pClamp 10	Molecular Devices	n/a
uEye Cockpit	iDS software suite	n/a
MultiClamp 700b commander	Molecular Devices	n/a
Fiji	Schindelin et al. (2012)	https://imagej.net/software/fiji/downloads
Deposited data		
Example code	Alexandre Charlet's lab	https://github.com/AngelBaudon/Canal.git
Other		
Vibratome	Leica Biosystems	VT1000S
pH meter	Hanna instruments	HI 2210
Micro-osmometer	Löser	Type 6
Ultrasonic cleaner	Branson	5510-MT
Amplifier	Axon Instruments	Digitizer
Digitizer	Axon Instruments	MultiClamp 700B
Microscope	Zeiss	Examiner A1
Manipulators	Sutter Instrument	MPC-325
Light source (patch)	Lumen Dynamics	XT640-W
LED light source	Lumencor	7-CLX-NA
Peristaltic pump	Gilson	Minipuls 3
Anti-vibration table	Photon Lines	63-7590M
Recording chamber	Multichannel systems	RC-26G
Spinning disk	CrEST	X-LIGHT
sCMOS camera	QImaging	optiMOS
uEye camera	iDS	UI-1240LE-NIR-GL
Electrode holder + Ag wire	Warner instruments	QSW-T15P
Flaming/Brown micropipette puller	Sutter Instrument	P-97
Borosilicate glass	Sutter instrument	BF150-86-7.5HP
Nalgene 4-mm syringe filters purple	Thermo Fisher Scientific	176-0020
26G needle	Agani	SAN2613R1
Syringe 1 mL	Sigma-Aldrich	Z683531
Syringe 20 mL	Sigma-Aldrich	Z116882
Syringe 50 mL	Sigma-Aldrich	Z118400
Ketamine	Virbac France	211101
Paxman	Virbac France	221631
Qualitative filter paper 413	VWR	516-0817
Scalpel	Fine Science Tools	10004-13
Scalpel blades	Fine Science Tools	10021-00
Dumont forceps	Fine Science Tools	11254-20
Bonn scissors	Fine Science Tools	14184-09
Fine scissors – Sharp-blunt	Fine Science Tools	14028-10
Paintbrush	Princeton	Round – natural red sable
Loctite Superglue-3	Dutscher	999227

Note: The resources listed here are what we use at the time of writing this protocol. There are currently many different alternatives and new versions of some products may become available in the future.

MATERIALS AND EQUIPMENT

- aCSF

Reagent	Final concentration (mM)	Amount
H ₂ O	n/a	1 L
NaCl	124	7.2416 g
KCl	2.5	0.1864 g
NaH ₂ PO ₄	1.25	0.1725 g
NaHCO ₃	26	2.1843 g
D-Glucose	15	2.7030 g
MgSO ₄	2	0.493 g
CaCl ₂	2	0.294 g

Should be stored at 4°C. Maximum storage time ~2 weeks.

- Perfusion solution

Reagent	Final concentration (mM)	Amount
H ₂ O	n/a	5 L
NMDG	93	90.7773 g
KCl	2.5	0.9319 g
NaH ₂ PO ₄	1.25	0.8625 g
NaHCO ₃	30	12.6015 g
HEPES	20	23.8310 g
D-Glucose	25	22.5250 g
L-Ascorbic Acid	5	4.4030 g
Thiourea	2	0.7612 g
Sodium Pyruvate	3	1.6506 g
N-Acetyl-L-Cysteine	10	8.1595 g
Kynurenic acid	2.5	2.3646 g
MgSO ₄	10	12.324 g
CaCl ₂	0.5	0.3675 g

Should be stored and used at 4°C. Maximum storage time ~2 weeks. If you prepare large volumes, you can freeze it at -20°C and keep it for up to 1 year.

Note: You will have to use a lot of HCl while adjusting the pH.

Alternatives: You can also use sucrose instead of NMDG. We use it at a concentration of 180 mM and adjust the N-acetyl-L-Cysteine to 5 mM instead of 10 mM.

- Internal solution for astrocyte patch-clamp

Reagent	Final concentration (mM)	Amount
H ₂ O	n/a	50 mL
KMeSO ₄	125	838.75 mg
HEPES	10	119.15 mg
BAPTA	10	314.4 mg
Na ₂ ATP	4	110.228 mg
Na ₂ GTP	0.4	10.4636 mg
MgCl ₂	4	19.042 mg

Should be stored at -20°C and used at 4°C. Maximum storage time ~1 year.

Note: This last solution should be prepared and used on ice as ATP/GTP is unstable at room temperature. We recommend weighing and adding these two components last. As soon as ATP/GTP is added, keep the solution at 4°C.

Note: For the aCSF and perfusion solutions- after adding all powders to the water, bubble the solution with carbogen for about 15–20 minutes to activate the bicarbonate pH buffer. For all solutions, titrate the pH to 7.3–7.4 at room temperature (RT; 20°C–25°C) (except the internal solution at 4°C to avoid ATP/GTP degradation), as needed, using HCl or NaOH to acidify or alkalinize the solution, respectively. Because CaCl₂ equilibrates slowly, we add it after pH titration.

If needed, adjust the osmolality to 300 ± 10 mOsm/kg by adding water or NMDG/glucose/sucrose to decrease or increase the osmolality, respectively.

Note: It is not recommended to adjust the osmolality as it will change ions concentrations. It is preferable to optimize the protocol beforehand to have the correct osmolality every time.

- Required tools

Equipment	Surgical instruments	Consumable
<ul style="list-style-type: none"> Carbogen gas supplier (95% O₂, 5% CO₂) Vibratome Leica VT1000S Heating bath Fluorescence microscope Recording chamber (Figure 1B) Peristaltic pump For calcium imaging: spinning disk (Figures 1A–1C) For BAPTA loading: Patch-clamp set-up (Figures 1A–1C) Recovery chamber (Figures 1E and 1F) pH meter Osmometer 	<ul style="list-style-type: none"> Scalpel Forceps Scissors Paintbrush Superglue 	<ul style="list-style-type: none"> Ketamine (400 mg/kg) Paxman (80 mg/kg) 1 mL/20 mL/50 mL syringe 26G needle Blotting paper aCSF Perfusion solution OGB1-AM SR101 PF-127 (20% in DMSO) Cremophor EL (0.5% in DMSO)

STEP-BY-STEP METHOD DETAILS

Calcium imaging of astrocytes

⌚ Timing: 3–7 h

Astrocytes, as with any glial cell, do not fire action potentials. However, they do exhibit calcium-based excitability in certain contexts ([Charles et al., 1991](#)). For instance, the cytosolic calcium concentration of astrocytes increases in response to many types of stimuli such as neurotransmitter signaling, mechanical stimulation and variations in pH ([Khakh and Benjamin, 2019](#)). The following protocol describes a method to monitor these calcium fluctuations in astrocytes.

Follow the initial steps (1–10) for slice preparation, as described in the preparation section above.

- Transfer the slices into an aCSF filled recording chamber (see [key resources table](#)) connected to a peristaltic pump that provides a continuous flow of oxygenated aCSF (~2 mL/min) at room temperature (or any temperature as needed by the experiment).
- Place a holding harp on top of the slice to prevent movement.

Note: make sure that the strings of the harp are not too close to the recording site. Otherwise, it will bend your slice and thereby prevent consistent focus with the microscope.

3. Use an Axio examiner Zeiss microscope (or Olympus BX51WI Japan for example) with a $4\times$ objective to identify your region of interest. Set the microscope to infrared differential interference contrast (IR-DIC, $\lambda = 750\text{--}790\text{nm}$) and visualize the image with the uEye cockpit software (or Andor iQ 3.2 for example).

Note: Use an appropriate atlas to identify landmarks that will help you locate your structure of interest.

4. Switch to a $40\times$ water-immersion objective and find the surface of the slice.
5. Open the MetaFluor software and click the “Configure” menu to set the following parameters:
 - a. Spinning disk pinhole diameter: $70\ \mu\text{m}$.
 - b. Spinning disk rotation speed: 15.000 rpm.
 - c. Wavelength: 575 nm for SR101, 475 nm for OGB.
 - d. Exposure time: 20 ms for SR101, 80 ms for OGB.
 - e. Illumination intensity: 220 μW for SR101, 580 μW for OGB.
 - f. Exposure time: 20 ms for SR101, 80 ms for OGB.
 - g. Sampling frequency: 2 Hz (500 ms interval between acquisitions).

⚠ CRITICAL: Before switching on the fluorescent light, do not forget to put your microscope in confocal mode. The high intensity of the wide-field mode will bleach the calcium indicator.

⚠ CRITICAL: Finely tune your illumination time and intensity to avoid fluorescence bleaching. To do so, we recommend starting at an illumination intensity of 0 μW and an illumination time of 20 ms then progressively increase both values. In our hands, we typically set the illumination intensity between 580 μW and 1040 μW and find that good OGB1 loading can be seen at an illumination time of 20 ms. We never illuminate more than 100 ms.

6. Cells labeled with SR101 are astrocytes.
 - a. Find a focal plane that includes several of them ([Figure 3A](#) & [Method video S1](#)).
 - b. Check the shape of the cells: a healthy cell must have a ramified morphology with observable proximal processes ([Figures 3A](#) and [3B](#)). If the cells exhibit a round, swelled shape, it may indicate that these cells are dead or dying. If so, refer to [Troubleshooting](#).
 - c. You can observe 3 kinds of cells: (1) the ones that are labeled with both markers (SR101 and OGB, yellow merge in [Figure 3A](#)), indicating that astrocytes are well loaded with both indicators; (2) the cells SR101 negative, that are probably neurons; and (3) cells labeled with SR101 but that are OGB1 negative.

Note: In this last configuration, try to run the experiment anyway, the labeling is maybe too weak to be seen at resting state but can be enough to detect calcium transients. If you did not see any variation of the OGB1 fluorescence, refer to [Troubleshooting](#).

Note: To guarantee a good signal/noise ratio, you must adjust the focal plane in such a way as to both see the cell and distinguish the proximal processes.

7. Click on “Save pictures” and choose an appropriate folder. Click on “Zero clock” and then “Start”. Your data must be saved as independent pictures in the selected folder. At the end of a 10-min recording, you should have 2400 pictures (1200 for the SR101 channel and 1200 for the OGB1 channel).

Note: Because the files produced are very large, be sure that you correctly set the sampling frequency regarding the event you want to observe. The sampling frequency should be at

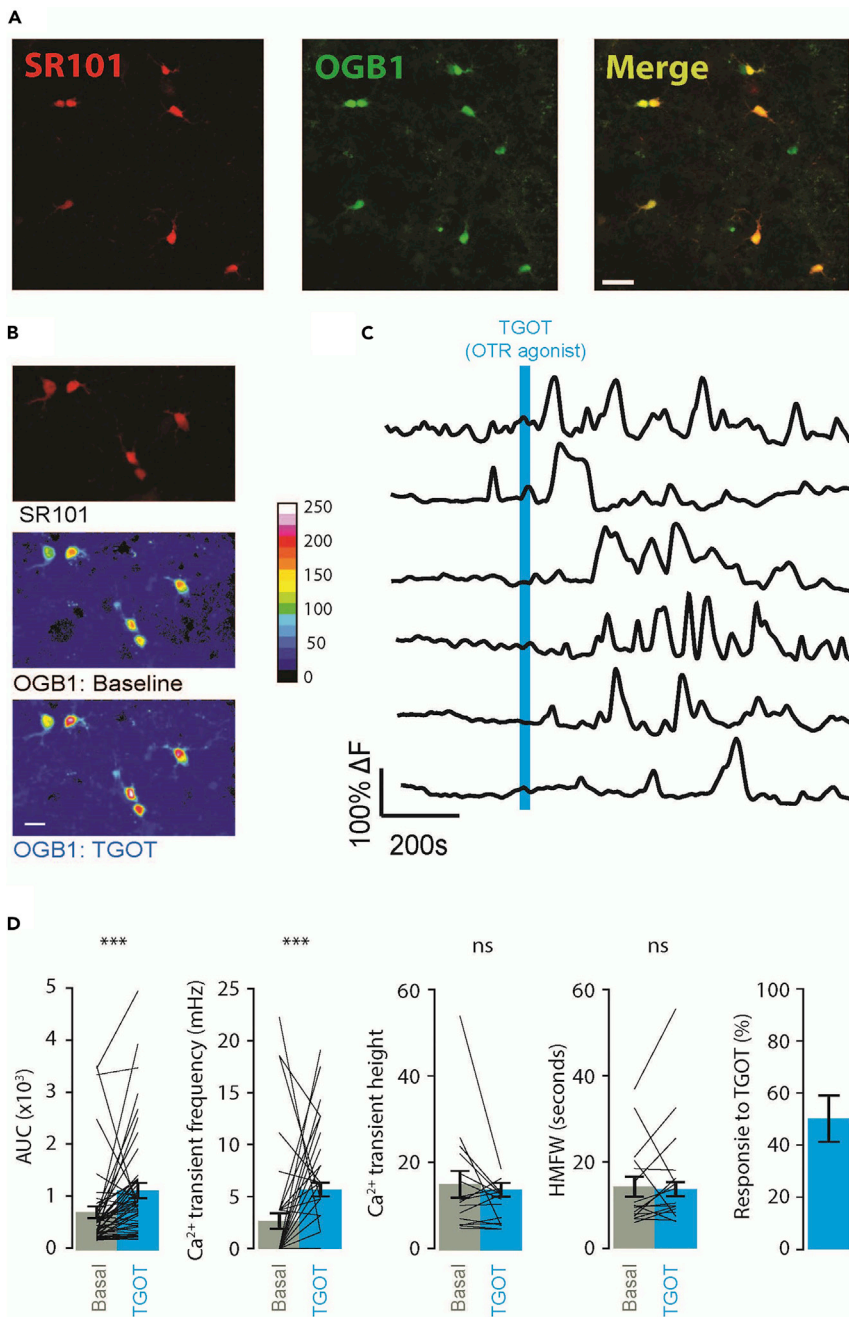


Figure 3. Expected results from a calcium imaging experiment

(A) Stacked picture of SR101 staining (left), OGB1 staining (middle) and the merge of both labels (right). Scale bar = 50 μm .

(B) Pseudo-colored images showing the increase of fluorescence after application of an OTR agonist (TGOT 1 nM 10 s duration) on OGB1-loaded astrocytes. Upper panel: SR101 staining; middle panel: basal OGB1 fluorescence; lower panel: OGB1 intensity after application of an OTR agonist (TGOT 1 nM, 10-s duration). Scale bar = 50 μm .

(C) Traces of OGB1 fluorescence over time. The blue bar represents the application of TGOT 1 nM 10-s duration.

(D) Quantification of the effect of TGOT 1 nM on astrocytic activity. From left to right: variation of AUC, frequency, calcium transient height, half-max full width (FWHM), and proportion of responsive cells after TGOT application. The gray histograms represent baseline values and the blue histograms represent the quantification of the TGOT effect. Data are represented as mean \pm SEM. *** $p < 0.001$, Paired t test.

least twice as high as the maximal frequency of the events recorded (see Nyquist-Shannon theorem). For somatic global calcium transients that last for more than 2 seconds, a 2 Hz sampling frequency is sufficient. In our hands, a 10-minute recording at 2 Hz results in an individual picture size of ~1 MB (~2.4 GB of pictures in total).

- At the desired time, apply a drug or any kind of stimulation to see if it changes astrocyte calcium activity. We apply an oxytocin receptor agonist, the TGOT at [1 nM] for 10 s through the perfusion system ([Figures 3B–3D](#)).

Note: If your perfusion aCSF is in a close loop, be sure to discard the solution for ~5 minutes to avoid contamination of your clean aCSF stock.

Patch-clamp-mediated BAPTA loading of astrocytes

⌚ Timing: 3–7 h

Astrocyte communication is largely based on intracellular calcium signaling ([Khakh and Benjamin, 2019](#)). Thus, blocking these transients using calcium chelators will inhibit astrocytic activity. As astrocytes create a large network interconnected via gap junctions, loading a chelator in just a few astrocytes is sufficient to block calcium transients across a local network. Thus, this approach can be used to observe the effects of blocking calcium-dependent astrocyte communication on the activity of a nearby neuronal network. In this section, we describe the detailed steps needed to perform patch clamp on an astrocyte and the protocol used to load BAPTA into the astrocytic network. This experiment can also be performed with other calcium chelators such as EGTA, but we choose to use BAPTA because its binding kinetics is ~40 times faster than EGTA, allowing for the blockade of local and rapid calcium transients ([Naraghi and Neher, 1997](#)).

Optional: this protocol can be used in combination with the calcium imaging of astrocytes. If you intend to do so, please follow the ‘optional’ steps such as this one that indicates what steps are required from both protocols.

Follow the initial steps (1–10, except step 9) for slice preparation, as described in the preparation section above.

Optional: If you intend to perform BAPTA loading together with calcium imaging, follow the initial steps (1–10, including step 9) for slice preparation, as described in the preparation section above.

- Transfer the slices into an aCSF filled recording chamber connected to a peristaltic pump that provides a continuous flow of oxygenated aCSF (~2 mL/min) at room temperature (or any temperature as needed by the experiment).
- Use an Axio examiner Zeiss microscope (or Olympus BX51WI Japan for example) with a 4× objective to identify your region of interest. Set the microscope to infrared differential interference contrast (IR-DIC, $\lambda = 750\text{--}790\text{ nm}$) and visualize the image with the uEye cockpit software (or Andor iQ 3.2 for example).
- Switch to a 40× water-immersion objective and find the surface of the slice.

Note: At this point, you should visualize the cells with infrared illumination to verify that the slice is ‘healthy’. Check that there are no or only a few dead cells, which can be discriminated by their round shape and absence of clear edges.

- Visualize SR101 labeled astrocytes by illuminating the slice with yellow ~575 nm light. Once you identify your shining star (i.e., the cell you want to patch), do not adjust the microscopic stage position (in neither the x nor y-axes) or you may lose track of it ([Figure 4A](#)).

Note: One should keep several considerations in mind when choosing a cell to patch: (1) Deep cells are harder to visualize and are more easily disrupted by the pipette-induced movement of the tissue above. (2) A healthy cell is not round. (3) Bigger cells are easier to patch.

Optional: If you intend to perform BAPTA loading together with calcium imaging, also refer to step 5 and 6 and try to find several healthy astrocytes in the same stage position.

Note: In uEye Cockpit, press 'Ctrl + right click' to place a marker on the screen. This will help you return to the cell more easily. Alternatively, place a small chunk of putty (e.g. Play Dough) on the screen for each target cell.

13. To get a pipette above the slice:

- Raise the objective far away from the slice, while still keeping the lens submerged in the solution.
- Take a pulled pipette (borosilicate glass; outer Ø: 1.5 mm; inner Ø: 0.86 mm; length: 7.5 cm, see [key resources table](#)) previously filled with the internal solution.

Note: To create a pipette filler: place a pipetman tip on a 1 mL syringe. Use a flame to heat the tip and pull it until it is thin enough to enter the pipette, blow air into it with the syringe while doing this to avoid clogging. Use a razor blade to cut the end of the pulled tip and then verify that it is not blocked by pushing water through it. If the water does not flow through the tip, replace it and start over. It may take several attempts to obtain a working tip (see [Figure 1D](#) for an example of how it should look).

- Insert the pipette onto the AgCl electrode.
- Put positive pressure (about 1 mL of air with a syringe). This will help avoid clogging your pipette while moving through the tissue. Position the pipette in the bath using the manipulator.
- If you are using pClamp, use the membrane test to determine the resistance of the pipette (if the signal is drifting, see [troubleshooting](#)). Otherwise, in voltage-clamp, apply a voltage step of 5–10mV and measure the current transients to calculate the pipette's resistance using Ohm's law. It must be $\sim 6 \pm 2 \text{ M}\Omega$ (see [troubleshooting](#) for more details). A lower value means the tip is too large (or broken) and a higher value means the tip is too thin. In either case, it will be difficult to patch a cell.

Note: The instruction manual of your pipette puller contains helpful instructions on how to pull the pipette to achieve the desired resistance.

- Under infrared light, bring the pipette tip under the objective using the micromanipulator. Move the pipette along the x and y axes until you see a shadow moving on the screen of the computer and then adjust the objective to focus on it. Then, move the pipette until the tip is in focus.

Note: While positioning the pipette tip, it is important to continuously monitor both the computer screen and the actual pipette to ensure the tip does not hit any obstacles (e.g. the objective).

⚠ CRITICAL: Once the pipette is in the bath, extreme caution must be used when moving it along the z-axis. Uncontrolled movement of the pipette can result in damage to both the tissue and the recording chamber.

- The next goal is to safely lower the pipette just above the slice.
 - First, lower the objective.

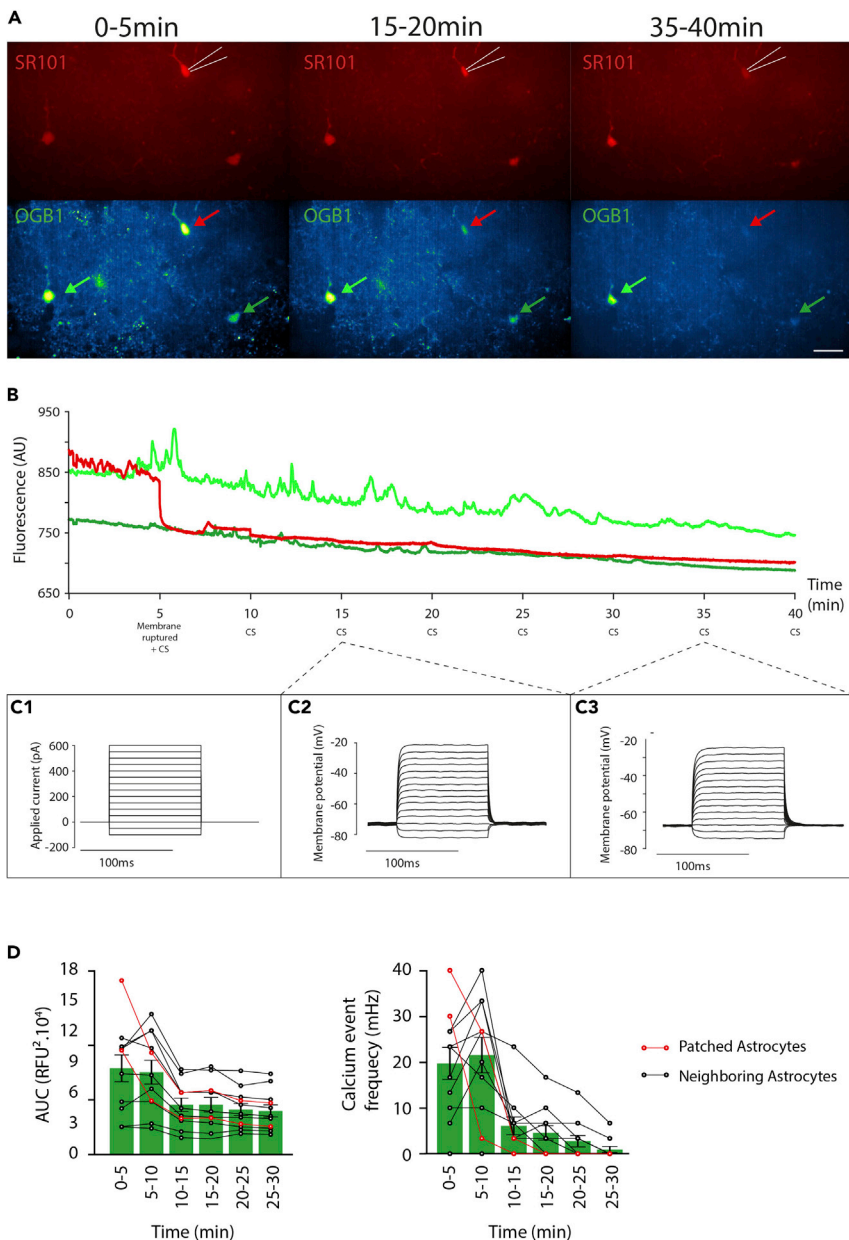


Figure 4. Patch-clamp mediated BAPTA loading in astrocytes

(A) Pseudo-colorized images showing SR101 (top) and OGB1 (bottom) at the beginning of the recording (left), after 15 min (middle) and 35 min (right) of recording. The white lines represent the pipette. The three arrows indicate the signals of the cells shown in (B). Scale bar = 50 μ m.

(B) Raw signals showing the evolution of OGB1 fluorescence from the same three cells shown in A that were recorded for 40 min. At 5 min, the patched cell membrane is ruptured (orange).

(C) Example of current step (CS) realized during the recording in (B). Left: command step of the CS: 15 steps of 100 ms starting at -100 pA and incremented by 50 pA. Right: membrane potential of the astrocyte recorded in response to the CS.

(D) Quantification of the effect of BAPTA loading in astrocytes. Left: Quantification of the area under the curve (AUC) of calcium measurement in astrocytes. This value is expressed in relative fluorescence unit² (RFU²). Right:

Quantification of calcium transients in astrocytes. The astrocyte membrane is ruptured at 5 min. The red points indicate the values for patched astrocytes and the black ones for neighboring cells. Data are represented as mean \pm SEM.

- ii. Then lower the pipette until you can see it again.
- iii. Repeat this sequence until you are just above the slice.

Note: you cannot go all the way down with the objective because you will bend/break the pipette and you cannot go down only with the pipette because you will not know when you will be near the tissue.

14. Once you are just above the tissue.
 - a. Position the pipette tip above the targeted cell, slightly to its side.
 - b. Switch the microscope channel to see the fluorescent labeling of astrocytes.
 - c. Lower the pipette down into the tissue until you are on the same level as the top of the target cell.
 - d. Move the pipette toward the cell (see [Method video S1](#)).

Note: To make positioning of the pipette easier, you can move the objective up and down to help identify your current location within the tissue.

Note: Usually, it is easier to approach the cell diagonally.

15. Two indicators can be used to confirm you are on the target cell.
 - a. The first is visual: the positive pressure within the pipette creates a visible deflection (dimple) on the membrane.
 - b. The second indicator is the pipette resistance: when you get close enough to the cell, the tip of the pipette becomes enclosed by a pocket of membrane and thus increases the resistance. You can expect an increase of about $0.2\text{ M}\Omega$ – $1\text{ M}\Omega$ (see [Method video S1](#)).
16. Release the positive pressure (this increases the resistance as more membrane enters the pipette).

Note: When releasing the positive pressure, the resistance should increase up to at least $15\text{--}20\text{ M}\Omega$. The better the pipette is positioned on the cell, the higher the resistance will go (sometimes even directly up to gigaseal).

17. Gently apply negative pressure by mouth until you achieve a gigaseal (i.e., a pipette resistance of several $\text{G}\Omega$).

Note: After reaching $100\text{ M}\Omega$, start holding the potential at the desired membrane potential value (-80 mV), this will help reach the gigaseal.

Note: Astrocytic membranes are much more fragile than neuronal membranes. If you are accustomed to patching neurons, then be extra gentle during seal formation and membrane opening.

Optional: To confirm that calcium has been correctly chelated by the BAPTA in the patched cell, start the calcium imaging (see step 7) once the giga seal is reached. Wait 5 min before opening the cell.

18. When the gigaseal is reached, apply negative pressure in the pipette by repetitive suctions until the membrane opens.
19. If the astrocyte opens correctly, you will see capacitive transients and the resistance will drop by several tens of $\text{M}\Omega$. You can also look at the calculated membrane resistance by clicking the "Cell" button on pClamp. This resistance must be $\sim 20\text{ M}\Omega$ for astrocytes and $\sim 200\text{ M}\Omega$ for neurons in the central amygdala.

Optional: If you are performing calcium imaging at the same time, you should see a drop in the fluorescence of the patched cell ([Figure 4B](#) & [Method video S1](#)).

20. Switch to current-clamp mode to check the resting membrane potential, which should be around $-80/-90$ mV.
 - a. Apply current steps of 15 steps starting at -100 pA incremented by 50 pA and lasting 100 ms each. This is to verify that the patched cell is truly an astrocyte.
 - b. Thus, the membrane potential should have increased to at least -30 mV and you should not have seen any action potentials ([Figure 4C](#)).

Note: If the patched cell is a neuron or even if you just patched a presynaptic terminal, you should see action potentials ([Bischofberger et al., 2006](#)).

21. Wait 20 min ([Wallraff et al., 2006](#)) to let the BAPTA diffuse in the astrocyte network. Monitor the access resistance regularly to make sure the membrane of the astrocyte is still open and that the astrocyte is still alive.

Optional: If you are performing calcium imaging and patch-mediated BAPTA loading simultaneously, you will observe an immediate fluorescence quenching in the patched cell and a progressive loss of fluorescence in the neighboring astrocytes after $10-20$ min. For more details, see [expected outcomes](#) and [Figure 4](#).

22. Remove the pipette very slowly and carefully along the x-axis, as this is the best direction for avoiding damage to the cell. It is extremely important to avoid any damage to the cell during this step, as the goal is to reseal the membrane.

Note: When the membrane is resealed, you should see the pipette resistance reach the $G\Omega$ range again as you will inevitably tear off a part of the membrane during removal.

23. Repeat all the steps from 13 to 21 on another astrocyte located approximately one screen (200 μ m) apart to ensure the efficient diffusion of BAPTA within the local network.

EXPECTED OUTCOMES

Here, we share a protocol to investigate the involvement of astrocytes and their networks in brain function. We present *ex vivo* approaches to both monitor astrocytic calcium activity ([Figure 3](#)) and interfere with their activity at the microcircuit scale ([Figure 4](#)).

While one can also investigate astrocytic membrane potential changes using patch clamp in a current clamp mode, tracking of fluorescence variations using a calcium sensor, such as OGB1, in the cytosol further allows one to test whether astrocytes respond to a given stimulus using calcium-associated mechanisms. To distinguish astrocytes from other cells, we use SR101 because it allows a relatively simple way to label astrocytes in wild-type mice. Thus, by selecting cells labeled with both SR101 and OGB1 ([Figure 3A](#)), we can restrict our measurements of calcium-mediated OGB1 fluorescence variations to putative astrocytes only ([Figures 3B and 3C](#)). Alternatively, one can use genetically labeled astrocytes (e.g., GFAP-GFP mice, [Zhuo et al., 1997](#)).

The protocol described here can achieve a variety of experimental goals. One classical experiment is the application of a given drug to quantify its effects on astrocytic calcium signaling. For example, we applied the oxytocin receptor agonist, TGOT [1 nM], for 10 s via the peristaltic perfusion system used to supply aCSF to the recording chamber. One of the outputs of this experiment was a video recording that allowed us to assess visually the effects of an applied pharmacological agent to astrocytic calcium activity. The output data can further be used to quantify several effects of interest

through calculations such as the global area under the curve (AUC), the frequency of calcium transients, the duration of calcium transients, etc. (Figure 3D). You can find an example of these calculations in the following section, [quantification and statistical analysis](#).

A fine analysis of the calcium signals may answer numerous critical questions regarding the upstream mechanisms that trigger calcium transients in astrocytes. However, this technique alone does not provide information about the downstream effects of calcium signaling in astrocytes. Therefore, we also present here a protocol to load the calcium chelator, BAPTA, specifically into a local astrocyte network to disrupt calcium-dependent cellular mechanisms (Figure 4). This approach does not alone produce results *per se* but it may be coupled to other recording techniques. For example, one method to validate BAPTA diffusion in the astrocytic network is to incorporate the use of calcium imaging. To do so, we load astrocytes with SR101 and OGB1 (See Calcium imaging of astrocytes) and then patch SR101 positive cells (See [patch-clamp-mediated BAPTA loading of astrocytes](#)). The output recording allows us to observe a rapid reduction of OGB1 fluorescence in the patched cell followed by a slower reduction of fluorescence in other cells within the same field of view (Figures 4A, 4B, and 4D; [Method video S1](#)). Another application of this method is to load BAPTA into astrocytes and then record the neuronal activity from a nearby network. For example, our group has previously used this method to uncover the critical role of astrocyte-mediated neuromodulation on oxytocin signaling mechanisms in amygdala neuronal networks ([Wahis et al., 2021](#)).

QUANTIFICATION AND STATISTICAL ANALYSIS

In this section, we provide some examples of how to analyze the calcium imaging data. Note that the following examples are by no means an exhaustive list of possible analyses, which should always be chosen within the context of the scientific question being addressed.

1. Launch the open-source FIJI software ([Schindelin et al., 2012](#), available here) and import your recordings.
2. Adjust the brightness and contrast to visualize the cells (Image → Adjust → Brightness/Contrast) and check the quality of your recording. If you see motion artifacts, correct them with a motion correction macro (see Nicholas Schneider's macro available here, instructions here). In our case, we perform recordings in a single plane, therefore all recordings that drift along the z-axis cannot be corrected and must be removed.
3. Run the Bleach correction module (Image → Adjust → Bleach Correction, documentation here). We use the "Simple ratio" method as we have found that it produces adequate correction with minimal distortion of the data.
4. Select the "Oval" tool on the FIJI toolbar and manually draw the Region of Interest (ROI) on the SR101 video, then add it to the ROI manager by pressing the [t] shortcut. Click "Show all" to see which ROIs you have already drawn.
5. Extract the fluorescence signal from each ROI by clicking "More → Multi Measure" in the ROI manager panel. A window containing a table of the results will pop up when it is complete. You can save the table directly or copy the results into a spreadsheet.
6. Open the saved results in the analysis software of your choice. Below, we describe an analysis pipeline that uses a python-based routine (available in the [resource availability](#) section), but the analysis can be applied to any programming language.
7. Preprocessing:
 - a. Read-in the ROI data extracted from Fiji and plot the SR101 data to check if the curve is stable. The intensity of the dye should be constant over time, so if the SR101 curve is not straight then consider rechecking the raw recording for motion or drift in the z-axis. If a motion correction routine is not enough to correct SR101 intensity changes, then exclude the recording from further analysis.
 - b. Correct potential micromovements by subtracting the OGB1 signal from the SR101 signal. Note that a simple subtraction method would introduce noise from the SR101 signal into

the OGB1 signal. For that reason, we perform a polynomial regression on the SR101 curve using the Savitzky-Golay filter of the `scipy.signal` library (`window = 51`, `order = 1`) to estimate the trend of the SR101 curve. Doing so, we can subtract the trend of the SR101 trace without introducing noise into the OGB1 signal.

- c. Smoothen the resulting curve without modifying the calcium transient dynamics by applying another, less-stringent polynomial filter (`savgol_filter`, `windows = 11`, `order = 3`).
- d. Define two analysis windows: one for the quantification of the baseline activity and another for the quantification of the effect of stimulation. In our recordings, we stimulate astrocytes by applying the oxytocinergic agonist TGOT [1nM] for 10 s, 5 min after the recording begins. Therefore, the windows we select are: (1) 0–5 min for baseline, and (2) 5–10 min for the TGOT effect.
- e. If the windows you choose have different sizes, calculate a ratio to normalize the data according to the duration of each window. For example, if the first window (baseline) is 5 min and the second is 10 min, you must normalize the analyzed parameters (number of calcium transients, area under the curve...) according to the relative duration of each window. To do so, calculate a ratio based on the duration of each window with the following formula:

$$r = \frac{\text{duration of window 1}}{\text{duration of window 2}}$$

8. Processing:

- a. Find the area under the curve (AUC) for each cell using a trapezoid method. Ensure that the function you choose to apply does not evaluate the negative AUC, otherwise it will bias your results by summing the upward and downward deflections. In our case, we remove all negative values before using the “`trapz`” function of the “`NumPy`” package. Split the resulting AUC values according to your analysis windows then sum the data and normalize it with the previously calculated ratio.
- b. Find calcium transients in your curve using the “`find_peak`” function of the “`scipy.signal`” library. The parameter of the detection depends on the events you want to identify. An important consideration here is the detection threshold, which must be proportional to the standard deviation (SD) of the curve. One issue with this method is that highly active cells have higher SDs, which results in fewer detectable peaks. To avoid this issue, we perform a non-stringent polynomial regression (`savgol_filter(windows = 31, order = 3)`) and subtract it from the curve to obtain the residuals (i.e., the noise without the peaks). We then calculate the SD of these residuals and use it as the threshold for peak detection. In our case, we use a minimal height of $8 \times \text{SD}$, a prominence of $5 \times \text{SD}$ and a minimal inter-peak distance of 10 points (corresponding to 5 s in our recordings with a 2 Hz sampling frequency). The height is the minimum height in absolute value and the prominence is the relative height compared to neighboring peaks. This last parameter avoids multiple detections of the same peak that satisfy the “height” parameter. Once you have the index of each peak, compute their frequency within each of the chosen analysis windows.
- c. For each calcium transient index, find the amplitude of each peak. Then, calculate the half-maximum amplitude to measure the Full Width at Half Maximum (FWHM) to evaluate the duration of each peak. We choose to compute the FWHM because it is more reliable than the total duration, wherein you have to find the precise foot peak, which can be especially difficult in calcium imaging due to the potential for slow rise/decay.
- d. Evaluate the responsiveness of each cell to the stimulation. To do so, compare the calcium transient frequency and the AUC during the baseline and drug exposure. We base the response criteria on both calcium transient frequency and AUC to cover the diverse variety of responses observed (e.g., numerous calcium transients and/or single important transient). The baseline activity of astrocytes is heterogeneous due to the stochastic occurrence of

calcium transients. Therefore, we do not evaluate the response based on the SD of the baseline, but rather as a percentage of calcium transient frequency and/or the AUC increase before versus after drug exposure. We classify an astrocyte as responsive if the frequency of calcium spike or AUC increases by 20% after drug exposure.

9. Run paired statistical tests to evaluate if the applied stimulus modified astrocyte activity. If you have two quantification windows, evaluate the normality of your data using a Shapiro-Wilk test and, depending on the result, run either a parametric paired t test or a non-parametric Wilcoxon test. If you have three or more quantification windows, check the normality of the data and their homoscedasticity with a Levene's test. If data follow a normal distribution and their variances are equal, run a One-Way repeated measure ANOVA followed by a pairwise Tukey HSD post-hoc. Otherwise, run a Friedmann test followed by a Conover post-hoc test and a Bonferroni correction of the p value.

LIMITATIONS

The present protocol provides a relatively easy method to selectively label, monitor and disrupt the activity of astrocytes. However, there are several technical limitations to consider.

First, the loading of the AM coupled calcium indicator involves the use of a detergent, which affects the viability of the cells. Indeed, if the slices spend too much time in the AM dye mix, you will likely see several dead cells under the microscope (i.e., swollen and circular).

Another potential problem of this dye loading method is the intracellular distribution of the indicator. While AM loading of calcium indicators is an easy way to infuse the dye in the cytosol of cells, it only provides calcium signals from the soma and the proximal processes. This is of particular importance for astrocytes because they have a huge surface/volume ratio, where the processes represent ~95% of the cell surface ([Khakh and Benjamin, 2019](#)) and therefore the inability of the dyes to reach the distal processes may have a significant impact on the resulting observations. To overcome this limitation, Khakh's laboratory has developed membrane-tethered variants of the GCaMP3 and GCaMP6f genetically encoded calcium indicators (reviewed in [Shigetomi et al., 2016](#)). Another potential approach is to patch astrocytes with a version of OGB1 that cannot cross the membrane. In this way, high concentrations of OGB1 can be achieved in the cytosol, which would cause the dye to diffuse further into the processes and thereby allow for better visualization. However, this latter approach involves a disruption of the astrocytic membrane and a dilution of the cytosolic content by the intra-pipette solution, which can severely affect astrocytic integrity.

Another limitation to consider is that calcium indicators tend to bleach easily. While this is not a problem for short recordings (<30 min), the change in gain can be substantial across longer recordings. Additionally, in this protocol, we load a non-ratiometric calcium indicator ([Maravall et al., 2000](#)). This can be a limitation if you want to compare the AUC across different astrocytes because it is impossible to load each cell identically and thus the gain will vary from cell to cell. However, this issue can be overcome by normalizing the data for each cell with its baseline values.

Since calcium indicators are derived from chelators (e.g., OGB comes from BAPTA), indicator loading in the cell perturbs the endogenous calcium toolbox. Indeed, it has been shown that the loading of such indicators changes the diffusion dynamics of calcium into the cell, shortening its reach and decreasing the concentration of free calcium ions in the cytosol ([Semyanov et al., 2020](#)). For these reasons, it is not recommended to couple that type of loading with the measurement of the downstream effects of calcium signaling.

We base our identification of astrocytes on SR101 staining. This method is widely used because it is quite simple to implement either *in vivo* or *ex vivo*. SR101 is taken up into the cytosol of astrocytes through the thyroid hormone transporter OATP1C1 ([Schnell et al., 2015](#)). However, the specificity of such labeling is controversial and quite heterogeneous among brain regions ([Hülsmann et al., 2017](#)).

In our case, all SR101-positive patched cells did not fire action potentials and had a low membrane resistance, strongly suggesting an astrocytic identity. Moreover, it has been shown that SR101 can be cytotoxic at high concentrations and produce seizure-like local field potential activity *in vivo* (Rasmussen and Nedergaard, 2016). In our hands, we did not observe excessive cell death during the experiments.

The size of the astrocytic network within the structure being studied introduces another limitation concerning the loading of BAPTA. Simply put, the more astrocytes within a given network, the harder it will be to disrupt the activity of the whole astrocytic network. This limitation could technically be overcome by patching more astrocytes; however, this would result in very long protocols. An alternative approach could be to disrupt astrocytic network function using genetic models. For instance, the exogenous expression of Calcium Exchanger (CalEx) in astrocytes can decrease calcium signaling in these cells by extruding cytosolic calcium (Nagai et al., 2021).

Finally, the present protocol describes how to monitor/disrupt astrocyte activity in brain slices. However, this approach introduces bias in that the slicing procedure considerably changes cell activity and connectivity. To overcome this issue, one can perform *in vivo* calcium imaging using genetically encoded calcium indicators, such as GCaMP (for a complete protocol, see Tang et al., 2021).

TROUBLESHOOTING

Problem 1

The slices roll when the razor blade cuts the brain (step 5 of “[Slice preparation](#)”).

Potential solution

Try to reduce the speed of the Vibratome or increase the vibration frequency of the blade. If this is not enough to produce good slices, be sure that your slicing milieu is cold enough (4°C) by adding some ice and/or some ethanol around the tank.

Problem 2

There are many dead cells in the slice (step 6 of “[calcium Imaging of astrocytes](#)”).

Potential solution

A high occurrence of cell death can be explained by several factors:

The brain extraction was too slow and/or it was damaged during the process.

The perfusion solution is not cold enough during the slicing procedure. To prevent this, you can put a thermometer in the slicing tank. If the temperature is above 4°C, add some ice until it reaches the very top of the slicing tank. You also can add some ethanol on the ice.

The incubation time of AM dye is too long. Consider reducing it. For some potentially cytotoxic indicators (Rhod2-AM), loading at room temperature instead of 37°C can increase cell viability.

The slices were agitated too much. Be careful that the bubbles present during the recovery period do not agitate your slices. Also, take extra care when transferring them to different locations. One alternative to consider is using the back of a Pasteur pipette instead of a brush.

Avoid using old solutions (aCSF, perfusion solution) and always ensure that there is no bacterial growth before using them. It is ideal to use fresh solutions for each recording day.

Always verify the pH and osmolality when preparing the solutions.

Regularly check that your slices are properly oxygenated.

Problem 3

It is hard to focus on the entire field of view when performing calcium imaging (step 6 of “[calcium imaging of astrocytes](#)”).

Potential solution

This problem can occur when the strings of the harp that hold the slice are too close to each other. In this case, the slice surface becomes bent and is no longer parallel to the optic plane of the microscope. To solve this, you can cut out a string from the middle of the harp and then position the harp on the slice such that your recording area lies in the gap you just created. If this does not solve the issue, then double-check that your recording chamber and microscope are perfectly horizontal and not tilted in any direction.

Problem 4

The slice moves during the calcium imaging (step 6 of “[calcium imaging of astrocytes](#)”).

Potential solution

The solution depends on the axis of the movement:

If the slice moves in the x/y axes, verify that your harp is correctly positioned at the bottom of the recording chamber. Use harps that fit perfectly in the chamber (as is the case with those provided by Harvard Apparatus). Alternatively, your harp may not be heavy enough to counterbalance the flow produced by the peristaltic pump. To correct this you can:

Build a heavier harp.

Build/buy an arena where the harp fits the chamber better.

Check that there is no air entering the tubing, as this can introduce air bubbles into the circuit, which then make the recording milieu vibrate as they pass through the recording chamber.

The flow of the peristaltic pump may be too high and should be reduced as needed.

If the slice moves in the z-axis, it is probably because the strings of your harp are spaced too far apart. Either move the slice to a narrower gap of the harp or try using a different harp.

Problem 5

The calcium indicators bleach too much (step 6 of “[Calcium Imaging of astrocytes](#)”).

Potential solution

If the calcium indicator bleaching is so strong that it will change the interpretation of your data, you have to adjust the duration and intensity parameters of the illumination. In our case, we never illuminate for more than 100 ms. For the illumination intensity, we find the best values are between 580 μ W and 1040 μ W. However, since all setups are different, we strongly recommend you try several intensity values within your setup.

Problem 6

OGB1 signal is absent/weak (step 6 of “[calcium imaging of astrocytes](#)”).

Potential solution

If you cannot see any signal in the green channel (OGB1), there is probably an issue with OGB1-AM solubilization in the Cremophor EL + PF-127 mix. This can be due to the degradation of the PF-127, which must be kept in an air-proof vial. We usually keep aliquots of PF-127 in 1mL tubes, covered with Parafilm. Issues in dye solubilisation can also be due to the sonication step. Consider increasing

the time/intensity of the sonication. You can also try to incubate the mix in a heating bath at 40°C for 20 min; however, in our hands, this produces less solubilisation of the mix.

Problem 7

Opening the cell is difficult (step 17 of “patch-clamp-mediated BAPTA loading of astrocytes”).

Potential solution

Patching small cells is more challenging than bigger ones. Consider some of the following steps to make it easier:

Try using a small pipette tip (around 6–8 MΩ) for smaller cells, but do not exceed 9 MΩ as this would make it even harder.

If after several trials you still struggle to achieve a gigaseal and/or cannot open the cell, it may be because you are not actually on the cell but rather only nearby. Try to get on the cell as you would normally and then move either slightly closer or away from it to understand how to get on a cell correctly. Practice makes perfect in this case.

Problem 8

During the membrane test, the signal is constantly drifting, even after doing the pipette offset (step 13 of “patch-clamp-mediated BAPTA loading of astrocytes”).

Potential solution

The recording electrode is probably no longer adequately chlorinated. To chlorinate it, run an electrolysis reaction in 3 M KCl. Connect the electrode to the positive pole of a battery and a cable to the negative one. Dip both in the KCl solution and let them sit for 15s. You should see the solution bubble.

Problem 9

The pipette is clogged (step 13 of “patch-clamp-mediated BAPTA loading of astrocytes”).

Potential solution

Try to remove the clog by applying a strong pressure (with the syringe for example). If the clog is still there, change the pipette.

RESOURCE AVAILABILITY

Lead contact

Further information and requests for resources and reagents should be directed to and will be fulfilled by the lead contact, Alexandre CHARLET acharlet@unistra.fr.

Materials availability

This study did not generate new unique reagents.

Data and code availability

This protocol did not include a particular code. However, to see an example of the code that can be used, feel free to check our public repository where our routines are available at <https://github.com/AngelBaudon/Canal.git>.

SUPPLEMENTAL INFORMATION

Supplemental information can be found online at <https://doi.org/10.1016/j.xpro.2022.101159>.

ACKNOWLEDGMENTS

This work was supported by the IASP Early Career Research grant 2012, FP7 Career Integration grant 334455, Initiative of Excellence (IDEX) Attractiveness grant 2013, IDEX Interdisciplinary grant 2015, University of Strasbourg Institute for Advanced Study (USIAS) fellowship 2014-15, Foundation Fyssen research grant 2015, NARSAD Young Investigator Grant 24821, ANR JCJC grant (to A.C.), ANR-DFG grant GR 3619/701 (to A.C. and V.G.), German Research Foundation (DFG) grants GR 3619/8-1, GR 3619/13-1, GR 3619/15-1, GR 3619/16-1, Training Research Group (GRK) 2174, and SFB Consortium 1158-2 for V.G. The authors thank Sophie Reibel and the Chronobiotron UMS 3415 for all animal care. We also thank BioRender, SciHub and StackOverflow.

AUTHOR CONTRIBUTIONS

Patch loading of astrocytes, E.C.C.; Calcium imaging, A.B.; Supervision, A.C. All authors wrote and edited the manuscript.

DECLARATION OF INTERESTS

The authors declare no competing interests.

REFERENCES

- Bischofberger, J., Engel, D., Li, L., Geiger, J.R., and Jonas, P. (2006). Patch-clamp recording from mossy fiber terminals in hippocampal slices. *Nat. Protoc.* 1, 2075–2081.
- Charles, A.C., Merrill, J.E., Dirksen, E.R., and Sanderson, M.J. (1991). Intercellular signaling in glial cells: calcium waves and oscillations in response to mechanical stimulation and glutamate. *Neuron* 6, 983–992.
- Delvendahl, I., Jablonski, L., Baade, C., Matveev, V., Neher, E., and Hülsmann, S. (2015). Reduced endogenous Ca^{2+} buffering speeds active zone Ca^{2+} signaling. *Proc. Natl. Acad. Sci.* 112, E3075–E3084.
- Hülsmann, S., Hagos, L., Heuer, H., and Schnell, C. (2017). Limitations of sulforhodamine 101 for brain imaging. *Front. Cell Neurosci.* 11, 44.
- Khakh, B.S., and Benjamin, D. (2019). The emerging nature of astrocyte diversity. *Annu. Rev. Neurosci.* 42, 187–207.
- Maravall, M., Mainen, Z.F., Sabatini, B.L., and Svoboda, K. (2000). Estimating intracellular calcium concentrations and buffering without wavelength ratioing. *Biophys. J.* 78, 2655–2667.
- Nagai, J., Bellafard, A., Qu, Z., Yu, X., Ollivier, M., Gangwani, M.R., Diaz-Castro, B., Coppola, G., Schumacher, S.M., Golshani, P., et al. (2021). Specific and behaviorally consequential astrocyte Gq GPCR signaling attenuation in vivo with IPARK. *Neuron* 109, 2256–2274.e9.
- Naraghi, M., and Neher, E. (1997). Linearized buffered Ca^{2+} diffusion in microdomains and its implications for calculation of $[\text{Ca}^{2+}]$ at the mouth of a calcium channel. *J. Neurosci.* 17, 6961–6973.
- Rasmussen, R., and Nedergaard, M.; Nicolas Caesar Petersen (2016). Sulforhodamine 101, a widely used astrocyte marker, can induce cortical seizure-like activity at concentrations commonly used. *Sci. Rep.* 6, 30433.
- Schindelin, J., Arganda-Carreras, I., Frise, E., Kaynig, V., Longair, M., Pietzsch, T., Preibisch, S., Rueden, C., Saalfeld, S., Schmid, B., et al. (2012). Fiji: an open-source platform for biological-image analysis. *Nat. Methods* 9, 676–682.
- Schnell, C., Shahmoradi, A., Wichert, S.P., Mayerl, S., Hagos, Y., Heuer, H., Rossner, M.J., and Hülsmann, S. (2015). The multispecific thyroid hormone transporter OATP1C1 mediates cell-specific sulforhodamine 101-labeling of hippocampal astrocytes. *Brain Struct. Funct.* 220, 193–203.
- Semyanov, A., Henneberger, C., and Agarwal, A. (2020). Making sense of astrocytic calcium signals – from acquisition to interpretation. *Nat. Rev. Neurosci.* 21, 551–564.
- Shigetomi, E., Patel, S., and Khakh, B.S. (2016). Probing the complexities of astrocyte calcium signaling. *Trends Cell Biol.* 26, 300–312.
- Tang, Y., Benusiglio, D., Lefevre, A., Küppers, S., Lapiés, O., Kerspenn, D., Charlet, A., and Grinevich, V. (2021). Viral vectors for opto-electrode recording and photometry-based imaging of oxytocin neurons in anesthetized and socially interacting rats. *STAR Protoc.* <https://doi.org/10.1016/j.xpro.2021.101032>.
- Wahis, J., Baudon, A., Althammer, F., Kerspenn, D., Goyon, S., Hagiwara, D., Lefevre, A., Bartczko, L., Boury-Jamot, B., Bellanger, B., et al. (2021). Astrocytes mediate the effect of oxytocin in the central amygdala on neuronal activity and affective states in rodents. *Nat. Neurosci.* 24, 529–541.
- Wakida, N.M., Gomez-Godinez, V., Li, H., Nguyen, J., Kim, E.K., Dynes, J.L., Othy, S., Lau, A.L., Ding, P., Shi, L., et al. (2020). Calcium dynamics in astrocytes during cell injury. *Front. Bioeng. Biotechnol.* 8, 912.
- Wallraff, A., Köhling, R., Heinemann, U., Theis, M., Willecke, K., and Steinhäuser, C. (2006). The impact of astrocytic gap junctional coupling on potassium buffering in the hippocampus. *J. Neurosci.* 26, 5438–5447.
- Zhuo, L., Sun, B., Zhang, C.L., Fine, A., Chiu, S.Y., and Messing, A. (1997). Live astrocytes visualized by green fluorescent protein in transgenic mice. *Dev. Biol.* 187, 36–42.

6.3 Publication: CaMK1D signalling in AgRP neurons promotes
ghrelin-mediated food intake.

Vivot K., Meszaros G., Pangou E., Zhang Z., Qu M., Erbs E., Yeghiazaryan G.,
Quiñones M., Grandgirard E., Schneider A., **Clauss--Creusot E.**, Charlet A., Faour
M., Martin C., Berditchevski F., Sumara I., Luquet S., Kloppenburg P., Nogueiras R.,
Ricci R. 2023.

Nature Metabolism.

CaMK1D signalling in AgRP neurons promotes ghrelin-mediated food intake

Received: 15 December 2021

Accepted: 25 April 2023

Published online: 05 June 2023

 Check for updates

Karl Vivot  ^{1,2,3,4}, Gergö Meszaros ^{1,2,3,4}, Evanthia Pangou  ^{1,2,3,4}, Zhirong Zhang  ^{1,2,3,4}, Mengdi Qu ^{1,2,3,4}, Eric Erbs  ^{1,2,3,4}, Gagik Yeghiazaryan ⁵, Mar Quiñones  ^{6,7}, Erwan Grandgirard  ^{1,2,3,4}, Anna Schneider ^{1,2,3,4}, Etienne Clauss-Creusot ^{4,8}, Alexandre Charlet  ^{4,8}, Maya Faour ⁹, Claire Martin  ⁹, Fedor Berditchevski  ¹⁰, Izabela Sumara ^{1,2,3,4}, Serge Luquet ⁹, Peter Kloppenburg  ⁵, Ruben Nogueiras  ^{6,11} & Romeo Ricci  ^{1,2,3,4,12} 

Hypothalamic AgRP/NPY neurons are key players in the control of feeding behaviour. Ghrelin, a major orexigenic hormone, activates AgRP/NPY neurons to stimulate food intake and adiposity. However, cell-autonomous ghrelin-dependent signalling mechanisms in AgRP/NPY neurons remain poorly defined. Here we show that calcium/calmodulin-dependent protein kinase ID (CaMK1D), a genetic hot spot in type 2 diabetes, is activated upon ghrelin stimulation and acts in AgRP/NPY neurons to mediate ghrelin-dependent food intake. Global *Camk1d*-knockout male mice are resistant to ghrelin, gain less body weight and are protected against high-fat-diet-induced obesity. Deletion of *Camk1d* in AgRP/NPY, but not in POMC, neurons is sufficient to recapitulate above phenotypes. In response to ghrelin, lack of CaMK1D attenuates phosphorylation of CREB and CREB-dependent expression of the orexigenic neuropeptides AgRP/NPY in fibre projections to the paraventricular nucleus (PVN). Hence, CaMK1D links ghrelin action to transcriptional control of orexigenic neuropeptide availability in AgRP neurons.

The central nervous system (CNS) orchestrates a complex array of processes mediating energy intake and expenditure. Hormonal, neuronal and nutritional signals according to changes in food absorption, energy storage and energy consumption in different organs reach the CNS, which in turn triggers corresponding changes in feeding behaviour and peripheral cellular metabolism¹.

Sensing of the nutrient status of the organism is governed by distinct neuronal cell populations, particularly within the arcuate

nucleus (ARC) of the hypothalamus². Neurons in this region provide specific projections to other hypothalamic nuclei, including the paraventricular nucleus of the hypothalamus (PVN), or to different extrahypothalamic brain regions that in turn coordinate corresponding behavioural responses³.

Orexigenic neuropeptide Y (NPY)- and agouti-related peptide (AgRP)-expressing neurons and anorexigenic proopiomelanocortin (POMC)-expressing neurons in the ARC of the hypothalamus are

¹Institut de Génétique et de Biologie Moléculaire et Cellulaire, Illkirch, France. ²Centre National de la Recherche Scientifique, Illkirch, France. ³Institut National de la Santé et de la Recherche Médicale, Illkirch, France. ⁴Université de Strasbourg, Strasbourg, France. ⁵Biocenter, Institute for Zoology, and Cologne Excellence Cluster on Cellular Stress Responses in Aging-Associated Diseases, (CECAD), University of Cologne, Cologne, Germany. ⁶Instituto de Investigación Sanitaria de Santiago de Compostela, Complexo Hospitalario Universitario de Santiago (CHUS/SERGAS), Santiago de Compostela, Spain. ⁷CIBER Fisiopatología de la Obesidad y Nutrición (CIBERObn), Instituto de Salud Carlos III, Santiago de Compostela, Spain. ⁸Centre National de la Recherche Scientifique, Institute of Cellular and Integrative Neurosciences, Strasbourg, France. ⁹Université Paris Cité, CNRS, Unité de Biologie Fonctionnelle et Adaptative, Paris, France. ¹⁰Institute of Cancer and Genomic Sciences, The University of Birmingham, Birmingham, UK. ¹¹Department of Physiology, CIMUS, University of Santiago de Compostela-Instituto de Investigación Sanitaria, Santiago de Compostela, Spain. ¹²Laboratoire de Biochimie et de Biologie Moléculaire, Nouvel Hôpital Civil, Strasbourg, France.  e-mail: vivot@igbmc.fr; romeo.ricci@igbmc.fr

primarily involved in the regulation of energy homeostasis. Leptin, ghrelin and insulin have emerged as key hormones acting on these neurons. Both leptin and insulin receptors are expressed in these neurons, and they have been found to activate POMC neurons and to inhibit AgRP/NPY neurons⁴. Ghrelin enhances the activity of AgRP/NPY neurons through its receptors, and it decreases the activity of POMC neurons through a ghrelin-receptor-independent mechanism⁵.

Dysfunction of these neuronal circuits contributes to overnutrition and obesity that eventually culminates in type 2 diabetes (T2D)⁶. Obesity and T2D are thus interlinked and complex metabolic disorders. Recent genome-wide association studies (GWASs) and GWAS meta-analyses have revealed complex polygenic factors influencing the development of both diseases. In fact, more than ~250 genetic loci have been identified for monogenic, syndromic or common forms of T2D and/or obesity-related traits^{7,8}. The contribution of single nucleotide polymorphisms (SNPs) to the pathogenesis of these diseases remains largely elusive.

SNPs in the intergenic region between CDC123 (cell division cycle protein 123) and CaMK1D (calcium/calmodulin-dependent protein kinase 1D) as well as in the CDC123 3'UTR on chromosome 10 are strongly associated with T2D in European and Asian populations^{9–11}. Among other variants, fine mapping has identified rs11257655 as the predominant SNP within this locus¹². The change from C to T in the enhancer region of the rs11257655 allele promotes DNA hypomethylation and the binding of the transcription factors FOXA1 and FOXA2 on the enhancer region, resulting in enhanced CaMK1D gene transcription^{13,14}. Thus, CaMK1D expression might be enhanced and could contribute to the development of T2D. Supporting clinical data in patients carrying such risk loci have revealed that CaMK1D might promote pancreatic β cell dysfunction¹⁵. However, direct experimental evidence for the latter conclusion is lacking thus far. Another study has proposed that CaMK1D stimulates hepatic glucose output, a mechanism contributing to T2D¹⁶.

CaMK1D (or CaMK18) is the fourth member of the CaMK1 subfamily. These kinases have been mainly shown to be important in neurons. CaMK1s control neuron morphology¹⁷, including axonal extension, growth cone motility¹⁸ and dendritogenesis¹⁹. It has been demonstrated that CaMK1s may also regulate neuronal function by controlling the long-term potentiation, a process involving persistent strengthening of synapses that leads to a long-lasting increase in signal transmission among neurons²⁰. However, specific non-redundant neuronal functions of any of the four members of the CaMK1 subfamily, including CaMK1D, have yet to be determined.

Using global and conditional *Camk1d*-knockout mice, we provide evidence for a role of CaMK1D in central regulation of food intake, while its function seems to be dispensable in the liver and in the pancreatic β cell in this context. We demonstrate that CaMK1D acts in hypothalamic AgRP neurons to control food intake in response to ghrelin. While CaMK1D in AgRP neurons is dispensable for ghrelin-stimulated increase in electrical neuronal activity and AMPK signalling, its absence reduces ghrelin-induced activatory CREB phosphorylation, AgRP transcription and AgRP/NPY abundance within the PVN. Our data thus unveil a ghrelin signalling mechanism in AgRP neurons that is necessary for efficient appetite stimulation.

Results

Camk1d^{−/−} mice are protected against obesity

To understand the function of CaMK1D in metabolism, we generated mice carrying a floxed allele of *Camk1d* (Extended Data Fig. 1a,b) and crossed them with the global Cre-mediated deleter, Rosa26-Cre²¹, to obtain whole-body knockout mice. Western blotting confirmed efficient deletion of *Camk1d* in different organs, including brain, pancreas and intestine (Fig. 1a). Whole-body *Camk1d*-knockout mice (*Camk1d*^{−/−} mice) were born in expected gender distribution (Extended Data Fig. 1c) and Mendelian ratios (Extended Data Fig. 1d) and developed without overt problems. Body and tibia lengths at 7 weeks of age

were equal between *Camk1d*^{−/−} and wild-type mice (*Camk1d*^{+/+} mice) (Extended Data Fig. 1e,f), excluding any major postnatal growth defect. However, body weight in *Camk1d*^{−/−} mice on a chow diet was significantly reduced at 21 weeks of age as compared with that of *Camk1d*^{+/+} mice. This difference was exacerbated when obesity was induced in mice fed a high-fat diet (HFD), reaching statistical significance at the age of 18 weeks (Fig. 1b). Quantitative nuclear magnetic resonance (qNMR) revealed that HFD-fed *Camk1d*^{−/−} mice, compared with *Camk1d*^{+/+} mice, had reduced fat mass, and there was no significant difference in lean mass or free body fluid (FBF) (Fig. 1c). *Leptin*-deficient mice (*ob/ob* mice) lacking CaMK1D also showed reduced body weight as compared with *ob/ob* mice, reaching statistical significance at the age of 14 weeks (Fig. 1d).

In line with reduced diet-induced obesity, fasting glucose levels in 14-week-old *Camk1d*^{−/−} mice on a HFD were significantly reduced as compared with those in control *Camk1d*^{+/+} mice (Fig. 1e). In fact, glucose levels in *Camk1d*^{−/−} mice on a HFD were similar to those in corresponding chow-diet-fed mice, indicating that they were protected from obesity-induced hyperglycaemia. There was no apparent difference in fasting glucose levels between *Camk1d*^{−/−} and *Camk1d*^{+/+} mice on a chow diet (Fig. 1e). The observed reduced fasting glucose levels correlated with reduced fasting insulin levels (Fig. 1f). Glucose tolerance was slightly, but not significantly, improved in *Camk1d*^{−/−} as compared with *Camk1d*^{+/+} mice on a chow diet (Fig. 1g). However, these differences became significant in mice on a HFD (Fig. 1h,i). While insulin tolerance was unaltered in *Camk1d*^{−/−} mice on a chow diet (Fig. 1j), it was significantly improved in *Camk1d*^{−/−} mice as compared with *Camk1d*^{+/+} mice on a HFD (Fig. 1k,l). Glucose-induced secretion of insulin (GSIS) was slightly but not significantly reduced in *Camk1d*^{−/−} mice as compared with that in *Camk1d*^{+/+} mice on a HFD (Extended Data Fig. 2a). GSIS from isolated islets of *Camk1d*^{−/−} mice was comparable to that from *Camk1d*^{+/+} mouse islets (Extended Data Fig. 2b).

To further exclude a primary role of CaMK1D in the pancreas, including in β cells, we crossed floxed mice with *Pdx1*^{Cre/+} mice²². Western blotting confirmed that deletion of *Camk1d* in the pancreas was efficient, while no apparent deletion was visible in brain (Extended Data Fig. 2c). The body weight and glucose tolerance of pancreas-specific *Camk1d*-knockout mice (*Pdx1*^{Cre/+}; *Camk1d*^{fl/fl} mice) were not different from those of floxed control mice (*Camk1d*^{fl/fl} mice), both when mice were on a chow diet and when they were on a HFD (Extended Data Fig. 2d–f), confirming that CaMK1D is dispensable in β cell function.

Hepatic insulin resistance leading to increased gluconeogenesis is an important mechanism contributing to obesity-related changes in glucose homeostasis²³. Therefore, we generated liver-specific *Camk1d*-knockout mice (*Alb*^{Cre/+}; *Camk1d*^{fl/fl} mice) using *Albumin*^{Cre/+} mice²⁴ and corresponding floxed control mice (*Camk1d*^{fl/fl} mice). Quantitative reverse transcription PCR (qRT–PCR) confirmed efficient deletion of *Camk1d* in the liver (Extended Data Fig. 2g). However, hepatic deletion of *Camk1d* did not affect body weight, glucose tolerance and insulin tolerance in mice on a chow diet, as well as those on HFD (Extended Data Fig. 2h–l). Thus, our data exclude any major functions of CaMK1D in pancreatic β cells and liver under both normal conditions and obesity.

Camk1d alters ghrelin-mediated food intake

To further understand reduced body weight and fat mass in *Camk1d*^{−/−} mice as compared with *Camk1d*^{+/+} mice, we next explored energy metabolism. In line with reduced body weight, cumulative food intake was decreased in *Camk1d*^{−/−} mice as compared with *Camk1d*^{+/+} mice on a chow diet as well as on HFD, reaching statistical significance at 20 weeks of age (Fig. 2a,b). Cumulative food intake was also reduced in *ob/ob* mice lacking *Camk1d* as compared with *ob/ob* mice, reaching statistical significance at the age of 12 weeks (Fig. 2c). Likewise, cumulative food intake after 24 h of fasting was significantly reduced in *Camk1d*^{−/−} mice throughout the observed period of refeeding, as compared with that in *Camk1d*^{+/+} mice (Fig. 2d).

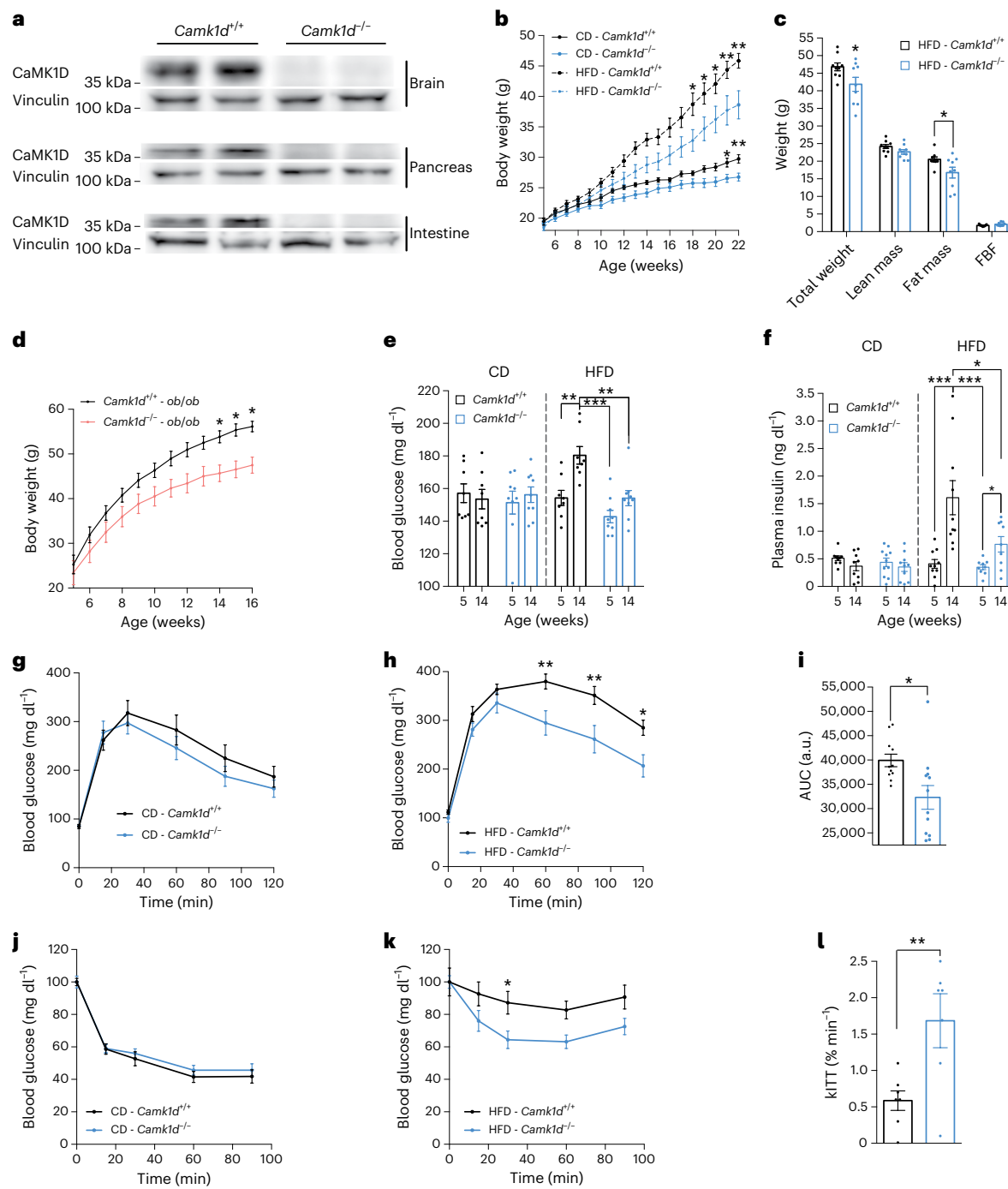


Fig. 1 | Global deletion of *Camk1d* gene reduces diet- and leptin deficiency-induced obesity in mice. **a**, Expression of CaMK1D protein in different tissues from the wild-type (*Camk1d*^{+/+}) and whole-body *Camk1d*-knockout (*Camk1d*^{-/-}) mice. **b**, Body weight of mice fed a chow diet (CD) (CD - *Camk1d*^{+/+} $n=9$; CD - *Camk1d*^{-/-} $n=11$) or a HFD (HFD - *Camk1d*^{+/+} $n=11$; HFD - *Camk1d*^{-/-} $n=11$). **c**, Body composition of mice fed a HFD, measured by qNMR ($n=9$ per group). FBF, free body fluid. **d**, Body weight of leptin-deficient mice (*ob/ob* mice) fed a chow diet (CD) ($n=7$ per group). **e**, Blood glucose levels after 4 h of fasting (CD - *Camk1d*^{+/+} $n=8$; CD - *Camk1d*^{-/-} $n=9$; HFD - *Camk1d*^{+/+} $n=8$; HFD - *Camk1d*^{-/-} $n=9$). **f**, Plasma insulin levels after 4 h of fasting (CD - *Camk1d*^{+/+} $n=9$;

CD - *Camk1d*^{-/-} $n=10$; HFD - *Camk1d*^{+/+} $n=10$; HFD - *Camk1d*^{-/-} $n=9$). **g-i**, Blood glucose levels during an IPGTT in mice with the indicated genotypes and diets. Corresponding areas under the curve (AUCs) are depicted (CD - *Camk1d*^{+/+} $n=9$; CD - *Camk1d*^{-/-} $n=11$; HFD - *Camk1d*^{+/+} $n=11$; HFD - *Camk1d*^{-/-} $n=12$). a.u., arbitrary units. **j-l**, Blood glucose levels during insulin tolerance test (ITT) in mice with the indicated genotypes and diets. Glucose decay rate during the ITT (kITTs) are depicted (CD - *Camk1d*^{+/+} $n=10$; CD - *Camk1d*^{-/-} $n=10$; HFD - *Camk1d*^{+/+} $n=7$; HFD - *Camk1d*^{-/-} $n=7$). Data are presented as mean values \pm s.e.m. * $P < 0.05$ and ** $P < 0.01$. Statistical tests included two-way ANOVA bonferroni post hoc test (**b-f,h,k**) and unpaired Student's *t* test (**i,l**).

Indirect calorimetry revealed that energy expenditure in *Camk1d*^{-/-} mice was equal to that in *Camk1d*^{+/+} mice on a HFD. Indeed, the regression-based analysis of covariance (ANCOVA) showed that there was no body-weight-independent metabolic rate (MR) difference

in the *Camk1d*^{-/-} mice relative to *Camk1d*^{+/+} mice (Fig. 2e). However, locomotor activity of *Camk1d*^{-/-} as compared with *Camk1d*^{+/+} mice was significantly reduced at the beginning of the night period after 24 h of fasting (Fig. 2f,g), in line with reduced appetite and reduced

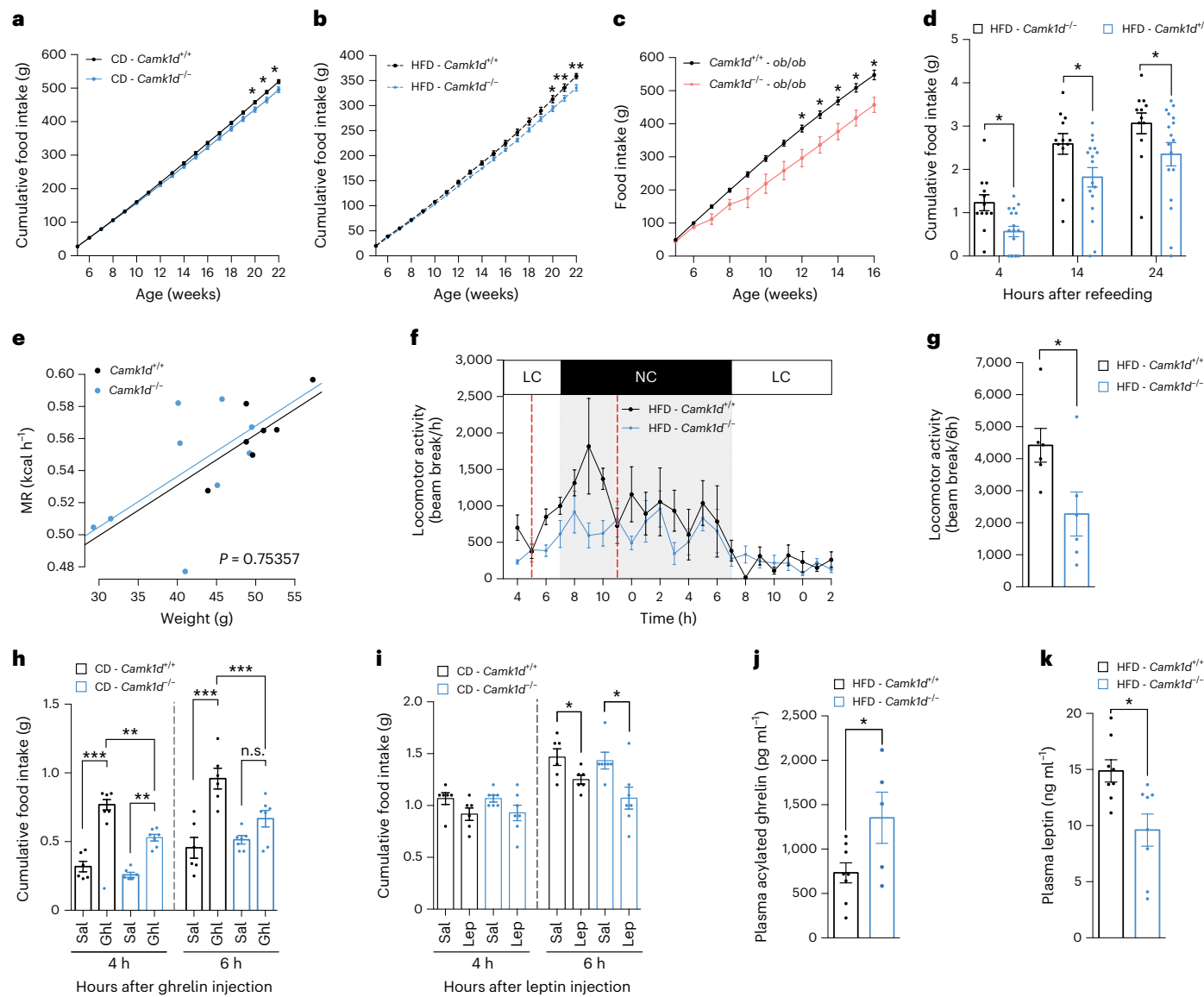


Fig. 2 | Deletion of *Camk1d* attenuates ghrelin-induced food intake. **a,b**, Cumulative food intake in mice (CD - *Camk1d*^{+/+} n = 9; CD - *Camk1d*^{-/-} n = 11; HFD - *Camk1d*^{+/+} n = 9; HFD - *Camk1d*^{-/-} n = 10). **c**, Cumulative food intake of leptin-deficient mice (*ob/ob* mice) fed with a chow diet (*Camk1d*^{+/+} n = 7; HFD - *Camk1d*^{-/-} n = 8). **d**, Cumulative food intake of mice on a HFD. Food intake was determined 24 h after food withdrawal (*Camk1d*^{+/+} n = 12; HFD - *Camk1d*^{-/-} n = 17). **e**, Regression-based analysis of absolute MR against body weight in HFD-fed control (*Camk1d*^{+/+}) and whole-body *Camk1d*-knockout (*Camk1d*^{-/-}) mice (*Camk1d*^{+/+} n = 7; HFD - *Camk1d*^{-/-} n = 9). The ANCOVA analysis was done with MR as a dependent variable, the genotype as a fixed variable and body mass as a covariate. **f,g**, Ambulatory activity over 24 h. Ambulatory activity was measured

with mice deprived of food for 24 h. AUC from 5 p.m. to 11 p.m. was calculated (n = 6 per group). **h**, Cumulative food intake after ghrelin injections (1 mg kg⁻¹) of mice on a chow diet. (*Camk1d*^{+/+} n = 6; *Camk1d*^{-/-} n = 7) **i**, Cumulative food intake after leptin injections (3 mg kg⁻¹) of mice on a chow diet. Food intake was determined 24 h after food withdrawal (*Camk1d*^{+/+} n = 6; *Camk1d*^{-/-} n = 7). **j,k**, Blood acylated ghrelin (*Camk1d*^{+/+} n = 8; HFD - *Camk1d*^{-/-} n = 5) (**j**) and blood leptin (n = 6 per group) (**k**) levels in mice on a HFD. Blood sampling was performed 4 h after food withdrawal. Data are presented as mean ± s.e.m. *P < 0.05 and **P < 0.01. Statistical tests included two-way ANOVA with bonferroni post hoc test (**a-d,h,i**), ANCOVA (**e**) and unpaired Student's t test (**g,j,k**).

food seeking in response to fasting. Thus, reduced obesity primarily correlated with reduced appetite and food intake.

Ghrelin is a gut-derived hormone that is released in response to fasting and that promotes feeding behaviour and adiposity²⁵. Given that the resistance to diet-induced obesity of *Camk1d*^{-/-} mice could be explained by reduced food intake, we next wondered whether the ghrelin response was affected in mice lacking *Camk1d*. To this end, we determined cumulative food intake upon intraperitoneal (i.p.) injections of ghrelin in mice on a chow diet. While *Camk1d*^{+/+} mice showed a significant increase in cumulative food intake at 4 and 6 h after ghrelin injection, such a response was almost absent in *Camk1d*^{-/-} mice (Fig. 2h). By contrast, the response to leptin was comparable in

Camk1d^{+/+} mice and *Camk1d*^{-/-} mice (Fig. 2i). Blood levels of acylated ghrelin were significantly higher in *Camk1d*^{-/-} than in *Camk1d*^{+/+} mice on a HFD (Fig. 2j), suggesting an adaptive response to a primary defect in ghrelin action. Conversely, blood levels of leptin were significantly lower in *Camk1d*^{-/-} mice than in *Camk1d*^{+/+} mice (Fig. 2k) on a HFD, correlating well with the degree of obesity.

To exclude any major anxiety-like behaviour or stress-induced anhedonia, we subjected mice to an open field and to a sucrose preference test, respectively. No major differences between genotypes could be observed (Extended Data Fig. 3a–h). Thus, global deletion of *Camk1d* results in compromised ghrelin action, which contributes

CaMK1D regulates ghrelin-induced food intake in AgRP neurons

Ghrelin stimulates central neurons to promote feeding. We thus next asked whether CaMK1D in the nervous system was mainly responsible for the observed phenotype in *Camk1d*^{-/-} mice. We therefore crossed *Camk1d*^{fl/fl} mice with *Nestin*^{Cre/+} mice, resulting in efficient deletion of *Camk1d* in brain, including hypothalamus, but not in other organs such as intestine and pancreas (Extended Data Fig. 4a). Indeed, body weight was significantly attenuated in nervous-system-specific *Camk1d*-knockout mice (*Nestin*^{Cre/+}; *Camk1d*^{fl/fl} mice) aged 17 weeks as compared with Cre and floxed control mice (*Nestin*^{Cre/+} mice and *Camk1d*^{fl/fl} mice) on a chow diet, as well as on a HFD (Extended Data Fig. 4b). Cumulative food intake was decreased in *Nestin*^{Cre/+}; *Camk1d*^{fl/fl} mice at the age of 16 weeks as compared with control mice on a chow diet (Extended Data Fig. 4c) and on a HFD (Extended Data Fig. 4d). Likewise, cumulative food intake after 24 h of fasting was significantly reduced in *Nestin*^{Cre/+}; *Camk1d*^{fl/fl} mice as compared with that in control mice after 4, 14 and 24 h of refeeding (Extended Data Fig. 4e). Consistently, while control mice showed a significant increase in cumulative food intake at 4 and 6 h after ghrelin injections, such a response was absent in *Nestin*^{Cre/+}; *Camk1d*^{fl/fl} mice (Extended Data Fig. 4f).

Ghrelin primarily acts on hypothalamic neurons in the ARC. In particular, it stimulates NPY/AgRP neurons to promote appetite²⁶. Given our results obtained in nervous-system-specific knockout mice, we next asked whether CaMK1D acts in AgRP neurons to control food intake. To this end, we crossed *Camk1d*^{fl/fl} mice with *Agrp*^{Cre/+} mice, resulting in efficient recombination of the *Camk1d* locus in hypothalamus, but not in the brain cortex, liver, tail and white blood cells (Extended Data Fig. 5a). qRT-PCR experiments revealed a 60% reduction in CaMK1D expression in the hypothalamic ARC of AgRP-neuron-specific *Camk1d*-knockout mice as compared with control mice. Expression of CaMK1D was unaffected in cortex or liver (Extended Data Fig. 5b). These results confirm significant, but not exclusive, expression and efficient deletion of CaMK1D in AgRP neurons. Strikingly, AgRP-neuron-specific *Camk1d*-knockout mice (*Agrp*^{Cre/+}; *Camk1d*^{fl/fl} mice) at the age of 18 weeks had significantly less body weight than did Cre and floxed control mice (*Agrp*^{Cre/+} mice and *Camk1d*^{fl/fl} mice) on a chow diet as well as on a HFD (Fig. 3a). Similar to nervous-system-specific knockout mice, *Agrp*^{Cre/+}; *Camk1d*^{fl/fl} mice showed significantly less cumulative food intake as compared with control mice on a chow diet (Fig. 3b) as well as on a HFD (Fig. 3c). Similar significant differences were observed in the cumulative food intake after 24 h of fasting (Fig. 3d) as well as in response to ghrelin injection (Fig. 3e). To confirm a role for CaMK1D in AgRP neurons of adult mice, we delivered AAVs carrying a Cre-driven expression cassette of small hairpin RNA (shRNA) against CaMK1D (AAV DIO sh*Camk1d*eGFP) or scramble shRNA (AAV DIO scramble eGFP) into the ARC of AgRP-Cre mice by stereotaxic injection. Enhanced green fluorescent protein (eGFP)-expressing cells were also AgRP-positive, confirming proper targeting (Fig. 3f). We found impaired ghrelin-induced

food intake in sh*Camk1d*-expressing-AAV-injected mice as compared with control-AAV-injected mice (Fig. 3g). We also used stereotaxic delivery of AAVs carrying a Cre-driven expression cassette of CaMK1D (AAV-DIO-CaMK1D-eGFP) or AAV-DIO-eGFP in *Agrp*^{Cre/+}; *Camk1d*^{fl/fl} mice and *Agrp*^{Cre/+} control mice. eGFP-expressing cells were also AgRP-positive, confirming proper targeting using stereotaxis (Fig. 3h). Ghrelin-induced food intake was significantly attenuated in *Agrp*^{Cre/+}; *Camk1d*^{fl/fl} mice as compared with that in *Agrp*^{Cre/+} control mice before AAV injections (Fig. 3i). qRT-PCR verified very efficient and specific CaMK1D re-expression in ARC, ventro-medial nucleus of the hypothalamus (VMH) and cortex verified very efficient and specific CaMK1D re-expression (Fig. 3j). Re-expression of CaMK1D-eGFP in AgRP neurons lacking *Camk1d* restored ghrelin-induced food intake in the same mice (Fig. 3k), while expression of CaMK1D in AgRP neurons of control mice had no additive effect. eGFP expression alone did not affect food intake in response to ghrelin (Fig. 3l). This suggests that CaMK1D acts specifically in adult AgRP neurons to control ghrelin-induced food intake, excluding an irreversible developmental defect. To further exclude major developmental defects, we next employed the designer receptors exclusively activated by designer drugs (DREADD) approach (hM3Dq receptor expression) in *Agrp*^{Cre/+}; *Camk1d*^{fl/fl} mice. DREADD activation is known to lead to a supraphysiologic activation of AgRP neurons, bypassing subtle receptor-mediated activation. Indeed, we found that food intake induced by the agonist clozapine N-oxide (CNO) was not affected in mice lacking CaMK1D in AgRP neurons (Fig. 3l,m). Importantly, responses to ghrelin did not change upon deletion of *CaMK1D* in anorexigenic POMC neurons (Extended Data Fig. 6a–f), suggesting that the effects of CaMK1D on food intake are specific to AgRP neurons.

To further evaluate the role of CaMK1D in AgRP-neuron-dependent energy metabolism, we next performed indirect calorimetry with *Agrp*^{Cre/+}; *Camk1d*^{fl/fl} mice and control mice on a chow diet. Although the cumulative food intake (Fig. 4a) was reduced in *Agrp*^{Cre/+}; *Camk1d*^{fl/fl} mice as compared with that of control mice, locomotor activity (Fig. 4b,c) was unchanged. The regression-based analysis of covariance (ANCOVA) confirmed that there was a body-weight-independent metabolic rate (MR) difference, with lower MR in *Agrp*^{Cre/+}; *Camk1d*^{fl/fl} mice than in control mice on a chow diet (Fig. 4d). Given the overall reduction in body weight, reduced energy expenditure was most likely compensating for compromised energy availability caused by reduced food intake. Altogether, our data thus suggest that CaMK1D acts in AgRP neurons to primarily control food intake in response to ghrelin.

Deletion of CaMK1D does not affect AgRP/NPY neuron activity

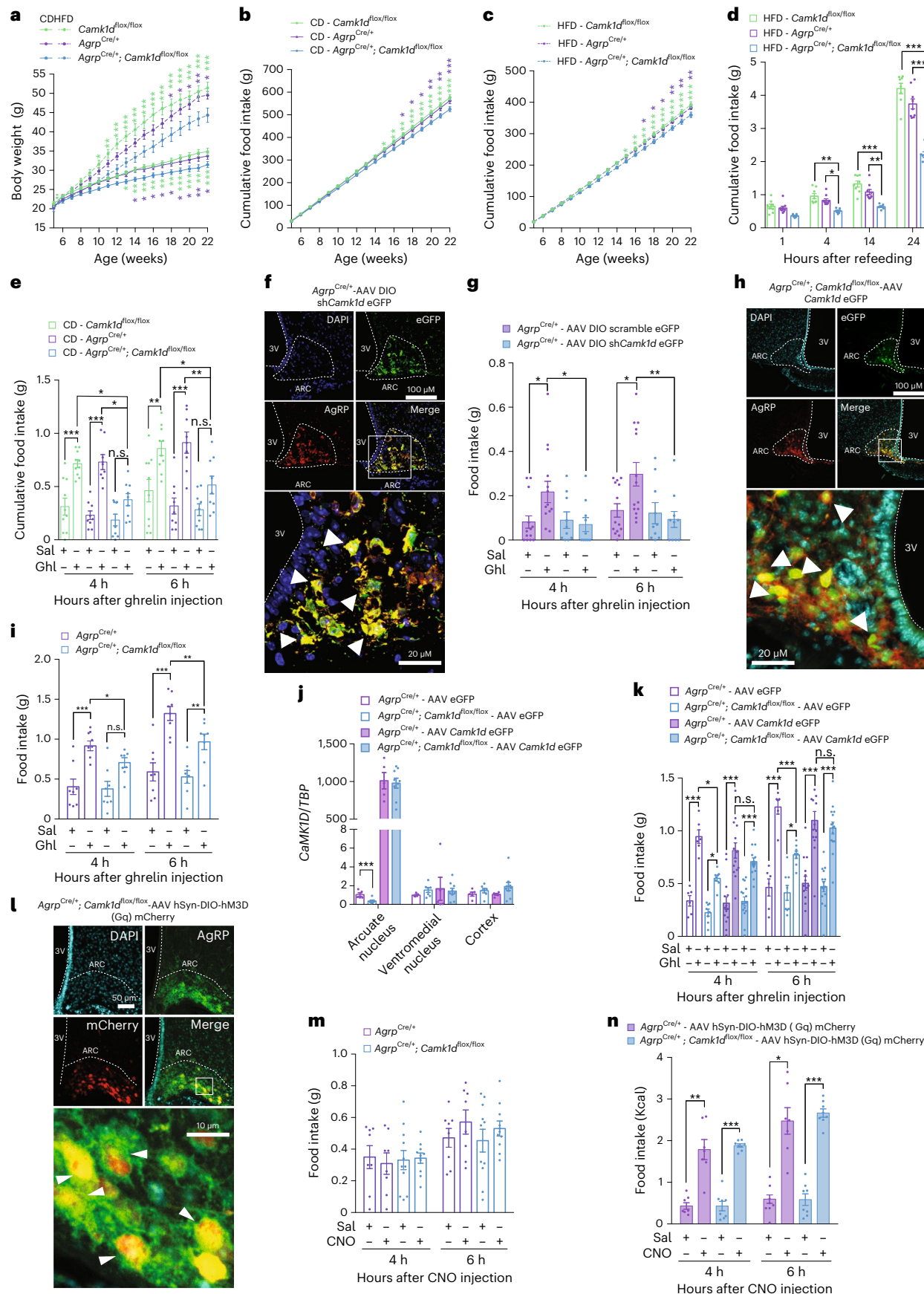
c-Fos expression is used as a marker for neuronal activity²⁷. To understand the function of CaMK1D in ghrelin-induced neuronal activity, we next explored c-Fos expression in NPY/AgRP neurons in the absence and presence of CaMK1D using NPY-GFP reporter mice²⁸. No differences in basal or ghrelin-induced c-fos expression in NPY-GFP-expressing cells in the ARC of *Camk1d*^{-/-} and *Camk1d*^{+/+} mice on a chow diet were

Fig. 3 | CaMK1D deletion in AgRP neurons leads to reduced body weight and food intake. **a**, Body weight of mice on a chow diet or a HFD (*Camk1d*^{fl/fl}: CD $n=15$, HFD $n=15$; *Agrp*^{Cre/+}: CD $n=14$, HFD $n=11$; *Agrp*^{Cre/+}; *Camk1d*^{fl/fl}: CD $n=16$, HFD $n=13$). **b,c**, Cumulative food intake of mice fed a chow diet or a HFD (*Camk1d*^{fl/fl}: CD $n=15$, HFD $n=15$; *Agrp*^{Cre/+}: CD $n=14$, HFD $n=11$; *Agrp*^{Cre/+}; *Camk1d*^{fl/fl}: CD $n=15$, HFD $n=12$). **d**, Cumulative food intake after 24 h of fasting (*Camk1d*^{fl/fl} $n=8$; *Agrp*^{Cre/+} $n=9$; *Agrp*^{Cre/+}; *Camk1d*^{fl/fl} $n=7$). **e**, Cumulative food intake after ghrelin injections (*Camk1d*^{fl/fl} $n=10$; *Agrp*^{Cre/+} $n=9$; *Agrp*^{Cre/+}; *Camk1d*^{fl/fl} $n=9$). **f**, Micrographs of nuclei (DAPI), AgRP neurons (red), viral eGFP (green) and merge (yellow) related to experiments shown in **g**. White arrows show AgRP-positive neurons expressing eGFP. **3V**, third ventricle. **g**, Cumulative food intake after ghrelin injections (AAV DIO scramble eGFP $n=13$; AAV DIO sh*Camk1d*eGFP $n=10$). **h**, Micrographs of nuclei (DAPI), AgRP neurons (red), viral eGFP (green) and merge (yellow) related to experiments shown in **j** and **k**.

White arrows show AgRP-positive neurons expressing eGFP. **i**, Cumulative food intake after ghrelin injection and before AAV injection ($n=8$ per group). **j**, Expression of *Camk1d* mRNA (*Agrp*^{Cre/+}: AAV eGFP $n=5$, AAV *Camk1d*eGFP $n=5$; *Agrp*^{Cre/+}; *Camk1d*^{fl/fl}: AAV eGFP $n=7$, AAV-*Camk1d*eGFP $n=9$). **k**, Cumulative food intake after ghrelin and AAV injections (*Agrp*^{Cre/+}: AAV eGFP $n=6$, AAV *Camk1d*eGFP $n=14$; *Agrp*^{Cre/+}; *Camk1d*^{fl/fl}: AAV eGFP $n=8$, AAV-*Camk1d*eGFP $n=15$). **l**, Micrographs of nuclei (DAPI), AgRP neurons (green), mCherry (red) and merge (yellow) related to experiments shown in **n**. White arrows show AgRP-positive neurons expressing mCherry. **m**, Cumulative food intake after CNO injections of mice before AAVs injection (*Agrp*^{Cre/+} $n=8$; *Agrp*^{Cre/+}; *Camk1d*^{fl/fl} $n=11$). **n**, Cumulative food intake after CNO injections and after AAV injection (*Agrp*^{Cre/+} $n=7$ and *Agrp*^{Cre/+}; *Camk1d*^{fl/fl} $n=8$). Data are presented as mean \pm s.e.m. * $P < 0.05$, ** $P < 0.01$ and *** $P < 0.001$. n.s., not significant. Statistical tests included two-way ANOVA with Bonferroni post hoc test (**a–e,g,i–k,m,n**).

found (Fig. 5a,b). To verify this finding, we compared the effect of ghrelin on AgRP neurons between both mouse lines using perforated patch clamp recordings in brain slices. To identify AgRP neurons, we

generated *Camk1d*^{-/-} and *Camk1d*^{+/+} mice carrying an eGFP reporter under the control of the *AgRP* promoter (*Camk1d*^{-/-}-AgRP-eGFP and *Camk1d*^{+/+}-AgRP-eGFP mice) (Fig. 5c). The ghrelin-induced increases in



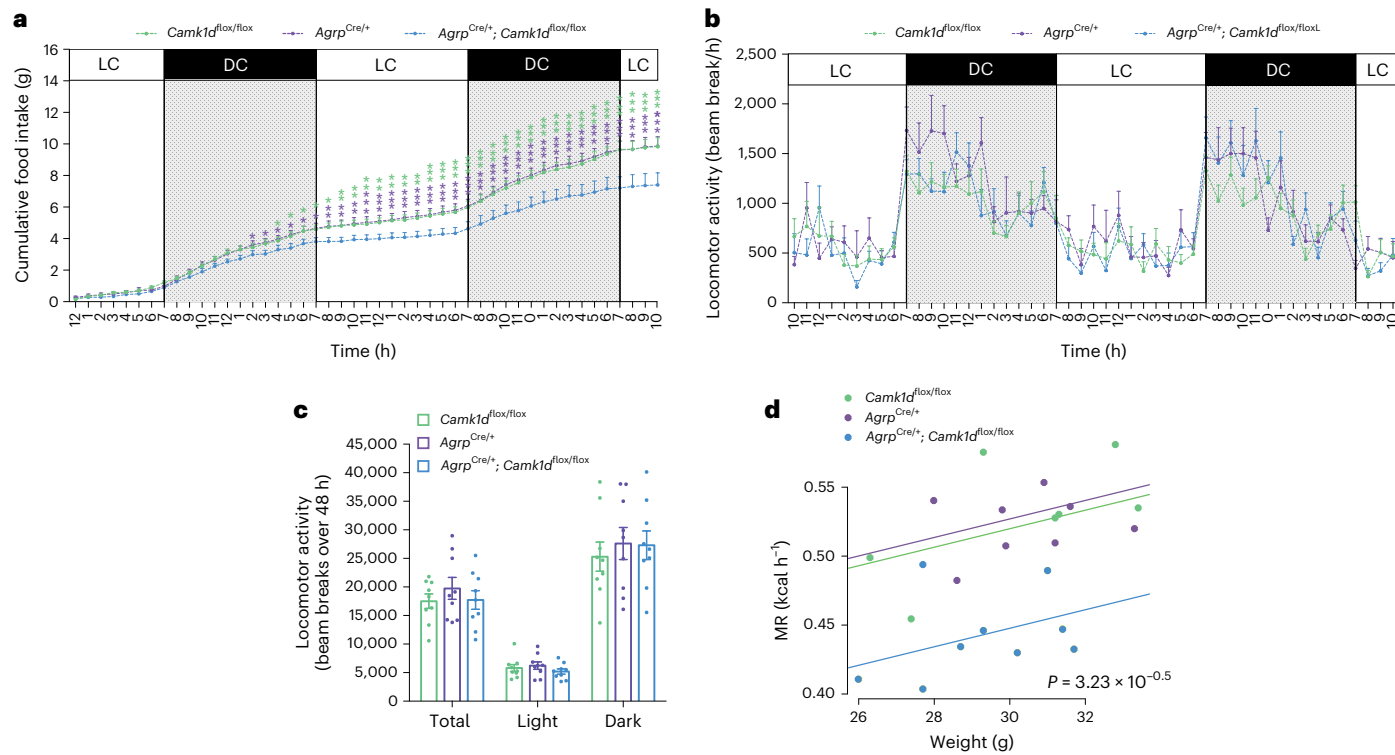


Fig. 4 | Conditional deletion of *Camk1d* in AgRP neurons decreases energy expenditure. **a**, Cumulative food intake in mice on a chow diet. Food intake was determined over 48 h during indirect calorimetric measurements (*Camk1d*^{fl/fl} n = 9; *Agrp*^{Cre/+} n = 10 and *Agrp*^{Cre/+}; *Camk1d*^{fl/fl} n = 9). LC, light cycle; DC, dark cycle. **b,c**, Locomotor activity over 48 h in mice on a chow diet (*Camk1d*^{fl/fl} n = 9; *Agrp*^{Cre/+} n = 9 and *Agrp*^{Cre/+}; *Camk1d*^{fl/fl} n = 9).

d, Regression-based analysis of absolute MR against body weight of mice on a chow diet. The ANCOVA analysis was done with MR as a dependent variable, the genotype as a fixed variable and body mass as a covariate. All indirect calorimetric measurements were done in automated cages (*Camk1d*^{fl/fl} n = 7; *Agrp*^{Cre/+} n = 8 and *Agrp*^{Cre/+}; *Camk1d*^{fl/fl} n = 9). Data are presented as mean ± s.e.m. Statistical tests included ANCOVA (d).

action-potential frequency in AgRP neurons of *Camk1d*^{-/-}-AgRP-eGFP mice were similar to those in *Camk1d*^{+/+}-AgRP-eGFP mice (*Camk1d*^{+/+}, n = 12; *Camk1d*^{-/-}, n = 10, P = 0.82) (Fig. 5d,e). Between the two mouse lines, we also found no significant differences in general intrinsic electrophysiological properties of AgRP neurons, such as spontaneous action-potential frequency, input resistance, excitability or whole-cell capacitance (Fig. 5f–i). Taken together, these data suggest that CaMKID is dispensable for ghrelin-stimulated activation of AgRP neurons.

Ghrelin activates CaMKID to induce AgRP/NPY expression

Lack of CaMKID did not affect the ghrelin-induced increase in electrical activity of AgRP neurons, prompting us to hypothesize that CaMKID acts downstream or independent of neuronal activity. We thus next asked whether CaMKID is activated upon ghrelin stimulation. We first used Phos-tag gels to address CaMKID phosphorylation in response to ghrelin in cultured primary hypothalamic cells isolated from *Camk1d*^{-/-} and *Camk1d*^{+/+} mice. Indeed, phosphorylated CaMKID, as marked by the upshifted band, increased upon ghrelin stimulation (Fig. 6a). Calcium/calmodulin directly activates calcium/calmodulin-dependent protein kinase I by binding to the enzyme, and indirectly promotes the phosphorylation and synergistic activation of the enzyme by calcium/calmodulin-dependent protein kinase kinase (CaMKK)²⁹. In line with above findings in cultured neurons, activatory phosphorylation of CaMKID significantly increased in hypothalamus of ghrelin-stimulated *Camk1d*^{+/+} mice, while no phosphorylation of CaMKID or total protein was visible in *Camk1d*^{-/-} samples (Fig. 6b,c). Thus, ghrelin activates CaMKID in hypothalamic cells.

Ghrelin stimulates AMPK activity in the hypothalamus³⁰. However, ghrelin-induced AMPK activity in primary hypothalamic neurons of *Camk1d*^{-/-} mice was equal to that in *Camk1d*^{+/+} mice, as shown by

assessment of activatory phosphorylation of AMPK and phosphorylation of its target acetyl-CoA carboxylase (ACC) (Fig. 6d–f). Ghrelin-induced cAMP response element (CRE)-binding protein (CREB) phosphorylation promotes expression of AgRP and NPY, which mediate the orexigenic action of ghrelin³¹. To monitor phosphorylation of CREB in response to ghrelin, we used immunofluorescence in the ARC of NPY-GFP reporter mice. NPY-GFP-positive neurons of *Camk1d*^{+/+} mice showed enhanced phosphorylated CREB in response to ghrelin, while ghrelin-induced phosphorylation was abolished in *Camk1d*^{-/-} mice (Fig. 6g,h). In line with reduced phosphorylation of CREB, Ghrelin-induced transcription of AgRP and NPY, but not POMC, was almost abolished in *Camk1d*^{-/-} cells (Fig. 6i), indicating that reduction of activatory CREB phosphorylation constitutes at least one plausible explanation for reduced expression of AgRP and NPY. NPY and AgRP projections in the PVN are dynamically regulated in response to ghrelin. While they increased in control mice in response to ghrelin, this increase was completely abolished in *Camk1d*-knockout mice. Notably, no differences in NPY and AgRP projections were found at baseline, suggesting again that a ghrelin-specific response is affected in the absence of CaMKID (Fig. 6j–m). Reduced levels, and thus decreased inhibitory action, of AgRP and NPY on predominantly anorexigenic neurons in the PVN is thus a likely mechanism underlying reduced food intake and body weight despite normal AgRP neuronal activity. Hence, CaMKID in AgRP neurons is required for CREB-dependent expression of the orexigenic neuropeptides AgRP and NPY, thereby regulating food intake and obesity.

Discussion

A possible role of CaMKID in obesity and T2D has been predicted on the basis of recent GWASs. However, the function of CaMKID in physiology and metabolic disease in vivo was unknown. In our study,

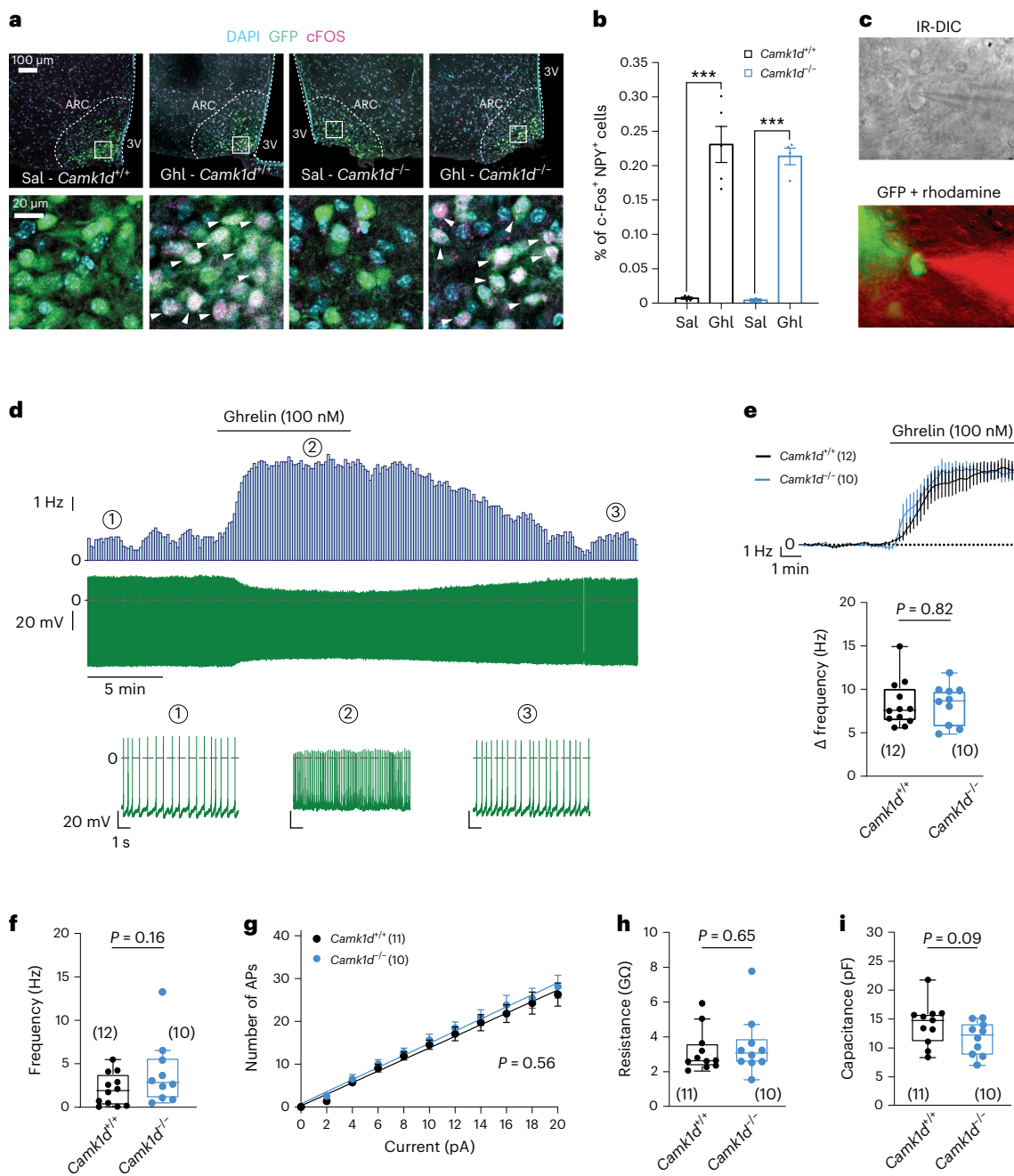
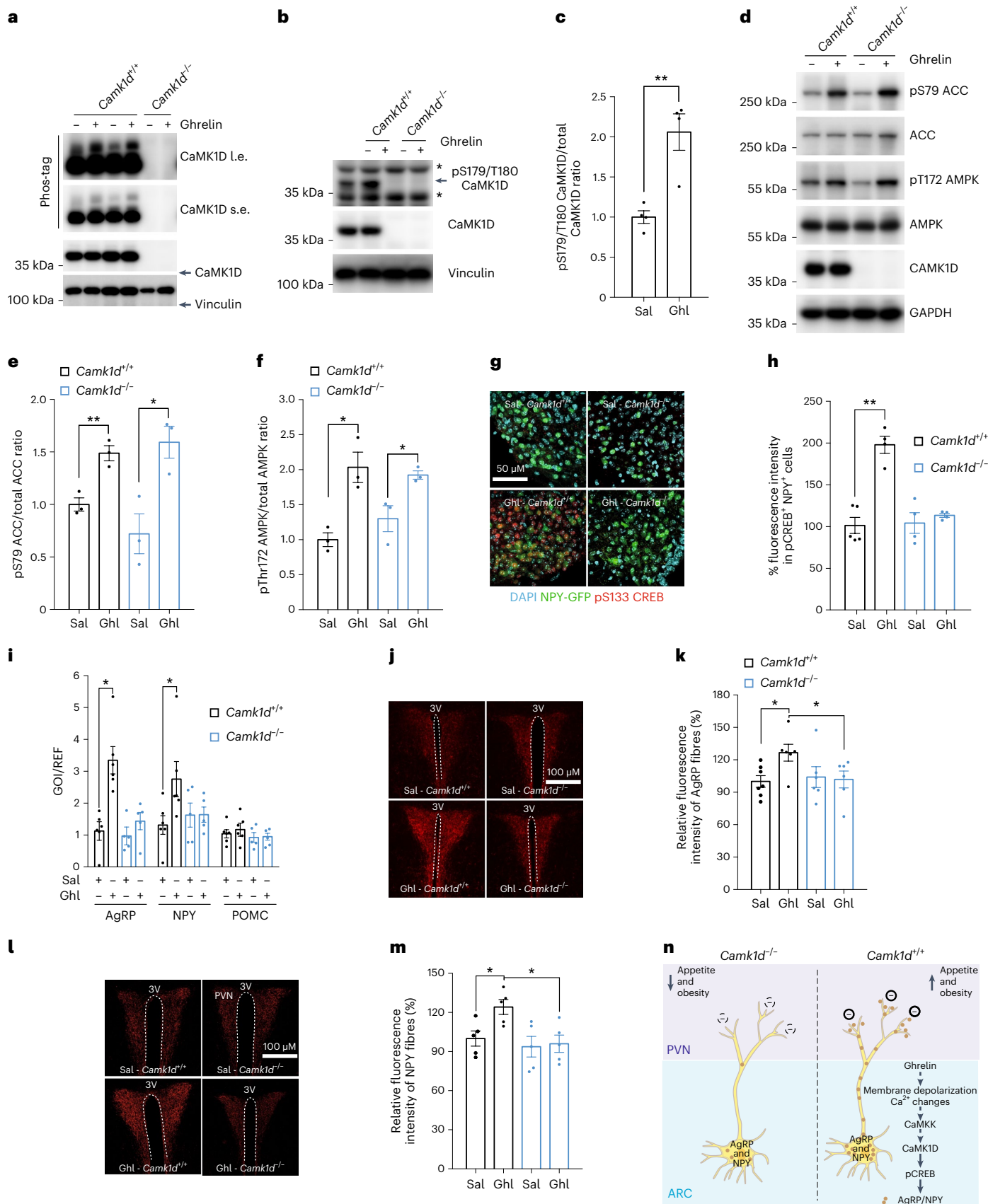


Fig. 5 | CaMK1D is dispensable for ghrelin-induced electrophysiological activation of AgRP/NPY neurons. **a, b,** Representative immunofluorescence and quantification of NPY-GFP⁺ and c-Fos⁺ cells in the ARC of mice. Animals were injected with 30 μg ghrelin (ghl) or vehicle (saline, sal), and, 2 h after injections, whole hypothalamus was removed. White arrows show NPY-positive neurons expressing c-Fos (Sal -Camk1d^{+/+} n=5; Ghl -Camk1d^{+/+} n=5; Sal -Camk1d^{-/-} n=3; Ghl -Camk1d^{-/-} n=4). **c,** AgRP neurons expressing eGFP (green) and the recording pipette contained tetramethyl rhodamine dextran (red) to monitor membrane integrity during the perforated patch clamp recording. Brightfield (top) and fluorescence (bottom) imaging are shown. **d,** Recording of an AgRP neuron from a Camk1d^{+/+} mouse during ghrelin (100 nM) bath application. Top, rate histogram; bin width, 10 s. Middle, original recording. Bottom, segments of the original recording in higher time resolution. The numbers indicate the time points from which the

segments originate. **e,** Ghrelin responses of AgRP neurons from Camk1d^{+/+} and in Camk1d^{-/-} mice, expressed as change in action-potential frequency. Top, mean (± s.e.m.) responses during the first 5 min of ghrelin application. Bottom, box plots showing the change in action-potential frequency measured between 6 and 8 min of ghrelin application. **f–i,** Basic electrophysiological properties of AgRP neurons in Camk1d^{+/+} and in Camk1d^{-/-} mice. **f,** Spontaneous action-potential frequency. **g,** Excitability assessed by the number of action potentials (APs) as a function of current pulse (1 s) amplitude. **h,** Input resistance. **i,** Whole-cell capacitance. The horizontal lines in the box plots show the median. The whiskers were calculated according to the Tukey method. ***P < 0.001. Statistical tests included unpaired Student's t test (**a**). Data in **e, f, h** and **i** were compared using the Mann–Whitney U test, and linear regressions in **g** were compared using the F-test. n values are given in brackets in the figure. Data are presented as mean values ± s.e.m.

using a loss-of-function approach in mice, we discovered an unpredicted role of CaMK1D in central control of food intake. We excluded a cell-autonomous role of CaMK1D in the liver and pancreas.

We found that CaMK1D is specifically required in AgRP neurons to promote ghrelin-induced food intake. Genetic studies have predicted that enhanced expression of CaMK1D contributes to



T2D^{13,14}, and our data also fit with a model in which enhanced CaMK1D signalling in AgRP neurons promotes obesity. Deletion of *Camk1d* in AgRP neurons is sufficient to trigger significant effects on

body weight and food intake, seen in global *Camk1d*-knockout mice, highlighting the importance of CaMK1D signalling in this subpopulation of neurons.

Fig. 6 | Lack of CaMK1D reduces ghrelin-induced AgRP/NPY expression and abundance in AgRP neuron projections to the PVN. **a**, Representative Phos-tag immunoblot of CaMK1D using lysates of hypothalamic cells from mice treated with 1 μM ghrelin or vehicle for 5 min, i.e., long exposure; s.e., short exposure. **b**, Representative immunoblot of CaMK1D phosphorylated at S179 and T180 (pS179/T180 CaMK1D) using lysates of whole hypothalamus from mice with the indicated genotypes. Vinculin was used as a loading control. Animals were injected with 30 μg ghrelin or vehicle, and, 2 h after injections, whole hypothalamus was removed and used for protein extraction. **c**, Quantification of CaMK1D phosphorylation ($n = 4$ per group). **d**, Representative immunoblots of pS79 ACC and pT172 AMPK using lysates of hypothalamic primary neurons from mice with the indicated genotypes treated with 1 μM ghrelin or vehicle for 5 min. **e,f**, Quantification of ACC ($n = 4$ per group) and AMPK phosphorylation ($n = 3$ per group). **g**, Representative immunofluorescence of pS133 CREB using hypothalamic slices of NPY-GFP mice with the indicated genotypes. Animals

were injected with 30 μg ghrelin or vehicle, and, 2 h after injections, whole brain containing hypothalamus was removed. Nuclei were stained with DAPI (blue); pS133 CREB is stained red, and NPY-GFP is green. PVN, paraventricular nucleus. **h**, Quantification of pS133 CREB fluorescence intensity in NPY-GFP⁺ neurons ($n = 4$ per group). **i**, Expression of AgRP, NPY and POMC mRNA in whole hypothalamus. Animals were injected with 30 μg ghrelin or vehicle, and whole hypothalamus was removed 2 h after injections (*Camk1d*^{+/+} $n = 6$; *Camk1d*^{-/-} $n = 5$). GOI, gene of interest; Ref, gene of reference (*Tbp*). **j–m**, Representative immunofluorescence and quantification of AgRP (Sal-*Camk1d*^{+/+} $n = 7$; Gh1-*Camk1d*^{+/+} $n = 6$; Sal-*Camk1d*^{-/-} $n = 6$; Gh1-*Camk1d*^{-/-} $n = 6$) and NPY (*Camk1d*^{+/+} $n = 5$; *Camk1d*^{-/-} $n = 5$) projections to the PVN. Animals were injected with 30 μg ghrelin, and, 2 h after injections, brain was removed. **n**, Schematic model depicting mechanisms underlying how CaMK1D promotes food intake. Data are presented as mean values ± s.e.m. * $P < 0.05$ and *** $P < 0.001$. Statistical tests included unpaired Student's *t* test (**c,e,f,h,i,k,m**).

CaMK1D is widely expressed in the CNS, and ghrelin has been reported to act in different hypothalamic and extrahypothalamic areas to induce feeding. We showed that CaMK1D is dispensable in anorexigenic POMC neurons. Although deletion of *Camk1d* in AgRP neurons largely recapitulates phenotypes seen in whole-body knockout mice, this does not fully exclude functions in other organs implicated in energy homeostasis that need to be further explored.

Importantly, CaMK1D is dispensable for ghrelin-stimulated electrical activity of AgRP neurons. This finding is in line with a model in which ghrelin-driven neuronal activity induces membrane depolarization and calcium changes, which in turn trigger CaMK1D activation and CaMK1D-dependent responses including CREB-dependent transcription³². Thus, our study has identified a signalling pathway in AgRP neurons that links neuronal activity to CREB-dependent transcription (Fig. 6n).

CREB-dependent transcription has been shown to regulate fundamental processes in neuronal development, activity-dependent dendritic outgrowth and synaptic plasticity³³. In AgRP neurons, CREB controls transcription of AgRP and NPY³¹. In accordance with this finding, we found that ghrelin failed to induce AgRP and NPY transcription in *Camk1d*-deficient hypothalamus and that AgRP and NPY abundance in projections to the PVN were reduced. In fact, it has been demonstrated that ghrelin fails to stimulate feeding upon chemical and genetic inhibition of AgRP and NPY^{26,34–37}. Although AgRP and NPY are crucial neuropeptides inhibiting anorexigenic neurons in the PVN, other CREB-dependent functions might be affected in *Camk1d*-deficient AgRP neurons that may also contribute to the observed metabolic phenotypes to be investigated in the future. Moreover, CaMK1D might also regulate CREB-independent functions still to be explored.

Deletion of the ghrelin receptor specifically in AgRP neurons^{38,39} does not precisely phenocopy body weight phenotypes seen in mice with AgRP-neuron-specific CaMK1D knockout. While Wu et al. reported differences exclusively in mice on a HFD, our study revealed changes in body weight of mice on a chow diet as well as on a HFD. Therefore, CaMK1D in AgRP neurons might be engaged by stimuli other than ghrelin that are yet to be identified.

Central ghrelin administration induced AMPK phosphorylation and activation, and ghrelin responses could be alleviated through AMPK inhibition⁴⁰. AMPK activation was dependent on calcium changes and on CaMK2activation⁴⁰. CaMKK is also known to activate CaMK1, including CaMK1D (Fig. 6g). Interestingly, AMPK activation was shown to occur in the VMH, since adenoviral delivery of a dominant negative isoform of AMPK into the VMH was sufficient to block ghrelin-induced food intake^{40–42}. Therefore, it has been suggested that AgRP/NPY levels in neurons in the ARC are regulated at a presynaptic level by AMPK signalling in neurons of the VMH. We found here that lack of *Camk1d* almost entirely abolished the increase in AgRP/NPY transcription in response to ghrelin. Yet, absence of *Camk1d* does not affect AMPK signalling in response to ghrelin in the hypothalamus. Given that AgRP-neuron-specific deletion of *Camk1d* is sufficient to

reduce food intake in response to ghrelin, we propose that the transcriptional control of AgRP/NPY expression primarily depends on CaMK1D signalling in AgRP neurons.

Elevated levels of cAMP led to CREB phosphorylation at Ser133 and alteration of this site have been found to abrogate CREB-dependent reporter gene activation⁴³. Protein kinase A (PKA) is the main mediator of cAMP-dependent phosphorylation of CREB. Indeed, ghrelin was shown to increase calcium through the cAMP–PKA pathway in NPY-expressing cells in the ARC of rats⁴⁴. However, we observe that phosphorylation of CREB depends, at least partially, on CaMK1D activity. In fact, CREB has been shown to be phosphorylated in vitro by both kinases, PKA and CaMK1 (ref. 32). Given that phosphorylation is reduced, but not abolished, in the absence of CaMK1D, both kinases might be necessary to exert robust CREB phosphorylation in response to ghrelin.

mTOR–S6K1 signalling has also been demonstrated to be involved in hypothalamic regulation of food intake in response to ghrelin through regulation of CREB phosphorylation and AgRP/NPY expression^{45,46}. However, it is unclear so far how and in which neurons mTOR–S6K1 regulates ghrelin responses. In fact, mTOR1 signalling in AgRP neurons has been shown to control circadian expression of AgRP and NPY, but was redundant for regulation of food intake⁴⁷.

Altogether, our results uncover a signalling mechanism that acts in AgRP neurons to control levels of AgRP and NPY, two main orexigenic neuropeptides centrally involved in promoting food intake. Uncontrolled CaMK1D signalling in AgRP neurons represents a valuable mechanism that promotes obesity and T2D.

Methods

Animals care

Animal care and all experimental procedures were approved by the local ethical committee (Com'Eth), in compliance with the French and European legislation on care and use of laboratory animals (APAFIS#18638-2019012510177514v4, APAFIS#21069-2019061411418629v2, APAFIS#37421-2022052012206789v4). Mice were individually housed under controlled temperature at 22 °C and humidity at 40% on a 12-h light/dark cycle, with unrestricted access to water and prescribed diet. Food was withdrawn only if required for an experiment. Body weight and food intake were determined weekly. Animals were fed with regular chow or a HFD. Chow contained 73.6% calories from carbohydrates, 18.1% calories from protein and 8.4% calories from fat (SAFE D04 from Safe) and HFD contains 20% calories from carbohydrates, 20% calories from protein and 60% calories from fat (D12492i from Research Diet). For all experiments, only male mice were used. All experiments were performed in adult mice aged 5–25 weeks.

Generation of transgenic mice

Camk1d conditional knockout and global knockout mice were generated according to the ‘knockout first’ strategy by the Institut Clinique de la Souris (ICS, Illkirch-Graffenstaden, France). 5' of exon 4 of the *Camk1d*

gene a SA-βGeo-pA (LacZ-neoR) trapping cassette was inserted flanked by two FRT sites, which disrupts gene function (knockout first allele). Furthermore, two LoxP sites were inserted 5' and 3' of exon 4. The FRT-recombinase (Flp) converted the 'knockout first' allele to a floxed allele (*Camk1d*^{flox/flox}), restoring gene activity (Extended Data Fig. 1a,b). Verification of correct targeting was done using southern blotting, as previously described⁴⁸. The sequences of the primers used to genotype the mice and to verify Cre-mediated recombination are provided in Extended Data Table 1. *Camk1d*^{flox/flox} mice were mated with Rosa26-Cre mice expressing Cre recombinase under control of the Rosa26 promoter (for global knockout)²¹, resulting in the deletion of the floxed exon. The breeding colonies were maintained by mating hemizygote *Camk1d*^{+/−} females to hemizygote *Camk1d*^{+/−} males. Mice were on a C57BL/6N/J mixed background. Tissue-specific deletion of *Camk1d* was obtained by mating floxed mice with transgenic mice expressing Cre recombinase under the control of a tissue-specific promoter, and breeding colonies were maintained by mating tissue-specific promoter Cre^{+/−}; *Camk1d*^{flox/+} to *Camk1d*^{flox/+} mice. All mice were on a C57BL/6N/J mixed background. All cre deleter mouse lines are listed in the reporting summary.

Blood collection and biochemical measurements

Blood samples obtained from the tail and collected in heparinized capillaries were used to measure fasted blood glucose and insulin levels. Animals were fasted at 8 a.m., and the samples were collected 4 h later. At the end of the experiment, blood was collected from the retro orbital sinus, put into tubes containing 0.2 μM EDTA and 4 mM Pefabloc SC, and centrifuged for 15 min at 3,000g to separate the plasma. Plasma was stored at −80 °C. Acylated ghrelin, leptin and insulin were measured by ELISA.

Glucose and insulin tolerance assays

Glucose tolerance test. After a 16-h fast, animals were injected i.p. with 2 g/kg (animals on CD) or 1 g/kg (animals on HFD) dextrose in 0.9% NaCl. Blood glucose was measured prior to and 15, 30, 45, 60, 90, and 120 minutes after injections. Blood glucose values were determined in a drop of blood sampled from the tail using an automatic glucose monitor (Accu-Check; Roche Applied Science). Plasma samples were collected at 0, 15 and 30 min for insulin measurements.

Insulin tolerance test. After a 5-hour fast, animals were injected i.p. with 0.75 IU kg^{−1} recombinant human insulin (Umaline; Lilly). Blood glucose levels were measured before and 15, 30, 40, 60 and 90 min after injections. kITT (percentage min^{−1}) was calculated using the formula as previously described⁴⁹. $kITT = 0.693 \times 100 / t_{1/2}$, where $t_{1/2}$ was calculated from the slope of the plasma glucose concentration, considering an exponential decrement of glucose concentration during the 30 min after insulin administration.

Automated cages phenotyping for indirect calorimetric measurements

Twenty-five-week-old mice were acclimated in metabolic chambers (TSE LabMaster System - Metabolic Phenotyping Facility, ICS) for 1 d before the start of the recordings. Mice were continuously recorded for 1 or 2 days, and measurements of locomotor activity (in the xy and z axes) and gas exchange (O₂ and CO₂) were made every 30 min. Energy expenditure was calculated according to the manufacturer's guidelines (PhenoMaster Software, TSE System). The respiratory quotient was estimated by calculating the ratio of CO₂ production to O₂ consumption. Values were corrected by metabolic mass (lean mass + 0.2 fat mass) as previously described⁵⁰. ANCOVA analysis was done as previously described⁵¹.

Animal length and body composition

Animal length was assessed with X-Ray MX-20 Specimen (Faxitron - Metabolic Phenotyping Facility, ICS). Digital X-ray pictures allowed the

measurement of whole body and tibia size of mice. Body composition was evaluated by qNMR using the minispec analyzer (Bruker BioSpin S.A.S., Metabolic Phenotyping Facility, ICS).

Leptin, ghrelin, CNO responsiveness

To assess leptin sensitivity, mice received an i.p. injection of either PBS or mouse recombinant leptin (3 mg kg^{−1}) 24 h after food withdrawal, and their food intake were monitored at 4 h and 6 h following the injections. The food intake after PBS injection was compared with the food intake after leptin administration. The orexigenic response to ghrelin and CNO was determined in mice that received an i.p. injection of either PBS, ghrelin (1 mg kg^{−1}) or CNO (0.6 mg kg^{−1}). Food intake was assessed 4 h and 6 h after injections.

Culture of primary cells of hypothalamus

Hypothalamus was dissected from E15.5 embryos and stored on ice in neurobasal medium (Gibco). Tissues were incubated for 20 min in a 37 °C water bath in 100 U ml^{−1} papain (Worthington) and 10 mg ml^{−1} DNase I (Worthington). Digestion was stopped with Ovomucoïde (Worthington). Tissues were transferred into 1 ml of adult neuronal growth medium consisting of neurobasal-A medium, 3 mM L-glutamine (Gibco), 1× B-27 supplement, 1× N-2 supplement and antibiotics. Tissues were gently triturated until uniform cellular dissociation was achieved. Cells were counted and plated into cell culture plates coated with poly-L-lysine (Gibco).

Western blotting

Cells were washed with ice-cold PBS on ice and snap-frozen in liquid nitrogen. Cell lysates for western blots were prepared using 1× Laemmli buffer (50 mM Tris-HCl pH6.8, 100 mM DTT, 8% SDS, 0.01% bromophenol blue, 10% glycerol) supplemented with phosphatase/protease inhibitors (Cell Signaling Technology) and incubated on ice for 10 min. After centrifugation at 16,000g for 10 min at 4 °C, cleared supernatant was transferred to the new tubes and was used immediately stored at −80 °C until used. Total protein was measured using the BCA method by Pierce BCA Protein Assay Kit (Thermo Fisher). Samples (20–50 μg of total protein content) were boiled and resolved on 10% acrylamide gels using standard Tris-Glycine SDS-PAGE or Phos-tag gels. Proteins were transferred to PVDF membranes (Millipore) and blotted with antibodies listed in the Antibodies section of Extended Data Table 1. For membrane blocking and primary antibody dilution, 5% BSA (wt/vol) in TBST was used. All incubations with primary antibodies were performed for 16 h at 4 °C. Blots were developed using SuperSignal West Pico (Pierce, Ref. 34580) or Luminata Forte Western HRP substrate (Merck Millipore, Ref. WBLUF0500).

Hypothalamic mRNA quantification

Total RNA from hypothalamus was extracted using an RNeasy Lipid Tissue Mini Kit (Qiagen) and quantified spectrophotometrically. Single-stranded cDNA was synthesized using SuperScript IV RNase Reverse Transcriptase (Invitrogen), according to the manufacturer's directions. Real-time PCR was carried out using an LightCycler 480 (Roche) with Fast SYBR Green Master Mix (Roche) and the primers listed in the primers section of Extended Data Table 1. Quantifications were done according to the Pfaffl method⁵².

Immunohistochemistry

Mediobasal hypothalamic sections from brains were prefixed with paraformaldehyde for 24 h and incubated in 30% sucrose (Thermo Fisher Scientific) for 24 h at 4 °C. Brains were embedded in optimal cutting temperature (OCT) compound, frozen at −80 °C and stored at −80 °C. Sections that were 30 μm thick were cut with a cryostat (Leica CM3050 S, France) and stored at 4 °C in sodium phosphate buffer. Sections were processed as follows. On day 1, free-floating sections were rinsed in PBS, incubated for 20 min in PBS containing 0.3% Tween-20 and then

rinsed three times, 10 min each, in PBS. Slices were incubated 1 h with 5% donkey serum in 0.3% PBS-T and then overnight or 72 h at 4 °C with the primary antibodies described in the antibodies section. Slides were rinsed three times for 10 min in 0.3% PBS-T and incubated for 60 min with secondary antibodies. Sections were rinsed three times for 10 min in PBS before mounting. Tissues were observed on a confocal laser scanning microscope, TCSSP8X with Leica software LAS X navigator, using a HC PL APO CS2 ×20/0.75 dry leica objective. The objectives and the pinhole setting (1airy unit) remained unchanged during the acquisition of a series for all images. Quantification of immuno-positive cells was performed using the cell counter plugin of ImageJ, taking as standard reference a fixed threshold of fluorescence.

Viral injections

Mice were anaesthetised with ketamine (130 mg kg⁻¹) and xylazine (13 mg kg⁻¹), diluted in saline (5 µl g⁻¹) and placed into a stereotaxic apparatus (World Precision Instruments). For postoperative care, mice were injected i.p. with buprenorphine (0.3 mg kg⁻¹). After exposing the skull via small incision, a small hole was drilled for injection. A Hamilton syringe connected to a 33 G needle was inserted into the brain and virus was injected. A micromanipulator (World Precision Instruments) was used to control injection speed at 50 nl min⁻¹, and the pipette was withdrawn 1 min after injection. For knock-down experiments, AAV8-SYN-LoxP-shRNA-CaMK1D-eGFP-LoxP or AAV8-SYN-LoxP-shRNA-Scramble-eGFP-LoxP (Universitat Autònoma de Barcelona; titre 1.12 × 10¹³ genome copies ml⁻¹) were bilaterally injected into the ARC (300 nl, AP: -1.40 mm, DV: -5.80 mm, ML: ±0.10 mm from bregma). For rescue experiments, AAV2/9-CAGs-Flex-CaMK1Dwt-eGFP (IGBMC molecular biology and Virus Core; titre 2.7 × 10¹³ genome copies ml⁻¹) were bilaterally injected into the ARC (300 nl, coordinates as above). For CNO experiments, hSyn-DIO-hM3D(Gq)-mCherry (IGBMC molecular biology and Virus Core, titre 1.5 × 10¹³ genome copie ml⁻¹) were bilaterally injected into the ARC (300 nl, coordinates as above). Mice were given a minimum of 2 weeks recovery and 1 week acclimation before being used in any experiments.

Electrophysiology

Experiments were performed on brain slices from 9–12-week-old male *Camk1d*^{+/+} and *Camk1d*^{-/-} mice that expressed eGFP selectively in AgRP neurons. Animals were kept under standard laboratory conditions, with tap water and chow available ad libitum, on a 12-h light/dark cycle. The animals were lightly anesthetized with isoflurane (B506; AbbVie Deutschland) and decapitated. Coronal slices (280 µm) containing the arcuate nucleus of the hypothalamus were cut with a vibration microtome (VT1200 S; Leica, Germany) in cold (4 °C), carbogenated (95% O₂ and 5% CO₂), glycerol-based modified artificial cerebrospinal fluid (GaCSF)⁵³.

Current-clamp recordings of GFP-expressing AgRP neurons were performed at -32 °C. Neurons were visualized with a fixed stage upright microscope (Zeiss AxioExaminer, Zeiss) using a ×40 water-immersion objective (W Plan-ApoChromat ×40/1.0 DIC M27, 1 numerical aperture, 2.5 mm working distance; Zeiss) with infrared differential interference contrast optics⁵⁴ and fluorescence optics. GFP-expressing AgRP neurons were identified by their anatomical location in the arcuate nucleus and by their fluorescent label.

Perforated patch experiments were conducted using protocols modified from refs. [55,56](#).

The spontaneous firing frequency was measured for 5 min after perforation. To measure intrinsic electrophysiological properties, series of hyperpolarizing and depolarizing current pulses were applied under current-clamp from a membrane potential of -70 mV. For input resistance and capacitance measurements, hyperpolarizing current steps with -2 pA increments were applied. For excitability measurements, depolarizing 1-s current steps with +2 pA increments were applied. The specific protocols are given in the Results.

To investigate the modulatory effect of ghrelin (031-31, Phoenix Pharmaceuticals), a 100 nM ghrelin was bath applied for 8–10 min. The ghrelin effect was analysed by comparing the action-potential frequencies that were measured during 2-min intervals that were recorded directly before and at the end of the peptide applications.

Data analysis of electrophysiological data

Data analysis was performed with Spike2 (version 7; Cambridge Electronic Design), Igor Pro 6 (WaveMetrics) and Graphpad Prism 8. If not stated otherwise, all calculated values are expressed as means ± s.e.m. The horizontal lines show the data's median. The whiskers were calculated according to the Tukey method. For comparisons of independent nonparametric distributions, the Mann–Whitney *U* test was used. Linear regressions were compared using the *F*-test. A significance level of 0.05 was accepted for all tests. Exact *P* values are reported if *P* > 0.05. In the figures, *n* values are given in brackets.

Quantification and statistical analysis

All statistical comparisons were performed with Prism 6 (GraphPad Software) or R software for ANCOVA analysis. All the data were analysed using either Student's *t* test (paired or unpaired) with equal variances or one- two-way ANOVA. In all cases, the significance threshold was automatically set to *P* < 0.05. ANOVA analyses were followed by Bonferroni post hoc test for specific comparisons only when overall ANOVA revealed a significant difference (at least *P* < 0.05).

Reporting summary

Further information on research design is available in the Nature Portfolio Reporting Summary linked to this article.

Data availability

All raw data related to the studies shown in figures and Extended Data Figures. Source data are provided with this paper.

References

1. Kim, K.-S., Seeley, R. J. & Sandoval, D. A. Signalling from the periphery to the brain that regulates energy homeostasis. *Nat. Rev. Neurosci.* **19**, 185–196 (2018).
2. Jais, A. & Brüning, J. C. Arcuate nucleus-dependent regulation of metabolism — pathways to obesity and diabetes mellitus. *Endocr. Rev.* **9**, 314–328 (2021).
3. Morton, G. J., Cummings, D. E., Baskin, D. G., Barsh, G. S. & Schwartz, M. W. Central nervous system control of food intake and body weight. *Nature* **443**, 289–295 (2006).
4. Timper, K. & Brüning, J. C. Hypothalamic circuits regulating appetite and energy homeostasis: pathways to obesity. *Dis. Model Mech.* **10**, 679–689 (2017).
5. Chen, S.-R. et al. Ghrelin receptors mediate ghrelin-induced excitation of agouti-related protein/neuropeptide Y but not pro-opiomelanocortin neurons. *J. Neurochem.* **142**, 512–520 (2017).
6. Zigman, J. M., Bouret, S. G. & Andrews, Z. B. Obesity impairs the action of the neuroendocrine ghrelin system. *Trends Endocrinol. Metab.* **27**, 54–63 (2016).
7. Bonnefond, A. & Froguel, P. Rare and common genetic events in type 2 diabetes: what should biologists know? *Cell Metab.* **21**, 357–368 (2015).
8. Locke, A. E. et al. Genetic studies of body mass index yield new insights for obesity biology. *Nature* **518**, 197–206 (2015).
9. Kooner, J. S. et al. Genome-wide association study in individuals of South Asian ancestry identifies six new type 2 diabetes susceptibility loci. *Nat. Genet.* **43**, 984–989 (2011).
10. Shu, X. O. et al. Identification of new genetic risk variants for type 2 diabetes. *PLoS Genet.* **6**, e1001127 (2010).

11. Zeggini, E. et al. Meta-analysis of genome-wide association data and large-scale replication identifies additional susceptibility loci for type 2 diabetes. *Nat. Genet.* **40**, 638–645 (2008).
12. Morris, A. P. et al. Large-scale association analysis provides insights into the genetic architecture and pathophysiology of type 2 diabetes. *Nat. Genet.* **44**, 981–990 (2012).
13. Thurner, M. et al. Integration of human pancreatic islet genomic data refines regulatory mechanisms at Type 2 Diabetes susceptibility loci. *eLife* **7**, e31977 (2018).
14. Xue, A. et al. Genome-wide association analyses identify 143 risk variants and putative regulatory mechanisms for type 2 diabetes. *Nat. Commun.* **9**, 2941 (2018).
15. Simonis-Bik, A. M. et al. Gene variants in the novel type 2 diabetes loci CDC123/CAMK1D, THADA, ADAMTS9, BCL11A, and MTNR1B affect different aspects of pancreatic beta-cell function. *Diabetes* **59**, 293–301 (2010).
16. Haney, S. et al. RNAi screening in primary human hepatocytes of genes implicated in genome-wide association studies for roles in type 2 diabetes identifies roles for CAMK1D and CDKAL1, among others, in hepatic glucose regulation. *PLoS ONE* **8**, e64946 (2013).
17. Buchser, W. J., Slepak, T. I., Gutierrez-Arenas, O., Bixby, J. L. & Lemmon, V. P. Kinase/phosphatase overexpression reveals pathways regulating hippocampal neuron morphology. *Mol. Syst. Biol.* **6**, 391 (2010).
18. Wayman, G. A. et al. Regulation of axonal extension and growth cone motility by calmodulin-dependent protein kinase I. *J. Neurosci.* **24**, 3786–3794 (2004).
19. Takemoto-Kimura, S. et al. Regulation of dendritogenesis via a lipid-raft-associated Ca²⁺/calmodulin-dependent protein kinase CLICK-III/CaMKIγ. *Neuron* **54**, 755–770 (2007).
20. Schmitt, J. M., Guire, E. S., Saneyoshi, T. & Soderling, T. R. Calmodulin-dependent kinase kinase/calmodulin kinase I activity gates extracellular-regulated kinase-dependent long-term potentiation. *J. Neurosci.* **25**, 1281–1290 (2005).
21. Soriano, P. Generalized lacZ expression with the ROSA26 Cre reporter strain. *Nat. Genet.* **21**, 70–71 (1999).
22. Gu, G., Dubauskaite, J. & Melton, D. A. Direct evidence for the pancreatic lineage: NGN3+ cells are islet progenitors and are distinct from duct progenitors. *Development* **129**, 2447–2457 (2002).
23. Hatting, M., Tavares, C. D. J., Sharabi, K., Rines, A. K. & Puigserver, P. Insulin regulation of gluconeogenesis. *Ann. NY Acad. Sci.* **1411**, 21–35 (2018).
24. Postic, C. et al. Dual roles for glucokinase in glucose homeostasis as determined by liver and pancreatic beta cell-specific gene knock-outs using Cre recombinase. *J. Biol. Chem.* **274**, 305–315 (1999).
25. Müller, T. D. et al. Ghrelin. *Mol. Metab.* **4**, 437–460 (2015).
26. Andrews, Z. B. et al. UCP2 mediates ghrelin's action on NPY/AgRP neurons by lowering free radicals. *Nature* **454**, 846–851 (2008).
27. Hoffman, G. E., Smith, M. S. & Verbalis, J. G. c-Fos and related immediate early gene products as markers of activity in neuroendocrine systems. *Front Neuroendocrinol.* **14**, 173–213 (1993).
28. van den Pol, A. N. et al. Neuromedin B and gastrin-releasing peptide excite arcuate nucleus neuropeptide Y neurons in a novel transgenic mouse expressing strong Renilla green fluorescent protein in NPY neurons. *J. Neurosci.* **29**, 4622–4639 (2009).
29. Haribabu, B. et al. Human calcium-calmodulin dependent protein kinase I: cDNA cloning, domain structure and activation by phosphorylation at threonine-177 by calcium-calmodulin dependent protein kinase I kinase. *EMBO J.* **14**, 3679–3686 (1995).
30. Andersson, U. et al. AMP-activated protein kinase plays a role in the control of food intake. *J. Biol. Chem.* **279**, 12005–12008 (2004).
31. Sakkou, M. et al. A role for brain-specific homeobox factor Bsx in the control of hyperphagia and locomotory behavior. *Cell Metab.* **5**, 450–463 (2007).
32. Sheng, M., Thompson, M. A. & Greenberg, M. E. CREB: a Ca²⁺-regulated transcription factor phosphorylated by calmodulin-dependent kinases. *Science* **252**, 1427–1430 (1991).
33. Flavell, S. W. & Greenberg, M. E. Signaling mechanisms linking neuronal activity to gene expression and plasticity of the nervous system. *Annu Rev Neurosci.* **31**, 563–590 (2008).
34. Aponte, Y., Atasoy, D. & Sternson, S. M. AgRP neurons are sufficient to orchestrate feeding behavior rapidly and without training. *Nat. Neurosci.* **14**, 351–355 (2011).
35. Chen, H. Y. et al. Orexigenic action of peripheral ghrelin is mediated by neuropeptide Y and agouti-related protein. *Endocrinology* **145**, 2607–2612 (2004).
36. Luquet, S., Perez, F. A., Hnasko, T. S. & Palmiter, R. D. NPY/AgRP neurons are essential for feeding in adult mice but can be ablated in neonates. *Science* **310**, 683–685 (2005).
37. Nakazato, M. et al. A role for ghrelin in the central regulation of feeding. *Nature* **409**, 194–198 (2001).
38. Wu, C.-S. et al. Suppression of GHS-R in AgRP neurons mitigates diet-induced obesity by activating thermogenesis. *Int. J. Mol. Sci.* **18**, 832 (2017).
39. Wang, Q. et al. Arcuate AgRP neurons mediate orexigenic and glucoregulatory actions of ghrelin. *Mol. Metab.* **3**, 64–72 (2014).
40. Anderson, K. A. et al. Hypothalamic CaMKK2 contributes to the regulation of energy balance. *Cell Metab.* **7**, 377–388 (2008).
41. López, M. et al. Hypothalamic fatty acid metabolism mediates the orexigenic action of ghrelin. *Cell Metab.* **7**, 389–399 (2008).
42. García, A., Alvarez, C. V., Smith, R. G. & Diéguez, C. Regulation of Pit-1 expression by ghrelin and GHRP-6 through the GH secretagogue receptor. *Mol. Endocrinol.* **15**, 1484–1495 (2001).
43. Gonzalez, G. A. & Montminy, M. R. Cyclic AMP stimulates somatostatin gene transcription by phosphorylation of CREB at serine 133. *Cell* **59**, 675–680 (1989).
44. Kohno, D., Gao, H.-Z., Muroya, S., Kikuyama, S. & Yada, T. Ghrelin directly interacts with neuropeptide-Y-containing neurons in the rat arcuate nucleus: Ca²⁺ signaling via protein kinase A and N-type channel-dependent mechanisms and cross-talk with leptin and orexin. *Diabetes* **52**, 948–956 (2003).
45. Martins, L. et al. Hypothalamic mTOR signaling mediates the orexigenic action of ghrelin. *PLoS ONE* **7**, e46923 (2012).
46. Stevanovic, D. et al. Ghrelin-induced food intake and adiposity depend on central mTORC1/S6K1 signaling. *Mol. Cell. Endocrinol.* **381**, 280–290 (2013).
47. Albert, V., Cornu, M. & Hall, M. N. mTORC1 signaling in AgRP neurons mediates circadian expression of AgRP and NPY but is dispensable for regulation of feeding behavior. *Biochem. Biophys. Res. Commun.* **464**, 480–486 (2015).
48. Codner, G. F. et al. Universal southern blot protocol with cold or radioactive probes for the validation of alleles obtained by homologous recombination. *Methods* **191**, 59–67 (2021).
49. Lundbaek, K. Intravenous glucose tolerance as a tool in definition and diagnosis of diabetes mellitus. *Br. Med J.* **1**, 1507–1513 (1962).
50. Even, P. C. & Nadkarni, N. A. Indirect calorimetry in laboratory mice and rats: principles, practical considerations, interpretation and perspectives. *Am. J. Physiol. Regul. Integr. Comp. Physiol.* **303**, R459–R476 (2012).
51. Müller, T. D., Klingenspor, M. & Tschöp, M. H. Revisiting energy expenditure: how to correct mouse metabolic rate for body mass. *Nat. Metab.* **3**, 1134–1136 (2021).
52. Pfaffl, M. W. A new mathematical model for relative quantification in real-time RT-PCR. *Nucleic Acids Res.* **29**, e45 (2001).

53. Ye, J. H., Zhang, J., Xiao, C. & Kong, J.-Q. Patch-clamp studies in the CNS illustrate a simple new method for obtaining viable neurons in rat brain slices: glycerol replacement of NaCl protects CNS neurons. *J. Neurosci. Methods* **158**, 251–259 (2006).
54. Dodt, H. U. & Ziegler, W. Visualizing unstained neurons in living brain slices by infrared DIC-videomicroscopy. *Brain Res.* **537**, 333–336 (1990).
55. Horn, R. & Marty, A. Muscarinic activation of ionic currents measured by a new whole-cell recording method. *J. Gen. Physiol.* **92**, 145–159 (1988).
56. Akaike, N. & Harata, N. Nystatin perforated patch recording and its applications to analyses of intracellular mechanisms. *Jpn. J. Physiol.* **44**, 433–473 (1994).

Acknowledgements

We thank T. Alquier at University of Montreal for helpful discussions and D. Dembele at the IGBMC for ANCOVA analysis. We thank the Imaging Center of the IGBMC (ICL), the IGBMC molecular biology and virus core facility, the Institut Clinique de la souris (ICS) core facilities and other core facilities for their support on this research. This work was supported by the Agence Nationale de la Recherche (ANR) (AAPG 2021 HypoCaMK), by the Fondation de Recherche Médicale (FRM) – Program: Equipe FRM (EQU201903007859, Prix Roger PROPICE pour la recherche sur le cancer du pancréas), by the FHU-OMAGE of region Grand-Est, from the European Foundation for the Study of Diabetes (EFSD)/Novo Nordisk Diabetes Research Programme and by the ANR-10-LABX-0030-INRT grant as well as the ANR-11-INBS-0009-INGESTEM grant, both French State funds managed by the ANR under the frame program Investissements d'Avenir. K.V. was supported by an Individual Fellowship (798961 INSULYSOSOME) in the framework of the Marie-Sklodowska Curie actions of the European Commission and a research grant from Société Francophone du Diabète. G.Y. received financial doctoral support from DFG-233886668/RTG1960. M. Quiñones was funded by a research contract Miguel Servet (CP21/00108) from the ISCIII co-funded by the European Union.

Author contributions

Conceptualization: R.R., R.N., P.K. and S.L. Software: E.G. Methodology: K.V., E.P., Z.Z., Ma.Q., G.Y., E.E., E.C.-C. and M. Qu. Validation: K.V. Formal

Analysis: K.V., C.M. Investigation: K.V., G.M., E.P., Z.Z., M. Quiñones., E.E., G.Y., M. Qu., A.S., M.F. C.M. Resources: E.E., F.B. Writing — Original Draft: R.R. and K.V., Supervision: K.V., S.L., P.K., R.N., A.C., I.S. and R.R., Funding Acquisition: R.R. and S.L.

Competing interests

The authors declare no competing interests.

Additional information

Extended data is available for this paper at <https://doi.org/10.1038/s42255-023-00814-x>.

Supplementary information The online version contains supplementary material available at <https://doi.org/10.1038/s42255-023-00814-x>.

Correspondence and requests for materials should be addressed to Karl Vivot or Romeo Ricci.

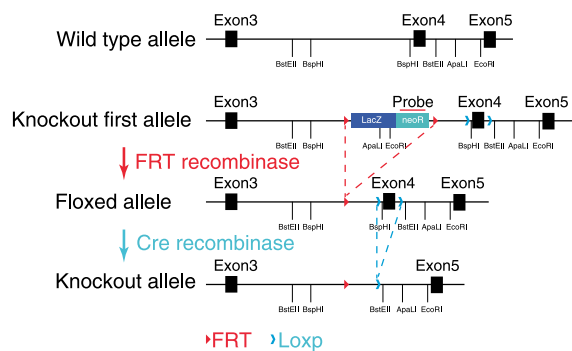
Peer review information *Nature Metabolism* thanks Timo D. Müller, Dominic Withers and the other, anonymous, reviewers for their contribution to the peer review of this work. Primary Handling editor: Ashley Castellanos-Jankiewicz, in collaboration with the *Nature Metabolism* team.

Reprints and permissions information is available at www.nature.com/reprints.

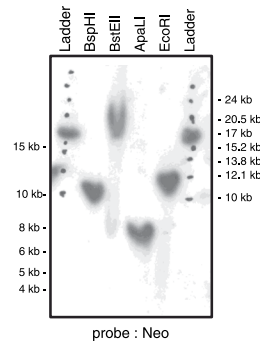
Publisher's note Springer Nature remains neutral with regard to jurisdictional claims in published maps and institutional affiliations.

Springer Nature or its licensor (e.g. a society or other partner) holds exclusive rights to this article under a publishing agreement with the author(s) or other rightsholder(s); author self-archiving of the accepted manuscript version of this article is solely governed by the terms of such publishing agreement and applicable law.

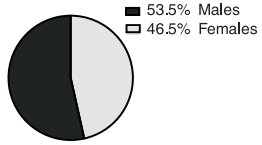
© The Author(s), under exclusive licence to Springer Nature Limited 2023

a**b**

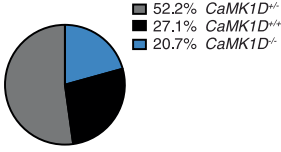
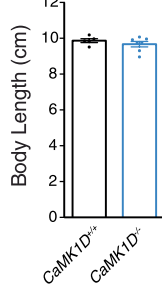
Restriction enzymes	Expected DNA size (kb)
BspHI	10.9
BstEII	18.2
ApaI	8.2
EcoRI	12.1

**c**

Females / Males Ratio

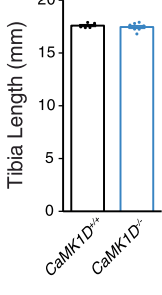
**d**

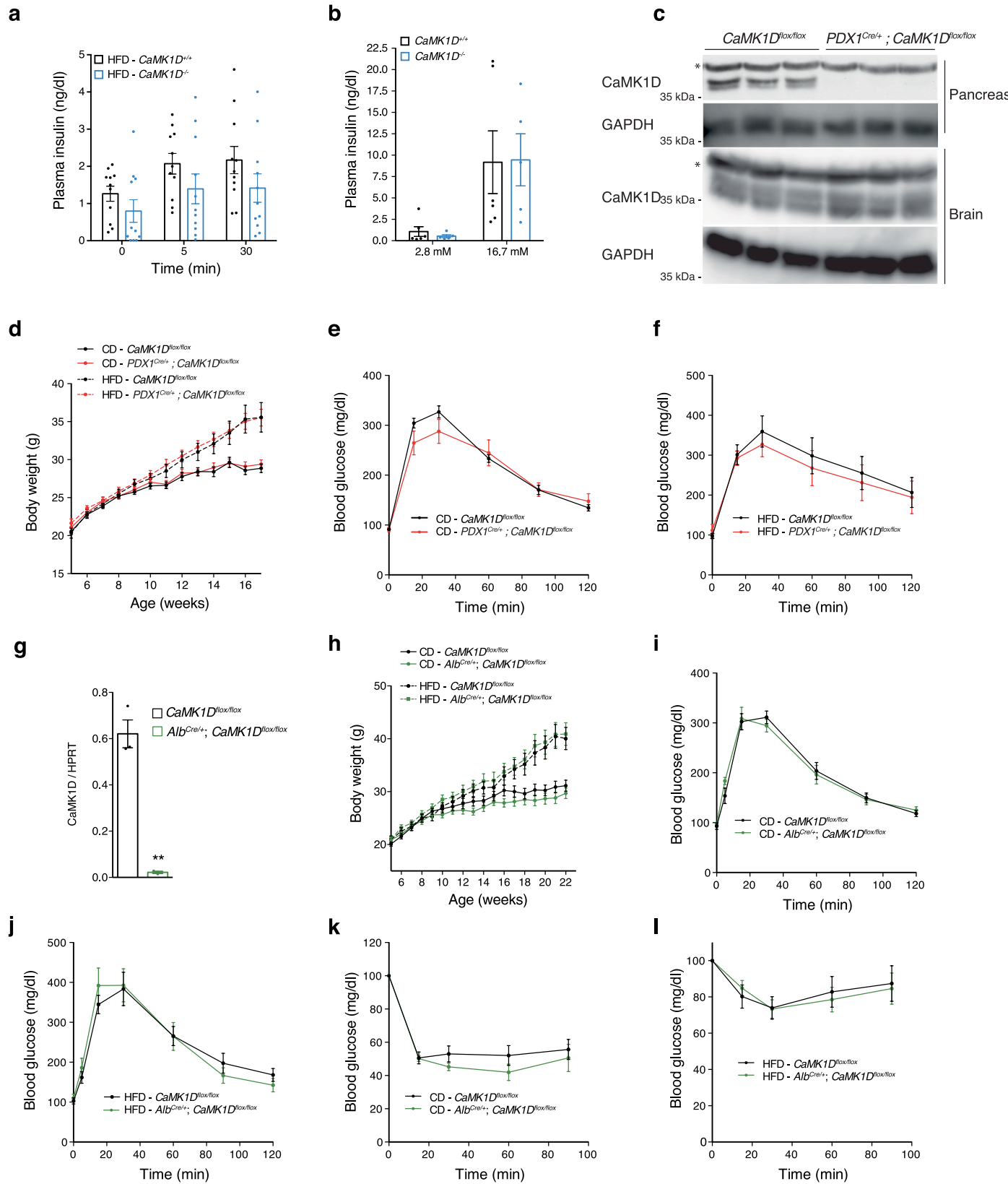
Mendelian Ratio

**e**

Extended Data Fig. 1 | Deletion of *CaMK1D* in mice does not affect body size and *CaMK1D* knockout mice are born without any gross abnormalities. **a**, Schematic screen of targeting of the *CaMK1D* locus using Knockout-first targeting strategy and generation of floxed and global knockout mice. For further details see material and methods. **b**, Validation of targeted ES clone by southern blot. Genomic DNA was digested using BspHI, BstEII, ApaI or EcoRI. The table

shows the expected size of bands corresponding to the restriction enzyme used. A probe recognizing the neoR cassette was used. **c**, Gender distribution of mice and **d**, Mendelian ratios of born mice with indicated genotypes. **e**, Body length and **f**, Tibia Length measurements of 7-week-old mice with indicated genotypes (*CaMK1D*^{+/+} n = 5; *CaMK1D*^{−/−} n = 7). Data are presented as mean values +/- SEM.

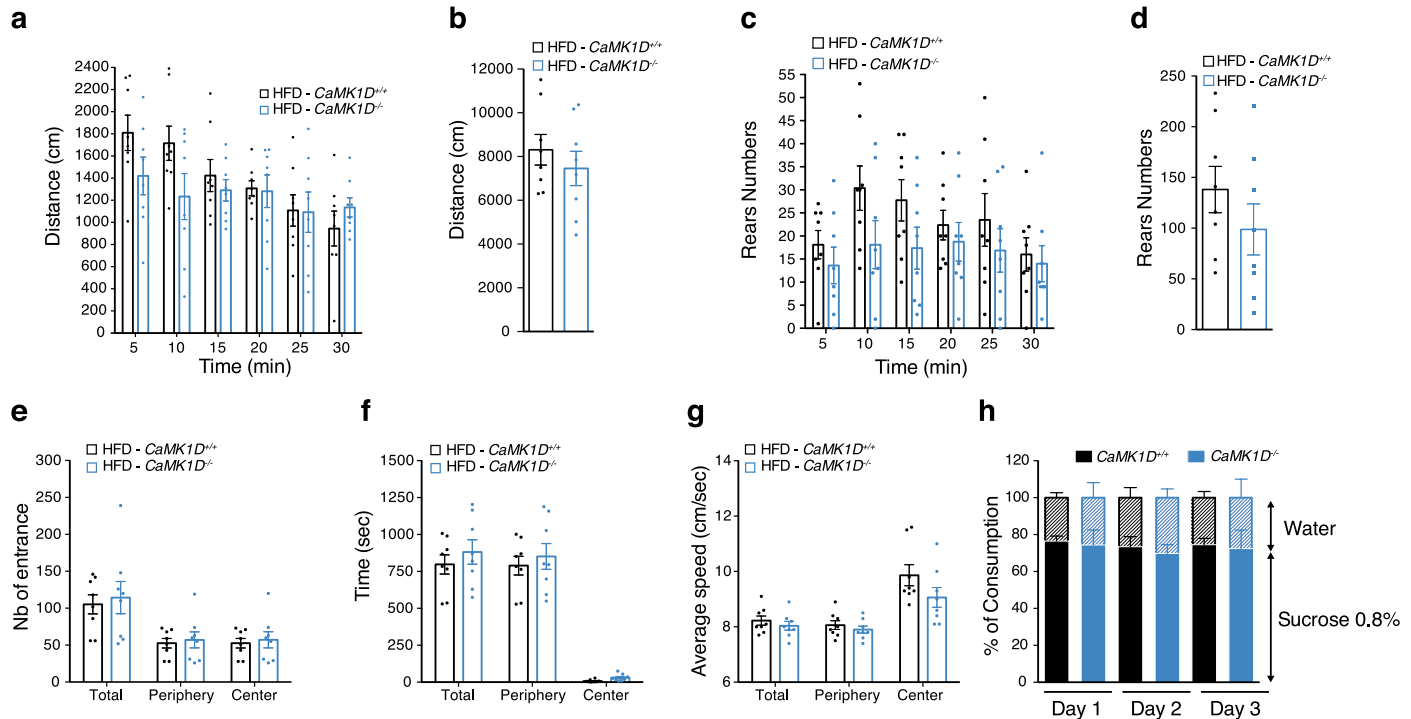
f



Extended Data Fig. 2 | See next page for caption.

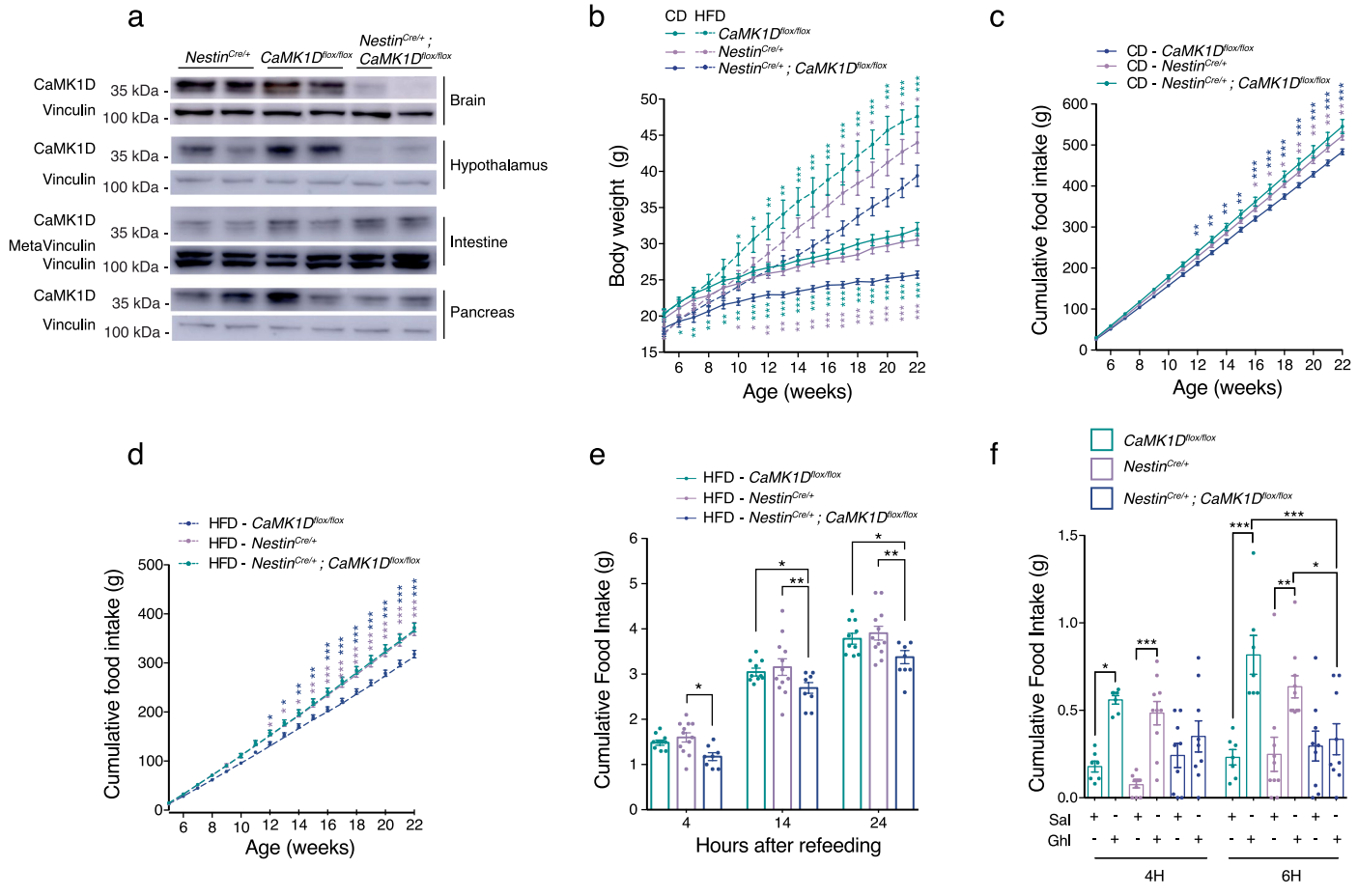
Extended Data Fig. 2 | CaMK1D signaling is redundant in pancreatic beta cell and liver function. **a**, Blood insulin levels during IPGTTs in mice on a High fat diet (HFD). (n = 11/group). **b**, Glucose-stimulated insulin secretion (GSIS) in pancreatic islets isolated from mice. (*CaMK1D*^{+/+} n = 6; *CaMK1D*^{-/-} n = 5). **c**, Expression of CaMK1D protein in pancreas and brain from mice with indicated genotypes. **d**, Body weight gain of mice on a Chow diet (CD) or on a High Fat Diet (HFD). (CD - *CaMK1D*^{fl/fl} n = 13; CD - *AgRP*^{Cre/+}; *CaMK1D*^{fl/fl} n = 13; HFD - *CaMK1D*^{fl/fl} n = 12; CD - *AgRP*^{Cre/+}; *CaMK1D*^{fl/fl} n = 10). **e-f**, Blood glucose levels during IPGTTs in mice on a CD (e), or on a HFD (f). (CD - *CaMK1D*^{fl/fl} n = 7; CD - *AgRP*^{Cre/+}; *CaMK1D*^{fl/fl} n = 6; HFD - *CaMK1D*^{fl/fl} n = 7; CD - *AgRP*^{Cre/+}; *CaMK1D*^{fl/fl} n = 8).

g, Expression of *CaMK1D* mRNA in liver from mice. (*CaMK1D*^{fl/fl} n = 3; CD - *Alb*^{Cre/+}; *CaMK1D*^{fl/fl} n = 3) **h**, Body weight gain of mice on a CD or on a HFD. (CD - *CaMK1D*^{fl/fl} n = 8; CD - *Alb*^{Cre/+}; *CaMK1D*^{fl/fl} n = 9; HFD - *CaMK1D*^{fl/fl} n = 8; HFD - *Alb*^{Cre/+}; *CaMK1D*^{fl/fl} n = 10). Blood glucose levels during an IPGTT in mice on a CD (i) or on a HFD (j). (CD - *CaMK1D*^{fl/fl} n = 6; CD - *Alb*^{Cre/+}; *CaMK1D*^{fl/fl} n = 7; HFD - *CaMK1D*^{fl/fl} n = 8; HFD - *Alb*^{Cre/+}; *CaMK1D*^{fl/fl} n = 5). Blood glucose levels during an ITT in mice on a CD (k) or on a HFD (l). (CD - *CaMK1D*^{fl/fl} n = 5; CD - *Alb*^{Cre/+}; *CaMK1D*^{fl/fl} n = 6; HFD - *CaMK1D*^{fl/fl} n = 12; HFD - *Alb*^{Cre/+}; *CaMK1D*^{fl/fl} n = 14). Data are presented as mean values +/− SEM.



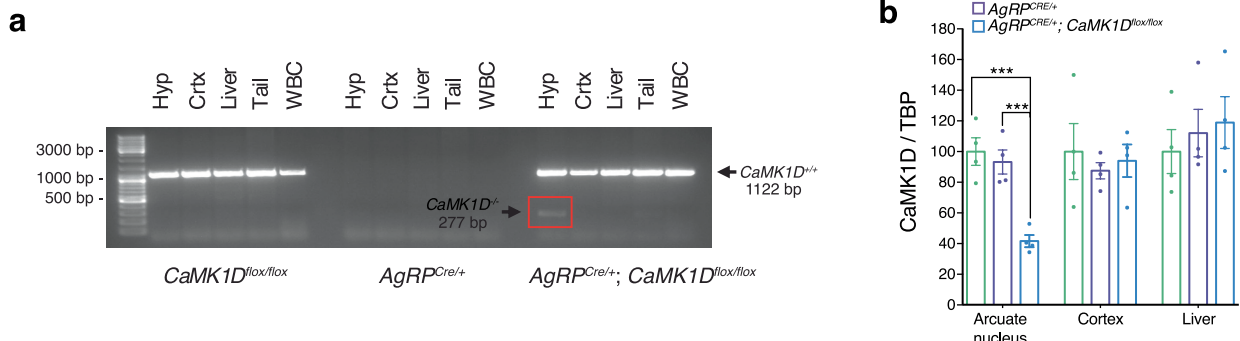
Extended Data Fig. 3 | Deletion of *CaMK1D* does not result in anxiety-like behavior and stress-induced anhedonia. **a**, Distance travelled each 5 min, and (**b**) in total. (**c**) Rear number each 5 min, and (**d**) in total. **e**, Number of entries in the center or periphery of the arena. **f**, Time spent in the center or periphery of

the arena. **g**, Average speed during an open field test. ($n = 8/\text{group}$). **h**, Amount of sucrose and water consumed over 3 day in while sucrose and water were both available in the same time. ($\text{CaMK1D}^{+/+} n = 8$; $\text{CaMK1D}^{-/-} n = 7$). Data are presented as mean values \pm SEM.

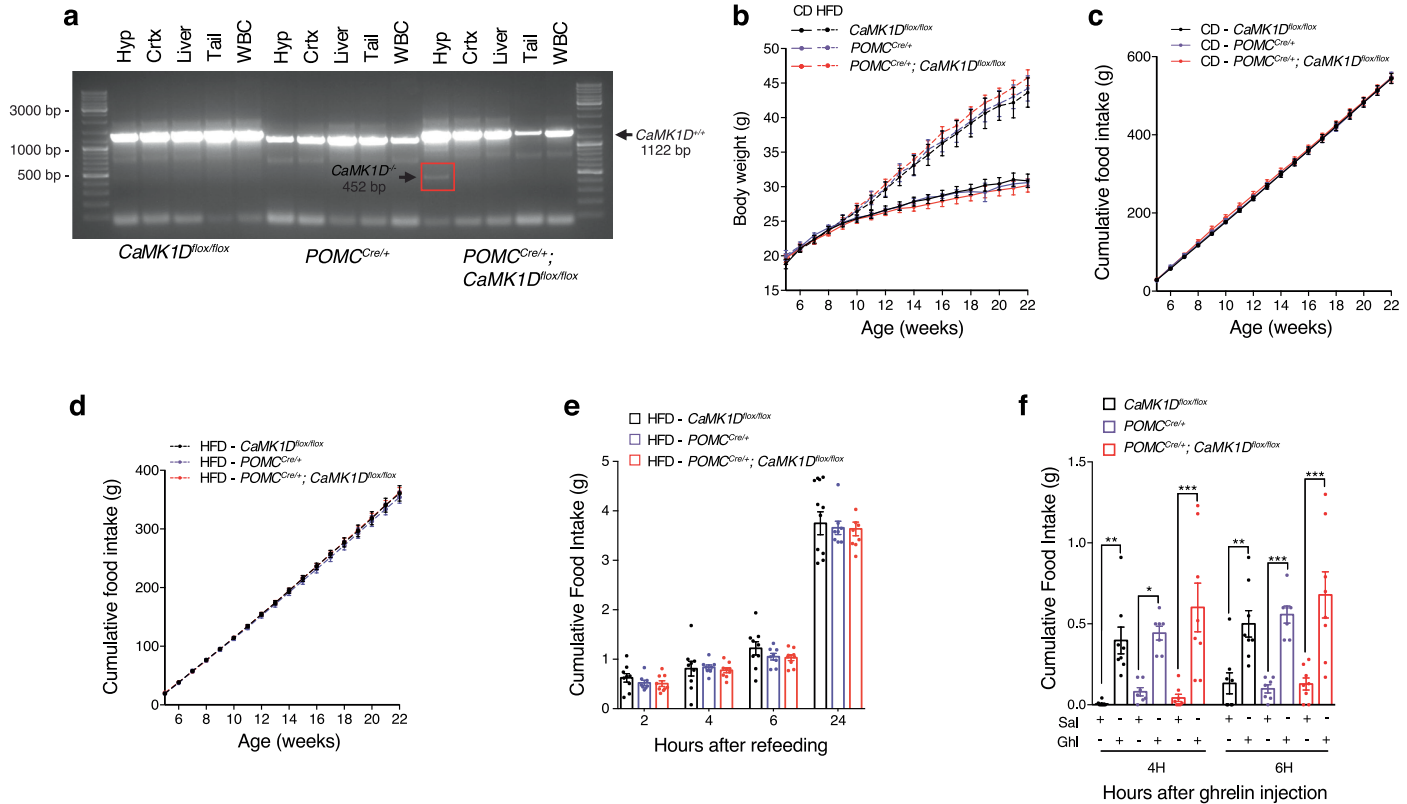


Extended Data Fig. 4 | Deletion of *CaMK1D* in the Nervous Tissue reproduces phenotypes in whole-body knockout mice. **a**, Expression of *CaMK1D* protein in mice. **b**, Body weight gain on a Chow diet (CD) or on a High Fat Diet (HFD). (CD - *CaMK1D*^{fl/fl} n = 12; CD - *Nestin*^{Cre/+} n = 11 and CD - *Nestin*^{Cre/+}; *CaMK1D*^{fl/fl} n = 10; HFD - *CaMK1D*^{fl/fl} n = 12; HFD - *Nestin*^{Cre/+}; *CaMK1D*^{fl/fl} n = 11). Cumulative food intake on (c) CD or on (d) HFD. (CD - *CaMK1D*^{fl/fl} n = 12; CD - *Nestin*^{Cre/+} n = 11 and CD - *Nestin*^{Cre/+}; *CaMK1D*^{fl/fl} n = 10;

HFD - *CaMK1D*^{fl/fl} n = 12; HFD - *Nestin*^{Cre/+}; *CaMK1D*^{fl/fl} n = 11) (*p ≤ 0.05). **(e)** Cumulative food intake. (*CaMK1D*^{fl/fl} n = 10; *Nestin*^{Cre/+} n = 12 and *Nestin*^{Cre/+}; *CaMK1D*^{fl/fl} n = 8). **(f)** Cumulative food intake after ghrelin injection (30 µg / day) on a CD. (*CaMK1D*^{fl/fl} n = 7; *Nestin*^{Cre/+} n = 10 and *Nestin*^{Cre/+}; *CaMK1D*^{fl/fl} n = 9). Data are presented as mean values +/- SEM. *p < 0.05, **p < 0.01 and ***p < 0.001. Statistical tests included two-way ANOVA bonferroni post hoc test (b,c,d,e,f).



Extended Data Fig. 5 | Deletion of *CaMK1D* in AgRP neurons. **a**, Verification of recombination in the *CaMK1D* locus in hypothalamus (Hyp), cortex (Crtx), liver, tail and white blood cells (WBC) from mice. **b**, Expression of *CaMK1D* mRNA in arcuate nucleus, cortex and liver from mice (n = 4 / group). Statistical tests included unpaired t-test (**b**). Data are presented as mean values +/- SEM.



Extended Data Fig. 6 | Deletion of *CaMK1D* in *POMC* neurons does not affect energy metabolism in mice. **a**, Verification of recombination in the *CaMK1D* locus in hypothalamus (Hyp), cortex (Crtx), liver, tail and white blood cells (WBC) from mice. **b**, Body weight gain on a Chow diet (CD) or on a High Fat Diet (HFD). (CD - *CaMK1D*^{fl/fl} n = 11; CD - *POMC*^{Cre/+} n = 8; CD - *POMC*^{Cre/+}; *CaMK1D*^{fl/fl} n = 8; HFD - *CaMK1D*^{fl/fl} n = 10; HFD - *POMC*^{Cre/+} n = 10 and HFD - *POMC*^{Cre/+}; *CaMK1D*^{fl/fl} n = 13). **c**, Cumulative food intake on a CD. (CD - *CaMK1D*^{fl/fl} n = 10; CD - *POMC*^{Cre/+} n = 8; CD - *POMC*^{Cre/+}; *CaMK1D*^{fl/fl} n = 8). **d**, Cumulative food

intake on a HFD. (HFD - *CaMK1D*^{fl/fl} n = 10; HFD - *POMC*^{Cre/+} n = 8; HFD - *POMC*^{Cre/+}; *CaMK1D*^{fl/fl} n = 10). **e**, Cumulative food intake. Food intake was determined 24 h after fasting. (*CaMK1D*^{fl/fl} n = 10; *POMC*^{Cre/+} n = 8; *POMC*^{Cre/+}; *CaMK1D*^{fl/fl} n = 10). **f**, Cumulative food intake after ghrelin injection. (*CaMK1D*^{fl/fl} n = 8; *POMC*^{Cre/+} n = 7; *POMC*^{Cre/+}; *CaMK1D*^{fl/fl} n = 8). Data are presented as mean values +/- SEM. **p < 0.01 and ***p < 0.001. Statistical tests included two-way ANOVA bonferroni post hoc test (f).

Extended Data Table 1 | Reagent or Resource

REAGENT or RESOURCE	SOURCE	IDENTIFIER
Antibodies		
Rabbit polyclonal anti-AMPKα1, Dilution 1:1000	This study	N/A
Rabbit polyclonal anti-phospho-Ser179/T180 CaMKII, Dilution 1:1000	This study	N/A
Rabbit polyclonal anti-Rosypho-Acetyl-CoA Carboxylase (Ser79) (Ser79), Dilution 1:1000	Cell Signaling Technology	Cat# 3661, RRID:AB_330337
Rabbit polyclonal anti-Acetyl-CoA Carboxylase, Dilution 1:1000	Cell Signaling Technology	Cat# 3662, RRID:AB_2219400
Rabbit monoclonal anti-phospho-AMPKα (Thr172) (4019), Dilution 1:1000	Cell Signaling Technology	Cat# 2535, RRID:AB_331250
Rabbit polyclonal anti-AMPKα2, Dilution 1:1000	Cell Signaling Technology	Cat# 2532, RRID:AB_330331
Rabbit monoclonal anti-phospho-CREB (Ser133) (87G3), Dilution 1:1000	Cell Signaling Technology	Cat# 9198, RRID:AB_2561044
Rabbit monoclonal anti-CREB (442D), Dilution 1:1000	Cell Signaling Technology	Cat# 9197, RRID:AB_2561277
Rabbit monoclonal anti-EGFR (9F6), Dilution 1:1000	Cell signaling Technology	Cat# 2520, RRID:AB_2247211
Goat polyclonal anti-Mouse IgG/P/ART, Dilution 1:200	R&D Systems	Cat# AF634, RRID:AB_2273824
Rabbit monoclonal anti-Vinculin (EF19V), Dilution 1:3000	Cell Signaling Technology	Cat# 13901, RRID:AB_2728768
Rabbit monoclonal anti-GAPDH, Dilution 1:5000	Sigma-Aldrich	Cat# G9545, RRID:AB_796208
Peroxidase Affinity Goat Anti-Rabbit IgG (H+L), Dilution 1:10000	Jackson ImmunoResearch Labs	Cat# 111-035-144, RRID:AB_2207391
Goat anti-Rabbit IgG, Alexa Fluor 488, Dilution 1:500	Thermo Fisher Scientific	Cat# A-11037, RRID:AB_2535905
Donkey anti-Rabbit IgG, Alexa Fluor 488, Dilution 1:500	Molecular Probes	Cat# A-21206, RRID:AB_2535792
Donkey anti-Goat IgG, Alexa Fluor 568, Dilution 1:500	Molecular Probes	Cat# A-11057, RRID:AB_142581
Chemicals, Peptides, and Recombinant Proteins		
Ghrelin (rat)	R&D Systems	Cat# 14651...
Recombinant Mouse Leptin Protein	R&D Systems	Cat# 498-OB-05M
L-Glutamine	Gibco™	Cat# 25920-021
B-27 supplement	Gibco™	Cat# 17500044
N2 supplement	Gibco™	Cat# A1370701
Pencillin / Streptomycin	Gibco™	Cat# 15140130
Penfloc® SC	Roche	Cat# 11429868001
Glucose	Euromedex	Cat# 13050
Urea	Life	H319
Papain	Worthington	WOK03178
DNAse I		
	Worthington	WOK03172
phosphatase/protein inhibitors		
	Gibco™	S027
Phenyl agarose		
	Saboda	W1W195-17991
SuperSignal™ West Pico PLUS Chemiluminescent Substrate		
	ThermoFisher Scientific	14580
Luminata Forte Western HRP		
	MerckMillipore	WBLUF0500
SuperScript IV Reverse Transcriptase		
	Invitrogen	18090200
FastStart Essential DNA Green Master		
	Roche Life Science	06924024001
Critical Commercial Assays		
Mouse Ultrasensitive Insulin ELISA	Alpco®	80-INSMSU-E01
Rat/Mouse Ghrelin (active)	MerckMillipore	EZRGRGA-90K
Lepin + MILPAN X MAP Rat Metabolic Hormone Magnetic Bead Panel - Metabolism Multiplex Assay	MerckMillipore	RHMHMAG-84K-02
Pierce™ BCA Protein Assay Kit	ThermoFisher Scientific	23225
KNeasy® Lipid Tissue Mini Kit	Qiagen	74664
Experimental Models: Mouse Lines		
<i>CaMKIIαCre/+</i>	This study	N/A
<i>B6.Cg-Tg(NestCre)RknJ = NestinCre</i>	The Jackson Laboratory	Stock No: 003771
<i>AgRPCre/+ = AgRPCre/+</i>	The Jackson Laboratory	Stock No: 012899
<i>B6.FVB-Tg(Prdm1flox/flox)J = POMCCre/+</i>	The Jackson Laboratory	Stock No: 010714
<i>Tg(Pdx1cre;EvIrt)BamJ = PDX1Cre/+</i>	The Jackson Laboratory	Stock No: 024968
<i>B6.Cg-Spcerb1tm1Mak/Mak</i>	The Jackson Laboratory	Stock No: 003574
<i>B6.FVB-Tg(Np-creGFP)JLowIJ = NpCre/GP</i>	The Jackson Laboratory	Stock No: 006417
<i>Gt(ROSA)26Sgk1tm1Krtb</i> = RO53.1	ICRS	MGI:3716464
Software and Algorithms		
Fiji Image Analysis	ImageJ	https://imagej.net/Fiji
Prism version 8.1.1	GraphPad	N/A
Primers (qPCR)		
Forward mAgRP	GCTCCACATGAAAGGCATCAGAA	
Reverse mAgRP	GGATCTAGCACCTCGCCCAA	
Forward mNPY	CCGGCTTGCGACACTACAT	
Reverse mNPY	TCCTTGTGTTGCTTCT	
Forward mPOMC	CCGGCCCAAGGACAAGGGT	
Reverse mPOMC	CTGGCCCTCTCTGTGGGGT	
Forward ncMK1D	CTCGACACCATGTGATTGCT	
Reverse ncMK1D	ACTACAGACGCTGAAAGTG	
Forward mTBP	TCGGCTTGCTGGGAAAGAT	
Reverse mTBP	CTGGCTTGCTGGGAAAGAT	

Antibodies, Chemicals, Peptides, Recombinant proteins, Critical Commercial assays, Mouse Lines, Software and Algorithms and Primers are listed in the table according to their supplier and identifier.

6.4 La grande traversée de l'ocytocine dans le système nerveux pour calmer les douleurs

Clauss Creusot E., Darbon P., Charlet A. 2023

Médecine Science

NOUVELLE

La grande traversée de l'ocytocine pour calmer la douleur

Étienne Clauss Creusot, Pascal Darbon, Alexandre Charlet

CNRS, université de Strasbourg,
Institut des neurosciences cellulaires
et intégratives (INCI), UPR3212, Strasbourg,
France.
acharlet@unistra.fr

L'ocytocine contrôle la douleur

L'ocytocine, un neuropeptide constitué de neuf acides aminés, est connue comme « l'hormone de l'amour ». Elle est plus généralement impliquée dans la promotion du bien-être en contrôlant, par exemple, les interactions sociales, le niveau d'anxiété ou la douleur [1]. L'ocytocine est synthétisée dans l'hypothalamus, une région du cerveau qui fait le lien entre le système nerveux et le système endocrinien [1], par au moins deux types de neurones ocytocinergiques : les neurones magnocellulaires, qui peuvent secréter l'ocytocine dans le sang, où elle agit comme une hormone, et les neurones parvocellulaires, qui la libèrent uniquement dans le système nerveux central, où elle agit alors comme un neuromodulateur. Ces deux types de neurones participent à l'action analgésique de l'ocytocine, par une combinaison d'actions « périphérique » et « centrale ». En effet, les neurones parvocellulaires vont, d'une part, stimuler la sécrétion d'ocytocine dans le sang par les neurones magnocellulaires, et d'autre part, libérer de l'ocytocine directement dans la moelle épinière.

Ainsi, l'action analgésique de l'ocytocine s'exerce à la fois sur l'activité des nocicepteurs périphériques situés dans les ganglions rachidiens et dans la peau, qu'elle atteint par voie sanguine [2], et directement sur les neurones de la moelle épinière [3].

La substance grise péri-aqueducale est impliquée dans le contrôle de la douleur

La douleur est une expérience sensorielle et émotionnelle complexe. Elle émane de l'intégration d'informations nociceptives par la moelle épinière et les centres supra-spinaux. En réponse, un système de contrôle descendant permet de moduler (atténuer ou exacerber) la douleur perçue en agissant sur la moelle épinière [4]. Ces contrôles sont exercés par un ensemble de structures cérébrales, notamment la substance grise péri-aqueducale ventrolatérale (vIPAG), située autour de l'aqueduc du mésencéphale et qui joue également un rôle clef dans la modulation des comportements défensifs [5]. L'activation de la vIPAG active des neurones dont les axones se projettent dans la région rostro-ven-

trale du myélencéphale, laquelle, par l'intermédiaire d'interneurones de la moelle épinière, exerce une action inhibitrice sur les neurones « wide dynamic range »¹ (WDR) de la couche V, qui sont impliqués dans le contrôle de la transmission de l'information nociceptive [5].

vIPAG et ocytocine : une nouvelle histoire d'amour ?

En combinant l'utilisation de vecteurs viraux et d'une lignée transgénique de rats, nous avons mis en évidence la présence de fibres ocytocinergiques et de récepteurs de l'ocytocine dans la vIPAG [6]. Les neurones synthétisant l'ocytocine qui projettent leurs axones vers la vIPAG constituent une population spécifique de neurones parvocellulaires peuplant le noyau paraventriculaire de l'hypothalamus. Les axones de ces neurones sont présents tout le long de l'axe rostro-ventral de la vIPAG et au contact des neurones exprimant le récepteur de l'ocytocine (*Figure 1*) [6].

¹ Neurones non spécifiques ou à large gamme réceptrice.

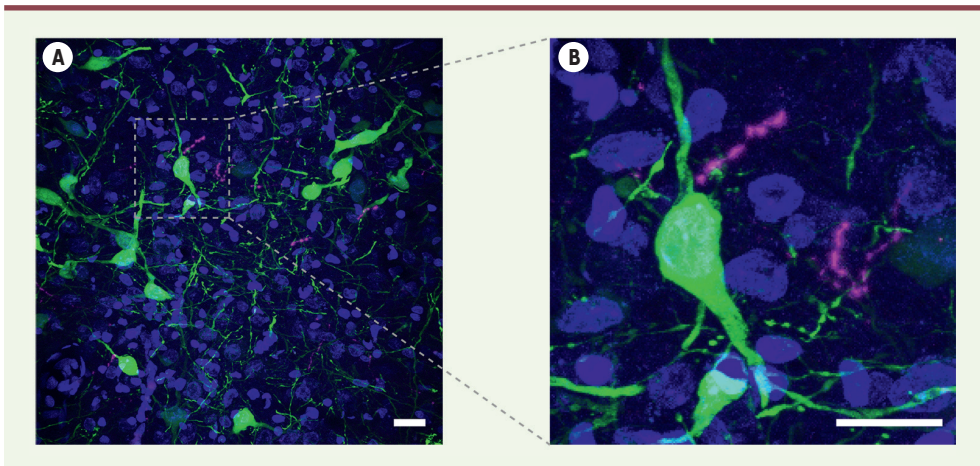


Figure 1. Dans la substance grise péri-aqueducale, les fibres oxytocinergiques provenant des neurones parvocellulaires de l'hypothalamus (en violet) sont situées à proximité des neurones exprimant le récepteur de l'oxytocine (en vert). L'activation de ces neurones par l'oxytocine atténue la douleur chez le rat. Les noyaux des cellules sont colorés en bleu. Barre d'échelle : 20 mm (© Charlet lab).

De plus, des expériences d'électrophysiologie *ex vivo* ont permis de vérifier que les récepteurs de l'oxytocine des neurones de la vIPAG sont fonctionnels : l'application d'agonistes du récepteur sur ces neurones augmente la fréquence de leurs potentiels d'action. Afin de mimer la libération physiologique d'oxytocine, nous avons alors dépolarisé spécifiquement les axones des neurones parvocytocine présents dans la vIPAG par une technique d'optogénétique (voir *Encadré 1*). Nous nous sommes assurés de la libération effective d'oxytocine par cette technique en utilisant conjointement un nouveau senseur de cette molécule, le GRAB_{oxytocine} (voir *Encadré 2*) [6]. L'enregistrement *in vivo* de

l'activité électrique des neurones de la vIPAG a montré que la stimulation des fibres oxytocinergiques entraîne l'activation d'environ un quart d'entre eux, et un enregistrement complémentaire dans la moelle épinière dans les mêmes conditions de stimulation a montré une inhibition des neurones « *wide dynamic range* » [6]. Il existe donc un circuit oxytocinergique à partir du noyau paraventriculaire de l'hypothalamus, qui permet de réduire l'activité de certains neurones de la moelle épinière par une action intermédiaire sur des neurones de la vIPAG.

Il restait à comprendre l'implication de ce circuit dans le contrôle effectif de la douleur. Deux modèles murins (rat) ont été utilisés : l'un de sensibilisation inflammatoire périphérique, l'autre de douleur neuropathique. Les sensibilités douloureuses de modalités mécanique (pression) et thermique (chaleur) ont été évaluées chez ces animaux avant et après stimulation de la libération d'oxytocine dans la vIPAG par optogénétique. Nous avons ainsi pu montrer que l'activation des neurones oxytocinergiques de l'hypothalamus dont les axones se projettent dans la vIPAG entraîne une analgésie transitoire chez les rongeurs [6].

Perspectives

Un nouveau circuit neuronal est donc impliqué dans le fort pouvoir analgésique de l'oxytocine. Une population spécifique de neurones parvocellulaires dans le noyau paraventriculaire de l'hypothalamus projette ses axones vers la vIPAG, où ils libèrent de l'oxytocine. L'activation de certains neurones de la vIPAG par l'oxytocine diminue à son tour l'activité des neurones de la moelle épinière codant l'intensité nociceptive (*Figure 2*). *In fine*, l'activation des neurones parvocellulaires produisant l'oxytocine induira une analgésie, comme nous l'avons montré en analysant la réponse de rongeurs femelles et de rats mâles souffrant de douleurs inflammatoires ou de neuropathie à des stimulus douloureux.

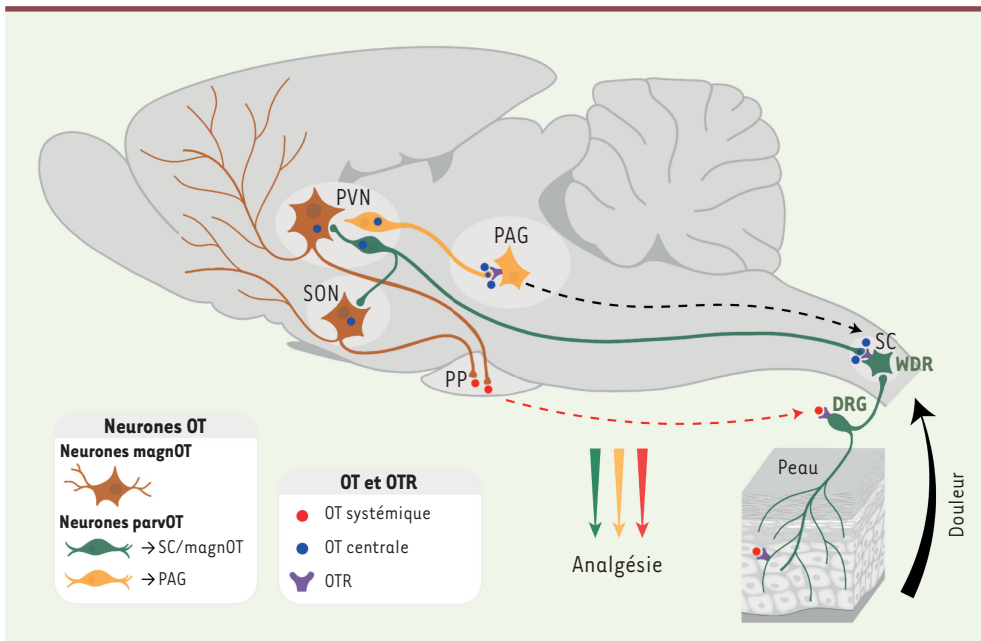
Cependant, malgré l'accumulation de preuves des bénéfices de l'oxytocine

1 L'optogénétique

L'optogénétique désigne une technique de stimulation (ou d'inhibition) de l'activité neuronale fondée sur l'expression artificielle d'un canal ionique « photoactivable », c'est-à-dire activable par une stimulation lumineuse. L'injection d'un vecteur viral permet, dans une population choisie de neurones, l'expression de ce canal ionique. Une stimulation lumineuse permet l'ouverture du canal, ce qui entraîne un flux entrant d'ions (ici, de cations) dans le neurone, et modifie donc son activité électrique (ici, dans le sens d'une augmentation, par dépolarisation) [7].

2 Un senseur d'oxytocine : GRAB_{oxytocine}

GRAB_{oxytocine} est un récepteur de l'oxytocine modifié (*G-protein-coupled receptor activation-based, GRAB*), couplé à une protéine fluorescente (*green fluorescent protein, GFP*). Lorsqu'une molécule d'oxytocine se lie à ce récepteur, il change de conformation, ce qui augmente l'intensité de la fluorescence de la GFP. Ce récepteur va donc agir comme un senseur d'oxytocine, ce qui permet, en induisant son expression dans certaines zones cérébrales, d'y mesurer la libération d'oxytocine [8].



magnocellulaires, magnOT) d'autre part, ce qui a pour effet d'atténuer la nociception. DRG : ganglions rachidiens ; PAG : substance grise péréqueducale ; OTR : récepteur de l'ocytocine ; PP : neurohypophyse ; SC : moelle épinière ; SON : noyau supraoptique de l'hypothalamus ; WDR : neurones « wide dynamic range ».

sur la douleur ou ses comorbidités [1-3, 7, 9], son utilisation médicale se heurte à deux obstacles : sa capacité à également activer les récepteurs de la vasopressine, ce qui peut entraîner des effets indésirables cardio-vasculaires, et sa demi-vie trop brève (une quinzaine de minutes au maximum), qui se traduit par un effet de courte durée, à l'image de l'analgésie mesurée dans notre étude chez le rat. Une stratégie pourrait être de synthétiser des agonistes du récepteur de l'ocytocine ayant une plus forte sélectivité pour ce dernier, tout en ayant une durée de vie plus longue. Récemment, un agoniste non-peptidérgique de l'ocytocine, LIT-001, a été synthétisé. Il possède une sélectivité pour le récepteur de l'ocytocine un peu plus faible que l'ocytocine, mais présente l'avantage de ne (presque) pas se lier au récepteur central de la vasopressine (récepteur V1a). L'injection intra-péritonéale de LIT-001 chez le rat entraîne une analgésie d'une durée de cinq heures environ, et la molécule peut être détectée

dans l'organisme jusqu'à cinq heures après l'injection [10]. S'il reste nécessaire de perfectionner ce nouvel outil pharmacologique, il ouvre une réelle perspective de modulation de l'activité du circuit ocytocinergique dans un but médical.

Dans un contexte où les médicaments analgésiques des paliers 2 et 3 utilisés actuellement sont essentiellement opioïdériques, comprendre le circuit par lequel l'ocytocine diminue la sensation douloureuse et développer, à partir de cette connaissance, de nouvelles molécules efficaces ouvre des perspectives thérapeutiques. En effet, l'activation d'un circuit physiologique du contrôle de la douleur par une molécule ayant peu d'effets indésirables est une alternative prometteuse à l'utilisation des opiacés. ♦

The great journey of oxytocin to alleviate pain

LIENS D'INTÉRÊT

Les auteurs déclarent n'avoir aucun lien d'intérêt concernant les données publiées dans cet article.

Figure 2. Deux populations distinctes de neurones parvocellulaires promeuvent une analgésie par la libération d'ocytocine dans le sang, la moelle épinière et la substance grise péréqueducale ventrolatérale. Nous faisons l'hypothèse que les stimulus douloureux activent deux populations de neurones parvocellulaires (parvOT) distinctes du noyau paraventriculaire de l'hypothalamus (PVN). Il en résulte une libération d'ocytocine (OT) dans diverses régions du système nerveux central d'une part, et dans la circulation sanguine (par activation des neurones

RÉFÉRENCES

- Jurek B, Neumann ID. The oxytocin receptor: from intracellular pathway to behavior. *Physiol Rev* 2018 ; 98 : 1805-908.
- Moreno-López Y, Martínez-Lorenzana G, Condés-Lara M, et al. Identification of oxytocin receptor in the dorsal horn and nociceptive dorsal root ganglion neurons. *Neuropep* 2013 ; 47 : 117-23.
- Eliava M, Melchior M, Knobloch-Bollmann SH, et al. A new population of parvocellular oxytocin neurons controlling magnocellular neuron activity and inflammatory pain processing. *Neuron* 2016 ; 89 : 1291-304.
- Lau BK, Vaughan CW. Descending modulation of pain: the GABA disinhibition hypothesis of analgesia. *Curr Opin Neurobiol* 2014 ; 29 : 159-64.
- Martines I, Tavares I. Reticular formation and pain: the past and the future. *Front Neuroanat* 2017 ; 11 : 51.
- Iwasaki M, Lefevre A, Althammer F, et al. An analgesic pathway from parvocellular oxytocin neurons to the periaqueductal gray in rats. *Nat Commun* 2023 ; 14 : 1066.
- Rost RK, Schneider-Warmer F, Schmitz D, et al. Optogenetic tools for subcellular applications in neuroscience. *Neuron* 2017 ; 96 : 572-603.
- Qian T, Wang H, Wang P, et al. A genetically encoded sensor measures temporal oxytocin release from different neuronal compartments. *Nat Biotech* 2023. doi: 10.1038/s41587-022-01561-2.
- Wahis J, Baudon A, Althammer F, et al. Astrocytes mediate the effect of oxytocin in the central amygdala on neuronal activity and affective states in rodents. *Nat Neurosci* 2021 ; 24 : 529-41.
- Hilfiger L, Zhao Q, Kerspern D, et al. A nonpeptide oxytocin receptor agonist for a durable relief of inflammatory pain. *Sci Rep* 2022 ; 10 : 3017.

7 References

- Agren, G., Lundeberg, T., Uvnäs-Moberg, K., Sato, A., 1995. The oxytocin antagonist 1-deamino-2-D-Tyr-(Oet)-4-Thr-8-Orn-oxytocin reverses the increase in the withdrawal response latency to thermal, but not mechanical nociceptive stimuli following oxytocin administration or massage-like stroking in rats. *Neurosci Lett* 187, 49–52.
- Arletti, R., Benelli, A., Bertolini, A., 1993. Influence of oxytocin on nociception and morphine antinociception. *Neuropeptides* 24, 125–129.
- Bagley, E.E., Ingram, S.L., 2020. Endogenous opioid peptides in the descending pain modulatory circuit. *Neuropharmacology* 173, 108131.
- Banerjee, A., Shen, P.-J., Ma, S., Bathgate, R.A.D., Gundlach, A.L., 2010. Swim stress excitation of nucleus incertus and rapid induction of relaxin-3 expression via CRF1 activation. *Neuropharmacology* 58, 145–155.
- Barrot, M., 2012. Tests and models of nociception and pain in rodents. *Neuroscience* 211, 39–50.
- Bathgate, R. a. D., Halls, M.L., van der Westhuizen, E.T., Callander, G.E., Kocan, M., Summers, R.J., 2013. Relaxin family peptides and their receptors. *Physiol Rev* 93, 405–480.
- Bathgate, R.A., Ivell, R., Sanborn, B.M., Sherwood, O.D., Summers, R.J., 2006. International Union of Pharmacology LVII: Recommendations for the Nomenclature of Receptors for Relaxin Family Peptides. *Pharmacol Rev* 58, 7–31.
- Bathgate, R.A.D., Lin, F., Hanson, N.F., Otvos, L., Guidolin, A., Giannakis, C., Bastiras, S., Layfield, S.L., Ferraro, T., Ma, S., Zhao, C., Gundlach, A.L., Samuel, C.S., Tregear, G.W., Wade, J.D., 2006. Relaxin-3: Improved Synthesis Strategy and Demonstration of Its High-Affinity Interaction with the Relaxin Receptor LGR7 Both *In Vitro* and *In Vivo*. *Biochemistry* 45, 1043–1053.
- Bathgate, R.A.D., Samuel, C.S., Burazin, T.C.D., Layfield, S., Claasz, A.A., Reyomas, I.G.T., Dawson, N.F., Zhao, C., Bond, C., Summers, R.J., Parry, L.J., Wade, J.D., Tregear, G.W., 2002. Human Relaxin Gene 3 (H3) and the Equivalent Mouse Relaxin (M3) Gene. *Journal of Biological Chemistry* 277, 1148–1157.

- Bazaz, A., Ghanbari, A., Vafaei, A.A., Khaleghian, A., Rashidy-Pour, A., 2022. Oxytocin in dorsal hippocampus facilitates auditory fear memory extinction in rats. *Neuropharmacology* 202, 108844.
- Behbehani, M.M., Fields, H.L., 1979. Evidence that an excitatory connection between the periaqueductal gray and nucleus raphe magnus mediates stimulation produced analgesia. *Brain Research* 170, 85–93.
- Beitz, A.J., 1985. The midbrain periaqueductal gray in the rat. I. Nuclear volume, cell number, density, orientation, and regional subdivisions. *J Comp Neurol* 237, 445–459.
- Bell, A., 2018. The neurobiology of acute pain. *Vet J* 237, 55–62.
- Bennett, G.J., Xie, Y.-K., 1988. A peripheral mononeuropathy in rat that produces disorders of pain sensation like those seen in man. *Pain* 33, 87–107.
- Blasiak, A., Blasiak, T., Lewandowski, M.H., Hossain, M.A., Wade, J.D., Gundlach, A.L., 2013. Relaxin-3 innervation of the intergeniculate leaflet of the rat thalamus - neuronal tract-tracing and *in vitro* electrophysiological studies. *Eur J Neurosci* 37, 1284–1294.
- Breivik, H., Eisenberg, E., O'Brien, T., OPENMinds, 2013. The individual and societal burden of chronic pain in Europe: the case for strategic prioritisation and action to improve knowledge and availability of appropriate care. *BMC Public Health* 13, 1229.
- Büllsbach, E.E., Schwabe, C., 1994. Functional importance of the A chain loop in relaxin and insulin. *Journal of Biological Chemistry* 269, 13124–13128.
- Büllsbach, E.E., Schwabe, C., 2000. The Relaxin Receptor-binding Site Geometry Suggests a Novel Gripping Mode of Interaction. *Journal of Biological Chemistry* 275, 35276–35280.
- Burazin, T.C.D., Bathgate, R.A.D., Macris, M., Layfield, S., Gundlach, A.L., Tregear, G.W., 2002. Restricted, but abundant, expression of the novel rat gene-3 (R3) relaxin in the dorsal tegmental region of brain. *J Neurochem* 82, 1553–1557.
- Busnelli, M., Chini, B., 2018. Molecular Basis of Oxytocin Receptor Signalling in the Brain: What We Know and What We Need to Know. *Curr Top Behav Neurosci* 35, 3–29.

Chenaf, C., Delorme, J., Delage, N., Ardid, D., Eschalier, A., Authier, N., 2018. Prevalence of chronic pain with or without neuropathic characteristics in France using the capture-recapture method: a population-based study. *Pain* 159, 2394–2402.

Cleary, D.R., Neubert, M.J., Heinricher, M.M., 2008. Are opioid-sensitive neurons in the rostral ventromedial medulla inhibitory interneurons? *Neuroscience* 151, 564–571.

Condés-Lara, M., Maie, I.A.S., Dickenson, A.H., 2005. Oxytocin actions on afferent evoked spinal cord neuronal activities in neuropathic but not in normal rats. *Brain Res* 1045, 124–133.

de Araujo, A.D., Mobli, M., Castro, J., Harrington, A.M., Vetter, I., Dekan, Z., Muttenthaler, M., Wan, J., Lewis, R.J., King, G.F., Brierley, S.M., Alewood, P.F., 2014. Selenoether oxytocin analogues have analgesic properties in a mouse model of chronic abdominal pain. *Nat Commun* 5, 3165.

de Ávila, C., Chometton, S., Calvez, J., Guèvremont, G., Kania, A., Torz, L., Lenglos, C., Blasiak, A., Rosenkilde, M.M., Holst, B., Conrad, C.D., Fryer, J.D., Timofeeva, E., Gundlach, A.L., Cifani, C., 2020. Estrous Cycle Modulation of Feeding and Relaxin-3/Rxfp3 mRNA Expression: Implications for Estradiol Action. *Neuroendocrinology* 111, 1201–1218.

Decosterd, I., Woolf, C.J., 2000. Spared nerve injury: an animal model of persistent peripheral neuropathic pain. *Pain* 87, 149–158.

DeLaTorre, S., Rojas-Piloni, G., Martínez-Lorenzana, G., Rodríguez-Jiménez, J., Villanueva, L., Condés-Lara, M., 2009. Paraventricular oxytocinergic hypothalamic prevention or interruption of long-term potentiation in dorsal horn nociceptive neurons: Electrophysiological and behavioral evidence. *Pain* 144, 320–328.

Del-Bel, E., De-Miguel, F.F., 2018. Extrasynaptic Neurotransmission Mediated by Exocytosis and Diffusive Release of Transmitter Substances. *Front Synaptic Neurosci* 10, 13.

Duvarci, S., Pare, D., 2014. AMYGDALA MICRO CIRCUITS CONTROLLING LEARNED FEAR. *Neuron* 82, 966.

Eliava, M., Melchior, M., Knobloch-Bollmann, H.S., Wahis, J., da Silva Gouveia, M., Tang, Y., Ciobanu, A.C., Triana del Rio, R., Roth, L.C., Althammer, F., Chavant, V.,

- Goumon, Y., Gruber, T., Petit-Demoulière, N., Busnelli, M., Chini, B., Tan, L.L., Mitre, M., Froemke, R.C., Chao, M.V., Giese, G., Sprengel, R., Kuner, R., Poisbeau, P., Seeburg, P.H., Stoop, R., Charlet, A., Grinevich, V., 2016. A New Population of Parvocellular Oxytocin Neurons Controlling Magnocellular Neuron Activity and Inflammatory Pain Processing. *Neuron* 89, 1291–1304.
- Erden, S., Nalbant, K., Kılınç, İ., 2022. Investigation of Relaxin-3 Serum Levels in terms of Social Interaction, Communication, and Appetite as a Biomarker in Children with Autism. *Clin Psychopharmacol Neurosci* 20, 135–142.
- Ermisch, A., Rühle, H.J., Landgraf, R., Hess, J., 1985. Blood-brain barrier and peptides. *J Cereb Blood Flow Metab* 5, 350–357.
- Esmaeilou, Y., Tamaddonfard, E., Erfanparast, A., Soltanalinejad-Taghiabad, F., 2022. Behavioral and receptor expression studies on the primary somatosensory cortex and anterior cingulate cortex oxytocin involvement in modulation of sensory and affective dimensions of neuropathic pain induced by partial sciatic nerve ligation in rats. *Physiol Behav* 251, 113818.
- Fevold, H.L., Hisaw, F.L., Meyer, R.K., 1930. THE RELAXATIVE HORMONE OF THE CORPUS LUTEUM. ITS PURIFICATION AND CONCENTRATION1. *J. Am. Chem. Soc.* 52, 3340–3348.
- Fields, H.L., Basbaum, A.I., 1978. Brainstem Control of Spinal Pain-Transmission Neurons. *Annu. Rev. Physiol.* 40, 217–248.
- Ge, Y., Lundeberg, T., Yu, L.-C., 2002. Blockade effect of mu and kappa opioid antagonists on the anti-nociception induced by intra-periaqueductal grey injection of oxytocin in rats. *Brain Research* 927, 204–207.
- Ghanem, K., Johnson, A.L., 2021. Proteome profiling of chicken ovarian follicles immediately before and after cyclic recruitment. *Mol Reprod Dev* 88, 571–583.
- Gimpl, G., Fahrenholz, F., 2001. The Oxytocin Receptor System: Structure, Function, and Regulation. *Physiological Reviews* 81, 629–683.
- Gong, L., Gao, F., Li, J., Yu, X., Ma, X., Zheng, W., Cui, S., Liu, K., Zhang, M., Kunze, W., Liu, C.Y., 2015. Oxytocin-induced membrane hyperpolarization in pain-sensitive

dorsal root ganglia neurons mediated by Ca²⁺/nNOS/NO/KATP pathway. *Neuroscience* 289, 417–428.

González-Hernández, A., Manzano-García, A., Martínez-Lorenzana, G., Tello-García, I.A., Carranza, M., Arámburo, C., Condés-Lara, M., 2017. Peripheral oxytocin receptors inhibit the nociceptive input signal to spinal dorsal horn wide-dynamic-range neurons. *Pain* 158, 2117–2128.

Gu, X.-L., Yu, L.-C., 2007. Involvement of Opioid Receptors in Oxytocin-Induced Antinociception in the Nucleus Accumbens of Rats. *The Journal of Pain* 8, 85–90.

Guadagno, A., Belliveau, C., Mechawar, N., Walker, C.-D., 2021. Effects of Early Life Stress on the Developing Basolateral Amygdala-Prefrontal Cortex Circuit: The Emerging Role of Local Inhibition and Perineuronal Nets. *Frontiers in Human Neuroscience* 15.

Han, Y., Yu, L.-C., 2009. Involvement of oxytocin and its receptor in nociceptive modulation in the central nucleus of amygdala of rats. *Neuroscience Letters* 454, 101–104.

Hanafy, S., Sabry, J.H., Akl, E.M., Elethy, R.A., Mostafa, T., 2018. Serum relaxin-3 hormone relationship to male delayed puberty. *Andrologia* 50.

Haugaard-Kedström, L.M., Shabani, F., Hossain, M.A., Clark, R.J., Ryan, P.J., Craik, D.J., Gundlach, A.L., Wade, J.D., Bathgate, R.A.D., Rosengren, K.J., 2011. Design, Synthesis, and Characterization of a Single-Chain Peptide Antagonist for the Relaxin-3 Receptor RXFP3. *J. Am. Chem. Soc.* 133, 4965–4974.

Hechter, D., Vahkal, B., Tiede, T., Good, S.V., 2022. Reviewing the physiological roles of the novel hormone-receptor pair INSL5-RXFP4: a protective energy sensor? *J Mol Endocrinol* 69, R45–R62.

Hisaw, F.L., 1926. Experimental relaxation of the pubic ligament of the guinea pig. *Proceedings of the Society for Experimental Biology and Medicine* 23, 661–663.

Hossain, M.A., Rosengren, K.J., Haugaard-Jönsson, L.M., Zhang, S., Layfield, S., Ferraro, T., Daly, N.L., Tregear, G.W., Wade, J.D., Bathgate, R.A.D., 2008. The A-chain of Human Relaxin Family Peptides Has Distinct Roles in the Binding and

Activation of the Different Relaxin Family Peptide Receptors. *Journal of Biological Chemistry* 283, 17287–17297.

Hsu, S.Y., Nakabayashi, K., Nishi, S., Kumagai, J., Kudo, M., Sherwood, O.D., Hsueh, A.J.W., 2002. Activation of Orphan Receptors by the Hormone Relaxin. *Science* 295, 671–674.

Hsu, S.Y.T., Semyonov, J., Park, J.-I., Chang, C.L., 2005. Evolution of the Signaling System in Relaxin-Family Peptides. *Annals of the New York Academy of Sciences* 1041, 520–529.

Hudson, P., Haley, J., John, M., Cronk, M., Crawford, R., Haralambidis, J., Tregear, G., Shine, J., Niall, H., 1983. Structure of a genomic clone encoding biologically active human relaxin. *Nature* 301, 628–631.

Hudson, P., John, M., Crawford, R., Haralambidis, J., Scanlon, D., Gorman, J., Tregear, G., Shine, J., Niall, H., 1984. Relaxin gene expression in human ovaries and the predicted structure of a human preprorelaxin by analysis of cDNA clones. *The EMBO Journal* 3, 2333–2339.

Ino, D., Tanaka, Y., Hibino, H., Nishiyama, M., 2022. A fluorescent sensor for real-time measurement of extracellular oxytocin dynamics in the brain. *Nature Methods* 19, 1286.

Iwasaki, M., Lefevre, A., Althammer, F., Clauss Creusot, E., Łapieś, O., Petitjean, H., Hilfiger, L., Kerspern, D., Melchior, M., Küppers, S., Krabichler, Q., Patwell, R., Kania, A., Gruber, T., Kirchner, M.K., Wimmer, M., Fröhlich, H., Dötsch, L., Schimmer, J., Herpertz, S.C., Ditzen, B., Schaaf, C.P., Schönig, K., Bartsch, D., Gugula, A., Trenk, A., Blasiak, A., Stern, J.E., Darbon, P., Grinevich, V., Charlet, A., 2023. An analgesic pathway from parvocellular oxytocin neurons to the periaqueductal gray in rats. *Nat Commun* 14, 1066.

Janak, P.H., Tye, K.M., 2015. From circuits to behaviour in the amygdala. *Nature* 517, 284–292.

Juif, P.-E., Breton, J.-D., Rajalu, M., Charlet, A., Goumon, Y., Poisbeau, P., 2013. Long-lasting spinal oxytocin analgesia is ensured by the stimulation of allopregnanolone synthesis which potentiates GABA(A) receptor-mediated synaptic inhibition. *J Neurosci* 33, 16617–16626.

Jurek, B., Neumann, I.D., 2018. The Oxytocin Receptor: From Intracellular Signaling to Behavior. *Physiological Reviews* 98, 1805–1908.

Kania, A., Gugula, A., Grabowiecka, A., De Ávila, C., Blasiak, T., Rajfur, Z., Lewandowski, M.H., Hess, G., Timofeeva, E., Gundlach, A.L., Blasiak, A., 2017. Inhibition of oxytocin and vasopressin neuron activity in rat hypothalamic paraventricular nucleus by relaxin-3-RXFP3 signalling: Relaxin-3-RXFP3 modulation of rat paraventricular nucleus activity. *J Physiol* 595, 3425–3447.

Kania, A., Szлага, A., Sambak, P., Gugula, A., Blasiak, E., Micioni Di Bonaventura, M.V., Hossain, M.A., Cifani, C., Hess, G., Gundlach, A.L., Blasiak, A., 2020. RLN3/RXFP3 Signaling in the PVN Inhibits Magnocellular Neurons via M-like Current Activation and Contributes to Binge Eating Behavior. *J. Neurosci.* 40, 5362–5375.

Katz, L.C., Burkhalter, A., Dreyer, W.J., 1984. Fluorescent latex microspheres as a retrograde neuronal marker for *in vivo* and *in vitro* studies of visual cortex. *Nature* 310, 498–500.

Katz, L.C., Iarovici, D.M., 1990. Green fluorescent latex microspheres: A new retrograde tracer. *Neuroscience* 34, 511–520.

Kim, J., Zhang, X., Muralidhar, S., LeBlanc, S.A., Tonegawa, S., 2017. Basolateral to Central Amygdala Neural Circuits for Appetitive Behaviors. *Neuron* 93, 1464-1479.e5.

Knobloch, H.S., Charlet, A., Hoffmann, L.C., Eliava, M., Khrulev, S., Cetin, A.H., Osten, P., Schwarz, M.K., Seeburg, P.H., Stoop, R., Grinevich, V., 2012. Evoked Axonal Oxytocin Release in the Central Amygdala Attenuates Fear Response. *Neuron* 73, 553–566.

Kocan, M., Sarwar, M., Hossain, M.A., Wade, J.D., Summers, R.J., 2014. Signalling profiles of H3 relaxin, H2 relaxin and R3(BΔ23-27)R/I5 acting at the relaxin family peptide receptor 3 (RXFP3). *Br J Pharmacol* 171, 2827–2841.

Kordower, J.H., Bodnar, R.J., 1984. Vasopressin analgesia: Specificity of action and non-opioid effects. *Peptides* 5, 747–756.

Kremer, M., Becker, L.J., Barrot, M., Yalcin, I., 2021. How to study anxiety and depression in rodent models of chronic pain? *Eur J Neurosci* 53, 236–270.

- Kuei, C., Sutton, S., Bonaventure, P., Pudiak, C., Shelton, J., Zhu, J., Nepomuceno, D., Wu, J., Chen, J., Kamme, F., Seierstad, M., Hack, M.D., Bathgate, R.A.D., Hossain, M.A., Wade, J.D., Atack, J., Lovenberg, T.W., Liu, C., 2007. R3(BΔ23–27)R/I5 Chimeric Peptide, a Selective Antagonist for GPCR135 and GPCR142 over Relaxin Receptor LGR7. *Journal of Biological Chemistry* 282, 25425–25435.
- Lau, B.K., Vaughan, C.W., 2014. Descending modulation of pain: the GABA disinhibition hypothesis of analgesia. *Current Opinion in Neurobiology*, SI: Neuromodulation 29, 159–164.
- Lee, H.-J., Macbeth, A.H., Pagani, J., Young, W.S., 2009. Oxytocin: the Great Facilitator of Life. *Prog Neurobiol* 88, 127–151.
- Leng, G., Ludwig, M., 2008. Neurotransmitters and peptides: whispered secrets and public announcements: Neurotransmitters and peptides. *The Journal of Physiology* 586, 5625–5632.
- Lewis, J.E., Woodward, O.R., Nuzzaci, D., Smith, C.A., Adriaenssens, A.E., Billing, L., Brighton, C., Phillips, B.U., Tadross, J.A., Kinston, S.J., Ciabatti, E., Göttgens, B., Tripodi, M., Hornigold, D., Baker, D., Gribble, F.M., Reimann, F., 2022. Relaxin/insulin-like family peptide receptor 4 (Rxfp4) expressing hypothalamic neurons modulate food intake and preference in mice. *Mol Metab* 66, 101604.
- Li, L., Wang, X., Yu, L.-C., 2010. Involvement of opioid receptors in the CGRP-induced antinociception in the nucleus accumbens of rats. *Brain Research* 1353, 53–59.
- Li, X.-H., Matsuura, T., Xue, M., Chen, Q.-Y., Liu, R.-H., Lu, J.-S., Shi, W., Fan, K., Zhou, Z., Miao, Z., Yang, J., Wei, S., Wei, F., Chen, T., Zhuo, M., 2021. Oxytocin in the anterior cingulate cortex attenuates neuropathic pain and emotional anxiety by inhibiting presynaptic long-term potentiation. *Cell Rep* 36, 109411.
- Liu, C., Chen, J., Kuei, C., Sutton, S., Nepomuceno, D., Bonaventure, P., Lovenberg, T.W., 2005a. Relaxin-3/Insulin-Like Peptide 5 Chimeric Peptide, a Selective Ligand for G Protein-Coupled Receptor (GPCR)135 and GPCR142 over Leucine-Rich Repeat-Containing G Protein-Coupled Receptor 7. *Mol Pharmacol* 67, 231–240.
- Liu, C., Chen, J., Sutton, S., Roland, B., Kuei, C., Farmer, N., Sillard, R., Lovenberg, T.W., 2003a. Identification of Relaxin-3/INSL7 as a Ligand for GPCR142. *Journal of Biological Chemistry* 278, 50765–50770.

Liu, C., Eriste, E., Sutton, S., Chen, J., Roland, B., Kuei, C., Farmer, N., Jörnvall, H., Sillard, R., Lovenberg, T.W., 2003b. Identification of Relaxin-3/INSL7 as an Endogenous Ligand for the Orphan G-protein-coupled Receptor GPCR135. *Journal of Biological Chemistry* 278, 50754–50764.

Liu, C., Kuei, C., Sutton, S., Chen, J., Bonaventure, P., Wu, J., Nepomuceno, D., Kamme, F., Tran, D.-T., Zhu, J., Wilkinson, T., Bathgate, R., Eriste, E., Sillard, R., Lovenberg, T.W., 2005b. INSL5 Is a High Affinity Specific Agonist for GPCR142 (GPR100). *Journal of Biological Chemistry* 280, 292–300.

Liu, C., Lovenberg, T.W., 2008. Relaxin-3, INSL5, and Their Receptors. In: Civelli, O., Zhou, Q.-Y. (Eds.), *Orphan G Protein-Coupled Receptors and Novel Neuropeptides, Results and Problems in Cell Differentiation*. Springer Berlin Heidelberg, Berlin, Heidelberg, pp. 213–237.

Lopez-Bendito, G., 2004. Preferential Origin and Layer Destination of GAD65-GFP Cortical Interneurons. *Cerebral Cortex* 14, 1122–1133.

Louvel, D., Delvaux, M., Felez, A., Fioramonti, J., Bueno, L., Lazorthes, Y., Frexinos, J., 1996. Oxytocin increases thresholds of colonic visceral perception in patients with irritable bowel syndrome. *Gut* 39, 741–747.

Loyd, D.R., Murphy, A.Z., 2006. Sex differences in the anatomical and functional organization of the periaqueductal gray-rostral ventromedial medullary pathway in the rat: A potential circuit mediating the sexually dimorphic actions of morphine. *J. Comp. Neurol.* 496, 723–738.

Loyd, D.R., Wang, X., Murphy, A.Z., 2008. Sex Differences in μ -Opioid Receptor Expression in the Rat Midbrain Periaqueductal Gray Are Essential for Eliciting Sex Differences in Morphine Analgesia. *J. Neurosci.* 28, 14007–14017.

Luis-Delgado, O.E., Barrot, M., Rodeau, J.-L., Ulery, P.G., Freund-Mercier, M.-J., Lasbennes, F., 2006. The transcription factor DeltaFosB is recruited by inflammatory pain. *J Neurochem* 98, 1423–1431.

Lundeberg, T., Uvnäs-Moberg, K., Agren, G., Bruzelius, G., 1994. Anti-nociceptive effects of oxytocin in rats and mice. *Neurosci Lett* 170, 153–157.

Ma, S., Blasiak, A., Olucha-Bordonau, F.E., Verberne, A.J.M., Gundlach, A.L., 2013. Heterogeneous responses of nucleus incertus neurons to corticotrophin-releasing factor and coherent activity with hippocampal theta rhythm in the rat. *J Physiol* 591, 3981–4001.

Ma, S., Bonaventure, P., Ferraro, T., Shen, P.-J., Burazin, T.C.D., Bathgate, R.A.D., Liu, C., Tregear, G.W., Sutton, S.W., Gundlach, A.L., 2007. Relaxin-3 in GABA projection neurons of nucleus incertus suggests widespread influence on forebrain circuits via G-protein-coupled receptor-135 in the rat. *Neuroscience* 144, 165–190.

Ma, S., Shen, P.-J., Burazin, T.C.D., Tregear, G.W., Gundlach, A.L., 2006. Comparative localization of leucine-rich repeat-containing G-protein-coupled receptor-7 (RXFP1) mRNA and [³³P]-relaxin binding sites in rat brain: Restricted somatic co-expression a clue to relaxin action? *Neuroscience* 141, 329–344.

Ma, S., Shen, P.-J., Sang, Q., Lanciego, J.L., Gundlach, A.L., 2009. Distribution of relaxin-3 mRNA and immunoreactivity and RXFP3-binding sites in the brain of the macaque, *Macaca fascicularis*. *Ann N Y Acad Sci* 1160, 256–258.

Ma, S., Smith, C.M., Blasiak, A., Gundlach, A.L., 2017. Distribution, physiology and pharmacology of relaxin-3/RXFP3 systems in brain. *Br J Pharmacol* 174, 1034–1048.

Madrazo, I., Franco-Bourland, R.E., León-Meza, V.M., Mena, I., 1987. Intraventricular Somatostatin-14, Arginine Vasopressin, and Oxytocin: Analgesic Effect in a Patient with Intractable Cancer Pain. *Stereotact Funct Neurosurg* 50, 427–431.

Manning, M., Misicka, A., Olma, A., Bankowski, K., Stoev, S., Chini, B., Durroux, T., Mouillac, B., Corbani, M., Guillon, G., 2012. Oxytocin and Vasopressin Agonists and Antagonists as Research Tools and Potential Therapeutics. *J Neuroendocrinol* 24, 609–628.

Martínez-Lorenzana, G., Espinosa-López, L., Carranza, M., Aramburo, C., Paz-Tres, C., Rojas-Piloni, G., Condés-Lara, M., 2008. PVN electrical stimulation prolongs withdrawal latencies and releases oxytocin in cerebrospinal fluid, plasma, and spinal cord tissue in intact and neuropathic rats. *Pain* 140, 265–273.

Martins, I., Tavares, I., 2017. Reticular Formation and Pain: The Past and the Future. *Front. Neuroanat.* 11, 51.

Mascagni, F., McDonald, A.J., 2003. Immunohistochemical characterization of cholecystokinin containing neurons in the rat basolateral amygdala. *Brain Research* 976, 171–184.

Matsumoto, M., Kamohara, M., Sugimoto, T., Hidaka, K., Takasaki, J., Saito, T., Okada, M., Yamaguchi, T., Furuichi, K., 2000. The novel G-protein coupled receptor SALPR shares sequence similarity with somatostatin and angiotensin receptors. *Gene* 248, 183–189.

McDonald, A.J., Mascagni, F., 2002. Immunohistochemical characterization of somatostatin containing interneurons in the rat basolateral amygdala. *Brain Research* 943, 237–244.

Menant, O., Andersson, F., Zelena, D., Chaillou, E., 2016. The benefits of magnetic resonance imaging methods to extend the knowledge of the anatomical organisation of the periaqueductal gray in mammals. *J Chem Neuroanat* 77, 110–120.

Millan, M.J., 1999. The induction of pain: an integrative review. *Progress in Neurobiology* 57, 1–164.

Millan, M.J., 2002. Descending control of pain. *Progress in Neurobiology*.

Mills, S.E.E., Nicolson, K.P., Smith, B.H., 2019. Chronic pain: a review of its epidemiology and associated factors in population-based studies. *Br J Anaesth* 123, e273–e283.

Miranda-Cardenas, Y., Rojas-Piloni, G., Martínez-Lorenzana, G., Rodríguez-Jiménez, J., López-Hidalgo, M., Freund-Mercier, M.J., Condés-Lara, M., 2006. Oxytocin and electrical stimulation of the paraventricular hypothalamic nucleus produce antinociceptive effects that are reversed by an oxytocin antagonist. *Pain* 122, 182–189.

Moraes-Ferreira, R., Brandao-Rangel, M.A.R., Gibson-Alves, T.G., Silva-Reis, A., Souza-Palmeira, V.H., Aquino-Santos, H.C., Frison, C.R., Oliveira, L.V.F., Albertini, R., Vieira, R.P., 2022. Physical Training Reduces Chronic Airway Inflammation and Mediators of Remodeling in Asthma. *Oxid Med Cell Longev* 2022, 5037553.

Moreau, J.-L., Fields, H.L., 1986. Evidence for GABA involvement in midbrain control of medullary neurons that modulate nociceptive transmission. *Brain Research* 397, 37–46.

Moreno-López, Y., Martínez-Lorenzana, G., Condés-Lara, M., Rojas-Piloni, G., 2013. Identification of oxytocin receptor in the dorsal horn and nociceptive dorsal root ganglion neurons.

Neugebauer, V., Mazzitelli, M., Cragg, B., Ji, G., Navratilova, E., Porreca, F., 2020. Amygdala, neuropeptides, and chronic pain-related affective behaviors. *Neuropharmacology* 170, 108052.

Noh, A.S.M., Chuan, T.D., Khir, N.A.M., Zin, A.A.M., Ghazali, A.K., Long, I., Ab Aziz, C.B., Ismail, C.A.N., 2021. Effects of different doses of complete Freund's adjuvant on nociceptive behaviour and inflammatory parameters in polyarthritic rat model mimicking rheumatoid arthritis. *PLoS One* 16, e0260423.

Ohlsson, B., Truedsson, M., Bengtsson, M., Torstenson, R., Sjolund, K., Bjornsson, E.S., Simren, M., 2005. Effects of long-term treatment with oxytocin in chronic constipation; a double blind, placebo-controlled pilot trial. *Neurogastroenterol Motil* 17, 697–704.

Orr, P.M., Shank, B.C., Black, A.C., 2017. The Role of Pain Classification Systems in Pain Management. *Crit Care Nurs Clin North Am* 29, 407–418.

Otero-García, M., Agustín-Pavón, C., Lanuza, E., Martínez-García, F., 2016. Distribution of oxytocin and co-localization with arginine vasopressin in the brain of mice. *Brain Struct Funct* 221, 3445–3473.

Paxinos, G., Franklin, K.B.J., 2013. Paxinos and Franklin's the mouse brain in stereotaxic coordinates, 4th ed. ed. Boston : Elsevier/Academic Press, Amsterdam.

Paxinos, G., Watson, C., 2013. The Rat Brain in Stereotaxic Coordinates. Elsevier Science.

Petersson, M., Alster, P., Lundeberg, T., Uvnäs-Moberg, K., 1996. Oxytocin increases nociceptive thresholds in a long-term perspective in female and male rats. *Neurosci Lett* 212, 87–90.

Petersson, M., Wiberg, U., Lundeberg, T., Uvnäs-Moberg, K., 2001. Oxytocin decreases carrageenan induced inflammation in rats. *Peptides* 22, 1479–1484.

Pidoplichko, V.I., Aroniadou-Anderjaska, V., Figueiredo, T.H., Wilbraham, C., Braga, M.F.M., 2021. Increased inhibitory activity in the basolateral amygdala and decreased anxiety during estrus: A potential role for ASIC1a channels. *Brain Research* 1770, 147628.

Principles Of Neural Science, Fifth KANDEL, n.d.

Qian, T., Wang, H., Wang, P., Geng, L., Mei, L., Osaka, T., Wang, L., Tang, Y., Kania, A., Grinevich, V., Stoop, R., Lin, D., Luo, M., Li, Y., 2023. A genetically encoded sensor measures temporal oxytocin release from different neuronal compartments. *Nat Biotechnol* 41, 944–957.

Raja, S.N., Meyer, R.A., Campbell, J.N., 1988. Peripheral mechanisms of somatic pain. *Anesthesiology* 68, 571–590.

Reynolds, D.V., 1969. Surgery in the Rat during Electrical Analgesia Induced by Focal Brain Stimulation. *Science* 164, 444–445.

Robinson, D.R., Gebhart, G.F., 2008. Inside information: the unique features of visceral sensation. *Mol Interv* 8, 242–253.

Ryan, P.J., Ross, S.I., Campos, C.A., Derkach, V.A., Palmiter, R.D., 2017. Oxytocin-receptor-expressing neurons in the parabrachial nucleus regulate fluid intake. *Nat Neurosci* 20, 1722–1733.

Samineni, V.K., Grajales-Reyes, J.G., Copits, B.A., O'Brien, D.E., Trigg, S.L., Gomez, A.M., Bruchas, M.R., 2017. Divergent Modulation of Nociception by Glutamatergic and GABAergic Neuronal Subpopulations in the Periaqueductal Gray.

Scott, D.J., Layfield, S., Riesewijk, A., Morita, H., Tregear, G.W., Bathgate, R. a. D., 2005. Characterization of the mouse and rat relaxin receptors. *Ann N Y Acad Sci* 1041, 8–12.

Shabanoor, F., Akhter Hossain, M., Ryan, P.J., Belgi, A., Layfield, S., Kocan, M., Zhang, S., Samuel, C.S., Gundlach, A.L., Bathgate, R.A.D., Separovic, F., Wade, J.D., 2012. Minimization of Human Relaxin-3 Leading to High-Affinity Analogues with

Increased Selectivity for Relaxin-Family Peptide 3 Receptor (RXFP3) over RXFP1. *J. Med. Chem.* 55, 1671–1681.

Smith, C.M., Shen, P.-J., Banerjee, A., Bonaventure, P., Ma, S., Bathgate, R.A.D., Sutton, S.W., Gundlach, A.L., 2010. Distribution of relaxin-3 and RXFP3 within arousal, stress, affective, and cognitive circuits of mouse brain. *J. Comp. Neurol.* 518, 4016–4045.

Spampanato, J., Polepalli, J., Sah, P., 2011. Interneurons in the basolateral amygdala. *Neuropharmacology* 60, 765–773.

Sudo, S., Kumagai, J., Nishi, S., Layfield, S., Ferraro, T., Bathgate, R.A.D., Hsueh, A.J.W., 2003. H3 Relaxin Is a Specific Ligand for LGR7 and Activates the Receptor by Interacting with Both the Ectodomain and the Exoloop 2. *Journal of Biological Chemistry* 278, 7855–7862.

Sun, W., Zhou, Q., Ba, X., Feng, X., Hu, X., Cheng, X., Liu, T., Guo, J., Xiao, L., Jiang, J., Xiong, D., Hao, Y., Chen, Z., Jiang, C., 2018. Oxytocin Relieves Neuropathic Pain Through GABA Release and Presynaptic TRPV1 Inhibition in Spinal Cord. *Front Mol Neurosci* 11, 248.

Sutton, S.W., Bonaventure, P., Kuei, C., Roland, B., Chen, J., Nepomuceno, D., Lovenberg, T.W., Liu, C., 2004. Distribution of G-Protein-Coupled Receptor (GPCR)135 Binding Sites and Receptor mRNA in the Rat Brain Suggests a Role for Relaxin-3 in Neuroendocrine and Sensory Processing. *Neuroendocrinology* 80, 298–307.

Taati, M., Tamaddonfard, E., 2018. Ventrolateral orbital cortex oxytocin attenuates neuropathic pain through periaqueductal gray opioid receptor. *Pharmacol Rep* 70, 577–583.

Talbot, K., Madden, V.J., Jones, S.L., Moseley, G.L., 2019. The sensory and affective components of pain: are they differentially modifiable dimensions or inseparable aspects of a unitary experience? A systematic review. *Br J Anaesth* 123, e263–e272.

Tanaka, M., Iijima, N., Miyamoto, Y., Fukusumi, S., Itoh, Y., Ozawa, H., Ibata, Y., 2005. Neurons expressing relaxin 3/INSL 7 in the nucleus incertus respond to stress. *European Journal of Neuroscience* 21, 1659–1670.

Tang, Y., Chen, Z., Tao, H., Li, C., Zhang, X., Tang, A., Liu, Y., 2014. Oxytocin activation of neurons in ventral tegmental area and interfascicular nucleus of mouse midbrain. *Neuropharmacology* 77, 277–284.

Taniguchi, H., He, M., Wu, P., Kim, S., Paik, R., Sugino, K., Kvitsani, D., Fu, Y., Lu, J., Lin, Y., Miyoshi, G., Shima, Y., Fishell, G., Nelson, S.B., Huang, Z.J., 2011. A Resource of Cre Driver Lines for Genetic Targeting of GABAergic Neurons in Cerebral Cortex. *Neuron* 71, 995–1013.

Taylor, J.H., McCann, K.E., Ross, A.P., Albers, H.E., 2020. Binding affinities of oxytocin, vasopressin and Manning compound at oxytocin and V1a receptors in male Syrian hamster brains. *J Neuroendocrinol* 32, e12882.

Terminology | International Association for the Study of Pain, n.d. . International Association for the Study of Pain (IASP).

Thompson, J.M., Neugebauer, V., 2017. Amygdala Plasticity and Pain. *Pain Res Manag* 2017, 8296501.

Tirko, N.N., Eyring, K.W., Carcea, I., Mitre, M., Chao, M.V., Froemke, R.C., Tsien, R.W., 2018. Oxytocin Transforms Firing Mode of CA2 Hippocampal Neurons. *Neuron* 100, 593-608.e3.

Treede, R.-D., Rief, W., Barke, A., Aziz, Q., Bennett, M.I., Benoliel, R., Cohen, M., Evers, S., Finnerup, N.B., First, M.B., Giamberardino, M.A., Kaasa, S., Kosek, E., Lavand'homme, P., Nicholas, M., Perrot, S., Scholz, J., Schug, S., Smith, B.H., Svensson, P., Vlaeyen, J.W.S., Wang, S.-J., 2015. A classification of chronic pain for ICD-11. *Pain* 156, 1003–1007.

Van Der Westhuizen, E.T., Christopoulos, A., Sexton, P.M., Wade, J.D., Summers, R.J., 2010. H2 Relaxin Is a Biased Ligand Relative to H3 Relaxin at the Relaxin Family Peptide Receptor 3 (RXFP3). *Mol Pharmacol* 77, 759–772.

Van Der Westhuizen, E.T., Sexton, P.M., Bathgate, R.A.D., Summers, R.J., 2005. Responses of GPCR135 to Human Gene 3 (H3) Relaxin in CHO-K1 Cells Determined by Microphysiometry. *Annals of the New York Academy of Sciences* 1041, 332–337.

Vanegas, H., Barbaro, N.M., Fields, H.L., 1984. Midbrain stimulation inhibits tail-flick only at currents sufficient to excite rostral medullary neurons. *Brain Research* 321, 127–133.

Veinante, P., Yalcin, I., Barrot, M., 2013. The amygdala between sensation and affect: a role in pain.

Wahis, J., Baudon, A., Althammer, F., Kerspern, D., Goyon, S., Hagiwara, D., Lefevre, A., Bartczko, L., Boury-Jamot, B., Bellanger, B., Abatis, M., Da Silva Gouveia, M., Benusiglio, D., Eliava, M., Rozov, A., Weinsanto, I., Knobloch-Bollmann, H.S., Kirchner, M.K., Roy, R.K., Wang, H., Pertin, M., Inquimbert, P., Pitzer, C., Siemens, J., Goumon, Y., Boutrel, B., Lamy, C.M., Decosterd, I., Chatton, J.-Y., Rouach, N., Young, W.S., Stern, J.E., Poisbeau, P., Stoop, R., Darbon, P., Grinevich, V., Charlet, A., 2021. Astrocytes mediate the effect of oxytocin in the central amygdala on neuronal activity and affective states in rodents. *Nat Neurosci* 24, 529–541.

Wang, J.-W., Lundeberg, T., Yu, L.-C., 2003. Antinociceptive role of oxytocin in the nucleus raphe magnus of rats, an involvement of μ -opioid receptor. *Regulatory Peptides* 115, 153–159.

Wang, X., Traub, R.J., Murphy, A.Z., 2006. Persistent pain model reveals sex difference in morphine potency. *American Journal of Physiology-Regulatory, Integrative and Comparative Physiology* 291, R300–R306.

Wang, Y.-F., Hatton, G.I., 2006. Mechanisms underlying oxytocin-induced excitation of supraoptic neurons: prostaglandin mediation of actin polymerization. *J Neurophysiol* 95, 3933–3947.

Watanabe, Y., Miyamoto, Y., Matsuda, T., Tanaka, M., 2011. Relaxin-3/INSL7 regulates the stress-response system in the rat hypothalamus. *J Mol Neurosci* 43, 169–174.

West, S.J., Bannister, K., Dickenson, A.H., Bennett, D.L., 2015. Circuitry and plasticity of the dorsal horn – Toward a better understanding of neuropathic pain. *Neuroscience* 300, 254–275.

Wierenga, C.J., Müllner, F.E., Rinke, I., Keck, T., Stein, V., Bonhoeffer, T., 2010. Molecular and Electrophysiological Characterization of GFP-Expressing CA1 Interneurons in GAD65-GFP Mice. *PLoS ONE* 5.

Wilkinson, T.N., Speed, T.P., Tregebar, G.W., Bathgate, R.A.D., 2005. Coevolution of the Relaxin-Like Peptides and Their Receptors. *Annals of the New York Academy of Sciences* 1041, 534–539.

Wolff, S.B.E., Gründemann, J., Tovote, P., Krabbe, S., Jacobson, G.A., Müller, C., Herry, C., Ehrlich, I., Friedrich, R.W., Letzkus, J.J., Lüthi, A., 2014. Amygdala interneuron subtypes control fear learning through disinhibition. *Nature* 509, 453–458.

Xiao, L., Priest, M.F., Nasenbeny, J., Lu, T., Kozorovitskiy, Y., 2017. Biased Oxytocinergic Modulation of Midbrain Dopamine Systems. *Neuron* 95, 368-384.e5.

Xie, L., Wu, H., Chen, Q., Xu, F., Li, H., Xu, Q., Jiao, C., Sun, L., Ullah, R., Chen, X., 2023. Divergent modulation of pain and anxiety by GABAergic neurons in the ventrolateral periaqueductal gray and dorsal raphe. *Neuropsychopharmacol.* 48, 1509–1519.

Yang, D., Wang, Y., Qi, T., Zhang, X., Shen, L., Ma, J., Pang, Z., Lal, N.K., McClatchy, D.B., Wang, K., Xie, Y., Polli, F., Maximov, A., Augustine, V., Cline, H.T., Yates, J.R., Ye, L., 2023. Phosphorylation of pyruvate dehydrogenase marks the inhibition of in vivo neuronal activity. *bioRxiv* 2023.03.13.532494.

Yang, J., Yang, Y., Chen, J.-M., Liu, W.-Y., Wang, C.-H., Lin, B.-C., 2007. Central oxytocin enhances antinociception in the rat. *Peptides* 28, 1113–1119.

Yeung, J.C., Yaksh, T.L., Rudy, T.A., 1977. Concurrent mapping of brain sites for sensitivity to the direct application of morphine and focal electrical stimulation in the production of antinociception in the rat: Pain 4, 23–40.

Young, W.S., Gainer, H., 2003. Transgenesis and the study of expression, cellular targeting and function of oxytocin, vasopressin and their receptors. *Neuroendocrinology* 78, 185–203.

Yu, S.-Q., Lundeberg, T., Yu, L.-C., 2003. Involvement of oxytocin in spinal antinociception in rats with inflammation. *Brain Research* 983, 13–22.

Zhang, B., Qiu, L., Xiao, W., Ni, H., Chen, L., Wang, F., Mai, W., Wu, J., Bao, A., Hu, H., Gong, H., Duan, S., Li, A., Gao, Z., 2021. Reconstruction of the Hypothalamo-Neurohypophysial System and Functional Dissection of Magnocellular Oxytocin Neurons in the Brain. *Neuron* 109, 331-346.e7.

Résumé

Le traitement des douleurs est un enjeu important au vu des dizaines de millions de personnes souffrant de douleurs chroniques dans le monde. La douleur est modulée entre autre par des neuropeptides, en faisant des cibles thérapeutiques de choix.

Ainsi, j'ai tout d'abord travaillé sur la relaxine-3, un peptide synthétisé dans le *nucleus incertus* qui agit sur le récepteur RXFP3. L'activation de ce dernier dans l'amygdale entraîne une antidouleur transitoire chez le rongeur. Nous avons donc essayé de caractériser l'effet de l'activation de RXFP3 sur les circuits neuronaux de l'amygdale pour expliquer cet effet antidouleur. Notre étude a montré que l'activation de ce récepteur n'induit aucun changement sur les neurones de l'amygdale.

Je me suis ensuite intéressé à l'ocytocine, un peptide hypothalamique déjà connu pour avoir un effet antidouleur. Dans ce cadre, j'ai utilisé un nouvel outil permettant de détecter la présence d'ocytocine : le Grab_{OT}. J'ai ainsi pu en faire la caractérisation pharmacologique ainsi que le mettre en application dans une étude où nous avons montré un circuit oxytocinergique impliquant la substance grise péréiaqueducale ventrolatérale dans la médiation de son effet antidouleur.

Mots clefs : douleur, relaxine-3, RXFP3, ocytocine, Grab_{OT}

Résumé en anglais

Treatment of pain is a major challenge knowing that dozens of millions of people suffer from chronic pain worldwide. Pain is modulated among others by neuropeptides, making them suitable therapeutical targets.

I started working on the relaxin-3, a peptide synthesized in the brain by the *nucleus incertus* that acts on the receptor RXFP3. The activation of this receptor in the amygdala triggers transitory analgesia in rodents. Therefore, we tried to characterize the effect of the modulation of RXFP3 on the neuronal circuits of the amygdala that could explain the analgesic effect. Our study showed that the activation of RXFP3 does not induce any changes on the neurons in the amygdala.

I then moved on the oxytocin, a hypothalamic peptide already known for its analgesic effect. I used a newly developed tool called Grab_{OT} that detect the presence of oxytocin in the extracellular space. I first performed a pharmacological characterization of this receptor and I had the opportunity to use it in a study where we showed an oxytocinergic circuit using the ventrolateral periaqueductal gray as a relay to mediate its analgesic effect.

Key words: pain, relaxin-3, RXFP3, oxytocin, Grab_{OT}